THE UNIVERSITY OF CHICAGO

MECHANISMS UNDERLYING SYNAPTIC CONNECTIVITY AND PLASTICITY IN THE DROSOPHILA NEUROMUSCULAR SYSTEM

A DISSERTATION SUBMITTED TO

THE FACULTY OF THE DIVISION OF THE BIOLOGICAL SCIENCES

AND THE PRITZKER SCHOOL OF MEDICINE

IN CANDIDACY FOR THE DEGREE OF

DOCTOR OF PHILOSOPHY

COMMITTEE ON DEVELOPMENT, REGENERATION, AND STEM CELL BIOLOGY

BY

YUPU WANG

CHICAGO, ILLINOIS

JUNE 2022

TABLE OF CONTENTS

LIST OF FIGURES

LIST OF TABLES

ACKNOWLEDGEMENTS

My graduate career, including the thesis presented here, would never have been possible without the support from my encouraging mentor, inspiring colleagues, and my beloved friends and family. The four years I spent in the University of Chicago are far more than just obtaining a Ph.D. degree; it is an embrace of a new culture, a challenge to gain independence, and a chance to further develop my personality.

To begin, I thank Dr. Robert Carrillo, who I first talked to in a bar during DRSB recruitment. I work with Robert in an extremely seamless manner sponsored by his open-mind and the friendly lab environment he created and maintains. I am grateful for his trust allowing me to explore scientific questions that interested me, and his endless emotional support during the hardest time in my graduate life. Beyond science, his humorous and thoughtful ideas, 24-hour open office, and our 2AM texts will remain in my memory forever.

In the Carrillo lab, I also have the greatest colleagues helping me not only in science, but maybe more importantly, to adapt to the new culture. The almighty Dr. James Ashley has knowledge for all questions, covering technology, research literature, science history, and even house building. The phrase I probably used more in the past four years was - “Question, James!”. I also deeply thank my friend Meike Lobb-Rabe, who brings enormous vitality into the lab and engages me as a science nerd. We discuss, collaborate, and help each other actively and unreservedly. I am also excited to welcome our new graduate students, Ruiling Zhang and Rio Salazar, who bring new blood, ideas, and personalities into the lab and will surely make new discoveries in the Carrillo lab.

I would like to give my deepest thank to Dr. Rick Fehon, who accepted me as a REU student in his lab in the summer of 2017. Being a meticulous scientist with huge enthusiasm and

rigorous responsibility, Rick became my role model. His gentle but encouraging mentorship inspired me to think deeply about my research and continues to motivate me. Two previous lab members, Jiajie Xu and William Yee, also helped me tremendously in my life, research, and graduate school applications. In addition, I am grateful for the international REU program, founded by Dr. Ilaria Rebay, Dr. Wei-Jen Tang, and Dr. Chenjian Li, as it allowed me to gain research experience and training in United States when I was an undergraduate student. The Fehon lab and the REU program brought me to the University of Chicago and introduced me to the world of *Drosophila*.

I also thank my thesis committee, Dr. Rick Fehon, Dr. Ellie Heckscher, and Dr. David Pincus for their support and encouragement to pursue my scientific questions, their technical and conceptual suggestions, and the "kind" pressure they put on me. My committee gave me enormous support and freedom, and I appreciate their support in allowing my early graduation to complete my Ph.D. studies.

In addition, I want to thank the 9th floor fly community. I will miss the exchange of ideas and the vivid chats in the fly room, and I am very glad to see the atmosphere is returning after the two years of isolation due to COVID restrictions. I also thank the DRSB cohort and past DRSB students for supporting each other through classes, research, and the quarantine time.

Beyond the University of Chicago, I would like to thank my friends here in United States and in China, especially Sihao Huang, Xiao Sun, Mingqi Dong, Shihong Gao, Dr. Ruilin Tian, and many others. Although we are distributed in different cities, we stay connected and support each other in every moment. I also thank my student mentor in Peking University, Dr. Yunyun Gong, who bestowed upon me admirable research ethics and showed me the beauty of electrophysiology, which became the technique used most during my graduate research.

Finally, I want to thank my parents, Hong Liu and Kai Wang, and my extended family. It was a hard decision to send their only child thousands of miles away to pursue his interests even when they were in urgent need of care due to health complications. Despite these challenges, I am fortunate to have such enlightened and strong people around me who support and love me. I believe our hearts are interconnected, and we will be proud of each other every moment.

I came to the United States for the “American dream”, and now I leave with a conscious mind and no regrets.

STATEMENT OF CONTRIBUTION

The majority of the work described in this thesis is my own; however, some are collaborations with colleagues. For the work described in Chapter 2, Dr. James Ashley and Meike Lobb-Rabe helped with Ib bouton counting (Figure 3.4, 3.8 and 3.9). For the work described in Chapter 3, most *dpr/DIP-GAL4* lines were generously provided by Dr. Kai Zinn and Dr. Hugo Bellen. Also, Dr. James Ashley, and previous lab members, Veera Anand and Purujit Chatterjee, helped with expression profiling. Meike Lobb-Rabe examined the expression level of *dprs* and *DIPs* in these *GAL4* lines (Figure 2.2). For exploratory experiments described in the Appendix, previous lab member Violet Sorrentino re-balanced deficiency stocks and screened a subset. Rio Salazar and Luciano Simonetta assisted with embryo dissections of *hkb* mutants. Sihao Huang helped with the Python coding used in AZ position mapping. All other experiments presented in this thesis were performed and analyzed by me under the supervision of Dr. Robert Carrillo.

ABSTRACT

Our daily life is filled with locomotion and emotion, two processes controlled by our sophisticated and delicate nervous system. During development, billions of neurons make connections with specific synaptic partners in both central and peripheral nervous systems. How such specificity is achieved and maintained is a long-standing question in neurobiology. A prevailing hypothesis is that cell surface proteins function as a “lock-and-key” to guide the recognition between pre- and postsynaptic neurons. We focus on two *Drosophila* immunoglobin subfamilies, the Dprs (defective proboscis extension response, 21 members) and DIPs (Dpr-interacting proteins, 11 members). Dprs and DIPs can form homophilic or heterophilic interactions, and these interactions are proposed to guide synaptic recognition. A small subset of Dprs and DIPs have been examined in larvae and adults, but most Dpr-DIP pairs have not been studied, in part, due to the likely redundancy and their unknown expression patterns.

To gain a deeper understanding of Dprs and DIPs, I conducted an expression profiling. We generated a Dpr/DIP GAL4 collection and examined their expression in larval sensory neurons and the neuromuscular system. I described detailed expression maps of each *dpr* and *DIP* in all larval sensory neurons, motor neurons, glial cells, and muscles. I found that similar neurons express similar *dprs* and *DIPs*. In addition, I uncovered previously unidentified motor neurons using these GAL4 lines and found specific *dprs* and *DIPs* that are required for synaptic recognition. In summary, the expression map and the GAL4 lines will provide the field an entry point and a genetic toolbox to explore the functions of Dprs and DIPs.

Dpr-DIP interactions were implicated in synaptic connectivity, and we wondered whether neuromuscular function was also affected when perturbing connectivity. In the *Drosophila* larval neuromuscular system, each muscle normally receives two glutamatergic motor neuron inputs.

We asked whether loss of one input will perturb synaptic function or instead, will induce morphological and/or functional compensatory changes from the nearby motor neuron input. Interestingly, we found that ablation of one neuron significantly induced morphological and functional compensation from adjacent healthy neurons – a process we termed "cross-neuron plasticity". We examined multiple motor neuron-muscle pairs and found different motor neurons have different compensability. Next, we investigated the mechanism underlying cross-neuron plasticity and found that an engulfment receptor, Draper, is required. In *draper* mutants, significant debris from degenerating neurons accumulated in glial cells and healthy neurons lose both morphological and functional plasticity, suggesting that Draper is required to transmit a signal to nearby healthy neurons. This study has implications for neurodegenerative diseases marked by synaptic dysfunction and eventual neuron death as cross-neuron plasticity could provide compensatory functional changes from the remaining neurons.

Taken together, my Ph.D. work focused on Dpr-DIP mediated synaptic recognition and cross-neuron plasticity. I described the expression of *dprs* and *DIPs* in the *Drosophila* larval nervous system and identified a new type of synaptic plasticity which empowers healthy neurons to respond to nearby neuronal cell death. These studies have expanded our understanding of synaptic connectivity and plasticity and have generated many exciting, testable hypotheses.

CHAPTER 1
INTRODUCTION

The way we perceive and respond to the environment relies on our precise and robust neuronal connections. In the human brain, ~90 billion neurons interconnect with each other to form complex but stereotyped neural networks (Herculano-Houzel, 2012). During development, each neuron must identify the correct synaptic partners among thousands of potential targets. Such specificity is achieved through a series of steps including axon pathfinding, partner recognition, and synaptic pruning. In the past few decades, researchers have identified genes and mechanisms underlying these processes in different neural circuits and in different model organisms from invertebrates like *Drosophila* and *C. elegan*s to vertebrates such as zebrafish and mice. Many of these genes are homologous to those involved in human nervous system development and diseases (Sanes and Zipursky, 2020, 2010). However, our current knowledge of how synaptic connections are specified is still relatively limited as only a few recognition molecules are characterized compared to the number of specific neural connections. Although many potential recognition molecules have been proposed, their function are yet to be explored. In addition, the downstream signaling pathways of these recognition molecules is not clear. Answering these questions will require systematic analyses of downstream components and technological innovations.

Once a specific neural connection is established, it is important to maintain its synaptic function to support robust brain operation. Although neurons are well protected by the dura and skull, they can still encounter external perturbations like physical injury and infection, or internal perturbations like immune responses and ageing. Interestingly, neurons or synapses can fine tune their function to maintain a homeostatic point; this process is known as synaptic plasticity (Citri

and Malenka, 2008). Several synaptic plasticity mechanisms have been found when perturbations occur either pre- or postsynaptically (Davis and Müller, 2015; Frank et al., 2020). However, the field has mostly focused on how synapses autonomously respond to perturbations and largely ignored how such perturbations affect nearby healthy neurons or synapses.

During aging or neurodegenerative diseases, such as amyotrophic lateral sclerosis (ALS), Alzheimer's disease, and brain stroke, neuronal cell death leads to a complete loss of neurons and the associated synapses, causing a larger defect beyond merely synaptic perturbation (Fricker et al., 2018). Extensive research and clinical work have focused on how to slow down neuronal cell death progression or to replace the dead neurons to restore function. However, it is of great interest to examine how the nearby healthy neurons respond to the death of their neighbors as these healthy neurons serve as great candidates to restore circuit function. Indeed, it has been well documented that sensory loss leads to adaption of the brain circuits to utilize the remaining senses to navigate, known as cross-modal recruitment and compensatory plasticity (Brussel et al., 2011; Lee and Whitt, 2015). In addition, (Hutson et al., 2019) observed an increase of dendritic branching in the remaining neurons in a spinal cord injury mouse model. Moreover, (Merlo et al., 2019) found that in Alzheimer's disease, the remaining healthy brain areas show increased activity. These studies provide exciting hints about the potential of the remaining healthy neurons to compensate the circuit damage. However, the phenotypes observed in these studies are only examined globally and have not been characterized in detail nor are the underlying mechanisms known.

My thesis work focused on the areas of synaptic connectivity and plasticity using the *Drosophila* nervous system as a model. First, I asked how synaptic connectivity is faithfully established during development through the interaction of CSPs. Second, I described

morphological and functional compensation in healthy neurons after ablating nearby neurons. I also characterized a potential mechanism for this synaptic plasticity. My work provides insights for how CSPs instruct nervous system wiring and how healthy neurons respond to adjacent neuron death, as seen in aging and neurodegenerative diseases, and sheds light on potential new therapies to recover circuit function after partial neuronal loss.

1.1 The *Drosophila* larval nervous system is an ideal model to study synaptic development and plasticity

Invertebrate models offer an extensive variety of experimental tools to address outstanding questions underlying developmental processes and diseases. *Drosophila* is an excellent invertebrate model utilized to study signaling pathways, embryo development, and tissue morphogenesis, due to their short lifespan (Figure 1.1), the genetic accessibility, and most importantly, the common developmental mechanisms shared with vertebrates.

The small size of *Drosophila* larvae and their semi-transparent epidermis facilitate their examination and access to the nervous system. The larval body plan is segmentally repeated including three thoracic segments (numbered T1 to T3), and nine abdominal segments (numbered A1 to A9) (Bloom, 1996). Each abdominal segment has a similar arrangement and layout of cells including the body wall muscles and the axons that innervate them. The larval nervous system is “simple” compared to the billions of connections in many vertebrates, but it still resembles the sophisticated vertebrate nervous system due to similar circuit assembly, shared neurotransmitters, and conserved developmental and plasticity mechanisms, thus making it a great model to approach complex neurobiology questions.

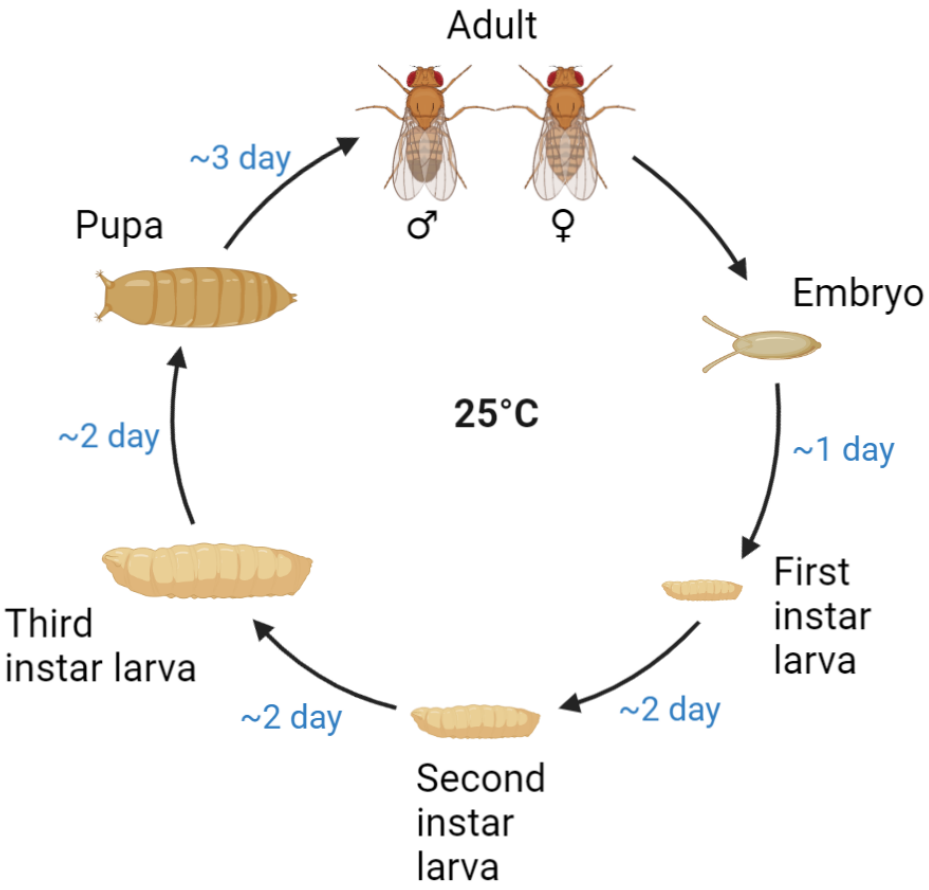

Figure 1.1 **Development and lifespan of *Drosophila melanogaster*.**
The larval stage of *Drosophila* takes about 5-6 days at 25°C to complete. Three instar stages transition the animal from embryo to pupa including first, second and third instar stages. The body structure is established by first instar and then expands in size during larval development.

1.1.1 Overview of the *Drosophila* larval nervous system

The *Drosophila* larval nervous system is comprised of two major components, the central nervous system (CNS) and the peripheral nervous system (PNS) (Figure 1.2), and it is established within the 24 hours of embryonic development (Figure 1.1) (Crews, 2019). The CNS contains approximately 10,000 neurons including 2,000 neurons located in the brain and the remaining in the ventral nerve cord (VNC) (Heckscher et al., 2014).

The larval VNC integrates and processes sensory motor control information as it contains the axon terminals of sensory neurons (SNs), interneurons, cell bodies and dendrites of motor neurons (MNs), and multiple types of glial cells (Niven et al., 2008; Urbach et al., 2016). SNs in the PNS receive external stimulation or proprioceptive information and transmit to the VNC where they connect to interneurons. Interneurons form a complex connectome to process information and transmit to MNs that innervate peripheral muscle fibers through neuromuscular junctions (NMJs) and instruct muscle contractions (Figure 1.2) (Gowda et al., 2021).

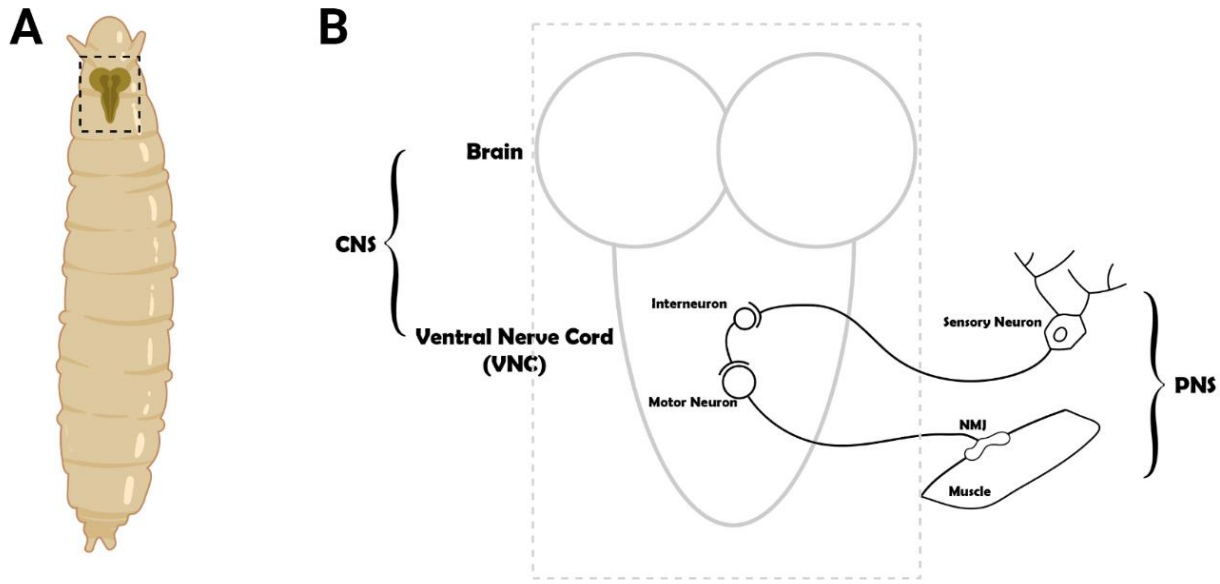

Figure 1.2 **Schematic of the *Drosophila* larval CNS and PNS.**
(A) The larval CNS is located at the anterior of the animal whereas the PNS is distributed along the body wall. (B) The larval CNS contains the brain and the VNC, which resemble the vertebrate brain and spinal cord, respectively. The VNC is also segmented (not shown in this schematic) and interneurons within the VNC receive inputs from sensory neurons and output through MNs to body wall muscles.

1.1.1.1 The ventral nerve cord (VNC)

The segmentally repeated *Drosophila* larval VNC resembles the vertebrate spinal cord albeit with fewer segments and significantly less neurons. In the VNC, each segment has a

defined set of MNs and interneurons surrounded by glial cells. The cell bodies are located in the outer layer of the VNC known as the cortex, and axons and dendrites project into the center region called the neuropil where synaptic connections are formed (Figure 1.3) (Ito et al., 1995).

The cells in each hemineuromere are generated from about 100 neuroblasts that divide and differentiate in a highly stereotyped manner (Urbach and Technau, 2003; Walsh and Doe, 2017). The location of each cell body is known, and each cell and its dendrites and axon are insulated by glial processes (Kottmeier et al., 2020). As the sensory and motor circuit processing centers, each hemineuromere receives and sends information through one nerve bundle which contains the incoming axons of SNs, the outgoing axons of MNs, and several peripheral glial cell types.

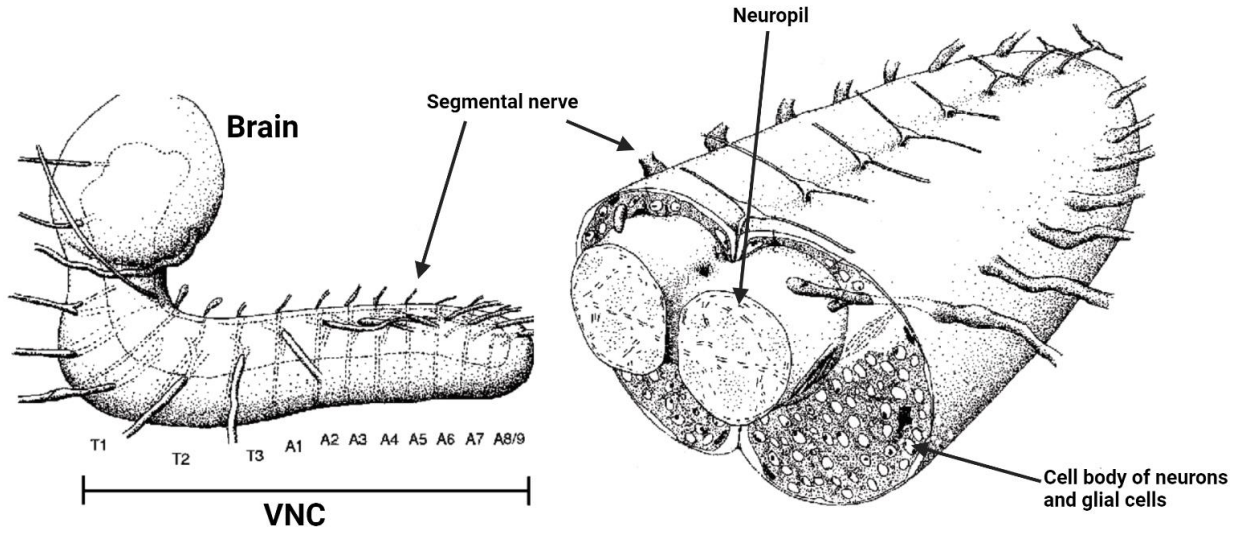

Figure 1.3 **Structure of the larval VNC.**
Cell bodies of neurons and glial cells are localized at the periphery of the VNC, and they extend their processes into the neuropil where synapses are formed. Images adapted from (Ito et al., 1995).

1.1.1.2 The sensory neurons (SNs)

In the PNS, each hemisegment has a set of SNs that respond to various external stimulation including heat and touch. Two morphologically distinct types of SNs can be classified in the larval body wall (Orgogozo and Grueber, 2005; Veling et al., 2019). Type-I SNs project a single dendrite that associates with chordotonal (ch) organs or external sensory (es) organs to detect mechanical and chemical stimuli. Type-II SNs are multidendritic neurons that transmit proprioceptive information. Type-II SNs can be further classified into bipolar dendrite (bd) neurons, tracheal dendrite (td) neurons, and dendritic arborization (da) neurons. The da neurons are then subdivided into four classes based on the complexity of their dendrite morphology (da-I, da-II, da-III and da-IV) (Figure 1B) (Grueber et al., 2002). A schematic of the SN map is provided in Figure 1.4A.

Although SNs from the same type are distributed throughout the hemisegment and project their afferent axons through different trajectories, their axon terminals innervate the same region in the VNC and contact common interneuron partners (Grueber et al., 2007; Landgraf et al., 2003b; Merritt and Murphey, 1992; Murphey et al., 1989). For example, the ventral, ventral', and lateral mechanosensory ch neurons all project to the ventral medial region of the VNC and share synapses with the same interneurons (Heckscher et al., 2015; Valdes-Aleman et al., 2021). Similarly, different classes of da neurons innervate unique sections of the VNC (Grueber et al., 2007; Merritt and Whitington, 1995; Schrader and Merritt, 2000) (Figure 1.4B). Therefore, the same class of SNs show similar axonal terminal morphology and share common synaptic partners in the VNC, suggesting that connectivity mechanisms may also be shared.

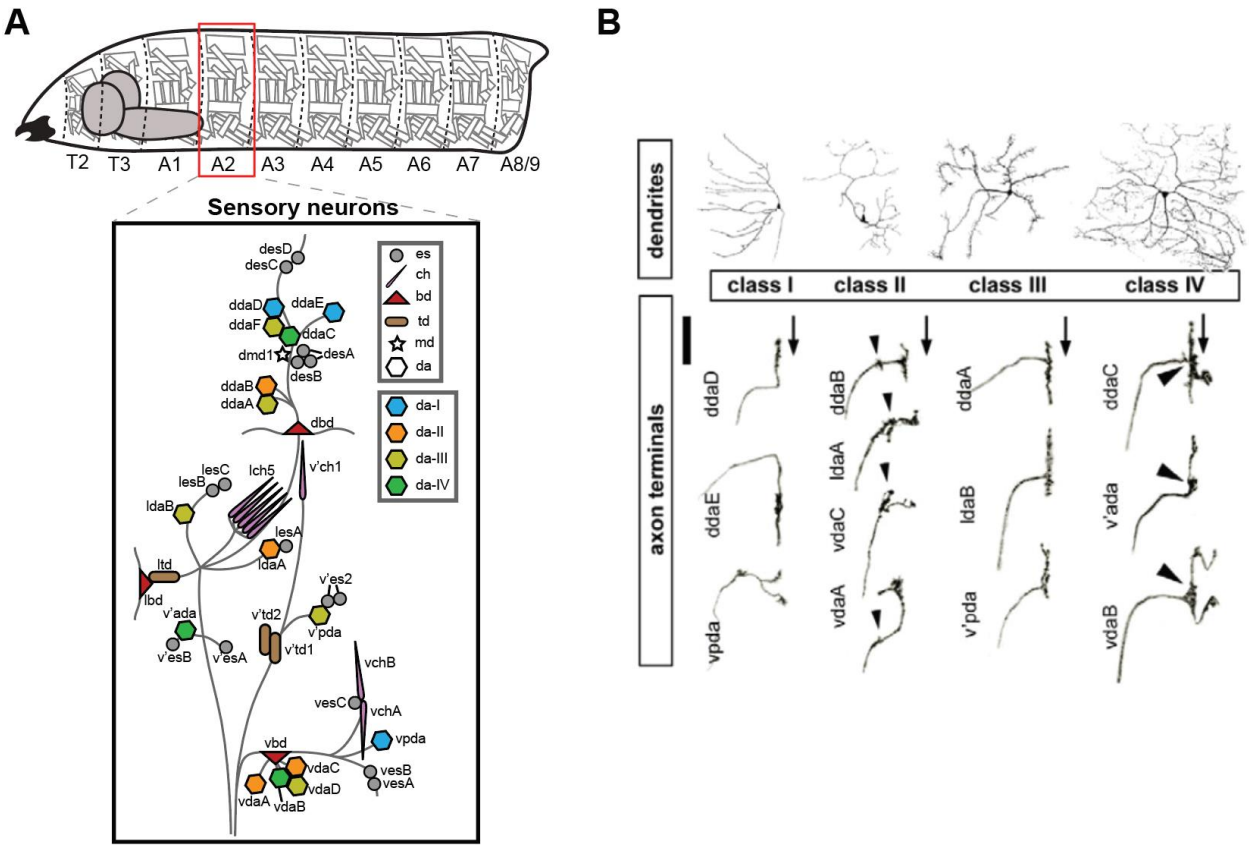

Figure 1.4 **Distribution and VNC projections of SNs.**
(A) In each hemisegment, different classes of SNs are located between muscles and epithelial tissue. Each color and shape combination represents a class of SNs, including es (grey), ch (purple), bd (red), td (brown), md (white star), da-I (blue), da-II (orange), da-III (yellow), da-IV (green) neurons. (B) Although the same class of da neurons are distributed far away from each other, they project to the same area in the VNC where they connect to common interneuron partners. Thus, they display similar axonal terminal morphology. Images adapted from (Grueber et al., 2007).

1.1.1.3 The motor neurons (MNs) and neuromuscular junction (NMJ)

Over four decades ago, the Jan and Jan lab introduced the larval neuromuscular system as a model to study synapse development and function, and it continues to be the system of choice in many labs investigating these areas of research (Jan and Jan, 1976). Each larval abdominal hemisegment consists of 30 muscles that are grouped into three major muscle groups – ventral,

lateral, and dorsal (Bate, 1990; Hooper, 1986; Zarin et al., 2019) – and further divided into six subgroups based on their orientation – dorsal longitudinal (DL), dorsal oblique (DO), ventral longitudinal (VL), ventral oblique (DO), ventral acute (VA), and lateral transverse (LT) (Figure 1.5A).

Innervating these muscles are 33 MNs classified as type-I (29), type-II (3), and type-III (1) based on their terminal morphology and neurotransmitter type (Choi et al., 2004; Hoang and Chiba, 2001; Landgraf et al., 1997; Zarin and Labrador, 2019). All MN axon terminals contain strings of bead-like structures called boutons which house the active zones (AZs) (Figure 1.5B-C). Type-I MNs are excitatory glutamatergic neurons, and they are further subdivided into type-I big (Ib) and type-I small (Is) according to their bouton size and innervation patterns. Ib MNs (in the larva named MN1-Ib to MN30-Ib corresponding to the muscle number) generally have larger boutons and innervate single muscle fibers whereas Is MNs have smaller boutons and innervate muscle groups (Choi et al., 2014; Lnenicka and Keshishian, 2000) (Figure 1.5B). The Is MN that innervates ventral muscles is referred to as the ventral common exciter (vCE), RP5, or MNISNb/d-Is, and the Is MN that innervates dorsal muscles is called the dorsal common exciter (dCE), RP2, or MNISN-Is (Broadus et al., 1995; Doe et al., 1988; Takizawa et al., 2007). Similarly, three neuromodulatory type-II MNs innervate the ventral, lateral, and dorsal muscle groups, and the single type-III MN primarily innervates m12 (Hoang and Chiba, 2001; Schmid et al., 1999).

The NMJ from each MN is highly stereotyped in terms of morphology and size, and the size of a NMJ can be estimated by the number of boutons or the number of AZs. AZs are the functional units within each bouton where neurotransmitter-filled vesicles are released. Each AZ is composed of the structural protein, Brunchpilot (BRP), and several functional proteins

including the calcium channel cacophony (Cac) (Figure 1.5C) (Kawasaki et al., 2000; Kittel et al., 2006). When an action potential travels from the axon to the presynaptic terminal, Ca^{2+} influx through voltage-gated calcium channels triggers the fusion of SNARE proteins on vesicles and cell membranes and the release of glutamate (Sauvola and Littleton, 2021). Postsynaptic ionotropic glutamate receptors bind glutamate triggering an influx of cations and an excitatory postsynaptic potential (EPSP) in the muscle (DiAntonio, 2006; Featherstone, 2005). Notably, even without an action potential, spontaneous vesicle fusion can occur and trigger a miniature EPSP (mEPSP) in the muscle.

On the muscle side, glutamatergic receptors cluster opposite to the AZ at type-I NMJs (Figure 1.5D) (DiAntonio, 2006). In addition, type-I boutons are surrounded by subsynaptic reticulum (SSR), a variation of the endoplasmic reticulum in muscles that is responsible for Ca^{2+} storage and release, that couples the presynaptic action potential and muscle contraction (Lahey et al., 1994). The postsynaptic structural protein, DLG, accumulates at the SSR and functions as a scaffold to set up the postsynaptic field (Guan et al., 1996). Immunostaining with an antibody against DLG allows visualization of the SSR and serves as a method to distinguish NMJ types. Specifically, type Ib boutons are surrounded by more SSR as compared to the type Is boutons, resulting in the differential staining of the two types (Guan et al., 1996). In addition, DLG is absent in types II and III boutons.

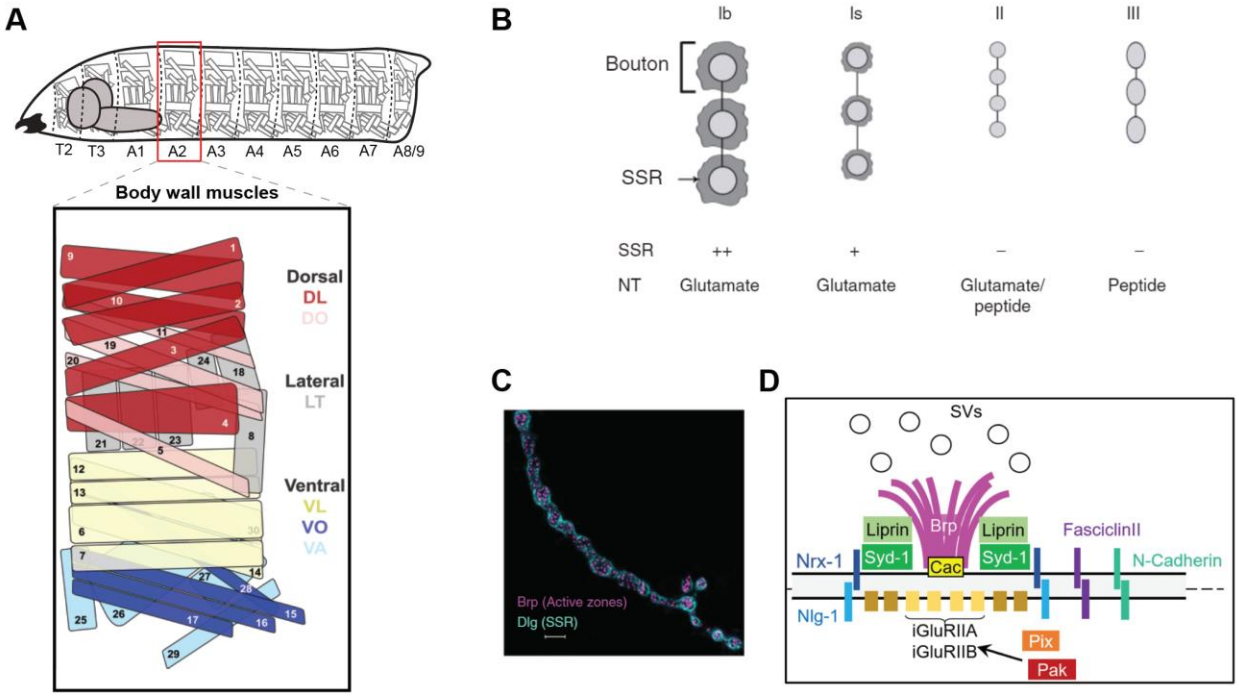

Figure 1.5 **Schematic of muscle groups and NMJ architecture.**
(A) Each hemisegment has 30 body wall muscles classified into six spatial groups, the dorsal longitudinal (DL), dorsal oblique (DO), ventral longitudinal (VL), ventral oblique (DO) ventral acute (VA), and lateral transverse (LT) muscle groups. Neurons innervating these muscles are not displayed. (B) Glutamatergic type-Ib and type-Is MNs differ in bouton size and the amount of surrounding SSR. Type-II and type-III MNs have even smaller boutons and no significant SSR accumulation. (C) Representative image of larval NMJ active zones (AZs, labeled by Brp) and the postsynaptic structural protein DLG. (D) Protein composition of the AZ and the postsynaptic field. Presynaptic scaffold protein Brp clusters the Ca^{2+} channel, Cac, and associates with synaptic vesicles. On the postsynaptic membrane, glutamate receptors form clusters and respond to glutamate neurotransmitters. Images adapted from (Menon et al., 2013).

1.1.1.4 The glial cells

The majority of cells in the vertebrate brain are glial cells. Glial cells were originally thought to only provide structural and metabolic support to neurons, but more recent studies reveal that glia function in all aspects of nervous system development and function (Altenhein et al., 2016; Crews, 2010; Freeman, 2015; Ito et al., 1995). In the *Drosophila* nervous system,

several types of glial cells have been characterized in the CNS and PNS and many share similar functions to vertebrate glial cells.

The outer layer of both the CNS and PNS are surrounded by perineurial glial cells (PG), which form a blood-brain barrier type structure (Altenhein et al., 2016; Beckervordersandforth et al., 2008). PG do not directly contact neurons, and instead, they contact the hemolymph and subperineurial glial cells (SPG) (Figure 1.6A-C) (Beckervordersandforth et al., 2008; Hilchen et al., 2008; Schwabe et al., 2005; Silies et al., 2007; Unhavaithaya and Orr-Weaver, 2012; Volkenhoff et al., 2015). PGs and SPGs are generated during embryonic stages and maintained throughout larval development (Kremer et al., 2017; Omoto et al., 2016; Stork et al., 2008). Septate junctions between SPGs coordinate their enormous growth during larval development (Banerjee et al., 2008; Carlson et al., 2000; Schwabe et al., 2005; Stork et al., 2008). At the NMJ, SPGs extend processes into the bouton areas and are responsible for removing excess synaptic materials during synaptic growth and pruning (Fuentes-Medel et al., 2009).

Drosophila larvae have an additional peripheral glial cell type, called wrapping glial cells (WG) (Figure 1.6C) (Bauke et al., 2015). WGs directly contact and wrap all axons from afferent SNs and efferent MNs. Each segmental nerve has four WGs, and each WG wraps approximately 3 mm of axons in third instar larva (Hilchen et al., 2013; Matzat et al., 2015).

In the CNS, cortex glial cells (CG) are interspersed between SPG and neuronal cell bodies (Figure 1.6B) (Beckervordersandforth et al., 2008; Pereanu et al., 2005). CGs form a network surrounding the entire lineage of a neuroblast including about 55 neurons (McLaughlin et al., 2019; Pereanu et al., 2005; Spéder and Brand, 2018). In addition to CGs, two neuropil associated glial cell types, ensheathing glial cells (EG) and astrocyte-like glial cells (AG) surround and invade the neuropil, respectively (Figure 1.6B). EGs have flattened cell bodies that

lay outside the neuropil surface, and send processes into the nerve root, resembling WGs (Beckervordersandforth et al., 2008; Peco et al., 2016; Pereanu et al., 2007). Highly polarized AGs resemble vertebrate astrocytes as they extend finely branched processes into the neuropil (MacNamee et al., 2016; Omoto et al., 2015; Peco et al., 2016; Stork et al., 2014). AGs participate in neural development and synaptic homeostasis as they were found important to tune critical periods and to balance excitatory/inhibitory synapses (Freeman et al., 2003; Stork et al., 2014).

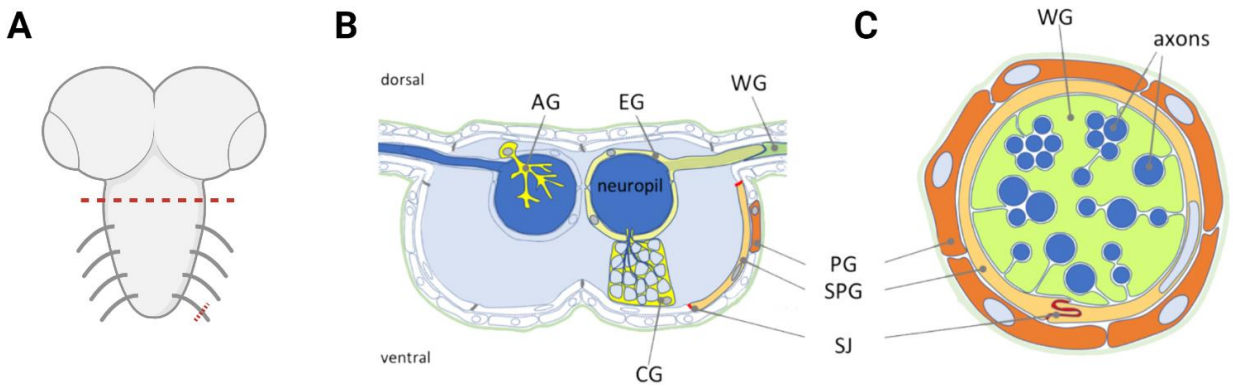

Figure 1.6 **Classification of glial cell types in the larval nervous system.**
(A) Schematic of the larval VNC. Red dashed lines represent the positions of cross-section shown in B and C. (B) A cross-section of the VNC showing astrocyte-like glial cells (AG), ensheathing glial cells (EG), cortex glial cells (CG), perineurial glial cells (PG), and subperineurial glial cells (SPG). (C) A cross-section of a segmental nerve showing PG, SPG, and wrapping glial cells (WG). Images adapted from (Yildirim et al., 2019).

1.1.1.5 The Drosophila nervous system resembles the vertebrate nervous system

One of the many strengths of using *Drosophila* larvae to study neural development and synaptic plasticity lies in its amenability to genetic manipulation and the fact that their nervous system is composed of many fewer cells. Although the larval nervous system is much simpler, it

still resembles the vertebrate nervous system due to similar circuit wiring patterns, synaptic components, and molecular mechanisms (Holland, 2016).

In the vertebrate nervous system, SNs project into the spinal cord where they connect to interneurons, which then transmit the signals to the motor cortex or directly to MNs. The brain controls locomotion and receives feedback through several orders of interneurons that reside in spinothalamic and corticospinal tracts (Curry and Gordon, 1972; Morin et al., 1951; Verhaart and Kramer, 1952). The *Drosophila* larva has a similar SN-interneuron-MN circuit wiring pattern that allows larva to quickly respond to its environment. Recent electron microscopy (EM) reconstruction of the larval VNC identified many descending interneurons that connect the brain and VNC, resembling the interneurons in the vertebrate spinal cord (Chen et al., 2021; Gerhard et al., 2017; Schneider-Mizell et al., 2016). Subsequent functional studies revealed an important role for these neurons in animal locomotion (Kim, 2017; Namiki et al., 2022; Schnell et al., 2017).

At the synaptic level, the *Drosophila* NMJs and excitatory synapses in the vertebrate CNS share the same neurotransmitter (L-glutamate) and similar synaptic machinery. For example, the *Drosophila* pre-synaptic SNARE protein, Complexin, was shown to be a regulator of synaptic vesicle fusion and neurotransmitter release, and its human homolog has been linked to a number of human neurological diseases (Cho et al., 2010; Hu et al., 2002; Huntwork and Littleton, 2007; Jorquera et al., 2012). In addition, the *Drosophila* postsynaptic structural protein DLG and its vertebrate homolog PSD-95 (also known as DLG4) were found to participate in synaptic plasticity and the stabilization of synaptic changes during long-term potentiation (Cho et al., 1992; Meyer et al., 2014; Stathakis et al., 1997). The vertebrate ionotropic AMPA/Kainate

glutamate receptors also resemble the two *Drosophila* ionotropic glutamate receptors at the NMJ: GluRIIA or GluRIIB (Marrus, 2004).

Drosophila and vertebrates also have similar glial cell types, especially at the functional level. In the vertebrate CNS, astrocytes are the most abundant glial cell type; astrocytes have complex projections that participate in formation of the blood brain barrier and create a nutrient exchange pathway between neurons and blood vessels (Suárez et al., 1995; Tao and Zhang, 2014). *Drosophila* have a similar cell type known as astrocyte-like glial cell (AG) (Figure 1.6B). In addition, the vertebrate CNS has oligodendrocytes that surround axons and form a specialized membrane called myelin (Baumann and Pham-Dinh, 2001; Shoykhet and Clark, 2011). In the PNS, Schwann cells have similar function as oligodendrocytes to provide myelination to axons (Bhatheja and Field, 2006). Although *Drosophila* axons are not myelinated, PGs, SPGs, and WGs wrap axons to provide insulation and protection, similar to oligodendrocytes and Schwann cells (Yildirim et al., 2019).

In summary, the *Drosophila* nervous system is an excellent model to study synaptic connectivity and plasticity. Similar to the vertebrate nervous system, *Drosophila* neurons and glia are intimately associated and required for normal synaptic development and function. The synaptic molecular machinery is also shared, and mechanisms uncovered in *Drosophila* can provide insight into vertebrate circuit development.

1.1.2 Electrophysiology and imaging technologies empower the functional study of the *Drosophila* nervous system

The simplicity of the *Drosophila* neuromuscular system allows for direct, physical access to synapses. In this section, I will discuss the electrophysiology and imaging tools that enable quantitative and robust functional examination of larval NMJs.

Based on the question at hand, neural activity can be examined at the synaptic resolution or more globally with behavioral analyses. At the synaptic level, genetically encoded Ca^{2+} sensors (GCaMPs) together with microscopy technologies allow for direct visualization of Ca^{2+} fluctuations (Nakai et al., 2001). Recent advances in genetically encoded neurotransmitter sensors expanded the toolbox and provide high-resolution, *in vivo* tracking of neurotransmitter release (Dong et al., 2021; Wan et al., 2021; Wu et al., 2022; Zhang et al., 2019). Unlike genetically encoded sensors, electrophysiological recordings require physical access to the cells to detect activity with electrodes. Several electrophysiology protocols, such as patch clamping, voltage clamping, and current clamping, have been developed to examine different aspects of channel gating, membrane potential dynamics, and action potential properties (Scanziani and Häusser, 2009). Finally, to study circuit activity, behavioral analyses can be utilized. Recent advances in developing GAL4 lines to target specific cells with optogenetic tools uncovered a series of neural circuits involved in *Drosophila* locomotion, foraging, navigation, and circadian rhythm (Lee et al., 2018; Pfeiffer et al., 2010, 2008).

1.1.2.1 Electrophysiology recording at Drosophila larval NMJ

The layout of the *Drosophila* larval neuromuscular system facilitates access to the NMJs for electrophysiology recordings (Jan and Jan, 1976). In a dissected larva, the nerve bundle can

be stimulated by a suction/stimulation electrode to simultaneously activate all motor axons in the corresponding hemisegment (Figure 1.7A). This stimulus will generate action potentials in MNs that travel to the NMJ to trigger Ca^{2+} influx and neurotransmitter release. The neurotransmitter, glutamate in this case, binds to glutamate receptors and opens cation channels to induce a change in the muscle membrane potential. Ca^{2+} is the major ion flowing into the muscle and triggers additional Ca^{2+} release from the SSR. The stimulation induces a membrane potential change, known as an EPSP, and can be detected by another electrode placed into the muscle (Figure 1.7A) (Imlach and McCabe, 2009; Jan and Jan, 1976; Kurdyak et al., 1994; Stewart et al., 1994; Zhang and Stewart, 2010).

EPSPs are characterized by a fast depolarization and a gradual return to the resting membrane potential (Figure 1.7B). In physiological saline, the EPSP amplitude of most muscles lies between 20-40 mV, and Ca^{2+} recycling restores the cell to resting membrane potential within 200 ms (Figure 1.7B) (Zhang and Stewart, 2010).

In addition to recording EPSPs, the electrode in the muscle can detect mEPSPs without presynaptic stimulation. mEPSPs are caused by spontaneous vesicle fusion and neurotransmitter release, and the amplitude of each mEPSP is ~1 mV (Figure 1.7C). The mEPSP amplitude represents the muscle response to a single synaptic vesicle, indicating the abundance and the density of glutamate receptors on the muscle membrane (Daniels et al., 2006; Huntwork and Littleton, 2007). The mEPSP frequency can also be calculated to determine the probability of spontaneous release (Newman et al., 2022, 2017). Finally, dividing the EPSP amplitude by the mEPSP amplitude estimates how many synaptic vesicles are released per stimulus, and this value is known as the quantal content (Martin, 1955). Overall, EPSP amplitude, mEPSP amplitude, mEPSP frequency, and quantal content provide important insights into NMJ function.

Each muscle fiber is innervated by two excitatory MNs, the type-Ib MN and the type-Is MN (Figure 1.7A) (Hoang and Chiba, 2001; Menon et al., 2013). Due to the stimulation of the entire nerve, the EPSP and mEPSP recorded in the muscle are a combination of both MNs inputs. Specifically, the EPSP amplitude is the sum of the Ib EPSP amplitude and the Is EPSP amplitude, and the mEPSP frequency is the sum of the Ib mEPSP frequency and the Is mEPSP frequency. In previous studies, researchers did not carefully distinguish the electrophysiology properties of Ib and Is MNs and assumed they were identical. More recent studies, however, revealed fundamental differences between tonic Ib MNs and phasic Is MNs (Aponte-Santiago et al., 2020; Aponte-Santiago and Littleton, 2020; Wang et al., 2021a). For example, Ib MNs trigger smaller mEPSP amplitudes but with a higher mEPSP frequency. These features correspond to the general properties of a tonic neuron – producing a sustained response and being activated during the course of the stimulus. Conversely, Is MNs trigger a larger mEPSP amplitude but with a lower mEPSP frequency, matching the phasic neuron properties – producing a transient response followed by quick adaptation (Newman et al., 2017). In addition, Ib MNs and Is MNs also produce different EPSP amplitudes in a muscle specific manner. Thus, it is important to distinguish the contribution of Ib and Is MNs when collecting electrophysiology data at the *Drosophila* larval NMJ.

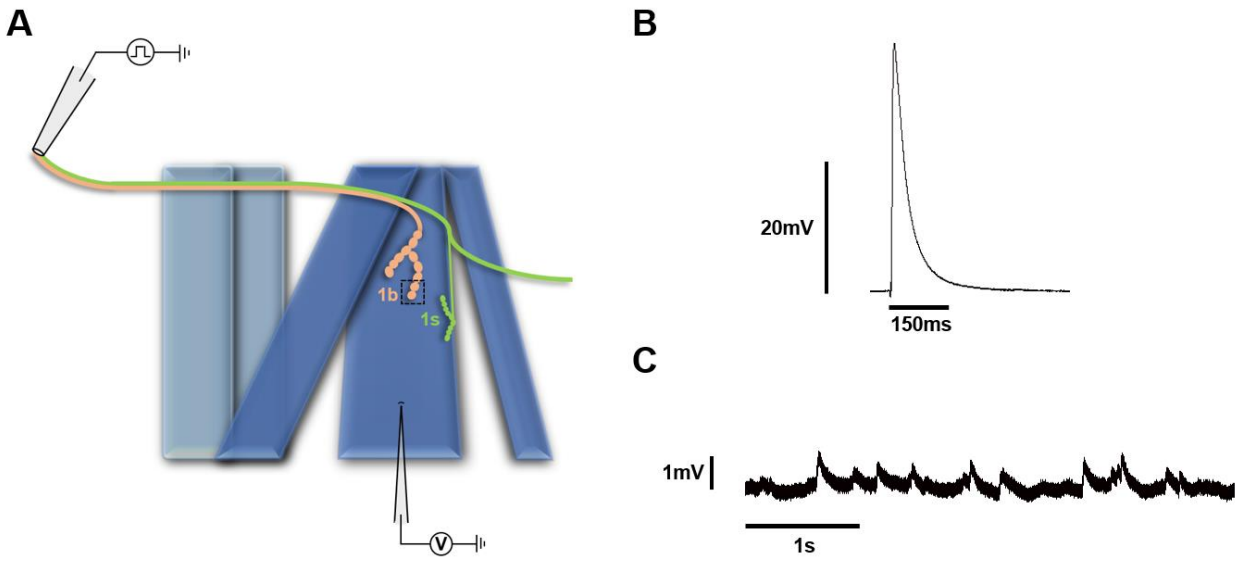

Figure 1.7 **Schematics of electrophysiology recording at larval NMJ.**
(A) A stimulating electrode generates action potential in MN axons and trigger synaptic release at NMJs. Recording electrode reads membrane potential changes from the muscle side. (B) Representative trace of EPSP showing its large amplitude and fast membrane recovery. (C) Representative trace of mEPSP showing the small amplitude and high frequency of mEPSPs.

1.1.2.2 The genetically encoded calcium sensor (GCaMP) allows for direct visualization of neural activity

GCaMP is a fusion protein comprised of green fluorescent protein (GFP), calmodulin (CaM), and a peptide sequence from myosin light-chain kinase (Nakai et al., 2001). Upon Ca^{2+} binding, conformational changes of GCaMP leads to fluorescence with an excitation wavelength of 488 nm and an emission wavelength of 510 nm. In recent years, the Janelia Research Campus generated a series of GCaMP variants with high sensitivity and resolution, allowing precise in vivo Ca^{2+} imaging (Chen et al., 2013; Dana et al., 2019).

Utilizing GCaMP imaging, direct Ca^{2+} release can be visualized at the *Drosophila* NMJ, allowing for visualization of activity from specific MNs (Figure 1.8A-B) (Akbergenova et al., 2018). This approach has enabled researchers to discover that subsets of AZs are specialized for

spontaneous neurotransmitter release versus evoked neurotransmitter release (Akbergenova et al., 2018; Buhl et al., 2013; Peled et al., 2014; Peled and Isacoff, 2011; Walter et al., 2014). Additionally, only a subset of AZs is capable of neurotransmitter release while others remain in a silent state (Figure 1.8C-D). Within these activated AZs, some show high release probability (Pr) for spontaneous release while others are more recruitable upon stimulation (Figure 1.8C-D). Therefore, morphological identical AZs are functionally heterogeneous and further characterization will reveal the underlying molecular differences.

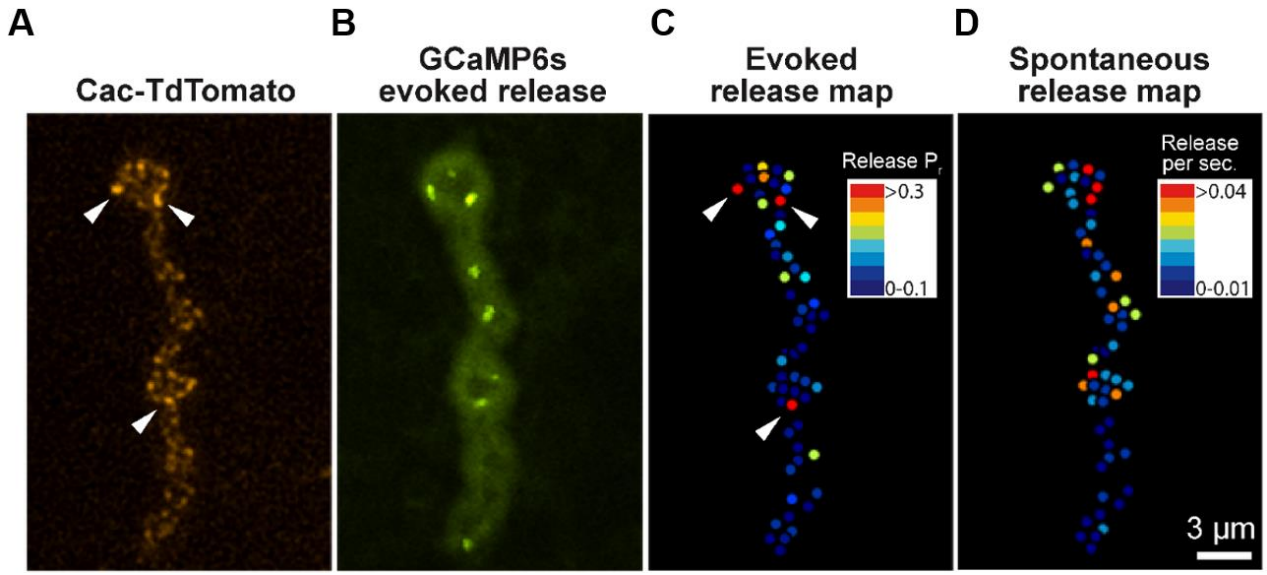

Figure 1.8 **Morphological identical AZs are heterogenous.**
(A) Endogenous labeling of Cac showing the positions of AZs. (B) GCaMP imaging reveal the positions of neurotransmitter release. Note that Cac abundance is positively correlated to the release probability (Pr). (C) Pr map of evoked neurotransmission. (D) Pr map of spontaneous neurotransmission. Comparison between (C) and (D) suggests that some AZs favor evoked neurotransmitter release, others favor spontaneous neurotransmitter release, and some remain silent. Images are adapted from (Akbergenova et al., 2018).

1.2 Roles of the Dpr-DIP interactome in nervous system development

Precise neural wiring is achieved through a series of steps including axon pathfinding, partner recognition, and synaptic pruning (Sanes and Zipursky, 2020; Zarin and Labrador, 2019).

Although the mechanisms underlying these processes are not completely understood, one prevailing model proposes that CSPs instruct chemo attraction and repulsion, self-avoidance, and synaptic partner recognition (Honig and Shapiro, 2020; Wit and Ghosh, 2016). CSPs fall into several protein families, including the immunoglobin superfamily (IgSF), the Cadherin protein family (Cdhs), the leucine-rich repeat protein family (LRRs), the receptor tyrosine kinases (RTKs), and many more (Jontes, 2017; Kurusu et al., 2008; Sanes and Zipursky, 2020; Zinn and Özkan, 2017). In vitro biochemical studies showed that subsets of these CSPs interact homo- or heterophilically, and many of these interactions are implicated in synaptic connectivity in both vertebrates and invertebrates (Cheng et al., 2019b; Honig and Shapiro, 2020; Özkan et al., 2013; Wit and Ghosh, 2016).

In a previous "interactome" screen, we and others identified two subfamilies of the Drosophila IgSF, the Defective proboscis response proteins (Dprs; 21 members) and the Dpr-interacting proteins (DIPs; 11 members) (Carrillo et al., 2015; Özkan et al., 2013; Tan et al., 2015). Dprs and DIPs are different from other CSPs found to wire the neural circuits because they have more family members and can interact both homo- and heterophilically, providing a vast repertoire of unique combinations for synaptic specificity. In this section, I will review current understanding about the function of CSPs, especially Dprs and DIPs, and discuss the open questions in the field.

1.2.1 Synaptic recognition is mediated by cell surface proteins

In the well-studied vertebrate retina, retinal ganglion cells require multiple CSPs, including Dscams and Sidekicks (Sdks) 1 and 2, to avoid self-synapses and form stereotyped connections, respectively (Garrett et al., 2018; Krishnaswamy et al., 2015; Yamagata and Sanes,

2019). Similarly, ON-OFF direction-selective ganglion cells and ON-OFF bipolar interneurons establish correct partnership by homophilic interactions of classical Cdhs (Duan et al., 2018, 2014). In hard wired invertebrate nervous systems, such as *C. elegans*, the heterophilic interaction between two IgSF proteins, Syg1 and Syg2, is required for HSNL motor neuron synapse formation (Shen et al., 2004; Shen and Bargmann, 2003). In the *Drosophila* mushroom body, neurons rely on different isoforms of Dscam1 to discriminate self-/non-self (Hattori et al., 2009; Wang et al., 2004; Zhan et al., 2004). In the olfactory system, epidermal growth factor (EGF)-repeat containing transmembrane Teneurin proteins, Ten-m and Ten-a, are required for the one-to-one matching between a subset of olfactory receptor neurons and projection neurons (Hong et al., 2012; Pederick et al., 2021).

Specificity challenges are also encountered in the *Drosophila* larval neuromuscular system. Several CSPs have been identified as recognition cues between MNs and muscles, including Toll (Inaki et al., 2010; Rose et al., 1997), Connectin (Nose et al., 1997, 1992), Capricious (Kurusu et al., 2008; Shishido et al., 1998) from the LRR family, and Fasciclin 2 (Davis et al., 1997; Winberg et al., 1998) and Fasciclin 3 (Chiba et al., 1995; Kose et al., 1997) from the IgSF. For example, loss of Teneurin signaling causes a 90% decrease of MN3-Ib innervation (Hong et al., 2012), and Toll null mutants revealed defects in 35% of MN6/7-Ib (Rose et al., 1997).

Although these CSPs have been implicated in synaptic recognition and the same set of CSPs can be utilized in different circuits, we still do not understand how most synaptic partners are recognized. Thus, examining new CSP family members and their functions are necessary to understand circuit wiring.

1.2.2 Biochemical feature of Dprs and DIPs

The *Drosophila* genome encodes ~1000 CSPs (Özkan et al., 2013). Most CSPs interact via specific domains, including the cadherin domain or the immunoglobulin (Ig) domain, and each CSP can have multiple domains and interacting partners, generating a large repertoire of interaction possibilities (Honig and Shapiro, 2020).

Dprs and DIPs are two subfamilies of the IgSF that contain 2 and 3 Ig domains, respectively. Through an *in vitro* biochemical binding assay, the interactome of 21 Dprs and 11 DIPs was established by (Özkan et al., 2013) and later refined by biochemical and biophysical approaches (Cheng et al., 2019a; Cosmanescu et al., 2018; Sergeeva et al., 2020) (Figure 1.9). Dprs and DIPs interact homo- or heterophilically through their first Ig domains. Some Dprs and DIPs interactions are highly specific, such as Dpr12-DIP-delta, and others are promiscuous, such as DIP-η which interacts with Dpr1-5 (Figure 1.9). The same Dpr or DIP interacts with its interacting partners through different interfaces, thus leading to different binding affinities (Honig and Shapiro, 2020). Evolutionarily, Dprs and DIPs are evolved from an ancestral Wirin gene, which produced a widely distributed family of two- and three- Ig domain molecules with neural wiring functions, including Dprs and DIPs, and the nematode RIG-5 and ZIG-8 and vertebrate IgLON family (Cheng et al., 2019b). The homologs also form homophilic and heterophilic interactions, and such interactions can be broken by mutations predicted by Dpr-DIP interactions (Cheng et al., 2019b). The biochemical and evolutionary relationship of these CSPs across species suggest conserved functional roles in the metazoan nervous system.

In addition to interacting with other CSPs, secreted molecules, and extracellular matrix, many CSPs signal intracellularly. Some CSPs, such as Ig proteins Nectins and Sdks, are single transmembrane proteins containing a transmembrane helix followed by a cytoplasmic region

which interacts with downstream signaling molecules (Takai et al., 2008; Yamagata, 2020). Other CSPs, such as the mammalian Contactins, are glycosylphosphatidylinositol (GPI) anchored proteins which are linked to the outer leaflet of cell membrane through a post-translational modification (Kinoshita, 2020; Zuko et al., 2011). How GPI anchored CSPs signal intracellularly is not well understood as they do not have typical intracellular domains. Some models include interactions with co-receptors or proteolytic cleavage to allow for interactions with other CSPs at longer distances. Most Dprs and DIPs do not have predicted transmembrane domains, suggesting that GPI modifications may allow for membrane association. Indeed, the mammalian IgLON orthologs are GPI-linked and preliminary data from our lab indicates that most can be cleaved from the membrane by phospholipase C. Future studies will examine the downstream signaling pathways of Dprs and DIPs.

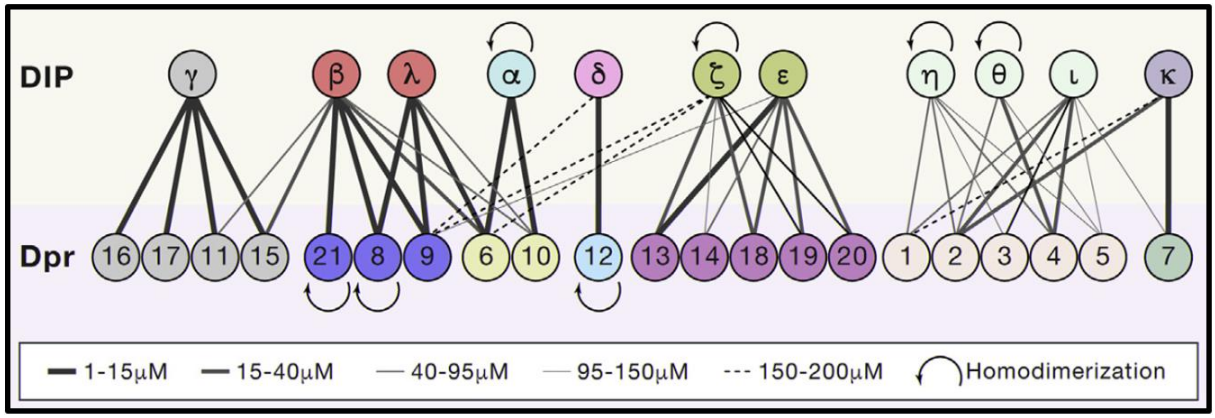

Figure 1.9 **The Dpr-DIP interactome**.
Dprs and DIPs form homophilic or heterophilic interactions with different binding affinities. The interactome is divided into seven sub-groups based on heterophilic interactions, represented by different colors within Dpr and DIP families. Image is adapted from (Honig and Shapiro, 2020).

1.2.3 Dpr-DIP interactions guide synaptic recognition, neural survival, and synaptic development

Dpr1 was discovered by the Montell lab in a screen for genes that regulate salt aversion (Nakamura et al., 2002) and was found to be part of a highly related Ig protein family. The discovery of the DIPs in 2013 and their interactions with Dprs spawned a newfound interest in these IgSF proteins (Özkan et al., 2013). The first functional study of a Dpr-DIP pair was reported by (Carrillo et al., 2015); Dpr11 and its partner DIP-γ were implicated in synaptic connectivity in the optic lobe and axon terminal development in the neuromuscular circuit. Several high-profile studies have been published in the past five years and a majority reveal that Dpr-DIP interactions instruct synaptic connectivity. Here, we review current knowledge about the function of Dprs and DIPs in different neural circuits.

1.2.3.1 Role of Dpr-DIP interactions in synaptic connectivity

In the larval neuromuscular system, DIP-α is only expressed in the two Is MNs that innervate the ventral and dorsal muscle groups, and a DIP-α interacting partner, Dpr10, is expressed in muscles (Figure 1.10A) (Ashley et al., 2019). Removal of either *DIP-α* or *dpr10* causes a complete loss of Is MN innervation of muscle 4 (we refer to this branch as m4-Is), while Is innervation on other muscles is only mildly unaffected (Figure 1.10B). Interestingly, overexpression of *DIP-α* or *dpr10* in either the MNs or the muscles will also lead to loss of m4-Is innervation, suggesting that expression levels of these CSPs are important for MN-muscle recognition (Figure 1.10C) (Ashley et al., 2019). In addition, site-specific disruption of the *DIP-α* homophilic interaction interface causes loss of m4-Is innervation, indicating DIP-α homodimerization is also involved in synaptic recognition (Cheng et al., 2019a).

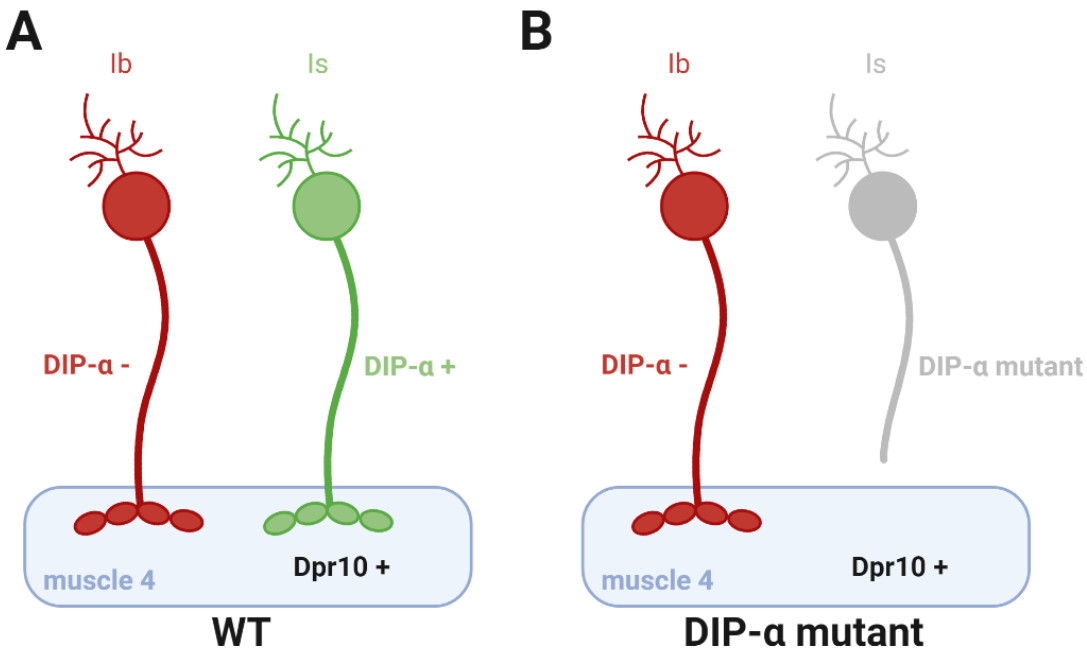

C

m4-Is innervation	mutation	pre-synaptic knock down	post-synaptic knock down	pre-synaptic overexpression	post-synaptic overexpression
DIP-α	X	X	√	X	X
Dpr10	X	√	X	X	X

Figure 1.10 **Function of Dpr10-DIP-α interactions at the larval NMJ.**
(A) Wild type m4 expresses Dpr10 and is innervated by the DIP-α negative Ib MN and the DIP-α positive Is MNs. (B) In *DIP-α* mutants, the Is MN no longer innervates m4. (C) Summary of m4-Is innervation in different genetic background. Note that overexpression of Dpr10 or DIP-α pre- or postsynaptically also disrupt m4-Is innervation.

Dpr10-DIP-α interactions are also implicated in synaptic connectivity in the adult visual system. DIP-α is expressed in several medulla neurons of the pupal optic lobe, including Dm1, Dm4, and Dm12, which innervate the M1, M3 and M3 medulla layers, respectively

(Cosmanescu et al., 2018; Tan et al., 2015; Xu et al., 2018). Lamina neuron 3 (L3) is presynaptic to Dm4 and Dm12 and expresses DIP-α interacting partners, Dpr6 and Dpr10. Disrupting Dpr6/10-DIP-α interaction leads to mistargeting defects in about 60% of Dm12 neurons which now ectopically innervate M8 (Xu et al., 2018). Substituting wild type *DIP-α*, *dpr6*, or *dpr10* with mutants that alter affinity and disrupt Dpr6/10-DIP-α interactions to varying degrees revealed a graded mistargeting defect (Xu et al., 2022, 2018). In addition, shifting Dpr6 and Dpr10 expression from M3 to M10 rerouted innervation of Dm4 and Dm12 to M10 (Xu et al., 2022, 2018). Overall, these studies showed that Dpr6/10 and DIP-α control synaptic connectivity in an affinity-dependent manner.

Similar connectivity defects in visual circuits are also observed in *dpr11* and *DIP-γ* mutants (Carrillo et al., 2015; Courgeon and Desplan, 2019; Menon et al., 2019). Photoreceptors in the retina detect different wavelengths of light, and in order for flies to properly navigate the environment, photoreceptors must innervate appropriate downstream synaptic partners. A subset of photoreceptors, called the yR7 type, connect to yellow Dm8 (yDm8) medulla neurons, and express the cognate interactors Dpr11 and DIP-γ, respectively (Courgeon and Desplan, 2019). Loss of *dpr11* and *DIP-γ* disrupt yR7-yDm8 synaptic connectivity. Neighboring synaptic partners pR7-pDm8 do not express *dpr11* or *DIP-γ* and as predicted, their connectivity is not perturbed in *dpr11* and *DIP-γ* mutants (Figure 1.11) (Courgeon and Desplan, 2019; Menon et al., 2019).

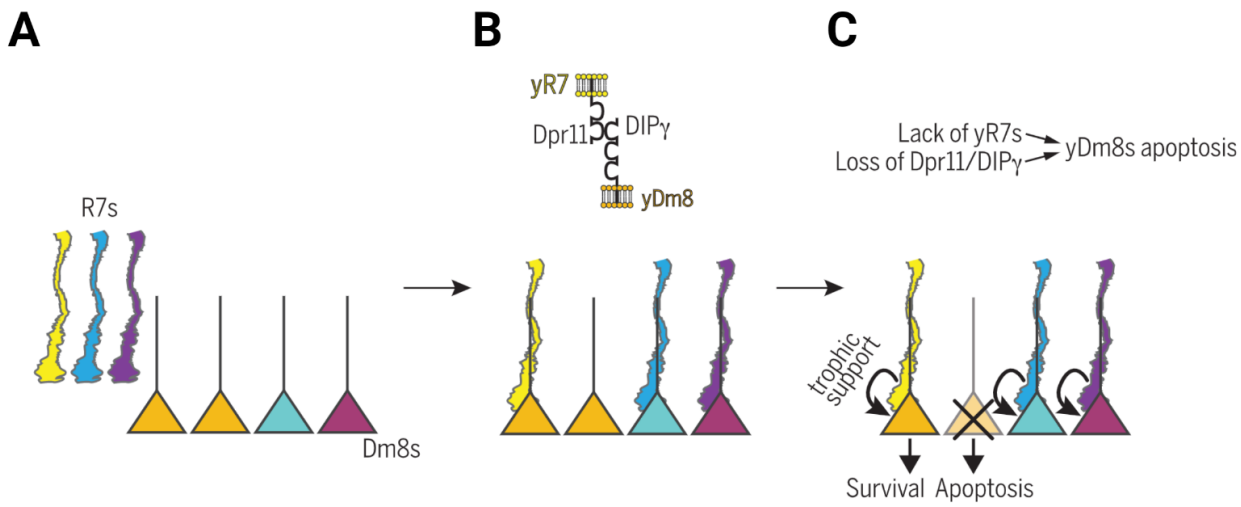

Figure 1.11 **Dpr11-DIP-γ interactions are required for yR7-yDm8 recognition and yDm8 cell survival.**
(A) Dm8 cell fate are specified independent of R7. (B) yR7 (yellow) expresses Dpr11 that interacts with DIP-γ expressed in yDm8 (yellow). Dpr11 negative pR7 (purple) connects to DIP-γ negative pDm8 (purple). (C) Dpr11-DIP-γ interactions provide trophic support to yDm8 as unmatched yDm8 neurons undergo apoptosis. Image is adapted from (Courgeon and Desplan, 2019).

In another study, DIP-β and DIP-γ were found in L4 neurons which normally innervate the proximal medulla layers (Xu et al., 2019). Double knock out of *DIP-β* and *DIP-γ* causes ectopic L4 synapses in the distal medulla layers, suggesting that DIP-β and DIP-γ restrict L4 synaptic connectivity (Xu et al., 2019). Additionally, this study indicates a default capacity of neurons to form a broad range of synapses and that synaptic specificity is achieved through a preference for specific partners.

In the *Drosophila* olfactory system, 50 classes of olfactory receptor neurons (ORNs) are primary odor responders which transmit information to 50 classes of specific projection neurons (PNs) in stereotypically positioned glomeruli in the antennal lobe. *dprs* and *DIPs* are expressed in the olfactory circuit and disrupting *dprs* and *DIPs* in ORNs lead to local projection defects of ORN axons and positioning defects in glomeruli (Barish et al., 2018). For example, *DIP-η*

knockdown in Or47b ORNs disrupts axon targeting leading to expansion and invasion of Or47b axons into neighboring glomeruli, and double knockdown of *DIP-η* and *DIP-δ* caused a split of the Or47b glomerulus (Barish et al., 2018). These results suggest that Dprs and DIPs may act independently or combinatorially to organize ORN axon terminals and glomerular positions.

In addition, Dpr-DIP interactions are also implicated in the *Drosophila* mushroom body (MB) where the intrinsic MB neurons, known as Kenyon cells (KCs), connect to the MB output neurons and dopaminergic neurons (DANs) (Bornstein et al., 2021). Dpr12 is expressed in γ-KC neurons and accumulates in γ4/5 region where it interacts with DAN-derived DIP-δ. Lack of *dpr12* or *DIP-δ* revealed defects in axon extension of γ-KC neurons and compartmentation in the MB. Importantly, these defects can be rescued by other Dpr-DIP pairs but not with other adhesive molecules (Bornstein et al., 2021). This study suggested that the matching of a Dpr-DIP pair mediates the formation of MB circuits via a mechanism that requires not solely adhesive functions.

In summary, interactions between Dprs and DIPs are important for synaptic connectivity and the same Dpr-DIP pair can be utilized in different circuits. However, the partial penetrance of most phenotypes described above suggests redundancy and the involvement of other recognition molecules to assemble neural circuits.

1.2.3.2 Role of Dpr-DIP interactions in neural survival

During nervous system development, programmed neuronal cell death contributes to a sculpting process to remove excess neurons born during neurogenesis. For example, failure to form synaptic connections can trigger canonical apoptotic pathways in the disconnected neuron to create space and save energy (Carvalho et al., 2008). Several studies revealed that Dpr-DIP

interactions do not only establish the synaptic connection, but also provide trophic support to both pre- and post-synaptic neurons as they actively signal to each other to avoid programmed cell death.

As described above, Dprs and DIPs are required in the olfactory system for proper ORN axon projection and innervation. In the same study, the researchers found that *DIP-η* knock down not only leads to invasion of Or47b axons into the Or88a glomerulus but also a decrease of Or88a cell numbers (Barish et al., 2018). Thus, *DIP-η* may non-cell autonomously affect cell survival of Or88a neurons. Conversely, knocking down the widely expressed *dpr10* in ORNs leads to cell death of Or47a neurons cell autonomously (Barish et al., 2018). These data suggest that Dprs and DIPs act pre- and postsynaptically to support cell survival.

Studies in the fly visual system have expanded the roles of Dprs and DIPs in neuron survival. The fate and differentiation of two types of Dm8 neurons, the yDm8 and pDm8, are determined before they are innervated by corresponding presynaptic partners yR7 and pR7 (Figure 1.11A). The yR7-yDm8 synaptic partnership requires the complementary expression of Dpr11 and DIP-γ, respectively (Figure 1.11B) (Courgeon and Desplan, 2019; Menon et al., 2019). During normal development, approximately 40% of yDm8s do not receive yR7 input and eventually undergo apoptosis (Figure 1.11C). Interestingly, loss of either *dpr11* or *DIP-γ* lead to yR7 and yDm8 not recognizing each other and subsequent excessive yDm8 cell death (Carrillo et al., 2015; Courgeon and Desplan, 2019; Menon et al., 2019). In addition, *DIP-α* null mutants or *dpr6, dpr10* double null mutants also show reduced numbers of Dm1, Dm4, and Dm12 neurons in an affinity-dependent manner (Xu et al., 2022, 2018). Interestingly, the affinity threshold for Dpr10-DIP-α mediated synaptic recognition is higher than the threshold for cell survival,

indicating that different downstream signaling pathways may underlie each function (Xu et al., 2022).

1.2.3.3 Role of Dpr-DIP interactions in synaptic development

After synaptic recognition, synapses must form and be maintained for proper function. Many CSPs and related signaling pathways are implicated in synaptic development in the *Drosophila* NMJ, such as Neurexin-Neuroligin interaction, Fasciclin II, Teneurin-a, Teneurin-m, and Dprs and DIPs (Davis et al., 1997; Winberg et al., 1998).

At the larval NMJ, Dpr11-DIP-γ interactions restrict synaptic bouton formation, presumably by downregulating BMP pathway activity. Disrupting *dpr11* or *DIP-γ* leads to both structural and functional alternations – an increase of small, immature boutons, known as satellite boutons, and an increase of the mEPSP frequency (Carrillo et al., 2015). At the adult NMJ, Dpr10-DIP-α interactions are required to establish and maintain MN terminal branches, specifically after MNs reach the muscle fields (Venkatasubramanian et al., 2019), suggesting roles in synaptic growth and maintenance, rather than initial axon sorting and MN-muscle recognition.

1.2.4 Open Questions

The floodgates of Dpr and DIP research were opened after the publication of the Dpr-DIP interactome, and the multifaceted roles of Dpr-DIP interactions are only beginning to be revealed. Many key questions related to Dprs and DIPs remain and are actively being explored, including their broad functions, the upstream regulation, and the downstream signaling pathways.

1.2.4.1 The broad functions of Dpr-DIP interactions

Compared to the vast Dpr-DIP interactome, studies to date have only examined a small subset of Dpr-DIP interactions likely due to several limitations. First, to study interacting CSP pairs, the expression of each CSP expedites functional analyses. However, the expression patterns of all Dprs and DIPs is unknown which hinders examination of phenotypes. For example, if a Dpr-DIP pair is selectively expressed in a pair of pre- and postsynaptic neurons, one can focus on those specific connections when examining mutants. A systematic expression profiling of Dprs and DIPs in different neural circuits will provide insights about candidate selection (Brovero et al., 2021). Second, genetic tools are limited to examine individual neurons from the overlapping tissue while simultaneously generating *dpr* and *DIP* mutations and not causing lethality. In the neuromuscular system and optical lobe, specific synaptic partners are more easily distinguishable and Mosaic Analysis with a Repressible Cell Marker (MARCM) facilitates examination of individual cells (Lee and Luo, 2001, 1999). Third, many fundamental development programs are regulated by redundant mechanisms to ensure proper function. Previous studies have revealed that circuit wiring also relies on redundant CSPs (Duan et al., 2018; Jontes, 2017). The Dpr-DIP interactome also suggests redundancy since most Dprs and DIPs interact with multiple members of the other family. Thus, simultaneous removal of multiple *dprs* and *DIPs*, alone or together with other CSPs, may uncover novel functions of Dpr-DIP interactions. However, to determine which *dprs* and *DIPs* to knockout will also require knowledge of their expression.

1.2.4.2 The upstream regulation of Dprs and DIPs

To achieve cell specific expression, as observed for many *dprs* and *DIPs*, genes must be under the control of combinations of transcriptional activators and repressors. However, there is limited knowledge about transcriptional factors that regulate *dprs* and *DIPs* (Courgeon and Desplan, 2019; Ma et al., 2021; Peng et al., 2018). Understanding how *dprs* and *DIPs* are transcriptionally regulated will provide insights about how transcriptional factors establish neural circuits. After transcription and translation, Dprs and DIPs must be localized to specific subcellular compartments, including dendrites and axon terminals, to enable Dpr-DIP transsynaptic interactions. Several studies in the optic lobe and the neuromuscular system revealed localization of specific Dprs and DIPs to synaptic sites, suggesting that they are not ubiquitously distributed throughout the cells (Ashley et al., 2019; Courgeon and Desplan, 2019). Engineering endogenously tagged Dprs and DIPs and combining these tools with live imaging will provide valuable insight into when and how these CSPs are localized to synapses.

1.2.4.3 The downstream signaling pathway of Dpr-DIP interactions

Although Dpr-DIP interactions have been implicated in multiple functions, the downstream signaling pathways are still unknown. How do Dpr-DIP interactions establish a stable synaptic connection? How do Dpr-DIP interactions ensure cell survival? And how do Dpr-DIP interactions promote synaptic growth? Dpr-DIP interactions may simply be adhesive but substituting with other adhesive CSPs does not rescue, suggesting that merely interacting is not sufficient (Bornstein et al., 2021). Therefore, unique downstream signaling pathways may exist for specific Dpr-DIP pairs and specific functions. However, most Dprs and DIPs seem to lack a

transmembrane domain suggesting that intracellular signaling is not direct, and instead, Dprs and DIPs may recruit co-receptors for signaling.

In summary, the field of Dprs and DIPs is still in its infancy, but exciting recent studies highlight their multifaceted roles in several aspects of nervous system development. Investments in expression profiling, tool building, and in-depth genetic analyses will expedite the simultaneous examination of many Dprs and DIPs to not only implicate other Dpr-DIP pairs in circuit wiring but potentially reveal novel functions for these CSPs.

1.3 Synaptic plasticity compensates dysfunction in neural circuits

One of the most remarkable features of the brain is its plasticity – the capacity of neural circuits and specific neurons to adapt to experiences or perturbations by modifying their neural activity. Normal brain functions, such as learning, can trigger short-term and long-term synaptic plasticity to build and store memories (France et al., 2022; Volianskis et al., 2013). Synaptic plasticity also enables synaptic homeostasis, a compensatory mechanism to regulate and maintain stable functionality in a changing environment (Goel and Dickman, 2021). In my thesis, I will refer to synaptic plasticity with this latter context and discuss the discovery of a new form of synaptic plasticity.

1.3.1 Neurons may counteract different types of perturbations

After initial synaptic connections are established, synapses must be sufficiently flexible to enable changes induced by various perturbations. Perturbations can act locally at specific synapses or more globally at the level of entire neurons or circuits and include physical

perturbations, biochemical perturbations, and perturbations caused by ageing and disease related neural degeneration.

Physical perturbations such as accidental injury, brain stroke, and intracerebral hemorrhage usually cause neural degeneration and/or neuronal cell death (Courtine et al., 2009; Moraud et al., 2016). Physical injury usually leads to severing of the axon from the cell body and Wallerian degeneration of the axon, a conserved process mediated by a reduction of NAD+ (Hoopfer et al., 2006; Osterloh et al., 2012; Wang et al., 2005). In addition to the cell autonomous changes, several studies also observed an increase of axonal branching from adjacent uninjured neurons in a mouse spinal cord injury model (Hutson et al., 2019; Moraud et al., 2016); however, the mechanisms and functional consequences of such compensatory branching is not known.

Biochemical perturbations are generally milder than physical injury, but they can still significantly alter synaptic function. Drug abuse, neural toxins, infections, and immune responses may alter the microenvironment or directly target the synapse, thus impairing synaptic function to different extents. Depending on the severity of the perturbation, synaptic plasticity mechanisms such as synaptic scaling, presynaptic homeostatic potentiation (PHP), and postsynaptic homeostatic depression (PHD), will maintain synaptic function at normal levels (Davis and Müller, 2015; Frank et al., 2020; Karunanithi et al., 2020b, 2020a; Srinivasan et al., 2021). For example, synaptic scaling is triggered by abnormal activity in presynaptic neurons; hyper-activating presynaptic neurons will lead to a down scaling of presynaptic boutons, whereas upscaling was observed at hypo-activated presynaptic neurons (Ackerman et al., 2021; Choi et al., 2014; Knodel et al., 2014; Wen and Turrigiano, 2021). Several mechanisms have been implicated in synaptic scaling, including activity-dependent increases of vesicular glutamate

transporter (VGLUT) expression, Ca^{2+} dependent modification of the IP3 receptor, and remodeling of the miRNA-induced silencing complex (miRISC) (Aguilar et al., 2017; Shao et al., 2022; Srinivasan et al., 2021). Further studies are needed to better understand how neurons dynamically regulate synaptic growth through these discrete pathways.

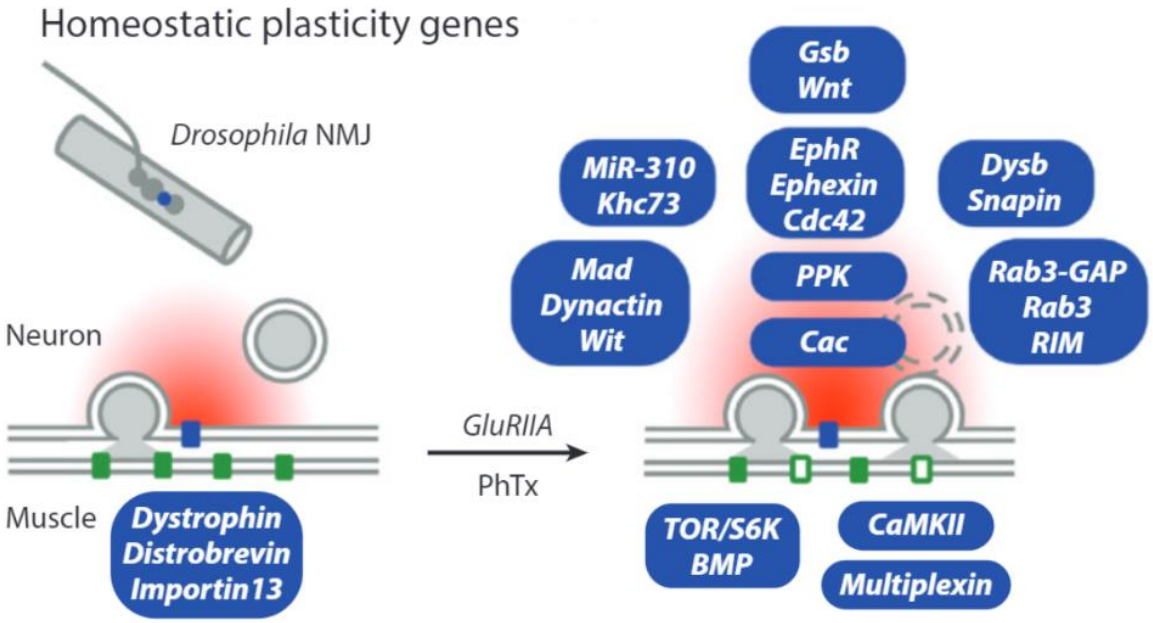

Figure 1.12 **Genes involved in PHP.**
Genetically mutate GluR subunit A (GluRIIA) or pharmacologically treat NMJ with philanthotoxin (PhTx) induces PHP. Many genes were found involved in PHP, including a retrograde signal derived from the muscle, and a complex response in presynaptic neuron. Images are adapted from (Davis and Müller, 2015).

On the other hand, PHP and PHD are fine scale synaptic plasticity mechanisms that act in the presynaptic side to maintain synaptic homeostasis when synaptic machineries are impaired. In PHP, genetic or pharmacological inhibition of postsynaptic GluRs will induce a compensatory increase of presynaptic neurotransmitter release through a series of mechanisms including down regulation of postsynaptic CaMKII activity (Goel et al., 2017; Li et al., 2018b, 2018a), retrograde

signaling cascade mediated by PlexB/Sema-2b (Orr et al., 2017), and RBP/RIM-dependent regulation of the presynaptic readily releasable pool (RRP) (Böhme et al., 2019; Mrestani et al., 2021; Müller et al., 2015) (Figure 1.12). Conversely, in PHD, presynaptic VGLUT overexpression leads to an increase of neurotransmitter vesicle size and a compensatory decrease of synaptic vesicle release (Gratz et al., 2019; Li et al., 2018b; Yeates and Frank, 2021), but the underlying molecular mechanisms are not well-studied.

In addition to physical and biological perturbations, ageing and neurodegenerative diseases are endogenous perturbations that challenge the nervous system. During ageing, memory, learning, motor coordination, and attention are gradually impaired with a corresponding significant loss of neuronal tissue in the brain (Peters, 2006). Neurodegenerative diseases, such as Alzheimer's disease and Parkinson's disease, tend to manifest in older individuals, but others, such as ALS, can be induced at younger ages (Erkkinen et al., 2018; Wang et al., 2020). Because cell death shares general features with many neurodegenerative diseases, many studies and therapeutics are examining way to prevent neuronal loss (Salman et al., 2021; Taoufik et al., 2018). Recent advances in artificial intelligence-based drug design and stimulation of adult stem cells to generate new neurons may provide new avenues for treating these diseases (Salman et al., 2021; Taoufik et al., 2018).

Taken together, neurons face multifaceted perturbations from external and internal sources. In many cases, small scale perturbations can be compensated by synaptic plasticity mechanisms. However, large scale neuronal cell death, as observed in many neurodegenerative diseases, is more damaging and whether synaptic plasticity can overcome these perturbations, potentially by altering nearby healthy neuron, is not known.

1.3.2 Neuronal cell death induces Draper-JNK pathway in glial cells

In the above section, we discussed potential causes of neuronal cell death. However, an important question remains – what are the effects of the dead or dying neuron to nearby tissues, including glial cells and other neurons? Using the *Drosophila* nervous system, the glial Draper-c-Jun N-terminal kinase (JNK) signaling pathway was found to be activated by neuronal cell death and is responsible for removing debris generated by the dying neuron (Awasaki et al., 2006; Freeman, 2015; Hoopfer et al., 2006; Lin, 2003; Logan et al., 2012; Lu et al., 2017; MacDonald et al., 2006). Thus, examining this pathway may provide novel insights into synaptic plasticity mechanisms that promote compensation between neurons.

1.3.2.1 Draper-JNK pathway is required for debris clearance after neuronal injury

Draper is an engulfment receptor expressed in various tissues including the salivary gland, glial cells, muscles, and epidermal cells and was found to mediate autophagy in a cell-autonomous manner or promote dendrite pruning and debris removal non-cell autonomously (Han et al., 2014; Hilu-Dadia et al., 2018; Lu et al., 2017; McLaughlin et al., 2019; McPhee et al., 2010; Purice et al., 2016).

During physical injury induced neuronal cell death, axonal debris activates Draper, possibly through known ligands, Six-Microns-Under, Pretaporter, and the membrane phospholipid phosphatidylserine (Ji et al., 2022; Kuraishi et al., 2009; Kurant et al., 2008; Park et al., 2021; Shacham-Silverberg et al., 2018; Tung et al., 2013). Draper activation signals to the nucleus via *Drosophila* JNK/activator protein-1 (AP1) and STAT92E to promote engulfment gene expression, including *draper* itself (Figure 1.13) (Doherty et al., 2014; Lu et al., 2017; Purice et al., 2016). Draper also activates a Src-family signaling cascade composed of Src42a

and Shark, which, together with the PTB-domain protein dCed-6, promote engulfment of axon debris. Glial specific *draper* knockdown leads to significant delays in axon debris, highlighting the role of glia in injury responses (Awasaki et al., 2006; Doherty et al., 2014; Lu et al., 2014; Ziegenfuss et al., 2012, 2008).

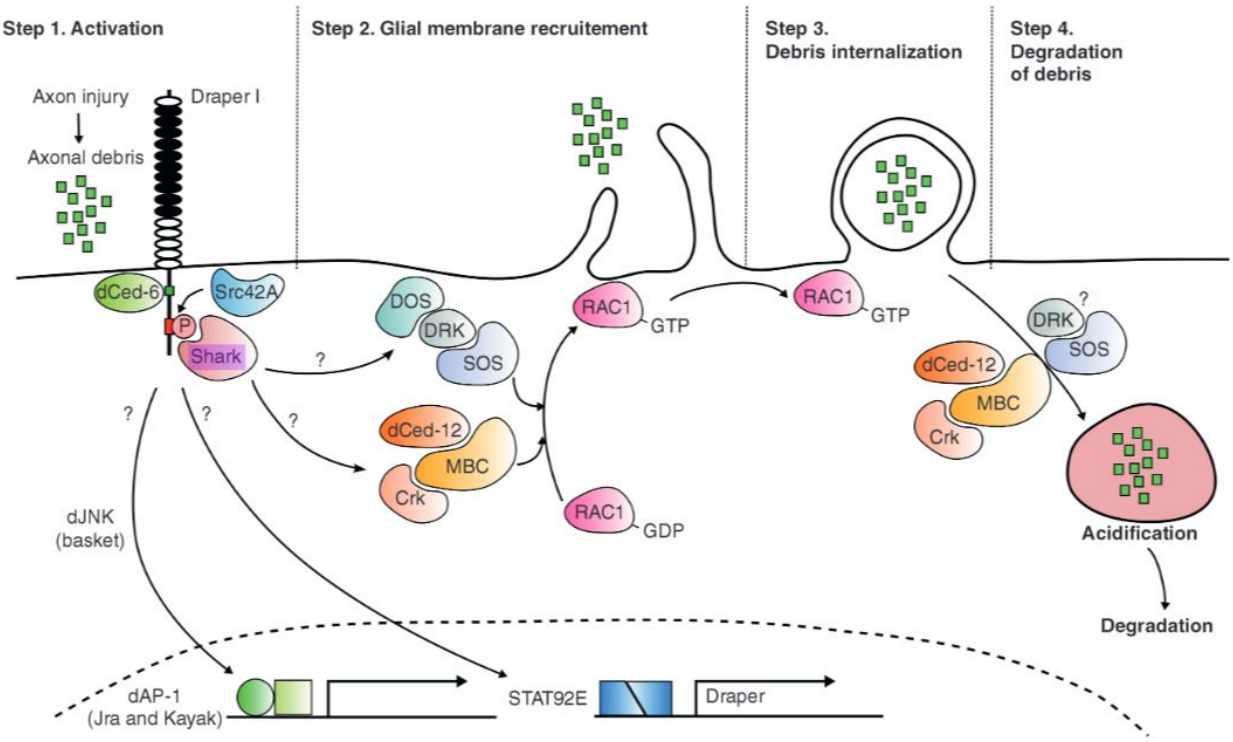

Figure 1.13 **Draper-mediated axonal debris removal.**
Axonal debris activates the Draper signaling pathway and leads to engulfment gene expression (Step 1). Glial membranes are then recruited to engulf and internalize the debris through dCed-6 and Rac1 (Step 2 and 3). Final acidification and degradation require the GEFs dCed-12/Mbc/Crk and Drk/Dos. Image is adapted from (Freeman, 2015).

1.3.2.2 Draper has different functions in glial cells and muscles

In addition to injury induced glial responses, Draper has an important role during normal synaptic development. During metamorphosis, extensive axon and dendrite pruning in the brain sculpt neural circuits in a Draper-dependent manner (Awasaki et al., 2006). At the larval NMJ,

Draper is expressed in both glial cells and muscles but absent in neurons (Fuentes-Medel et al., 2009). During larval development, the NMJ is continuously expanding, and the Draper/Ced-6 pathway modulate the synaptic growth speed (Wu et al., 2009). Specifically, muscle-derived Draper is responsible for removing immature and unstable boutons, also known as ghost boutons, whereas glial Draper is important for removing presynaptic debris generated by excess synaptic growth (Fuentes-Medel et al., 2009).

1.3.3 Open Questions

In the above section, we discussed the consequences of different types of perturbations to the nervous system. Perturbations that only affect synaptic function can trigger pre- and postsynaptic plasticity mechanisms to compensate for dysfunction and limit damage to the circuit. Other perturbations can lead to neuronal cell death and trigger debris removal mechanisms, but how cell death impacts the entire circuit function is not well understood. An exciting hypothesis is that the remaining healthy neurons may potentially compensate for the functional loss of other circuit members by elevating their synaptic release, thus providing an entry point for restoring circuit function. Recent data revealed that uninjured, healthy neurons detect nearby cell death by Draper-dependent glial signaling (Hsu et al., 2020). Therefore, glial cell roles in normal development and under perturbed states may share signaling components to enable normal circuit function.

In my thesis, I will address fundamental questions about synaptic plasticity and ask whether and how neuronal cell death induces compensation from nearby healthy neurons. Revealing the contribution of remaining healthy neurons to circuit function will significantly

enhance our understanding of synaptic plasticity and provide new perspectives of how to restore synaptic function.

CHAPTER 2
SYSTEMATIC EXPRESSION PROFILING OF DPRS AND DIPS REVEALS CELL SURFACE CODES IN DROSOPHILA LARVAL MOTOR AND SENSORY NEURONS

2.1 Introduction

In complex nervous systems, neurons must identify their correct partners to form synaptic connections. The prevailing model to ensure correct recognition posits that cell surface proteins (CSPs) in individual neurons act as identification tags (Sperry, 1963). Thus, knowing what cells express which CSPs would provide insights into neural development, synaptic connectivity, and nervous system evolution.

A recent interactome screen of a subset *Drosophila* CSPs revealed many novel interactors, including interactions between two IgSF subfamilies, the Dprs and DIPs (Carrillo et al., 2015; Özkan et al., 2013; Tan et al., 2015). The 21 Dprs interact with 11 DIPs heterophilically and some members also interact homophilically. Additionally, most Dprs and DIPs are promiscuous and interact with several members of the other family. Since the discovery of the Dpr-DIP interactome, interactions between Dprs and DIPs have been implicated in synaptic connectivity, cell survival, and synaptic growth (Ashley et al., 2019; Bornstein et al., 2021; Carrillo et al., 2015; Courgeon and Desplan, 2019; Menon et al., 2019; Sanes and Zipursky, 2020; Venkatasubramanian et al., 2019; Xu et al., 2019, 2022, 2018). However, most studies focused on Dprs and DIPs have implicated only a small subset, likely due to low-penetrance targeting defects and molecular redundancy. For example, in the larval neuromuscular circuit, loss of DIP-α leads to complete loss of muscle 4 innervation by a specific

motor neuron; however, neuromuscular junctions (NMJs) on other muscles formed by the same neuron are unaffected, suggesting different synaptic recognitions utilize different pairs of CSPs even within the same neuron (Ashley et al., 2019). Thus, obtaining a complete expression map of families of CSPs in individual neurons within specific circuits would facilitate subsequent functional studies.

Different approaches are available to map the expression patterns of genes of interest. Modern technologies like single cell RNA sequencing (scRNAseq) provide enormous information about gene expression in each cell type and has been successfully applied in the fly nervous system (Avalos et al., 2019; Li, 2020; Tang et al., 2009). However, most scRNAseq datasets do not capture the dynamic expression during development, and it is difficult to identify individual cell types from heterogenous clusters. Another approach, possibly more accurate for closely related cells, is to generate genetic reporter lines for genes of interest and directly visualize their expression. For example, in *Drosophila*, a collection of GAL4 drivers representing Gr taste receptors were used to map the projection of Gr expressing neurons (Kwon et al., 2014). These genetic reporters together with imaging allow unambiguous characterization of gene expression at a higher spatial and temporal resolution.

In this study, we interrogate the expression patterns of *dprs* and *DIPs*. These IgSF CSPs form extensive interactions and are highly enriched in the nervous system, suggesting important roles in circuit development. To access the expression of these genes, we and others generated a collection of GAL4 lines of 19 *dprs* and 11 *DIPs*. We utilized different UAS reporters to examine expression of *dprs* and *DIPs* in the *Drosophila* larval neuromuscular and sensory circuits. The distinct and stereotyped morphologies and positions of these cells allow us to unambiguously identify the reporter gene expression patterns. Here, we generated expression

maps of *dprs* and *DIPs* in MNs, SNs, and muscles, and found that each MN and SN expresses a unique subset of *dprs* and *DIPs*. Utilizing hierarchical clustering, we found that the same class of SNs expresses similar *dprs* and *DIPs*, suggesting roles in identifying overlapping synaptic partners. Finally, the highly distinct expression patterns of *dprs* and *DIPs* in MNs revealed previously unidentified MNs. The expression analyses generated by this study will benefit future functional studies of Dprs and DIPs in the motor and sensory circuits. The genetic tools and pipeline provided here will facilitate expression studies of *dprs* and *DIPs*, and other CSPs, in other *Drosophila* neural circuits to promote the discovery of identification tags utilized for circuit assembly.

2.2 Results

2.2.1 Generating a GAL4 collection of *dprs* and *DIPs*

Using *Drosophila* Minos-Mediated Integration Cassette (MiMIC) insertions followed by Trojan conversion, and CRISPR-Mediated Integration Cassette (CRIMIC) insertions, we and others generated a collection of GAL4 lines of all *DIPs* and *dpr1-dpr19* (Diao et al., 2015; Kanca et al., 2019; Lee et al., 2018; Nagarkar-Jaiswal et al., 2015b; Venken et al., 2011) (Figure 2.1A). The *Drosophila* line information and contributors are summarized in Table 2.1. For each *dpr*- and *DIP-GAL4*, the cassette is inserted into a common intron or the 5'UTR shared by all isoforms (Figure 2.1A). Therefore, GAL4 expression should report the expression of all isoforms of each gene. Insertion of the *SA-T2A-GAL4-PolyA* tail should generate truncated transcripts because of the presence of the PolyA tail (Logan et al., 1987; Zhang et al., 2015). In addition, the presence of a T2A-GAL4 leads to an arrest during translation at the T2A site followed by a reinitiation of translation at the GAL4 sequence (Diao et al., 2015; Szymczak-Workman et al.,

2012). To confirm the disruption of the gene of interest, my colleague Meike Lobb-Rabe measured transcript expression by qRT-PCR using primers downstream of the insertion site and confirmed that most GAL4 lines are loss-of-function alleles. For example, in homozygous viable GAL4 lines, *DIP-α-GAL4* and *DIP-ζ-GAL4* showed no detectable *DIP-α* and *DIP-ζ* mRNA, respectively suggesting they are null alleles (Figure 2.2). Several GAL4 lines, like *DIP-β-GAL4* and *dpr15-GAL4*, showed a reduction in mRNA levels, whereas some lines like *DIP-ι-GAL4* and *dpr16-GAL4* showed no change in mRNA expression. Although these GAL4 lines do not show a significant loss of transcription, the T2A sequence should still disrupt translation and generate mutant proteins. For homozygous lethal lines, we examined mRNA levels in heterozygous animals and found most GAL4 lines show expression near 50% (Figure 2.2), suggesting these GAL4 lines are severe loss-of-function alleles. The qRT-PCR results are summarized in Table 2.2. In summary, approximately 70% of the insertions cause a severe disruption of transcription.

Because most GAL4 insertions are mutants, we used heterozygotes to map *dpr* and *DIP* expression. Loss of a single copy of any *dpr* or *DIP* did not affect gross viability, cell survival, or synaptic connectivity in heterozygotes as revealed by postsynaptic marker, DLG, and presynaptic marker, anti-horseradish peroxidase (HRP; a marker for all neuronal membranes (Jan and Jan, 1982)). Thus, the *dpr/DIP-GAL4* driver lines should faithfully report the cells that express *dprs* and *DIP*s (Lee et al., 2018; Nagarkar-Jaiswal et al., 2015a).

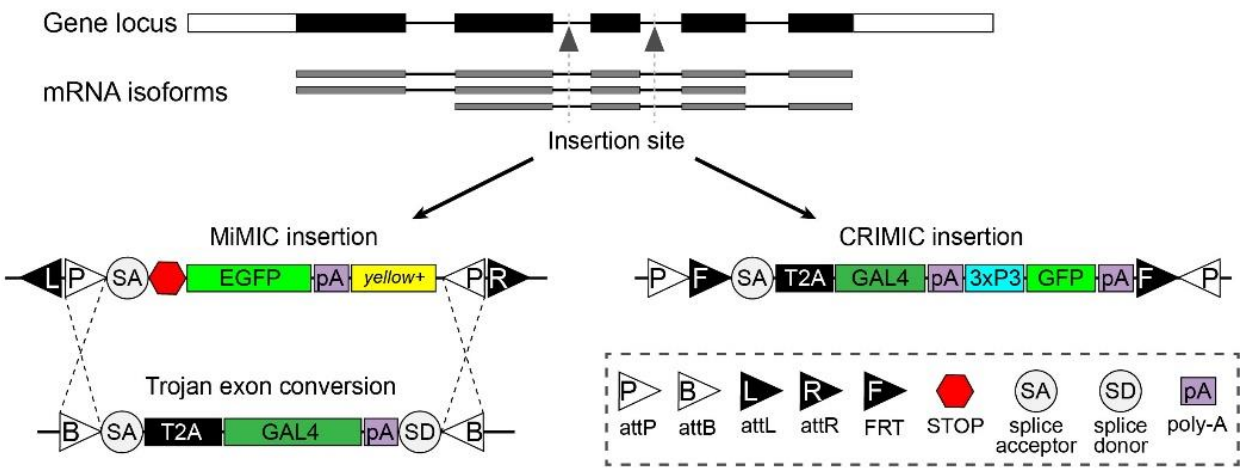

Figure 2.1 **Schematic of GAL4 insertion.**
MiMIC or CRIMIC cassettes were inserted into a common intron or 5'UTR to capture the expression of all isoforms for each *dpr* and *DIP*. MiMIC insertions were flanked by two attP sites which are later swapped by a GAL4 exon or T2A-GAL4 trojan exon.

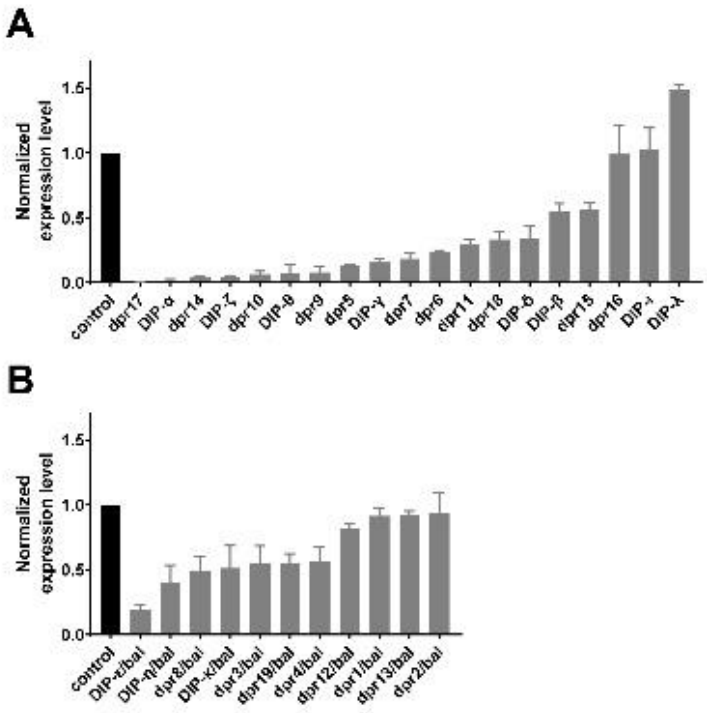

Figure 2.2 **Respective mRNA level in *dpr/DIP-GAL4* lines.**
(A) qRT-PCR results of homozygous viable *dpr/DIP-GAL4* lines. mRNA levels were double normalized to control animal and Rpl32 internal control. (B) qRT-PCR results of homozygous lethal *dpr/DIP-GAL4* lines. mRNA levels were double normalized to control animal and Rpl32 internal control.

2.2.2 Profiling *dprs* and *DIPs* expression in MNs, muscles, glial cells, and SNs

The unique morphology of MN axon terminals allows us to unambiguously determine MN identities. To examine the expression of *dprs* and *DIPs* in MNs, we first crossed each GAL4 line to a fluorescent reporter line and monitored reporter expression at third instar NMJs (Figure 2.3). GAL4 lines derived from MiMIC insertions were crossed to a GFP reporter, whereas CRIMIC GAL4 lines were crossed to an mCherry reporter as CRIMIC insertions carry a 3XP3-GFP marker that expresses in glial cells and the lateral bipolar dendrite (lbd) neuron. To identify all NMJs, we labeled preparations with antibodies against DLG and HRP and confirmed that the gross muscle innervation was normal in *dpr/DIP-GAL4* heterozygous lines. GFP or RFP labeling of NMJs revealed the corresponding MNs that express each *dpr* and *DIP*. We followed this pipeline for each *dpr*/*DIP*-GAL4 to record expression in all MNs, muscles, glial cells, and SNs.

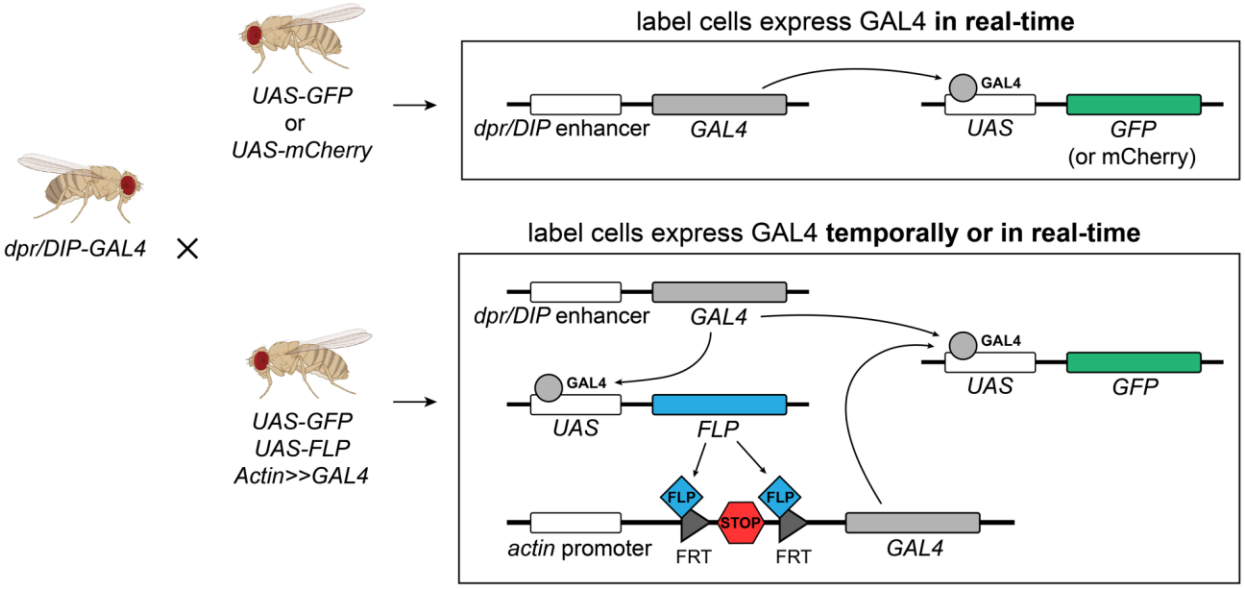

Figure 2.3 **Schematic showing the experimental procedure.**
Each *dpr/DIP-GAL4* line was crossed to a real-time reporter (*UAS-GFP* or *UAS-mCherry*) and a permanent reporter (*UAS-GFP*, *UAS-FLP*, *actin-(FRT.STOP)-GAL4*) to reveal the dynamic expression of *dprs* and *DIPs*.

2.2.2.1 Expression of dprs and DIPs in MNs

We mapped the expression of *dprs* and *DIPs* in all larval MNs. The expression of GAL4 and the fluorescent reporter should correlate with the endogenous gene expression. In prior work, we observed expression of *dpr6*, *dpr10*, *dpr11*, *DIP-α*, and *DIP-γ* in MNs (Ashley et al., 2019; Carrillo et al., 2015). Here, we confirmed these expression patterns; for example, *DIP-α* was selectively expressed in Is MNs but not in Ib MNs (Figure 2.4A). Our data also revealed that several *dprs* and *DIPs* are not always expressed at the same level in a specific MN. For example, *DIP-δ-GAL4* only labeled 22% of abdominal MN12-Ib (10 out of 45 MN12-Ib examined, Figure 2.4B). Similarly, *dpr16-GAL4* was expressed in 10 out of 25 MN30-Ib and 9 out of 25 MN14-Ib examined. Additionally, some *dprs* and *DIPs* are expressed in a gradient along the anterior to posterior axis. For example, *dpr2* showed high expression in MN1-Ib in the anterior but became undetectable from abdominal segment 4 (A4) to the posterior (Figure 2.5A). *DIP-ζ-GAL4*, on the other hand, labeled anterior MN16/17-Ib weakly (also known as MN15/16/17-Ib from (Hoang and Chiba, 2001; Kim et al., 2009)) but was much stronger in the posterior (Figure 2.5B). Note that *dpr2* also has a variable expression in MN9-Ib (Figure 2.5A). These complex expression patterns suggest intricate regulatory mechanisms of *dprs* and *DIPs*.

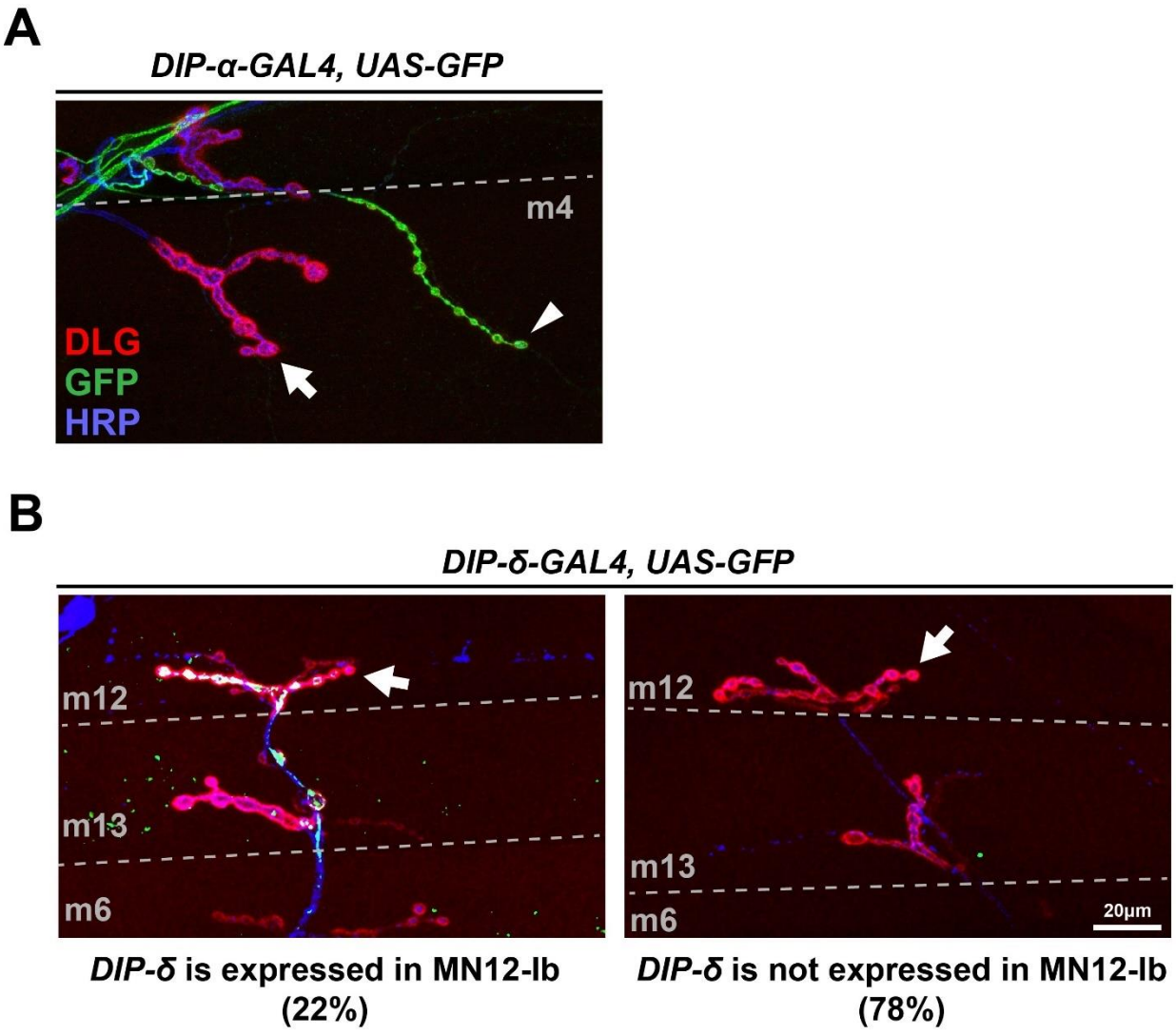

Figure 2.4 **Expression of *DIP-α* and *DIP-δ* in MNs.**
(A) Representative image showing the expression of *DIP-α* in Is MNs (arrowhead) but not in adjacent Ib MNs (arrow). (B) Representative images showing the varied expression of *DIP-δ* in MN12-Ib (arrow). Note that 22% MN12-Ib express *DIP-δ* (left) whereas 78% do not express (right).

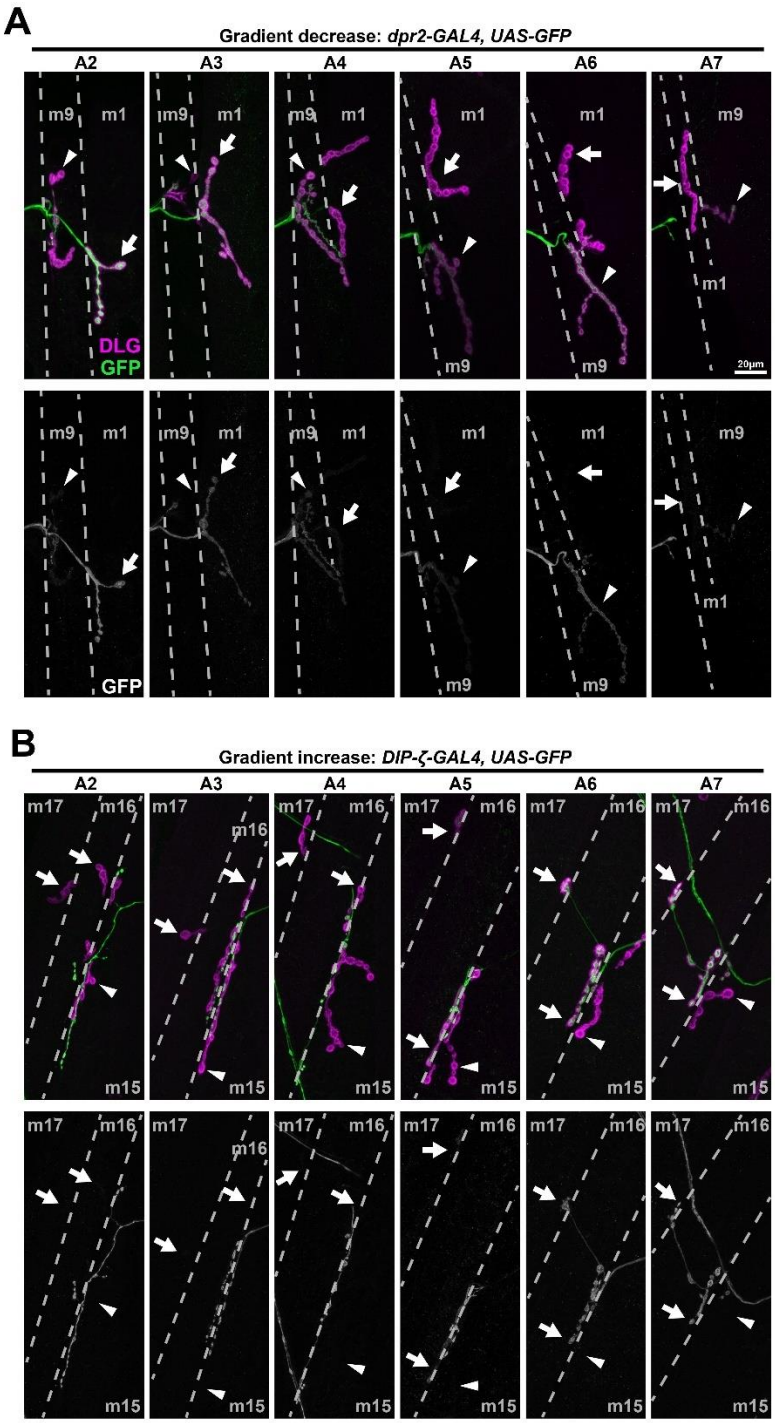

Figure 2.5 **Some *dprs* and *DIPs* are expressed in a gradient.**
(A) Example of a decrease in expression of *dpr2-GAL4* in MN1-Ib (arrows) from anterior hemisegment A2 to posterior hemisegment A7. Note that the expression in nearby MN9-Ib (arrowheads) is also not robust as it was not expressed in A2 and A3 but expressed in A4 to A7. (B) Example of an increase in expression of *DIP-ζ-GAL4* in MN16/17-Ib (arrows) from anterior hemisegment A2 to posterior hemisegment A7. Note that the expression in nearby MN15/16-Ib (arrowheads) was always absent.

Work from our lab and others suggested that Dprs and DIPs are synaptic recognition molecules (Ashley et al., 2019; Bornstein et al., 2021; Carrillo et al., 2015; Courgeon and Desplan, 2019; Menon et al., 2019; Venkatasubramanian et al., 2019; Xu et al., 2021, 2018). In the fly neuromuscular circuit, MN axons explore the musculature field beginning in embryonic stage 14 and synaptic markers are observed in stage 16 (Yoshihara et al., 1997). A traditional UAS reporter in third instar larva will only report real-time expression and will not reveal if a *dpr* or *DIP* is temporally expressed earlier in development. To capture the temporal expression patterns of *dprs* and *DIPs*, we utilized a permanent labeling reporter to constantly label the GAL4-expressing neuron (Figure 2.3). This method takes advantage of the FLP-out system to remove a stop codon within two FRT sites and activate an *actin*-GAL4 to maintain GAL4 expression in any cells that expressed the gene of interest GAL4. Interestingly, we observed only a few *dprs* and *DIPs* that are temporally expressed in MNs. For example, MN21/22-Ib is not labeled when *dpr9-GAL4* is crossed to *UAS-GFP*, but with the permanent labeling reporter, the same neuron showed strong expression (Figure 2.6). It is noteworthy that the CRIMIC cassettes are excisable by Flippase as well due to the presence of flanking FRT sites (Figure 2.1). However, because of the activation of the permanent *actin-GAL4*, the excision of CRIMIC cassettes does not pose a technical issue.

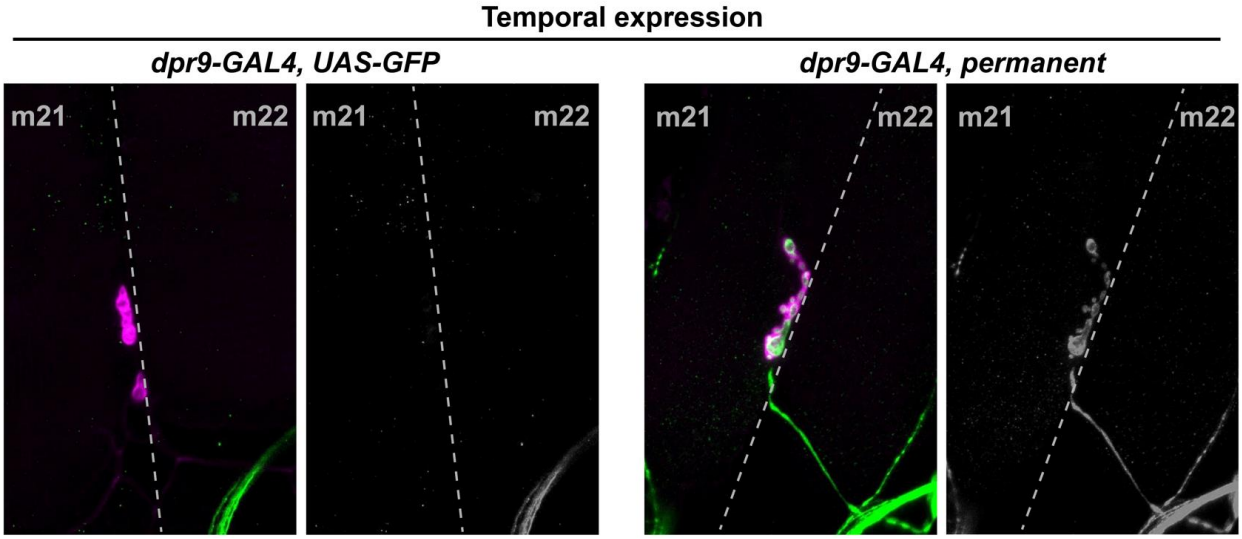

Figure 2.6 **Some *dprs* and *DIPs* are temporally expressed in MNs.**
Example of temporal expression of *dpr9-GAL4* in MN21-Ib. MN21-Ib was not labeled by *dpr9-GAL4*>GFP animals, but 50% of MN21-Ib were labeled in the cross to the permanent reporter.

We summarized the expression of *dprs* and *DIPs* in all MNs in Figure 2.7. Here, we included variable expression patterns (defined by how frequent a cell expresses the reporter) and gradient and temporal expression patterns. Criteria for each expression category is described in the methods. In general, *dprs* are expressed in many MNs while *DIPs* are expressed much more selectively. Each MN expresses at least one *DIP*, and overall, each MN has a unique *dpr* and *DIP* expression signature. For example, we found that additional *DIPs* (*DIP-γ*, *-ε*, *-ζ*, *-η*, *-θ*, *-κ*) are also expressed in Is MNs. Interestingly, *DIP-ε* is expressed only in the ventral Is (vCE) whereas *DIP-η* is expressed only in the dorsal Is (dCE) (Figure 2.7). Taken together, we generated a *dpr/DIP* expression map in all larval MNs and found that each MN expresses a unique subset.

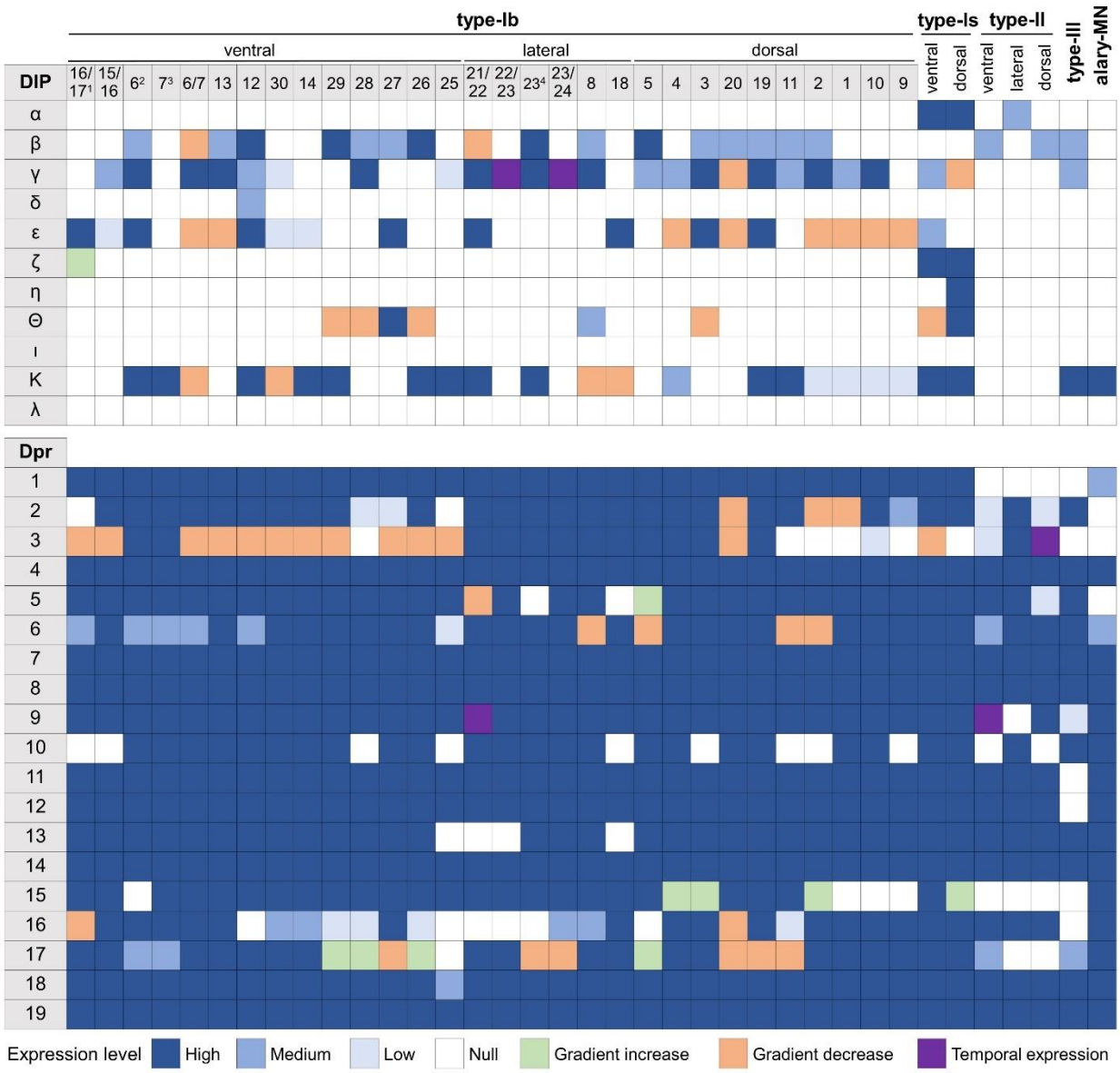

Figure 2.7 **Expression map of *dprs* and *DIPs* in all larval MNs.**
Each column represents a MN including type-Ib, type-Is, type-II, type-III and the alary MN. Expression of each gene in each MN is characterized into a specific category as indicated in the legend.
[1] (Hoang and Chiba, 2001) names this neuron as MN15/16/17-Ib.
[2] Represents MN6-Ib only in A2 hemisegments, see further characterization below.
[3] Represents MN7-Ib only in A2 hemisegments, see further characterization below.
[4] Represents the newly identified MN23-Ib, see further characterization below.

2.2.2.2 Expression of dprs and DIPs in muscles

In a previous study, we observed *dpr10* expression in ventral and dorsal muscles and its interacting partner, *DIP-α,* in Is MNs (Ashley et al., 2019). To label muscle nuclei and report both temporal and real-time gene expression, we used the G-TRACE system (Evans et al., 2009) that takes advantage of FLP-FRT and GAL4/UAS (Figure 2.8A). If a GAL4 is transiently expressed, then cell nuclei will be GFP positive. However, if the cell nuclei are labeled by both GFP and RFP, this may suggest the GAL4 is consistently expressed. We utilized the G-TRACE system and confirmed expression of *dpr10* in all longitudinal muscles, but not in oblique or transverse muscles (Figure 2.8B-C). This expression pattern suggests distinct transcriptional regulation programs between muscle groups (Bate, 1990). In addition, we found that a small subset of muscles, such as m5 and m8, showed inconsistent expression of *dpr10* (Figure 2.8B, arrow). Also, all muscle nuclei co-labeled with GFP and RFP in *dpr10-GAL4>G-TRACE,* suggesting that *dpr10* expression is maintained throughout larval development.

We examined other *dprs* and *DIPs* and found that *dpr19* is expressed in all muscles (Figure 2.8D), including the oblique and transverse muscles (Figure 2.8E). Unlike *dpr10*, most muscle nuclei in *dpr19-GAL4>G-TRACE* are only GFP positive, suggesting that *dpr19* is temporally expressed and turned off in late larval stages. To confirm this temporal expression, we examined *dpr19-GAL4>mCherry* first instar larvae and observed a high level of muscle expression, which we did not observe in third instar (Figure 2.9). Taken together, we showed that muscles express many fewer *dprs* and *DIPs* compared to motor and sensory neurons (Figure 2.8F). These results suggest that a subset of *dprs* and *DIPs* may function in the MN-muscle recognition and others in premotor neuron-MN recognition.

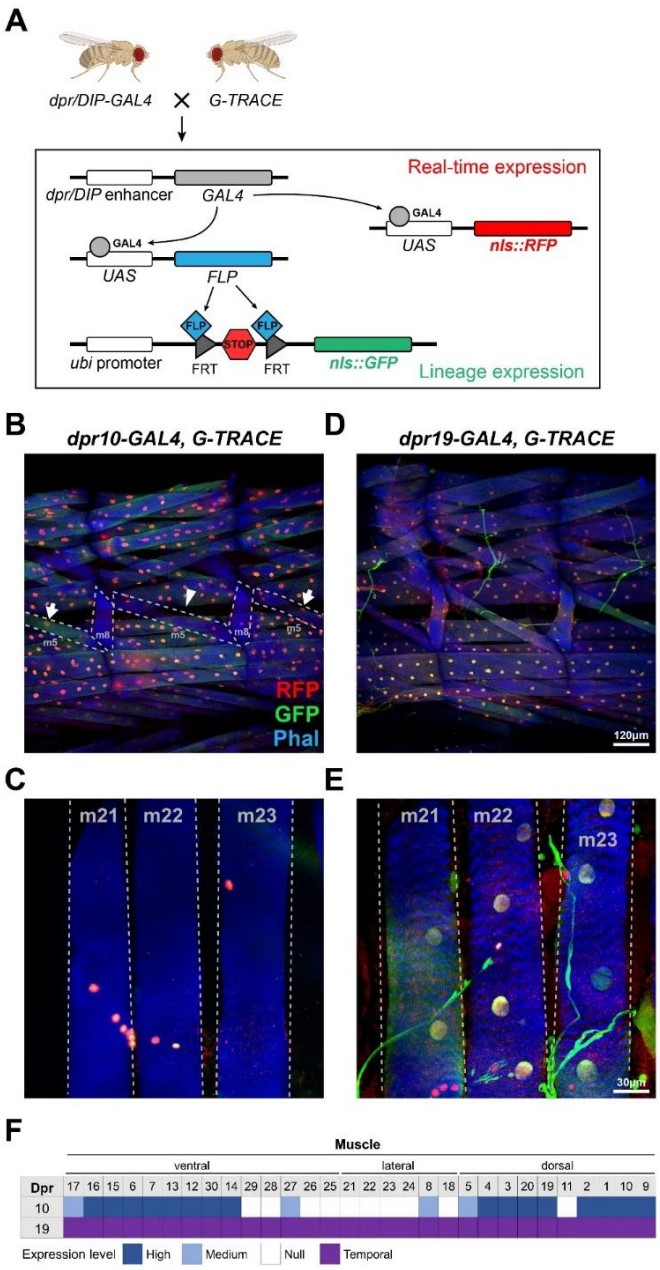

Figure 2.8 **Using the G-TRACE system to probe expression of *dprs* and *DIPs* in muscles.** (A) Schematic depiction showing the cross between *dpr/DIP-GAL4* and the *G-TRACE* reporter. Red signal represents real-time GAL4 expression and green signal represents earlier GAL4 expression. (B-C) *dpr10* is consistently expressed in most muscles (B) but absent in transverse muscles (C) and some deeper ventral muscles. Expression in some muscles is not consistent. For example, in some hemisegments m5 nuclei are not labeled (arrowhead), but an adjacent hemisegment shows labeling of m5 nuclei (arrows). *dpr10* expression is maintained throughout development as revealed by co-labeling with GFP and RFP. (D-E) *dpr19* is expressed in all muscles (D) including transverse muscles (E). Compared to *dpr10*, these nuclei have less RFP intensity, which may indicate that *dpr19* is temporally expressed in early development and turned off later. (F) Expression map of *dpr10* and *dpr19* in muscles.

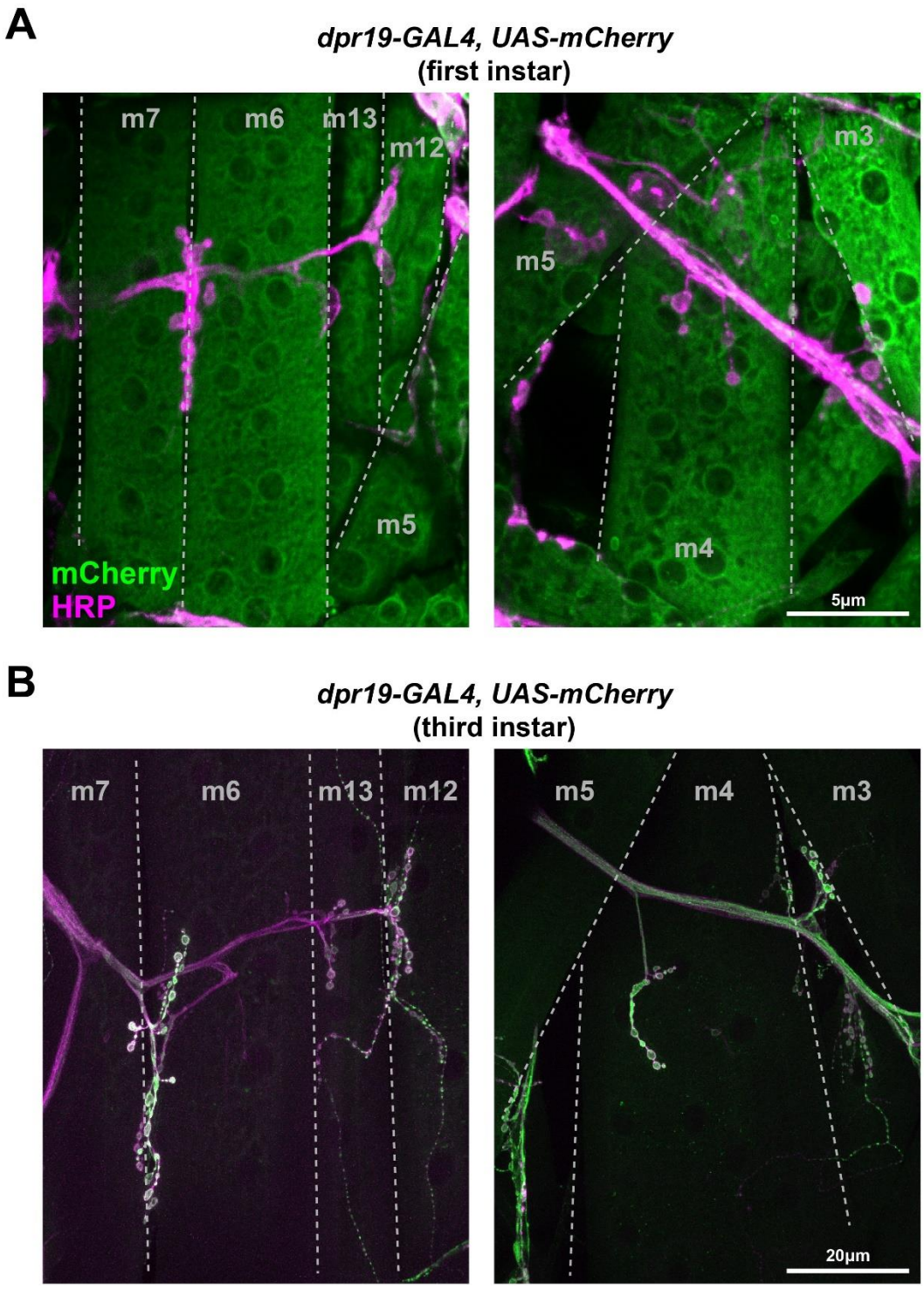

Figure 2.9 ***dpr19* is expressed in muscles in early larval development.**
(A) Representative images of *dpr19-GAL4>mCherry* in first instar larvae. *dpr19* is expressed in ventral (left) and dorsal (right) muscles. (B) Representative images of *dpr19-GAL4>mCherry* in third instar larvae. *dpr19* is not expressed in ventral (left) or dorsal (right) muscles.

2.2.2.3 Expression of dprs and DIPs in glial cells

In the *Drosophila* larval peripheral nervous system, glia play important roles in nervous system development and extensively interact with MN axons (Kottmeier et al., 2020). Therefore, we examined the glial expression of *dprs* and *DIPs*.

To unambiguously distinguish glial and neuronal expression, we used G-TRACE to probe glial expression. We crossed each *dpr/DIP-GAL4* line to the G-TRACE reporter and found that *dpr1* is expressed in glia (Figure 2.10). Additionally, *dpr1* expression is highly dynamic since some glia temporarily express *dpr1* while others maintain *dpr1* expression. This result suggests that Dpr1 in glia and its interacting partners DIP-η, DIP-θ and DIP-ι in MNs (Figure 1.X) may be involved in glia-neuron interactions to guide various processes including neuronal development, axon path finding, and synaptic homeostasis (Bittern et al., 2020; Yildirim et al., 2019).

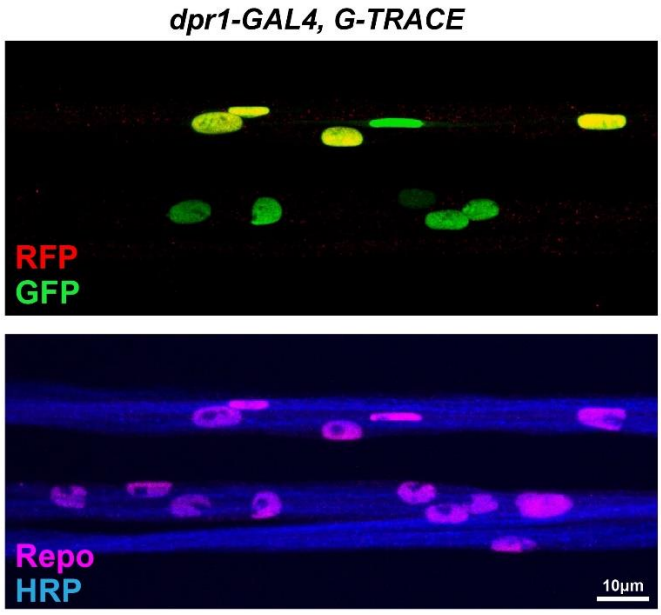

Figure 2.10 **The G-TRACE system revealed *dpr1* expression in peripheral glial cells.** *dpr1* is the only *dpr/DIP* expressed in peripheral glial cells. *dpr1-GAL4* is expressed in subsets of peripheral glial cells as indicated by some glial nuclei labeled by both GFP and RFP, some only by GFP, and some lacking both GFP and RFP.

2.2.2.4 Expression of dprs and DIPs in SNs

Two distinct types of SNs can be classified in the larval body wall, and they are subclassified into different classes based on their morphology and function. Here, we examined expression of *dprs* and *DIPs* in larval SNs using similar approaches. We labeled larvae with anti-HRP to locate the cell bodies of SNs. The *dpr/DIP* expression map in all SNs is shown in Figure 2.11. Similar to MNs, *DIPs* are more sparsely expressed in SNs compared to *dprs* which are broadly expressed. However, several *dprs* (*dpr14*, *dpr15*, and *dpr17*) are only expressed in a subset of SNs, unlike their broad expression pattern in MNs. We also observed that some *dprs* and *DIPs* are temporally expressed. For example, the dorsal da neurons (ddaA, C, F and D) are labeled when *dpr5-GAL4* is crossed to the permanent labeling reporter, but not in *dpr5-GAL4>UAS-GFP* animals (Figure 2.12).

Taken together, we generated expression data for *dprs* and *DIPs* in SNs (Figure 2.11) and showed that each SN expresses a unique subset of *dprs* and *DIPs*, providing support for their roles as identification tags.

Figure 2.11 **Expression map of *dprs* and *DIPs* in all larval SNs.**
Each column represents a SN. Expression of each gene in each SN is characterized into a specific category as indicated in the legend.

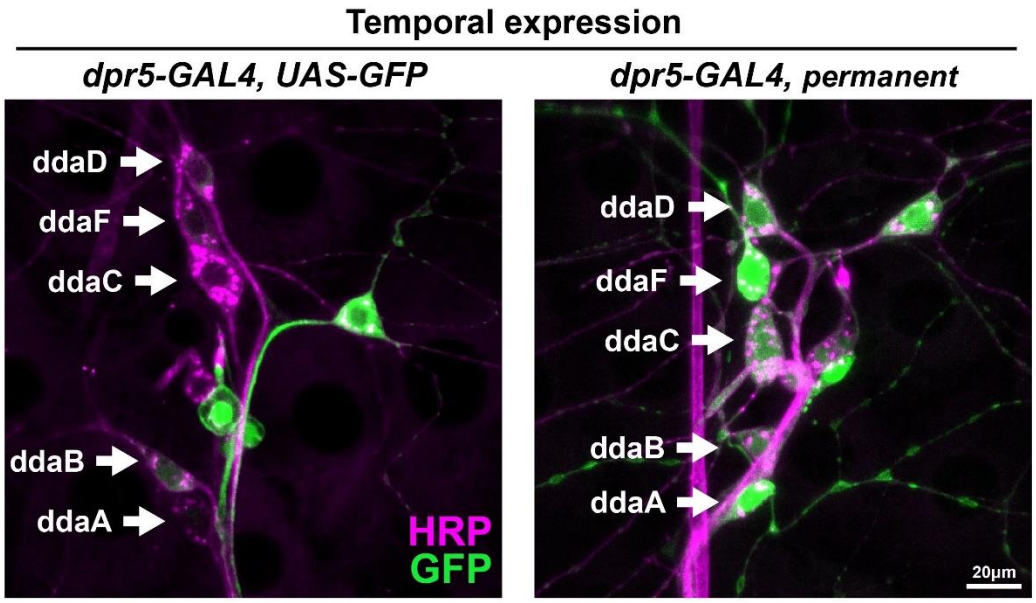

Figure 2.12 **Temporal expression of *dpr5* in the dorsal da neuron cluster.** ddaA, ddaC, ddaF and ddaD are not labeled in *dpr5-GAL4>GFP* larvae but are robustly labeled in the cross to the permanent reporter. Therefore, *dpr5* is temporally expressed in these SNs. ddaB is labeled in the cross to the real-time reporter with a low frequency, thus *dpr5* is considered as low expression in ddaB.

2.2.3 SNs in the same class express similar subsets of *dprs* and *DIPs*

Larval SNs can be divided into types based on their morphology and function, including ch, es, bd, td and da neurons. Although SNs from the same type are distributed throughout the body wall and project their afferent axons through different trajectories, their axon terminals innervate the same region in the VNC and contact common interneuron partners (Grueber et al., 2007; Landgraf et al., 2003b; Merritt and Murphey, 1992; Murphey et al., 1989). For example, the ventral, ventral', and lateral mechanosensory ch neurons all project to the ventral medial region of the VNC and share synapses with some interneurons (Heckscher et al., 2015; Valdes-Aleman et al., 2021). Similarly, different classes of da neurons innervate unique sections of the VNC (Grueber et al., 2007; Merritt and Whitington, 1995; Schrader and Merritt, 2000). Overall,

these innervation patterns suggest that SNs from the same class may share similar identification tags to wire with common interneurons.

Dprs and DIPs have been implicated in synaptic partner recognition so we hypothesized that shared *dpr*/*DIP* expression may be utilized by the same type/class of neurons to instruct connectivity. To test this model, we generated an unbiased hierarchical clustering of SNs based on their *dpr/DIP* expression (Figure 2.13A). Surprisingly, we found a high correlation between SN types/classes and expression of *dprs* and *DIPs*. For example, most es neurons are grouped together, as well as all ch neurons, indicating that these two subclasses of type-I SNs can be distinguished by their expression of *dprs* and *DIPs*. Similarly, subclasses of da neurons are clustered separately. We found that da-I neurons are identifiable by expression of *DIP-θ* and the lack of *dpr2*, *dpr6*, *dpr9*, *dpr11*, *dpr13*, and da-II/da-III neurons are grouped by expression of *dpr2* and *dpr18*, and the lack of *dpr9* (Figure 2.13A). These results suggest that SNs in the same type/class may utilize similar sets of *dprs* and *DIPs* to recognize common interneuron targets.

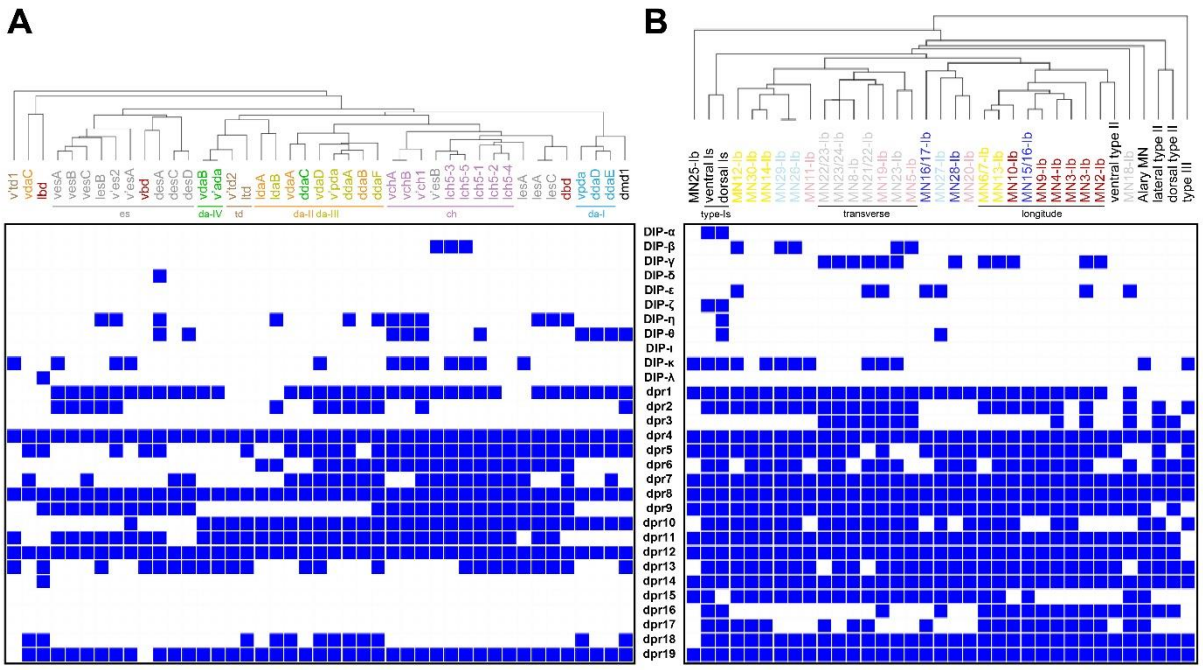

Figure 2.13 **Hierarchical clustering of SNs and MNs reveals shared expression patterns of *dprs* and *DIPs* in neurons from the same class.**
(A) SNs from the same class are clustered together based on the expression pattern of *dprs* and *DIPs*. For example, most es neurons (grey), all chordotonal neurons (purple), and da neurons fall into distinct clusters. (B) Modulatory MNs (II and III) and type-Is MNs are distinct from the main type-Ib cluster. However, individual type-Ib MNs are not easily distinguished based on their expression of *dprs* and *DIPs*.

2.2.4 Expression of *dprs* and *DIPs* is more diversified in MNs

Next, we examined if MNs that project to the same muscle groups also share the same expression patterns of *dprs* and *DIPs*. Muscles are grouped into three main spatial and functional groups – ventral, lateral, dorsal – and further divided into six subgroups based on their orientation – dorsal longitudinal (DL), dorsal oblique (DO), ventral longitudinal (VL), ventral oblique (DO) ventral acute (VA), and lateral transverse (LT) (Figure 1.X) (Bate, 1990; Hooper, 1986; Zarin et al., 2019). Each muscle is normally innervated by one Ib MN and previous studies showed that Ib MNs innervating a muscle group project their dendrites to the same region in the

VNC neuropil where they receive input from common premotor neurons (Kim et al., 2009; Landgraf et al., 2003a, 1997; Landgraf and Thor, 2006; Mauss et al., 2009; Zarin et al., 2019). Thus, if Ib MNs of the same muscle group share premotor neuron partners, they may share wiring molecules. We generated an unbiased hierarchical clustering based on expression of *dprs* and *DIPs* for all MNs (Figure 2.13B). Type-Is, type-II and type-III MNs form independent clusters and are distinct from Ib MNs. For example, *DIP-α*, *DIP-ζ*, *dpr6* and *dpr16* are expressed in type-Is MNs, and lateral and dorsal type-II MNs are identified by the lack of *DIP-κ*, *dpr15*, *dpr17* and the expression of *dpr3* and *dpr16* (Figure 2.13B). However, within Ib MNs, only the MNs innervating LT and DL muscles are clustered together, whereas the other MNs appear randomly distributed. These results suggest that based on the expression patterns of *dprs* and *DIPs*, MNs can be clustered by their type, but Ib MNs cannot be further clustered by the muscles they innervate. MNs must identify distinct pre- and postsynaptic partners which may explain the inability to cluster Ib MNs based on their expression patterns of *dprs* and *DIPs*. Therefore, more complex identification codes may be necessary for MNs to distinguish both pre- and postsynaptic partners.

2.2.5 *dpr*/*DIP* expression maps reveal additional MNs

The map of *Drosophila* MNs and SNs was established decades ago using dye backfills (Broadus et al., 1995; Hoang and Chiba, 2001; Landgraf et al., 2003b). However, fluorescent dyes have some technical limitations since they do not always flow into every terminal structure, which may have resulted in some neurons being overlooked. In this study, we used a genetic approach to probe individual neurons and revealed three uncharacterized MNs – MN23-Ib, MN6-Ib (A2) and MN7-Ib (A2).

2.2.5.1 MN23-Ib

Most Ib MNs have a single muscle target. However, some Ib MNs innervate two muscles in close proximity, likely due to shared recognition cues. For example, a previous study found that Ib MNs innervating the lateral muscles can synapse with neighboring muscles and thus named these neurons MN21/22-Ib, MN22/23-Ib, and MN23/24-Ib (Figure 2.14A) (Hoang and Chiba, 2001). These innervation patterns were later confirmed by MARCM analysis (Kim et al., 2009).

In our analyses, we observed that m23 has several Ib NMJ branches and m24 has only one NMJ (Figure 2.14B). While a single MN can form several branches on a muscle, we found some *dpr*/*DIP-GAL4s* that only label one Ib branch on m23 and no other branches on lateral muscles (Figure 2.14C). These data suggest the existence of an additional MN that solely innervates m23, and we named it MN23-Ib. The bouton size and DLG labeling intensity of M23-Ib boutons indicates that it is a type-Ib NMJ. *DIP-β* and *DIP-κ* are expressed in MN23-Ib and not in the nearby MN22/23-Ib and MN23/24-Ib (Figure 2.14C). Note that MN23/24-Ib forms long, linear Ib NMJs on the underside of m23 before it reaches m24 (Figure 2.14A and C). We also found that *dpr5* was expressed in MN23/24-Ib and nearby MN22/23-Ib, but not in MN23-Ib (Figure 2.14D), providing further evidence for an additional Ib MN solely innervating m23. Additional *dprs* and *DIPs* are expressed in both MN23-Ib and MN23/24-Ib (Figure 2.14B). Thus, we describe a previously unidentified Ib MN that innervates m23.

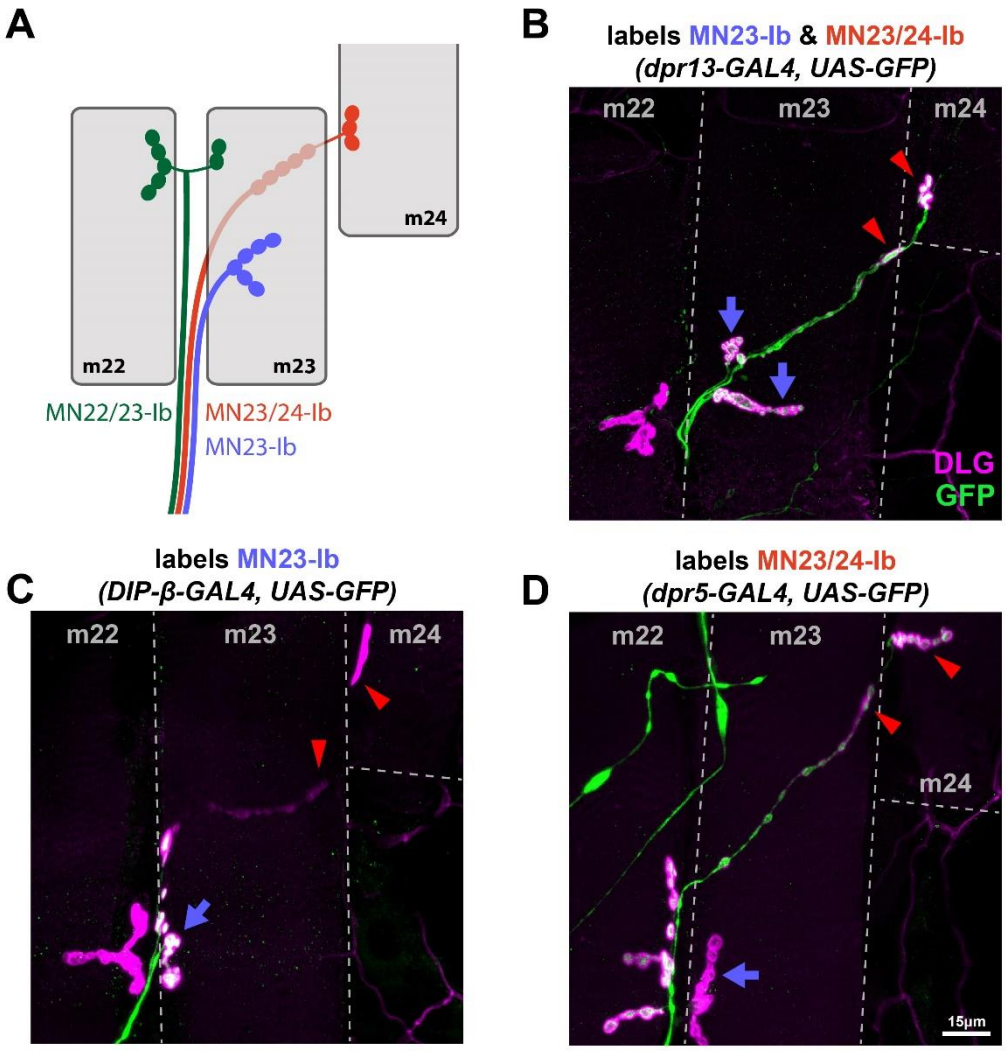

Figure 2.14 **Differentially expressed *dprs* and *DIPs* reveal a MN that solely innervates m23.**
(A) Schematic depiction of transverse muscles 22, 23 and 24 (grey) with previously identified MN22/23-Ib (green), MN23/24-Ib (red) and newly identified MN23-Ib (blue). (B) Representative image showing *dpr13-GAL4* expression in both MN23/24-Ib (red arrowheads) and MN23-Ib (blue arrows). Thus, all boutons on m23 and m24 are labeled by GFP. (C) Representative image showing *DIP-β-GAL4* expression in MN23-Ib (blue arrow). Boutons underneath m23 and boutons from m22, m24 (red arrowheads) are not labeled by GFP, thus *DIP-β-GAL4* is not expressed in MN22/23-Ib and MN23/24-Ib. (D) Representative image showing *dpr5-GAL4* expression in MN22/23-Ib and MN23/24-Ib (red arrowheads), but not in MN23-Ib (blue arrow). The lack of GFP in the arbor on m23 indicated the existence of a MN that solely innervates m23.

2.2.5.2 MN6-Ib and MN7-Ib

Another example of a dual-targeting Ib MN is MN6/7-Ib (also known as RP3 in the embryo) (Schmid et al., 1999; Sink and Whitington, 1991a, 1991b). The innervation pattern of MN6/7-Ib was initially identified by dye fill labeling and MARCM (Hoang and Chiba, 2001; Kim et al., 2009; Sink and Whitington, 1991b). Due to the ease of accessibility of m6 and m7, MN6/7-Ib is extensively used for studies of synaptic connectivity, synaptic growth, and synaptic homeostasis.

Based on these previous studies, we predicted that if a *dpr* or *DIP* were expressed in MN6/7-Ib, the Ib NMJs on both m6 and m7 would be completely fluorescently labeled (Figure 2.15A, right). Surprisingly, in A2, we observed several *dpr*/*DIP-GAL4s* that are expressed in Ib MNs that have large NMJs on m6 and others that are expressed mainly in the Ib NMJs on m7 (Figure 2.15A, left). For example, *DIP-β, DIP-γ*, and *DIP-ε* were expressed in a MN that mainly innervates m6 (Figure 2.15B), whereas *dpr15* was expressed in a MN that mainly innervates m7 (Figure 2.15C). These expression patterns suggested that two Ib MNs innervate m6 and m7 in A2. Hereafter, we named these MNs as MN6-Ib and MN7-Ib. Prior studies hinted at the possibility of two MNs based on the larger synaptic terminal area on m6/7 in A2 compared to A3-A6 (Lnenicka and Keshishian, 2000). However, it was thought that the larger synaptic area was due to a large NMJ from a single Ib MN. In the larval neuromuscular circuit, the number of boutons reflect the size of the NMJ. We quantified the m6 and m7 Ib NMJs and observed a significantly larger arbor in A2 compared to A3 (Ib NMJ on m6: 34.2 on A2 and 18.5 on A3; Ib on m7: 23.1 on A2 and 11.7 on A3) (Figure 2.16). Taken together, m6 and m7 in A2 are innervated by two Ib MNs.

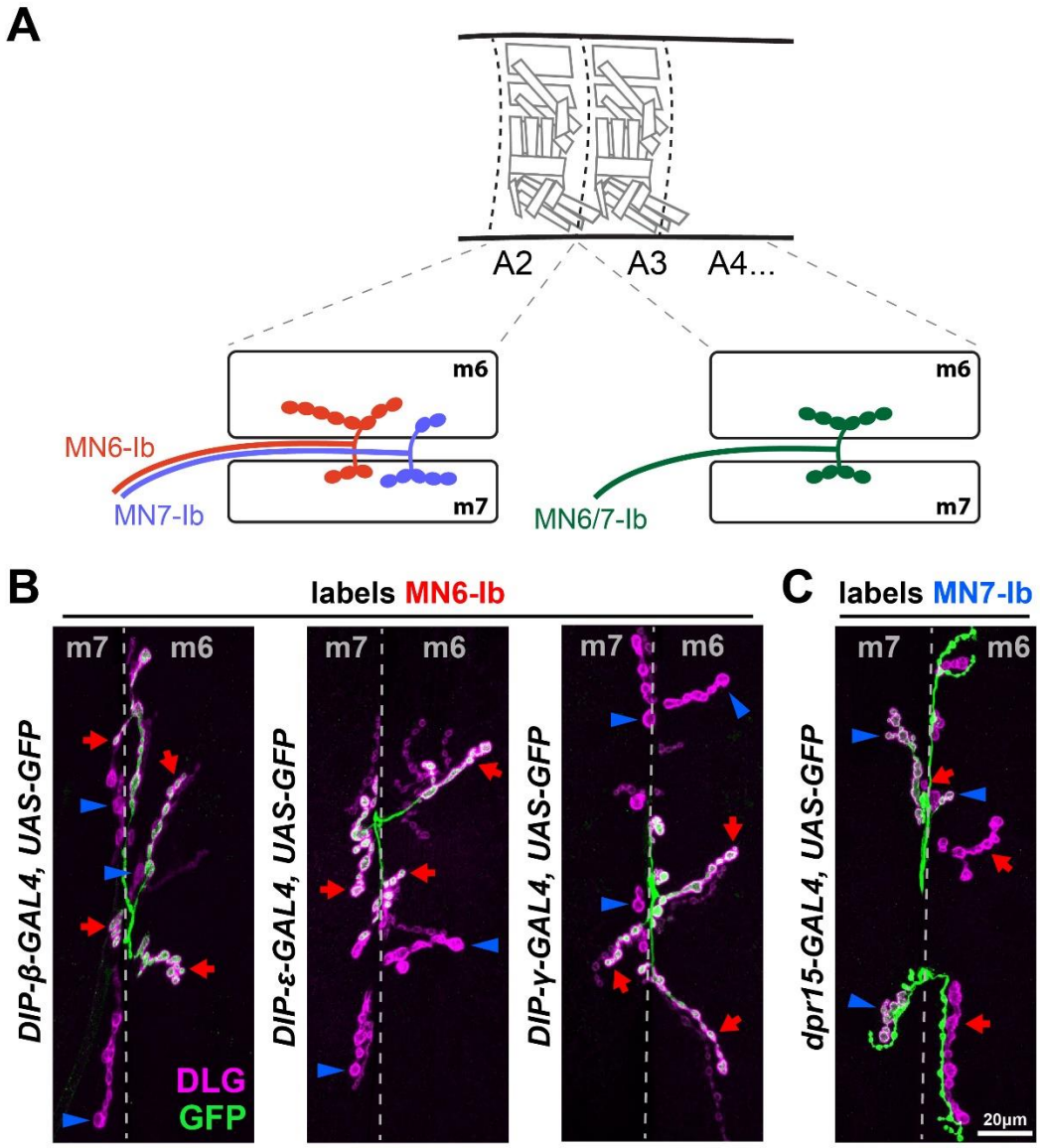

Figure 2.15 **Differentially expressed *dprs* and *DIPs* reveal MN6-Ib and MN7-Ib in segment A2.**
(A) Schematic depiction of MN6-Ib (red) and MN7-Ib (blue) in segment A2, and MN6/7-Ib in A3-A7 (green). MN6-Ib preferentially innervates m6 but also forms a small NMJ on m7, whereas MN7-Ib prefers m7 but also forms a small NMJ on m6. (B) Representative images showing that *DIP-β*, *DIP-ε* and *DIP-γ* are specifically expressed in MN6-Ib (red arrows), but not in MN7-Ib (blue arrowheads). Note that MN6-Ib forms boutons with both m6 and m7, since there is a small GFP positive type-Ib NMJ on m7 (red arrows on m7). Conversely, the lack of GFP in most m7 type-Ib NMJ and the small m6 type-Ib NMJ (blue arrowheads) indicate MN7-Ib also dual innervates both muscles. (C) Representative image showing that *dpr15* is specifically expressed in MN7-Ib (blue arrows) but not in MN6-Ib (red arrowheads). MN6-Ib and MN7-Ib also show dual innervation patterns in this genetic background.

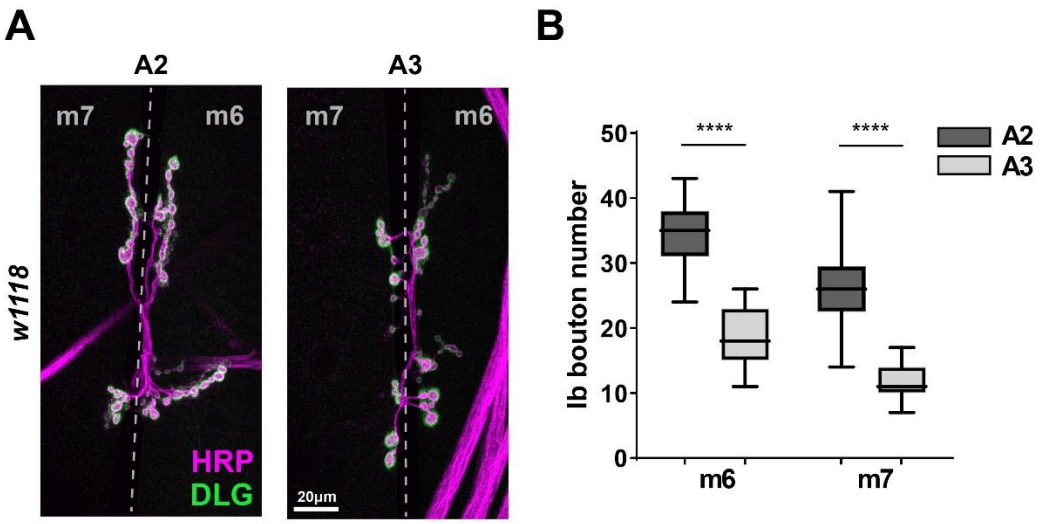

Figure 2.16 **Larger Ib NMJs on m6 and m7 in A2.**
(A) Representative images showing larger type-Ib NMJs on m6 and m7 in A2 compared to A3. (B) Bouton number counts from m6 and m7 in A2 and A3 confirmed that A2 NMJs are double the size of A3.

A recent study reported a GAL4 driver (*GMR79H07-GAL4*) that labels MN6-Ib in A2 (Aponte-Santiago et al., 2020). We tested this driver and confirmed MN6-Ib expression; however, it sometimes labels MN7-Ib NMJs or both MN6-Ib and MN7-Ib (Figure 2.17). We examined MN6-Ib and MN7-Ib further to better understand their innervation patterns and dendritic projections. Interestingly, we found that MN6-Ib and MN7-Ib preferentially innervate their corresponding muscle, but sometimes, these MNs also form minor NMJs on the neighboring muscle (Figure 2.15A). Next, we monitored the frequency of dual innervation of each MN using *GMR79H07-GAL4* and found that 68.2% of MN6-Ib and 72.7% of MN7-Ib innervate both muscles (Figure 2.18A). We also determined the size of each NMJ by counting Ib boutons and found that on average MN6-Ib forms 48.6 boutons on m6 and 5.9 boutons on m7, while MN7-Ib forms 3.1 and 30.8 boutons on m6 and m7, respectively (Figure 2.18B).

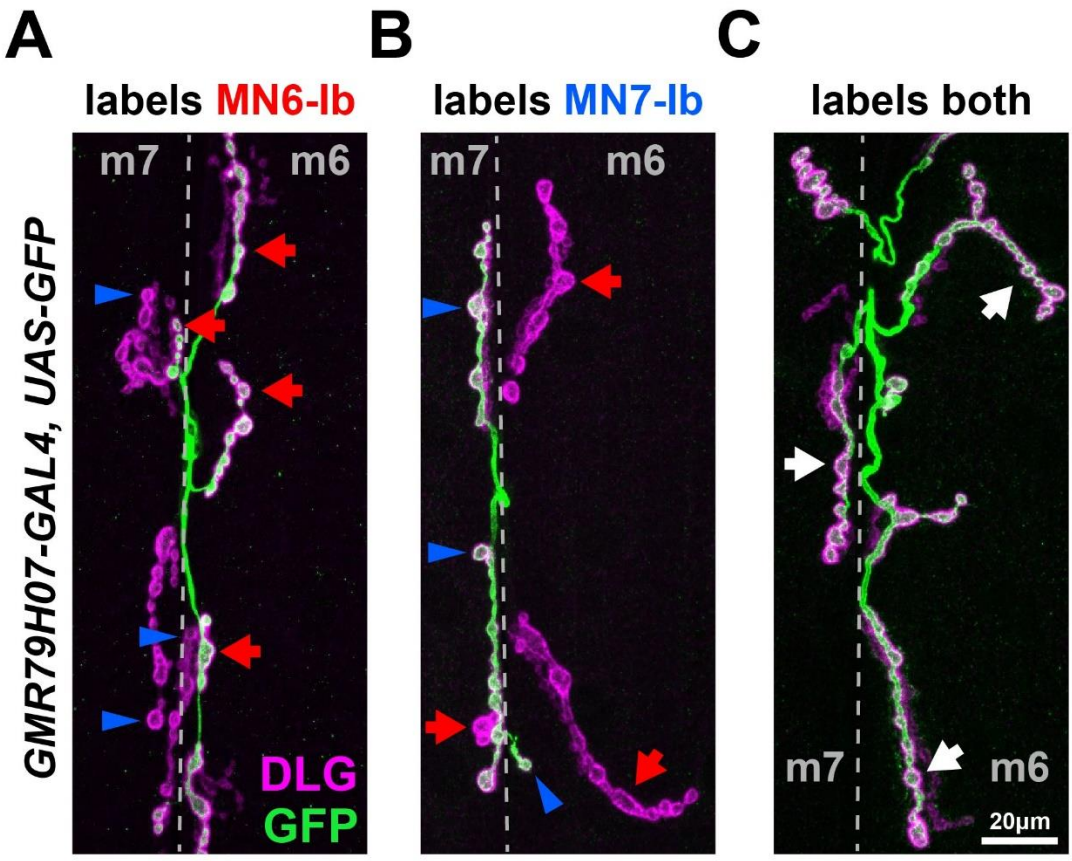

Figure 2.17 ***GMR79H07-GAL4* randomly labels MN6-Ib and MN7-Ib.**
A previous study reported that *GMR79H07-GAL4* labels type-Ib NMJs on m6 in A2 (Aponte-Santiago et al., 2020). We crossed this driver to *UAS-GFP* and found inconsistent expression patterns since it (A) sometimes only labels MN6-Ib (red arrows), (B) sometimes only labels MN7-Ib (blue arrowheads), or (C) sometimes labels both MNs (white arrows). These expression patterns support the existence of MN6-Ib and MN7-Ib and their dual innervation properties.

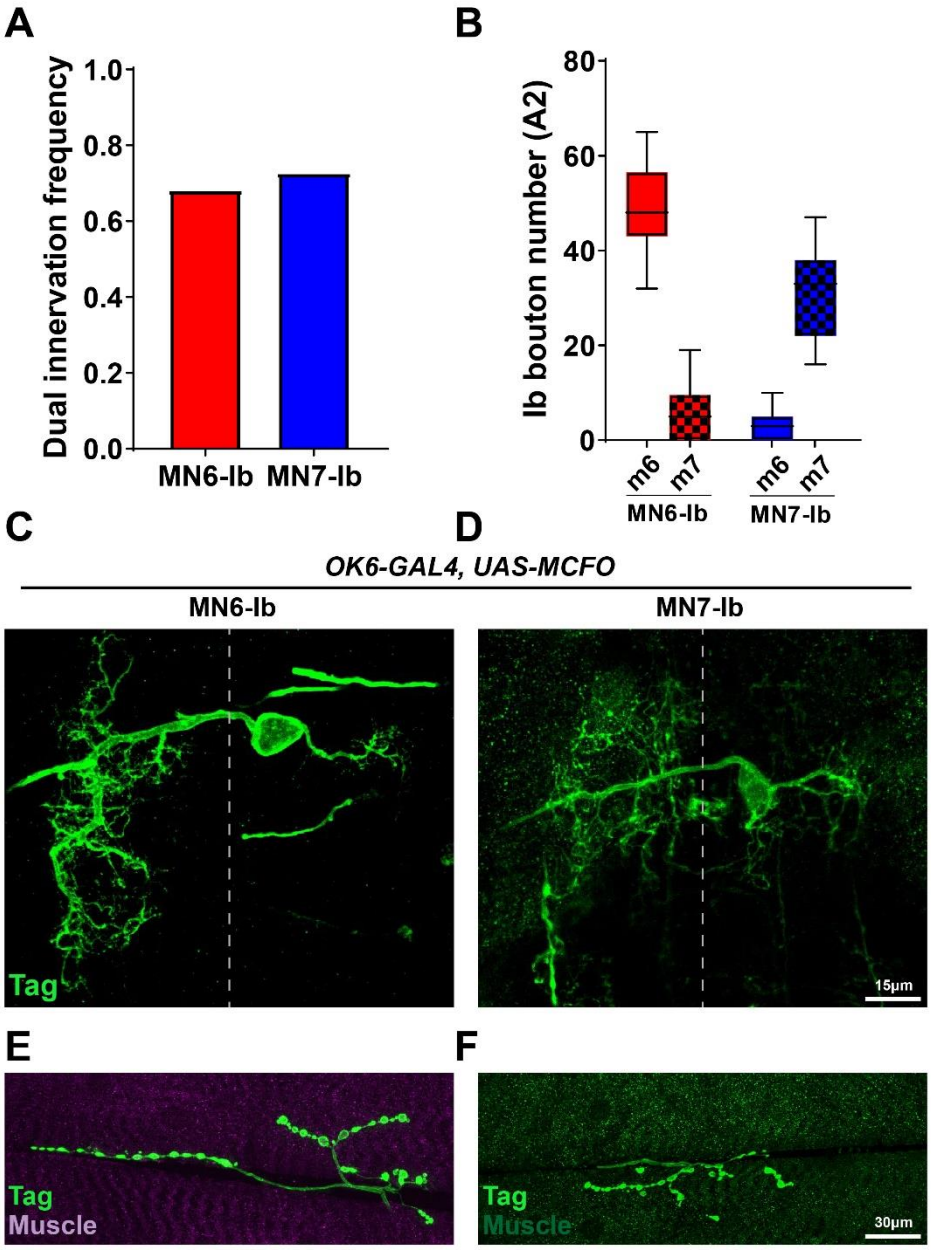

Figure 2.18 **Further characterization of MN6-Ib and MN7-Ib.**
(A) Quantification of the dual innervation frequencies of MN6-Ib and MN7-Ib. 68.2% of MN6-Ib also innervate m7 and 72.7% of MN7-Ib also innervate m6. (B) Quantification of MN6-Ib and MN7-Ib NMJ sizes on both muscles. (C-D) A pan MN driver *OK6-GAL4* driving MCFO revealed the dendritic morphology of MN6-Ib and MN7-Ib in the VNC. (E-F) Corresponding NMJ images from the same neuron shown in C (MN6-Ib) and D (MN7-Ib).

MN6/7-Ib (RP3) is derived from neuroblast 3-1 (NB3-1) (Schmid et al., 1999; Sink and Whitington, 1991a, 1991b). To visualize the dendritic projections of MN6-Ib and MN7-Ib, we examined their cell body position in the VNC and dendrite morphology using a pan MN driver, *OK6-GAL4*, with multi-color FLP-out (MCFO) (Nern et al., 2015). We found that the cell bodies of MN6-Ib and MN7-Ib are both localized at the dorsal neuropil and project axons to the contralateral hemineuromere. They also extend a small dendritic arbor to the ipsilateral side (Figure 2.18C-F). These features are shared with RP3 (MN6/7-Ib) (Kim et al., 2009). These data suggest that these two MNs likely both originated from NB3-1. Overall, we identified and confirmed the presence of two Ib MNs in A2 that preferentially innervate m6 or m7.

2.2.6 *dpr15* is required for MN7-Ib dual innervation

One interesting question is how do morphological similar MN6-Ib and MN7-Ib recognize both m6 and m7 but maintain a unique preference. To date, the only differences between these two MNs are the differentially expressed *dprs* and *DIPs*. As synaptic partner recognition CSPs, we wonder whether any of these differentially expressed *dprs* and *DIPs* contribute to the innervation patterns of MN6-Ib and MN7-Ib. Here, we found that *dpr15* is required for MN7-Ib dual innervation on m6 and m7. To distinguish MN6-Ib and MN7-Ib in a *drp15* mutant background, we cross *dpr15-GAL4* to a deficiency line spanning the *dpr15* locus in combination with an *UAS-GFP* reporter. *dpr15-GAL4* is a hypomorph as it reduces about 50% of mRNA transcripts. In *dpr15* mutants, we observed a significant decrease in the dual innervation frequency of MN7-Ib as it does not recognize the opposite m6, while it still recognizes m7 correctly (Figure 2.19A-B). In addition, the dual innervation frequency of MN6-Ib is not affected

(Figure 2.19C). Notably, *dpr15* is expressed in MN7-Ib, suggesting it acts cell autonomously to control synaptic recognition of MN7-Ib.

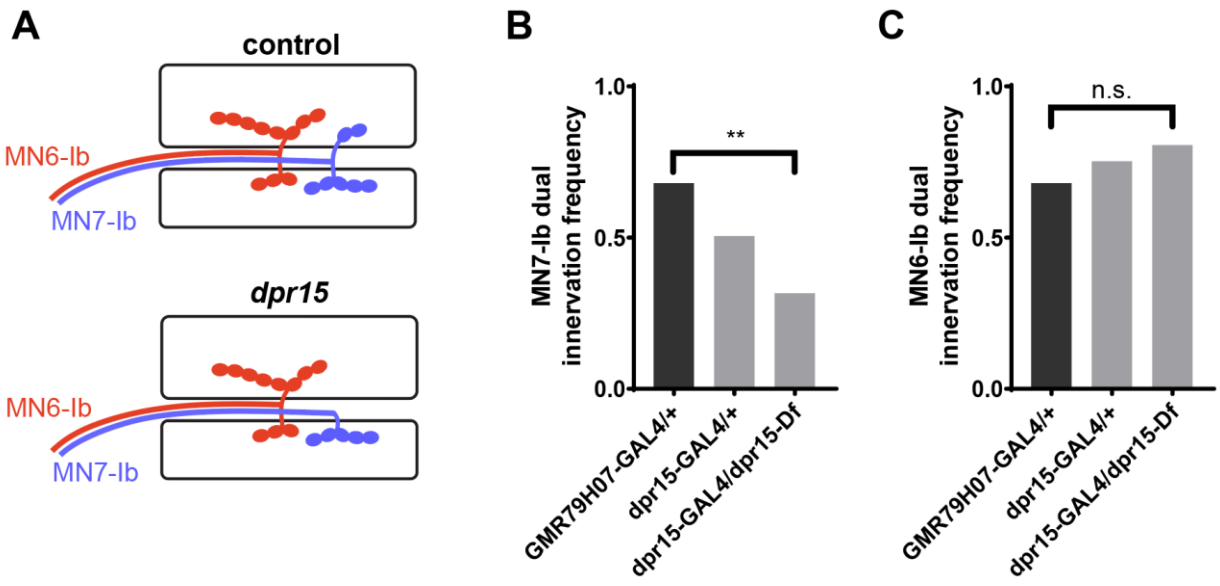

Figure 2.19 ***dpr15* is required for MN7-Ib dual innervation.**
(A) Schematic showing the dual innervation patterns of MN6-Ib and MN7-Ib in control animals and lack of MN7-Ib dual innervation in *dpr15* mutants. (B) Quantification of MN7-Ib dual innervation frequency suggests that *dpr15* affects synaptic recognition between MN7-Ib and m6. (C) Quantification of MN6-Ib dual innervation frequency shows that *dpr15* is not required for synaptic recognition of MN6-Ib. **p<0.01, chi-square test.

2.3 Discussion

Dprs and DIPs play important roles in nervous system development, and they are widely expressed across many neural circuits. Several labs have utilized the GAL4/UAS system to visualize expression of *dprs* and *DIP*s in olfactory neurons (Barish et al., 2018), adult leg MNs and SNs (Venkatasubramanian et al., 2019), optic lobe neurons (Cosmanescu et al., 2018), and fru P1 neurons (Brovero et al., 2021). While these studies revealed unique *dpr*/*DIP* expression in the respective neurons, the depth of the expression map was limited due to the less complete

GAL4 collection at the time, and some studies only focused on a global expression pattern without characterization of individual cell types.

Here, we reported a collection of GAL4 enhancer trap lines for all *DIPs* and 19 *dprs*, and examined their expression in larval MNs, muscles, peripheral glia, and SNs. Interestingly, we found that many *dprs* and *DIPs* are expressed in patterns including different expression levels, anterior-posterior gradients, and temporal expression. Our expression analyses also revealed previously uncharacterized larval MNs that differentially express *dprs* and *DIPs*. In addition, we found that *dpr15* is required for MN7-Ib dual innervating both m6 and m7. The *dpr*/*DIP* expression map identified here, along with the GAL4 lines that are also hypomorphs or loss-of-function alleles, will facilitate examination of Dpr-DIP interactions in development of motor, sensory, and many other circuits.

2.3.1 Insights from *dpr*/*DIP* expression maps to functional studies

The goal of developing expression maps for *dprs* and *DIPs* in MNs and SNs is to instruct the functional study of Dpr-DIP interactions. Here, we discuss potential directions based on our expression map that may serve as an entry point for future research.

Based on our expression map, all muscles express *dpr19* and most also express *dpr10*. Dpr10 and Dpr19 interact with DIP-α/β/λ and DIP-ε/ζ, respectively, and a majority of MNs express at least one of these DIPs. Thus, Dpr-DIP interactions could instruct MN-muscle recognition and/or act combinatorially with other synaptic connectivity molecules. In addition, some MNs do not express any of these DIPs suggesting other CSPs are involved in MN-muscle recognition.

Another way to approach the function of Dpr-DIP interactions is focusing on the commonly or differentially expressed *dprs* and *DIPs*. Hierarchical clustering analyses of SNs grouped SNs from the same class together based on the expression of *dprs* and *DIPs*, suggesting that similar SNs have common *dprs* and *DIPs*. Future studies can determine the *dpr*/*DIP* expression maps in the downstream interneurons to identify synaptic partners that express cognate Dpr-DIP pairs. However, one should also note that cluster analysis based solely on binary *dpr* and *DIP* expression ignores expression levels and localization of proteins which are important determinants for circuit wiring. Combining these with other parameters such as transcription factor expression can refine the clustering results and reduce unlikely correlations.

Instead of commonly expressed genes, differentially expressed *dprs* and *DIPs* in similar projecting neurons can shed light on connectivity mechanisms. For example, MN6-Ib and MN7-Ib identified in this study have similar morphology and innervation patterns, but with a preference for m6 and m7, respectively. One interesting question is how these neurons distinguish their muscle targets to generate such preference. Based on the expression map, MN6-Ib and MN7-Ib co-express a large subset of *dprs* and *DIPs*, but *DIP-β*, *DIP-γ*, *DIP-ε*, and *dpr15* are selectively expressed. Further examination of these genes found that *dpr15* is required for MN7-Ib innervation of m7. Similar approaches can be adapted to other MNs that innervate neighboring muscles.

The Dpr-DIP interactome (Carrillo et al., 2015; Cosmanescu et al., 2018; Özkan et al., 2013) revealed promiscuity in the interactions and our expression maps showed that many cells co-express many *dprs* and *DIPs*, suggesting redundant mechanisms for synaptic recognition. Several subfamilies of CSPs are implicated in recognition, but loss-of-function mutants rarely are 100% penetrant. For example, loss of Teneurin signaling causes a 90% decrease of MN3-Ib

innervation (Hong et al., 2012), and *Toll* null mutants revealed defects in 35% of MN6/7-Ib (Rose et al., 1997). These data suggested other CSPs are required in the recognition between MNs and their respective muscles. Utilizing the *dpr*/*DIP* expression maps, co-expressed *dprs* and *DIPs* can be simultaneously knocked out in specific MNs or SNs to examine redundancy. For example, the dorsal Is MN expresses six DIPs, and DIP-α is required for Is innervation of m4 but only partially required for Is innervation of other muscles. If redundant DIP codes are required for specific innervations, a sextuple *DIP* mutant should reveal complete loss of dorsal Is NMJs.

2.3.2 CSP expression patterns in the fly nervous system

CSPs can serve several functions in nervous system development including molecular codes for partner recognition and self-avoidance. CSP expression patterns can suggest different functions - the expression of CSPs could be deterministic to instruct stereotyped synaptic connectivity or stochastic to avoid dendritic overlap and self-synapses. For example, Capricious is robustly expressed in MN12-Ib and some dorsal MNs (Nose, 2012; Shishido et al., 1998), and loss-of-function and gain-of-function approaches revealed neuromuscular wiring defects, suggesting that the robust expression of Capricious instructs synaptic partner recognition. In our study, we showed that many *dprs* and *DIPs* are robustly expressed in SNs and MNs, indicating their potential roles in synaptic wiring.

On the other hand, some CSPs are stochastically expressed in subsets of cells. For example, probabilistic splicing of Dscam1 generates random isoform expression in SNs to mediate dendritic self-avoidance by inhibitory homophilic interactions (Miura et al., 2013). Interestingly, we found that many *dprs* and *DIPs* are also stochastically expressed in MNs and

SNs. Such irregular expression patterns may suggest additional functions of *dprs* and *DIPs* in circuit formation.

In this study, we also uncovered some *dprs* and *DIPs* that are expressed in a gradient along the anterior to posterior axis. Such patterns are reminiscent of the expression of several Hox genes in the VNC. For example, Ubx and Abd-A are highly expressed in anterior segments whereas Abd-B is mainly in the posterior (Estacio-Gómez and Díaz-Benjumea, 2013; Meng and Heckscher, 2020). These transcriptional factors were proposed to set up segmental cues in the nervous system, but the downstream genes and pathways are not completely understood. The similar expression patterns suggest that gradient transcriptional factors may regulate segmental development, in part, through *dprs* and *DIPs.*

2.3.3 *dpr*/*DIP-GAL4* collection to enable neuron identification and manipulation

The map of *Drosophila* MNs and SNs was established decades ago using dye backfills (Broadus et al., 1995; Hoang and Chiba, 2001; Landgraf et al., 2003b). However, fluorescent dyes have some technical limitations since they do not always flow into every terminal structure, which may have resulted in some neurons being overlooked. In this study, we used a genetic approach to probe individual neurons and revealed three uncharacterized MNs – MN23-Ib, MN6-Ib (A2) and MN7-Ib (A2).

In addition, the GAL4 lines in this study provide genetic access to manipulate subsets of neurons. In the *Drosophila* motor circuit, several studies have identified reporters that are expressed in subsets of motor neurons, muscles, and interneurons (Aponte-Santiago et al., 2020; Li et al., 2014; Pérez-Moreno and O'Kane, 2018; Wang et al., 2021a). However, the coverage of these reporters is very limited (i.e., only a small number of cells can be targeted). To generate

new genetic tools for targeting subsets of MNs, the *dpr*/*DIP* expression maps can be inspected for partially overlapping or non-overlapping *dpr/DIP-GAL4s* and converted to split-GAL4 or GAL80, respectively. Thus, the expression data in the present study and the MiMIC/CRIMIC lines provide a pipeline to expand the genetic toolbox and to label and manipulate neurons in a highly specific manner.

2.3.4 Using the *dpr*/*DIP* code to annotate single cell RNA sequencing data

Recent advances in single cell RNA sequencing (scRNAseq) provide a powerful, high-throughput approach to identify large scale gene expression patterns. Various *Drosophila* neural tissues have been analyzed by scRNAseq (Li, 2020). However, most studies report the transcriptome of large cell clusters including MNs, ganglion cells, neuroblasts, and glial cells due to the difficultly of matching single cell reads to a specific cell type and identity, impeding detailed analyses from scRNAseq data.

One method to deconvolve these large cell clusters is sorting cells before performing scRNAseq. On the other hand, researchers may also use the scRNAseq data to identify specific drivers, and then identify which neuron expresses this driver (Simon and Konstantinides, 2021). However, this approach reduces the scale because only a few cell types can be identified in this manner. Utilizing the expression of a gene family known to be differentially expressed within a specific subset of cells can provide a more complete examination. For example, the *dpr*/*DIP* expression map would generate a cell-specific atlas to annotate clusters in scRNAseq data and help to identify individual MNs from a MN cluster in a larval VNC sample (Nguyen et al., 2021; Vicidomini et al., 2021). In addition to *dprs* and *DIPs*, other CSP subfamilies have been reported in several scRNAseq datasets, suggesting that expression maps of other subfamilies and even

combinations of subfamilies can be utilized to refine cell types in datasets (Kurmangaliyev et al., 2020; Ma et al., 2021; Xie et al., 2021).

2.3.5 Limitations of using GAL4 lines to profile expression patterns

In the current study, we presented the expression map of *dprs* and *DIPs* in a variety of cells using a GAL4 collection. However, several caveats exist. First, using a GAL4/UAS approach will not provide spatial information about where Dprs and DIPs are localized subcellularly – in axons or dendrites. Future work will generate endogenously tagged versions of, or antibodies against, Dprs and DIPs. In addition, using the current GAL4/UAS pipeline, we cannot unequivocally identify specific interneurons that express *dprs* and *DIPs* due to their indistinguishable cell morphologies in the densely packed VNC. Transcription factor staining and generation of split GAL4s can reveal interneurons identities but at relatively low throughput. Finally, utilizing a lineage tracing system, we uncovered temporally expressed *dprs* and *DIPs*. However, neither of our approaches revealed when *dprs* and *DIPs* were first expressed. Embryo or early-stage larval dissection will provide more temporal resolution.

2.4 Methods and materials

2.4.1 *Drosophila* and antibody resources

All *dpr*/*DIP-GAL4* lines are listed in Table 2.1. Other lines used in this study are listed in Table 2.3. Antibodies for immunostaining are listed in Table 2.4.

2.4.2 Fly genetics

When examining available *dpr/DIP-GAL4* lines to confirm the GAL4 insertion sites and the version of GAL4 used, we found that the original *dpr13-GAL4* no longer contained the GAL4 sequence (Barish et al., 2018; Brovero et al., 2021). Here, we generated new *dpr13-GAL4* and *dpr8-GAL4* from respective MiMIC insertion lines using Trojan exons (Diao et al., 2015). To generate *DIP-λ* CRIMIC insertions, gRNA (5'-AGCATCTATCGCTTGTGAAAGGG-3') was designed to target the coding intron. The insertion sites and GAL4 versions are indicated in Table 2.1.

2.4.3 qRT-PCR

Five larvae per genotype were collected and homogenized using pellet pestles (Fisher Scientific). All samples tested contained a mix of males and females, except for *dpr8-GAL4*, where only females were used due to its location on the X-chromosome and its inability to homozygous. RNA was extracted using RNAqueous Total RNA Isolation Kit (ThermoFisher AM1912) and subsequently treated with DNaseI for 30 minutes at 37°C to remove genomic DNA. cDNA was generated from 1 μg of RNA using random hexamers and SuperScript IV First-Strand Synthesis System (ThermoFisher 18091050) and remaining RNA was removed using RNase H at 37°C for 20 minutes. Primers were designed to be 18-23 bp long, amplify 100-200 bp, and have a melting temperature ~60°C (Table 2.2). All primer locations are downstream of mapped GAL4 insertion sites and were validated with control cDNA. qRT-PCR was performed with Power SYBR Green PCR Master Mix (Bio-Rad 4368577) and run on a QuantStudio 3 (ThermoFisher). All reactions were normalized to the housekeeping gene RpL32

and control flies, yielding ΔΔCt values (Ponton et al., 2011). Relative Fold Change was calculated as 2^-ΔΔCt. Each reaction was run in technical and biological triplicates.

2.4.4 Dissection and immunocytochemistry

Larval dissections and immunostaining were performed as previously described (Ashley et al., 2019). Briefly, wandering third instar larvae were dissected along the dorsal midline in PBS on a Sylgard plate and stretched out with insect pins. To visualize alary muscles, larva was dissected from the ventral side. Dissected body walls were washed once with PBS and fixed for 30min with 4% paraformaldehyde. Samples were then washed three times with PBT (PBS+0.05% TritonX100). Samples were incubated with primary antibody at 4°C overnight, washed three times with PBT, and then incubated in secondary antibody at room temperature for 2 hours. Samples were finally mounted in 30 µl vectashield (Vector Laboratories). Representative images were taken with a Zeiss LSM800 confocal microscope with a 40X plan-neofluar 1.3NA objective and processed with ImageJ.

2.4.5 Examining expression of *dprs* and *DIPs* in MNs and SNs

We dissected six third instar larvae from each cross and immunostained for GFP/RFP, DLG and HRP. Mounted slices were examined under Zeiss AxioImager M2 with a Lumen light engine with a 20X plan-apo 0.8NA objective. Each sample was examined twice with the same criteria to reduce human error. To map the expression of *dprs* and *DIPs* in MNs, NMJs of each MN was identified by labeling for DLG or HRP, and then examined for GFP/RFP colocalization. For expression in SNs, SN cell bodies were located by HRP, and then examined for GFP/RFP colocalization. We counted all MNs and SNs from anterior to posterior hemisegments

(abdominal segment A2-A7) to gain a full *dpr/DIP* expression map across the body wall. Note that we did not observe the third type-Is MN (MNSNa-Is) described by (Hoang and Chiba, 2001). The pipeline and criteria of determining the expression level is below (Figure 2.20).

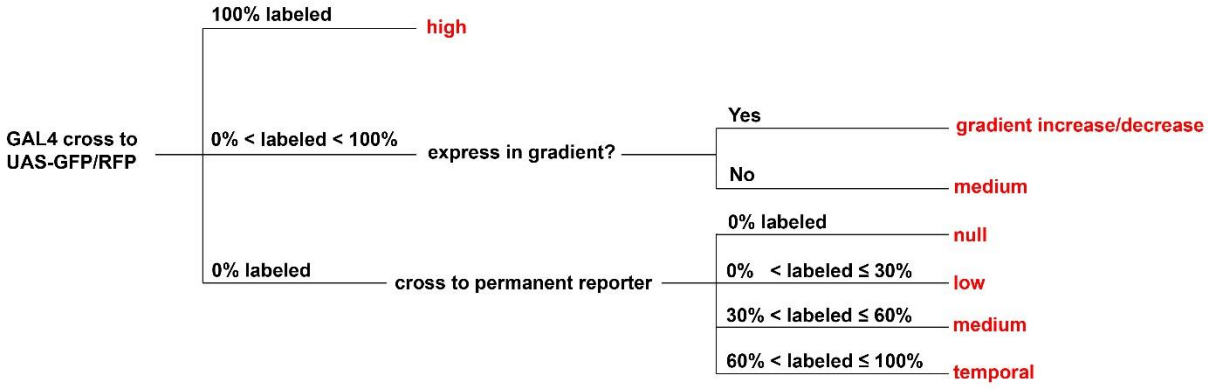

Figure 2.20 **Criteria to determine the expression of GAL4 in a certain MN/SN.** A graphical flow chart depicting how we scored the *dpr/DIP* expression data into categories.

1. In *dpr/DIP-GAL4>GFP/RFP* animals, if the reporter gene expressed constantly in a specific MN/SN in all hemisegments, then this GAL4 line is counted as "high expression level" in this MN/SN. If the fluorescent reporter is not expressed consistently in a specific MN/SN, then: (1) if the fluorescent reporter shows a gradient increase or decrease along the anterior to posterior axis, then the expression of this GAL4 line is reported as "gradient increase" or "gradient decrease", respectively; (2) if the reporter gene does not express in a gradient, but randomly expresses in a specific MN/SN, then the expression is counted as "medium expression level" in this MN/SN. Note we did not record gradient expression for SNs, because the reporter expression had higher variation in SNs comparing to MNs.

2. In the cross between *dpr/DIP-GAL4* and the permanent labeling reporter, we first confirmed the high, medium, and gradient expression level described above. Then, if a GAL4 line showed no expression in the cross to *UAS-GFP/RFP* but did show expression in the cross to the permanent labeling reporter, we counted how frequent this MN/SN is labeled: (1) if the labeling frequency is lower than 30% across all hemisegments, then this GAL4 is recorded as "low expression level" in this MN/SN because the expression could be too low to detect in the cross to *UAS-GFP/RFP* but sufficient to trigger some FLP-out; (2) if the labeling frequency is between 30%-60%, then this GAL4 expression is recorded as "medium expression level" in this MN/SN; (3) if the labeling frequency is higher than 60%, then this GAL4 expression is considered as "temporal expression" as it indicates a high GAL4 expression level temporally in early developmental stages because it triggers high frequency FLP-out. Finally, if a GAL4 is not expressed in both the cross to UAS-GFP/RFP or permanent reporter, it is recorded as "null expression".

dpr10-GAL4 was crossed to *UAS-GFP* together with *MHC-GAL80* to prevent muscle GFP expression, because high level of muscle GFP will mask NMJs and SN cell bodies. In addition, muscles expressing *dprs* (*dpr10* and *dpr19*) were not crossed to the permanent labeling reporter.

2.4.6 Examining expression of *dprs* and *DIPs* in glia and muscles

We examined expression of *dprs* and *DIPs* in glia and muscles with the G-TRACE reporter (Evans et al., 2009). We dissected 6 larvae from each cross and immunostained for GFP, RFP, HRP, and Repo. Glial expression was confirmed by GFP/RFP colocalization with Repo. Muscle expression was confirmed by GFP/RFP positive muscle nuclei. Although the cross to

UAS-GFP/RFP and the permanent labeling line also showed muscle expression, the diffusible GFP signal impeded the clear distinction of muscle boundaries.

2.4.7 Hierarchical clustering using *dpr/DIP* expression

To perform hierarchical clustering, the expression of *dprs* and *DIPs* were first converted to binary values of "0" and "1". Robust expression including high expression and temporal expression were considered as "1", whereas medium and low expression, and gradient expression were considered as "0". We reasoned that robust expression of *dprs* and *DIPs* may suggest more a significant role in the respective cell. Binary data was subjected to hierarchical analysis using Morpheus (Broad Institute) (Metric: Cosine Similarity; Method: Average). Figures were exported and color coded in Adobe Illustrator to indicate different types of MNs and SNs.

2.4.8 Bouton number and dual innervation counting

To quantify m6 and m7 NMJs in wild type animals, we located Ib NMJs by DLG labeling and counted bouton number by HRP labeling. To measure the MN6-Ib or MN7-Ib NMJ sizes in *GMR79H07-GAL4>GFP* animals, we first looked for GFP colocalization with DLG to distinguish MN6-Ib and MN7-Ib. For example, if the major Ib arbor on m6 is GFP positive, then it is formed by MN6-Ib, and the GFP negative boutons are formed by MN7-Ib. We then counted the bouton numbers of each Ib arbor by HRP labeling. Student t-test was used for comparison between two groups (followed by Welch's correction in cases of unequal variance, Prism 8), and Chi-square test was used for comparing innervation frequency. Error bar indicates standard error of the mean (SEM).

Table 2.1 ***dpr/DIP-GAL4* lines used in this study.**

GAL4 line	GAL4 derived from	Insertion site	Genotype	Sources
DIP-α-GAL4	MI10680 (T2A-GAL4)	6th coding intron	*y^{1} w* Mi{Trojan-GAL4.1}DIP-α$^{MI10680\text{-}TG4.1}$*	GDP#
DIP-β-GAL4	MI01971 (GT-GAL4)	5' UTR intron	*y^{1} w* Mi{GT-GAL4}DIP-β$^{MI01971\text{-}GAL4}$*	(BL#90316)
DIP-γ-GAL4	MI03222 (GT-GAL4)	5' UTR intron	*Mi{GT-GAL4}DIP-γ$^{MI03222\text{-}GAL4}$*	(BL#90315)
DIP-δ-GAL4	MI08287 (T2A-GAL4)	4th coding intron	*Mi{Trojan-GAL4.1}DIP-δ$^{MI08287\text{-}TG4.1}$*	(BL#90320)
DIP-ε-GAL4	MI11827 (T2A-GAL4)	1st coding intron	*Mi{Trojan-GAL4.1}DIP-ε$^{MI11827\text{-}TG4.1}$/CyO,Dfd-YFP*	(BL#67502)
DIP-ζ-GAL4	MI03838 (T2A-GAL4)	2nd coding intron	*Mi{Trojan-GAL4.0}DIP-ζ$^{MI03838\text{-}TG4.0}$*	(BL#90317)
DIP-η-GAL4	MI07948 (T2A-GAL4)	4th coding intron	*Mi{Trojan-GAL4.1}DIP-η$^{MI07948\text{-}TG4.1}$/CyO,Dfd-YFP*	(BL#90318)
DIP-θ-GAL4	MI03191 (T2A-GAL4)	2nd coding intron	*Mi{Trojan-GAL4.1}DIP-θ$^{MI03191\text{-}TG4.1}$/CyO,Dfd-YFP*	GDP#
DIP-ι-GAL4	CR00997 (T2A-GAL4)	1st coding intron	*Tl{CRIMIC-TG4.1}DIP-ι$^{CR00997\text{-}TG4.1}$*	(BL#83243)
DIP-κ-GAL4	CR01146 (T2A-GAL4)	1st coding intron	*Tl{CRIMIC-TG4.1}DIP-κ$^{CR011146\text{-}TG4.1}$,Gpo3$^{CR01114\text{-}TG4.1X}$/CyO,Dfd-YFP*	(BL#83252)
DIP-λ-GAL4	CR70096 (T2A-GAL4)	2nd coding intron	*Tl{CRIMIC-TG4.0}DIP-λ$^{CR70096\text{-}TG4.0}$*	This study
dpr1-GAL4	MI12729 (T2A-GAL4)	1st coding intron	*Mi{Trojan-GAL4.1}dpr1$^{MI12729\text{-}TG4.1}$/CyO,Dfd-YFP*	GDP#
dpr2-GAL4	MI05656 (T2A-GAL4)	4th coding intron	*Mi{Trojan-GAL4.1}dpr2$^{MI05656\text{-}TG4.1}$/CyO,Dfd-YFP*	GDP#
dpr3-GAL4	MI05963 (T2A-GAL4)	1st coding intron	*Mi{Trojan-GAL4.1}dpr3$^{MI05963\text{-}TG4.1}$/CyO,Dfd-YFP*	GDP#
dpr4-GAL4	CR00485 (T2A-GAL4)	1st coding intron	*Tl{CRIMIC-TG4.1}dpr4$^{CR00485\text{-}TG4.1}$/TM6,Sb,Hu,Dfd-YFP*	(BL#79271)
dpr5-GAL4	MI11085 (T2A-GAL4)	2nd coding intron	*Mi{Trojan-GAL4.1}dpr5$^{MI11085\text{-}TG4.1}$*	GDP#
dpr6-GAL4	MI01358 (T2A-GAL4)	1st coding intron	*Mi{Trojan-GAL4.1}dpr6$^{MI01358\text{-}TG4.1}$*	GDP#
dpr7-GAL4	MI05719 (T2A-GAL4)	1st coding intron	*Mi{Trojan-GAL4.1}dpr7$^{MI05719\text{-}TG4.1}$*	(BL#78385)
dpr8-GAL4	MI11830 (T2A-GAL4)	1st coding intron	*Mi{Trojan-GAL4.1}dpr8$^{MI11830\text{-}TG4.1}$*	This study
dpr9-GAL4	MI03594 (T2A-GAL4)	3rd coding intron	*Mi{Trojan-GAL4.1}dpr9$^{MI03594\text{-}TG4.1}$*	GDP#
dpr10-GAL4	MI03557 (T2A-GAL4)	1st coding intron	*Mi{Trojan-GAL4.1}dpr10$^{MI03557\text{-}TG4.1}$*	GDP#
dpr11-GAL4	MI01743 (T2A-GAL4)	1st coding intron	*Mi{Trojan-GAL4.1}dpr11$^{MI01743\text{-}TG4.1}$*	GDP#
dpr12-GAL4	MI01695 (T2A-GAL4)	1st coding intron	*Mi{Trojan-GAL4.1}dpr12$^{MI01695\text{-}TG4.1}$/CyO,Dfd-YFP*	GDP#
dpr13-GAL4	MI05577 (T2A-GAL4)	2nd coding intron	*Mi{Trojan-GAL4.0}dpr13$^{MI05577\text{-}TG4.0}$/CyO,actin-GFP*	This study
dpr14-GAL4	CR00516 (T2A-GAL4)	1st coding intron	*Tl{CRIMIC-TG4.1}dpr14$^{CR00516\text{-}TG4.1}$*	(BL#80586)
dpr15-GAL4	MI01408 (T2A-GAL4)	3rd coding intron	*Mi{Trojan-GAL4.1}dpr15$^{MI01408\text{-}TG4.1}$/TM6,Sb,Hu,Dfd-YFP*	(BL#66827)
dpr16-GAL4	MI05173 (T2A-GAL4)	1st coding intron	*Mi{Trojan-GAL4.1}dpr16$^{MI05173\text{-}TG4.1}$*	GDP#
dpr17-GAL4	MI08707 (T2A-GAL4)	1st coding intron	*Mi{Trojan-GAL4.1}dpr17$^{MI08707\text{-}TG4.1}$/TM6,Sb,Hu,Dfd-YFP*	(BL#76200)
dpr18-GAL4	CR01009 (T2A-GAL4)	1st coding intron	*Tl{CRIMIC-TG4.1}dpr18$^{CR01009\text{-}TG4.1}$*	(BL#83245)
dpr19-GAL4	CR00996 (T2A-GAL4)	1st coding intron	*Tl{CRIMIC-TG4.1}dpr19$^{CR00996\text{-}TG4.1}$/CyO,Dfd-YFP*	(BL#83242)

GDP# : *Drosophila Gene Disruption Project*

Table 2.2 **mRNA level and primer information.**

Gene	Tested Genotype	(norm.) mRNA level	Primer	Sequence
DIP-α	*DIP-α$^{MI10680\text{-}GAL4}$*	0.02±0.02	*DIP-α-qPCR-F*	GGAGTACCGCCATCGGTCTC
			DIP-α-qPCR-R	GGCTTCGACGTGACACTCG
DIP-β	*DIP-β$^{MI01971\text{-}GAL4}$*	0.55±0.11	*DIP-β-qPCR-F*	GAGCACGTGGTCATCCGAAG
			DIP-β-qPCR-R	GGAGGCAATGCACATGTAGGC
DIP-γ	*DIP-γ$^{MI03222\text{-}GAL4}$*	0.16±0.04	*DIP-γ-qPCR-F*	GAGAGCCTCCGATCAGACCG
			DIP-γ-qPCR-R	CCTGCACATCGATACAACCC
DIP-δ	*DIP-δ$^{MI08287\text{-}GAL4}$*	0.35±0.16	*DIP-δ-qPCR-F*	GGCAACTATCGATGCATCTCG
			DIP-δ-qPCR-R	GTCGTTGCGTGATGAGGGTATG
DIP-ε	*DIP-ε$^{MI11827\text{-}GAL4}$/CyO,Dfd-YFP*	0.20±0.06	*DIP-ε-qPCR-F*	CGGCCAAGACCCAGTATGG
			DIP-ε-qPCR-R	GATTTTGTTGCCGTCATCGCG
DIP-ζ	*DIP-ζ$^{MI03838\text{-}GAL4}$*	0.04±0.004	*DIP-ζ-qPCR-F*	GTGGAAGCCACAGTCGGATTG
			DIP-ζ-qPCR-R	GAGGCAGTGGTTGGAGGATATG
DIP-η	*DIP-η$^{MI07948\text{-}GAL4}$/CyO,Dfd-YFP*	0.41±0.23	*DIP-η-qPCR-F*	GGCAGTAACGTGACGCTCAAATG
			DIP-η-qPCR-R	CGAGGGAGGGACTCCATTGG
DIP-θ	*FRT40A, DIP-θ$^{MI03191\text{-}GAL4}$*	0.08±0.10	*DIP-θ-qPCR-F*	CTCCTGCAGAACGTAACGGTG
			DIP-θ-qPCR-R	GCGTGAGTTATGCTCATGCG
DIP-ι	*DIP-ι$^{CR00997\text{-}GAL4}$*	0.89±0.20	*DIP-ι-qPCR-F*	GGGATGCCCTACTCACGTGTG
			DIP-ι-qPCR-R	CATCCGCGATCCGATTCCTG
DIP-κ	*DIP-κ$^{CR011146\text{-}GAL4}$/CyO,Dfd-YFP*	0.51±0.30	*DIP-κ-qPCR-F*	GACACGCAGACGATCCTGTC
			DIP-κ-qPCR-R	CGTGTTCACTTGGCACATGTAC
DIP-λ	*DIP-λ$^{CR70096\text{-}GAL4}$*	1.50±0.05	*DIP-λ-qPCR-F*	CACCCACATGGTCTCACTAAATCC
			DIP-λ-qPCR-R	CTCTGGATTATGTTCTGGGTGG
dpr1	*dpr1$^{MI12729\text{-}GAL4}$/CyO,Dfd-YFP*	0.92±0.10	*dpr1-qPCR-F*	GAGCCCAAGATGTCCCTGTC
			dpr1-qPCR-R	GAATATGTTGCCCAGCTCGTGG
dpr2	*dpr2$^{MI05656\text{-}GAL4}$/CyO,Dfd-YFP*	0.93±0.27	*dpr2-qPCR-F*	CGTCGGCGCAGGATATTGG
			dpr2-qPCR-R	GATGACATTGACCACCACGCTG
dpr3	*dpr3$^{MI05963\text{-}GAL4}$/CyO,Dfd-YFP*	0.55±0.24	*dpr3-qPCR-F*	GGACGCTGCATGTGAAGGC
			dpr3-qPCR-R	GCCTTGAAGTGCAGATCGGG
dpr4	*dpr4$^{CR00485\text{-}GAL4}$/TM6,Sb,Hu,Dfd-YFP*	0.56±0.20	*dpr4-qPCR-F*	CGGATTCGGGCAACTACACG
			dpr4-qPCR-R	GCACGGACGTGGATGAAAGG
dpr5	*dpr5$^{MI11085\text{-}GAL4}$*	0.13±0.02	*dpr5-qPCR-F*	CACGGAGCCCAAGATCAGTC
			dpr5-qPCR-R	CGTGTCCTTGTGCCACAGC
dpr6	*dpr6$^{MI01358\text{-}GAL4}$*	0.23±0.03	*dpr6-qPCR-F*	CCATCACCAGGACACGGAGG
			dpr6-qPCR-R	GACACGCCGCCTCTTGATG
dpr7	*dpr7$^{MI05719\text{-}GAL4}$*	0.18±0.10	*dpr7-qPCR-F*	GCACAGCCAAGAGACAGTGG
			dpr7-qPCR-R	GCCAGGGCAATAGTGCTATCCC
dpr8	*dpr8$^{MI11830\text{-}GAL4}$/FM7,Dfd-YFP*	0.49±0.19	*dpr8-qPCR-F*	GAATTTGGGCAATCGCACG
			dpr8-qPCR-R	CGCAATGTCCAATCCTCGG
dpr9	*dpr9$^{MI03594\text{-}GAL4}$*	0.08±0.09	*dpr9-qPCR-F*	GGGCGATACGACCACATCG
			dpr9-qPCR-R	CTCCCCTGGAAACGGAATGG
dpr10	*dpr10$^{MI03557\text{-}GAL4}$*	0.06±0.05	*dpr10-qPCR-F*	GGGCTGTCGTGTCAAGCATC
			dpr10-qPCR-R	GCCCACTTGATCTGCAGGG
dpr11	*dpr11$^{MI01743\text{-}GAL4}$*	0.30±0.06	*dpr11-qPCR-F*	GTGTCCAGCTGCAAGTTGTGG
			dpr11-qPCR-R	GGTTGGGATCCAGTTGCGTG
dpr12	*dpr12$^{MI01695\text{-}GAL4}$/CyO,Dfd-YFP*	0.82±0.05	*dpr12-qPCR-F*	CGGCATGTACGAGTGCCAG
			dpr12-qPCR-R	CGTACTGCGGTGGTGTAGGAC
dpr13	*dpr13$^{MI05577\text{-}GAL4}$/CyO,actin-GFP*	0.92±0.06	*dpr13-qPCR-F*	GTTCAGTGCCACGCACTTGAAG
			dpr13-qPCR-R	CAGCGTTGAACCTGGGGTTA
dpr14	*dpr14$^{CR00516\text{-}GAL4}$*	0.04±0.02	*dpr14-qPCR-F*	GGTGGTGCATGTGCTGAACG
			dpr14-qPCR-R	CACTTGTCCCAAGCCCAATCC
dpr15	*FRT82B, dpr15$^{MI01408\text{-}GAL4}$*	0.57±0.09	*dpr15-qPCR-F*	CCATTGTCCTCCACGTGCTG
			dpr15-qPCR-R	CTTGTGGTGGCTTTGCTGGTG
dpr16	*dpr16$^{MI05173\text{-}GAL4}$*	0.99±0.38	*dpr16-qPCR-F*	CACTCCGGCAACTACACGTG
			dpr16-qPCR-R	CCCGTGACCCAGTCTGTGG
dpr17	*FRT82B, dpr17$^{MI08707\text{-}GAL4}$*	0.01±0.01	*dpr17-qPCR-F*	CGGCGCAACCTGACAATGC
			dpr17-qPCR-R	GCATGCGCACCCATGAAACG
dpr18	*dpr18$^{CR01009\text{-}GAL4}$*	0.33±0.11	*dpr18-qPCR-F*	GCCGTGTCGGTATGCTCAAG
			dpr18-qPCR-R	CGCCAATTGTTCGGGTACTGG
dpr19	*dpr19$^{CR00996\text{-}GAL41}$/Cyo,Dfd-YFP*	0.55±0.13	*dpr19-qPCR-F*	CCTGAATCCCTCGGTCAGTG
			dpr19-qPCR-R	CATGGCCGCCGTTTTCTCAC
Rpl32	ALL		*Rpl32-qPCR-F*	ATGCTAAGCTGTCGCACAAATG
			Rpl32-qPCR-R	GTTCGATCCGTAACCGATGT

Table 2.3 ***Drosophila* lines used in this study.**

Genotype	Source
OK6-GAL4	BL#64199
GMR79H07-GAL4	gift from Troy Littleton, MIT
MHC-GAL80	gift from Timothy Mosca, Thomas Jefferson University
10XUAS-mCD8::GFP	BL#32184
20XUAS-mCherry	BL#52268
UAS-2XEGFP; actin-(FRT.STOP)-GAL4,UAS-FLP	permanent reporter, gift from Ellie Heckscher, UChicago
UAS-nRedStinger, UAS-FLP, Ubi-p63E(FRT.STOP)-nStinger	G-TRACE, BL#28280
R57C10-FLP;;UAS-MCFO	BL#64089
yw; Sp/CyO; loxP(Trojan-GAL4)x3	BL#60311
yw; loxP(Trojan-GAL4)x3; Dr/TM3,Sb,Ser	BL#60310
yw,Cre,vas-phiC31:int	BL#60299

Table 2.4 **Antibodies used in this study.**

Antibody	Concentration and Source
Rabbit anti-GFP	1:40k, gift from Michael Glozter, University of Chicago
Rabbit anti-HA	1:1000, Cell Signaling C29F4
Mouse anti-DLG	1:100, Developmental Studies Hybridoma Bank 4F3
Mouse anti-Repo	1:100, Developmental Studies Hybridoma Bank 8D12
Mouse anti-Myosin	1:100, Invitrogen A31466
Chicken anti-GFP	1:500, Invitrogen A10262
Chicken anti-RFP	1:500, Novus Biologicals NBP2-25158
Chicken anti-V5	1:500, Bethyl Laboratories A190-118A
Rat anti-Flag	1:200, Novus Biologicals NBP1-06712
Goat anti-Rabbit Alexa 488	1:500, Invitrogen A11008
Goat anti-Rabbit Alexa 568	1:500, Invitrogen A11036
Goat anti-Mouse Alexa 568	1:500, Invitrogen A11031
Goat anti-Mouse Alexa 647	1:500, Invitrogen A32728
Goat anti-Chicken Alexa 488	1:500, Invitrogen A11039
Donkey anti-Chicken Cy3	1:500, Jackson Immunological Research 703-165-155
Goat anti-Rat Alexa 647	1:500, Invitrogen A21247
Goat anti-HRP Alexa 647	1:100, Jackson Immunological Research 123-605-021
Goat anti-Phalloidin Alexa 405	1:100, Invitrogen A30104

CHAPTER 3

NEURONAL CELL DEATH INDUCES STRUCTURAL AND FUNCTIONAL PLASTICITY

3.1 Introduction

The nervous system is characterized by complex wiring patterns that include different neurons converging onto the same postsynaptic cell. This wiring paradigm is found in pyramidal neurons that receive input from excitatory and inhibitory contacts (Megías et al., 2001), and in esophageal striated muscles that receive enteric and vagal nerve inputs (Neuhuber and Wörl, 2016). While dynamic regulation of individual synapses has been examined (Berry and Nedivi, 2017; Kruijssen and Wierenga, 2019), interplay between nearby neurons has been predominantly studied by monitoring postsynaptic spine changes (Chistiakova et al., 2019; Hedrick et al., 2016; Jungenitz et al., 2018). Understanding how nearby neurons respond to perturbations on their neighbors will shed light on the etiologies of neurodegenerative disorders, such as ALS, which display progressive neuronal cell death and devastating functional consequences (Agudelo et al., 2020; Park et al., 2020).

Analysis of individual inputs in the central nervous system is complicated by the high density of converging inputs on the same target cell. The *Drosophila* larval neuromuscular circuit, however, circumvents this with a simple, hard-wired connectivity map as each muscle normally receives two excitatory inputs, the Ib MN and Is MN. Therefore, we utilize the larval NMJ to examine how MNs respond to perturbations on their neighbors.

Due to the fact that all MN axons are wrapped together in segmental nerve, electrophysiology recording cannot tease apart the activity of individual neurons, thus impeding

us to set up baseline Ib and Is activity in a wild type background. We first confirmed neural activity of Ib and Is MNs using GCaMP imaging together with electrophysiology. Specifically, we examined three muscles, m6, m12 and m4, and found different contributions of Ib and Is on these muscles. Next, we ablated Is MNs and examined changes on nearby Ib NMJs. We found that all three Ib NMJs increased their bouton numbers and rate of spontaneous neurotransmitter release and some Ib NMJs also partially increased their evoked neurotransmission, indicating both structural and functional plasticity. In addition, we analyzed conditions where Is MN cell bodies and axons are unaffected but only specific muscle innervations are missing. Surprisingly, we found that Ib synaptic plasticity does not initiate if only the local Is innervations are lost, suggesting a signal from the axon or cell body is required. Overall, an ablation-dependent synaptic plasticity mechanism instructs neighboring MNs to compensate the death of a circuit member and provides insights into nervous system plasticity in both healthy and disease states.

3.2 Results

3.2.1 Ib and Is MNs contribute to postsynaptic activity in a target-specific manner

Converging inputs contribute to the overall postsynaptic response. In this study, we examined to what extent one input can influence the nearby input's structure and function. To address this, we first determined the activity contribution of each MN on the postsynaptic muscle target in a wild-type condition. We chose m6, m12 and m4 because 1) prior studies showed that each Ib contributes a unique percentage of the total postsynaptic activity, 2) these muscles have been frequently analyzed in NMJ studies (Menon et al., 2013; Nose, 2012), and 3) the Ib and Is innervation patterns on these muscles enabled identification of common and muscle-specific

principles (all muscles have unique Ib MNs but m6 and m12 are innervated by the same Is MN) (Figure 3.1A).

We measured the Ib MN contribution to the total EPSP on a muscle by muscle basis. We combined NMJ electrophysiology with a postsynaptically targeted GCaMP, SynapGCaMP6f (*MHC-CD8-GCaMP6f*; (Newman et al., 2017)). Some of the earliest evidence for the existence of two distinct MN populations was uncovered over 40 years ago (Jan and Jan, 1976) through observations that different voltage injections elicited two populations of muscle EPSPs. It was later found that lower voltage injection generated action potentials in Ib MNs (Lnenicka and Keshishian, 2000), therefore we varied the stimulus protocol to independently elicit and record EPSPs from Ib alone and Ib+Is together. SynapGCaMP6f fluorescence changes at Ib and Is NMJs confirmed whether the recorded EPSPs were due to Ib alone or Ib+Is activity (Figure 3.1B). Using this procedure, the average total EPSP amplitude (Ib+Is) in m6 was 31.55 mV and the average Ib-derived EPSP was 17.17mV (Figure 3.1C, F). Thus, the MN6-Ib contributes 54% of the total m6 EPSP (Figure 3.1I). Interestingly, at m12, MN12-Ib contributes 31% of the total EPSP, and at m4, MN4-Ib represents 62% (Figure 3.1D, E, G-I). Thus, we determined the contribution of each MN (Ib and Is) to the postsynaptic muscle activity in wild type larvae and found that the relative strength of each Ib MN differed between muscles, with the MN4-Ib contributing the most and the MN12-Ib the least. Notably, MN6-Ib and MN12-Ib contributions are different even though they are innervated by the same Is MN. These data established a model in which to introduce perturbations and examine synaptic plasticity.

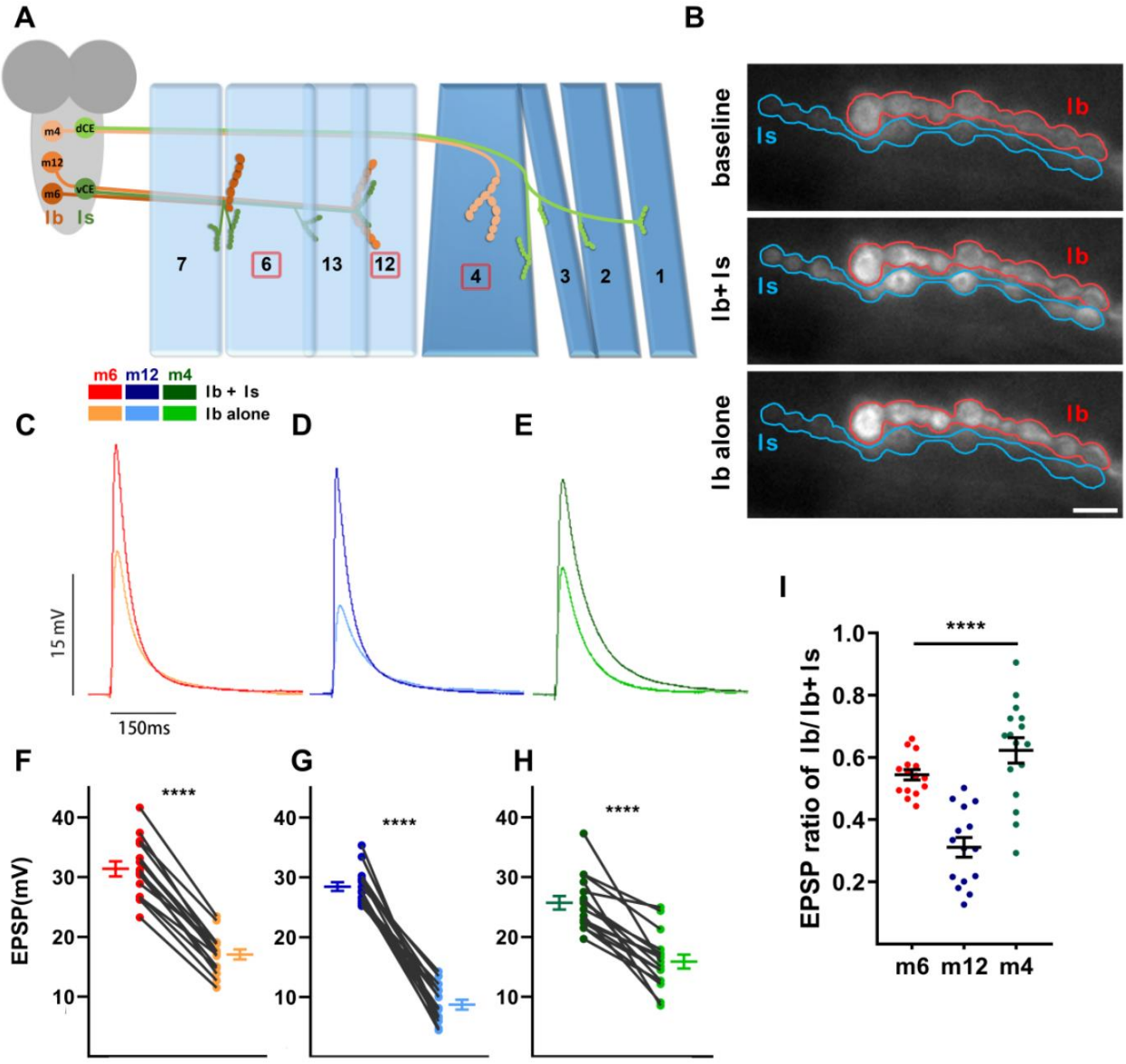

Figure 3.1 **Ib and Is MNs differentially contribute to the total EPSPs.**
(A) Schematic of the innervation pattern of a subset of Is MNs (vCE: dark green, dCE: light green) and Ib MNs (MN6-Ib: rust, MN12-Ib: orange, MN4-Ib: peach). Muscles analyzed in this study are marked by the red boxes. (B) Representative frames showing the baseline fluorescence (top), Ib+Is firing event (middle) and Ib alone firing event (bottom), of m6 in *MHC-CD8-SynapGCaMP6f* larvae (Ib: red, Is: blue). (C-E) Representative traces of Ib+Is and Ib alone on (C) m6, (D) m12, and (E) m4. Traces and graphs are color-coded as indicated in the color key. (F-H) Paired EPSP amplitudes of (F) m6 ($t_{(14)}$=18.60, p<0.0001, paired t test), (G) m12 ($t_{(14)}$=15.73, p<0.0001, paired t test) and (H) m4 ($t_{(15)}$=7.43, p<0.0001, paired t test). (I) Calculated EPSP ratios of Ib/Ib+Is of m6, m12 and m4 ($F_{(2,43)}$=26.03, p<0.0001, one-way ANOVA, Tukey post hoc test). Error bars indicate ±SEM. ****p<0.0001. n (NMJs/larva) are 15/12, 15/12, and 16/15 respectively.

3.2.2 Cell-specific genetic ablation of Is MNs by ectopic *hid,rpr* expression

To begin to examine if one input can respond to perturbations in an adjacent input, we needed to disrupt one MN and monitor the impact on the nearby MN. Therefore, we need drivers that specifically express within subsets of these MNs. To gain genetic access specifically to the Is MNs, we examined a GAL4 driver derived from the *DIP-α* promoter. In the adult neuromuscular circuit, this driver (hereafter referred to as *A8-GAL4*, or *A8*) was found to express in a small subset of MNs (Venkatasubramanian et al., 2019). We used *A8-GAL4* to drive *UAS-GFP* and found expression in only two pairs of segmentally repeated neurons in the third instar VNC (Figure 3.2A-B, arrows). The labeled neurons located ventrally in the VNC have axons that project medially and dorsally towards the neuropil (Figure 3.2C arrow). The other *A8*-expressing neurons are located in the dorsal region of the VNC and showed an ipsilateral projection with a large dendritic arbor (Figure 3.2D, arrowhead). Examination of nerves exiting the VNC showed two axons in each bundle (Figure 3.2B and D asterisks), suggesting that these *A8* positive neurons are MNs. The dorsal neurons were co-labeled with the transcription factor Even-skipped (Eve), which labels three medial neurons, aCC, pCC, and MNISN-Is (Broadus et al., 1995; Doe et al., 1988), and thus these neurons were confirmed as MNISN-Is (also called the dorsal common exciter, dCE) based on their location (Figure 3.2B). *Drosophila* larval MNs make connections with their muscle targets with very high fidelity, allowing us to unequivocally determine the identity of the MNs based on their innervation pattern. In *A8>GFP* third instar larvae, one axon innervates the ventral muscles including muscles 6, 7, 12, and 13, similar to the connectivity pattern of MNISNb/d-Is (also called the ventral common exciter, vCE; (Meng et al., 2020)). The other axon innervates the dorsal muscles, corresponding to dCE (Figures 3.2E-F).

Importantly, *A8* does not label any other MNs but only a few additional cells in one segment of the VNC (Figure 3.2A, carets). In summary, *A8* labels two Is MNs within each hemisegment.

We used *A8-GAL4* to drive *head involution defective* (*hid*) and *reaper* (*rpr*) in vCE and dCE. *hid* and *rpr* have important functions in programmed cell death, and ectopic expression of both genes more reliably induces neuronal death than either gene alone (Pauls et al., 2014; Zhou et al., 1997). As shown in Figure 3.2A-F, *A8>GFP* robustly labels Is MNs but in third instar larvae that ectopically express *hid,rpr* (*A8>GFP,hid,rpr*), all vCE or dCE cell bodies and NMJs are absent (Figure 3.2G-J). Thus, expression of *hid,rpr* is sufficient to genetically ablate Is MNs.

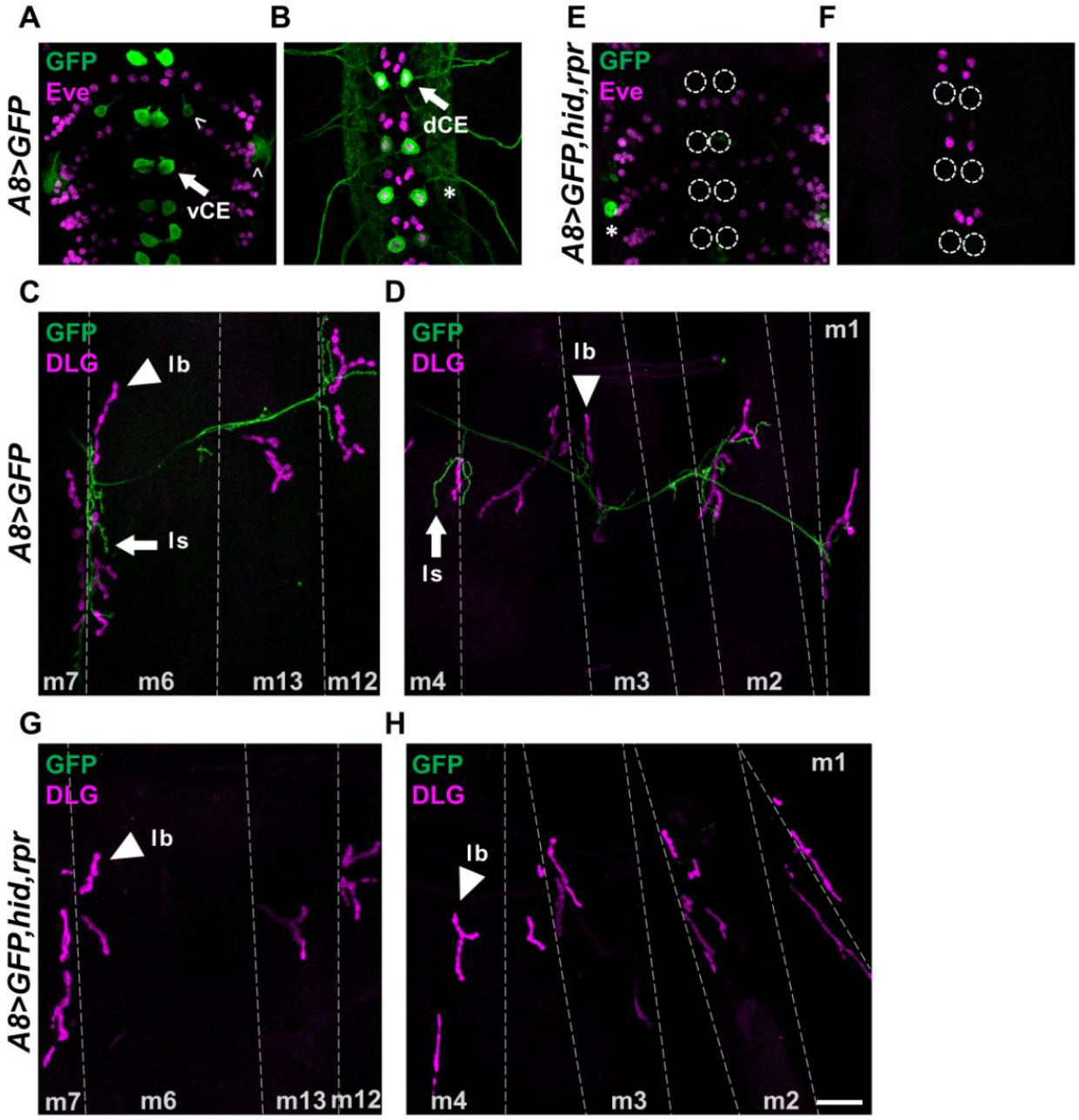

Figure 3.2 ***A8-GAL4* drives expression in Is MNs and can be used to ablate Is MNs.** (A-B) Representative third instar larval VNC Z-sections showing (A) ventral and (B) dorsal cell bodies labeled with GFP (green) and Eve (magenta, labels nuclei of dCE and other neurons), in *A8>GFP*. Arrows indicate GFP positive vCE and dCE cell bodies. Carets indicate other cells that express *A8*. Asterisks indicate two axons exiting the VNC. (C-D) 3D representations of *A8* expressing neurons in the VNC viewed from (C) lateral and (D) dorsal sides (same VNC as A-B). Arrow in (C) shows a ventral cell (left, green) that projects an axon to the dorsal midline. Arrowhead in (D) shows an ipsilateral projection from a dorsal cell. Heat map colors are as follows: red denotes the dorsal most region and blue denotes the ventral most region. Asterisks indicate axons exiting the VNC similar to (B).

Figure 3.2 (continued) (E-F) Representative third instar larval abdominal hemisegment labeled with GFP (green) and the DLG (magenta), in *A8>GFP*. (E) Ventral muscles (m6, m7, m13 and m12) innervated by vCE and (F) dorsal muscles (m4, m3, m2 and m1) innervated by dCE. Arrows indicate Is NMJs and arrowheads indicate Ib NMJs. (G-H) Representative third instar larval VNCs lacking (G) vCE and (H) dCE labeled with GFP (green) and Eve (magenta) in *A8>GFP,hid,rpr*. Dashed circles mark the absence of vCE and dCE. Note that both vCE and dCE cell bodies are ablated by the third instar stage. Asterisk marks a GFP positive cell that remained. (I,J) Representative third instar larval abdominal hemisegment showing (I) ventral muscles and (J) dorsal muscles, labeled with GFP (green) and DLG (magenta) in *A8>GFP,hid,rpr*. Note all NMJs from vCE and dCE are absent (no GFP). Arrowheads indicate Ib NMJs.

To determine the timing of *hid,rpr* induced cell death, we examined earlier developmental stages and visualized GFP in Is MN cell bodies and NMJs in *A8>GFP* and *A8>GFP,hid,rpr*. Neuromuscular innervation is established at embryonic stage 16 (Broadie and Bate, 1993; Halpern et al., 1991; Yoshihara et al., 1997), so we focused on stage 15 and later stages including stage 17 and first instar larvae. In stage 15 embryo controls (*A8>GFP*), only a subset of Is MNs are detected since not all dCE cell bodies (Eve positive) are co-stained with GFP and no vCE cell bodies are observed (Figure 3.3A-B). Age matched *A8>GFP,hid,rpr* embryos showed similar GFP expression patterns to controls (Figure 3.3C-D); thus, no cell death occurred before neuromuscular innervation. By embryonic stage 17, more vCE and dCE cell bodies expressed *A8* but the lack of GFP in some cells suggests that *A8* expression has not reached maximal levels (Figure 3.3E-F). In stage 17 *A8>GFP,hid,rpr* embryos, cells were undergoing apoptosis as revealed by significant decreases in GFP and by loss of Eve staining (suggesting nuclear degradation) (Figure 3.3G-H). Finally, in *A8>GFP* early first instar larvae, all vCE and dCE cell bodies were labeled (Figure 3.3I-J) and NMJs were present (Figure 3.3M). Age-matched *A8>GFP,hid,rpr* larvae completely lacked vCE and dCE cell bodies (Figure 3.3K and L), although some Is NMJs were still observed (Figure 3.3M-N), suggesting that Is NMJs

were established before ablation in this genetic background. By late first instar stage, *A8>GFP,hid,rpr* larvae showed no traces of Is NMJs on m6, m12 and m4 (Figure 3.3O). Taken together, *A8-GAL4* is specifically expressed in vCE and dCE and driving ectopic expression of cell death genes with *A8* triggers apoptosis in Is MNs during early developmental stages.

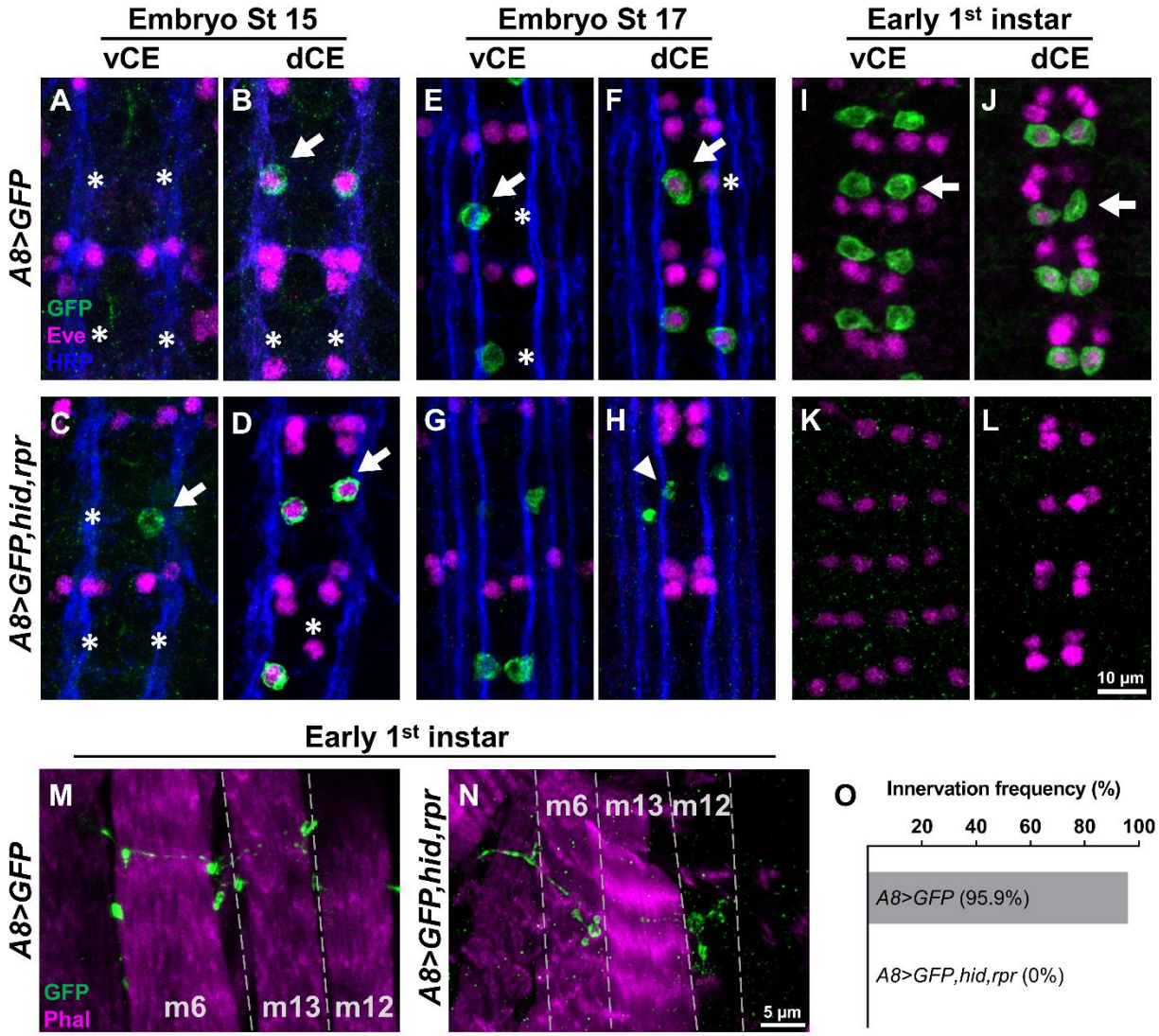

Figure 3.3 ***A8>hid,rpr*-induced cell death occurs after Is innervation.**
(A-L) Representative images depicting the presence or absence of vCE and dCE cell bodies from (A-D) embryonic stage 15, (E-H) stage 17 and (I-L) early first instar larval VNCs labeled with GFP (green), Eve (magenta), and Fasciclin 2 (blue) in control (*A8>GFP*) and Is ablated (*A8>GFP,hid,rpr*) animals. Arrows and asterisks indicate the cells expressing or not expressing *A8*, respectively. *A8* expression begins at (A-B) embryonic stage 15. In *A8>GFP,hid,rpr*, vCEs and dCEs undergo apoptosis starting at (G-H) embryonic stage 17, noted by the loss of Eve staining in dCE and GFP positive debris (indicated by arrowhead), and are completely absent in (K-L) early first instar larvae. (M-N) Representative Is NMJs labeled with GFP (green) and a muscle marker, phalloidin (magenta), in (M) control and (N) Is ablated early first instar larvae. Note Is NMJs are labeled by GFP in control animals and some Is NMJs are still present in *A8>GFP,hid,rpr* animals, suggesting *A8>GFP,hid,rpr*-induced cell death happens after Is NMJ formation. (O) Innervation frequency of Is MNs in control and Is ablated late first instar larvae. Three muscles (m6, m12, and m4) were pooled and analyzed together. All Is NMJs were eliminated in Is ablated animals by this stage. n (NMJs/larva) are 76/5 and 86/5 for (O).

3.2.3 Ib NMJs expand upon loss of adjacent Is MNs

NMJ structural plasticity can be induced by perturbation of synaptic function (Budnik et al., 1990; Goel et al., 2019; Jarecki and Keshishian, 1995; Perry et al., 2020; Sigrist et al., 2003). Here, we examined whether loss of Is MNs can induce structural changes at adjacent Ib NMJs. The size of each NMJ is well characterized (represented by the number of boutons) and this allows us to observe structural changes due to perturbations. We genetically ablated Is MNs (vCE and dCE) and counted the number of boutons on m6, m12, and m4 in wandering third instar larvae (NMJ expansion is complete (Li et al., 2002)). We observed an increase in the number of Ib boutons on all three muscles (Figure 3.4A-G) when comparing to *A8>GFP* controls, suggesting that Ib NMJs expanded when adjacent Is MNs were ablated. Because m4-Is innervation frequency is ~80% in wild type (Aponte-Santiago et al., 2020; Ashley et al., 2019), we used *A8>GFP* to confirm the presence of m4-Is in controls and excluded muscles lacking Is innervation. Interestingly, we also found an increase in small budding boutons, called satellite boutons, emanating from Ib boutons (Figure 3.4D-F, insets, and 3.4H). These structures represent immature but functional boutons as they contain all synaptic machinery and postsynaptic receptors (Carrillo et al., 2015; Dickman et al., 2006; Lee and Wu, 2010). Thus, all Ib NMJs initiate structural plasticity mechanisms to respond to loss of adjacent Is MNs.

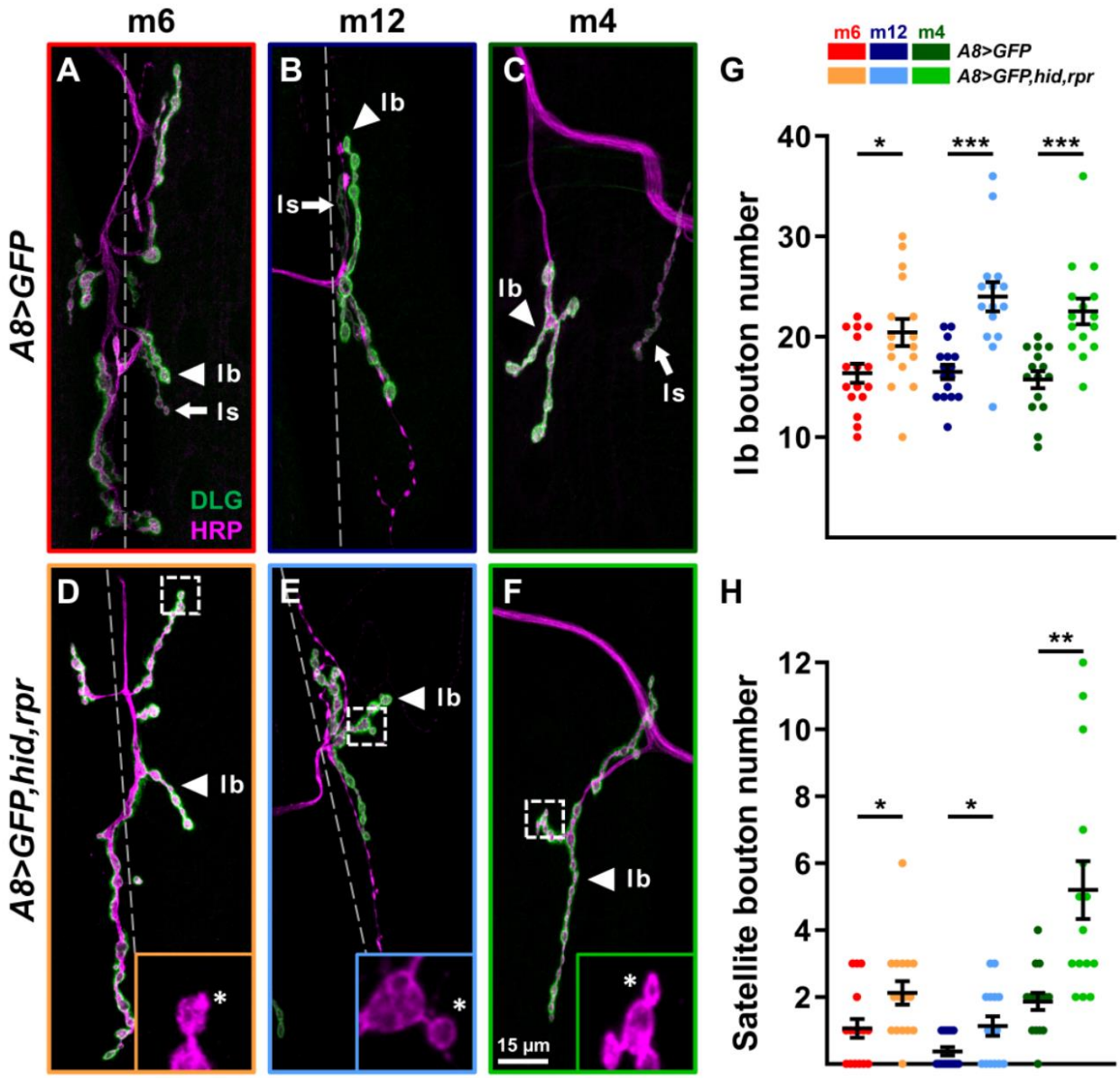

Figure 3.4 **Ib NMJs expand upon ablation of Is MNs.**
(A-F) Representative NMJ arbors (Ib arbors and Is arbors, arrowheads and arrows, respectively) of (A,D) m6, (B,E) m12 and (C,F) m4 labeled with DLG (green) and HRP (magenta) in control (*A8>GFP*) and Is ablated (*A8>GFP,hid,rpr*) third instar larvae. Insets are 5X zoomed images of corresponding dashed regions in (D-F). Satellite boutons are indicated by asterisks. Note Is NMJs are absent in Is ablated animals. Images and graphs are color-coded as indicated in the color key. (G) Quantification of Ib bouton number of m6 ($t_{(30)}$=2.458, p=0.02, unpaired t test), m12 ($t_{(26)}$=4.449, p=0.0001, unpaired t test), and m4 ($t_{(28)}$=4.431, p=0.0001, unpaired t test) in control and Is ablated animals (satellite Ib boutons were not included). (H) Quantification of satellite boutons of m6 ($t_{(30)}$=2.359, p=0.025, unpaired t test), m12 ($t_{(19.05)}$=2.397, p=0.0269, unpaired t test with Welch's correction), and m4 ($t_{(16.41)}$=3.682, p=0.0019, unpaired t test with Welch's correction) in control and Is ablated animals. Error bars indicate ±SEM. *p<0.05, **p<0.01, ***p<0.001. n (NMJs/larva) are 16/8, 16/8, 16/8, 15/8, 15/8, and 15/8 respectively.

3.2.4 Ib NMJs elevate their rate of spontaneous release upon loss of Is MNs

To determine to what extent perturbations on one synaptic input can influence the nearby input's functional synaptic plasticity, we first examined Ib spontaneous neurotransmitter release at muscles where Is MNs are ablated. Ib and Is MNs have unique spontaneous release properties. For example, Ib-derived spontaneous events (stimulus-independent release of neurotransmitter vesicles; also referred to as mini EPSPs, mEPSPs), have smaller amplitudes compared to Is-derived mEPSPs (Newman et al., 2017; Nguyen and Stewart, 2016). Therefore, ablation of Is inputs should shift the mean mEPSP amplitude towards the smaller Ib-like amplitude if there is no compensation. We performed current clamp recordings from m6, m12 and m4. Indeed, *A8>GFP,hid,rpr* revealed decreased mEPSP amplitudes compared to *A8>GFP* controls, and a significant shift in cumulative amplitude probability distribution (Figure 3.5A-G). Due to the inability of standard NMJ electrophysiology experiments to distinguish between Ib and Is mEPSPs in controls, we are unable to unambiguously determine if the Ib mEPSP amplitudes are affected by the loss of Is inputs. Nonetheless, we can conclude Ib NMJs cannot fully restore the average mEPSP amplitudes to wild type levels.

Another measure of stimulus-independent activity is the rate of spontaneous neurotransmitter release. In prior studies, mEPSP frequencies were found to be higher at Ib NMJs than Is NMJs (*e.g.*, 2.3 Hz at m4-Ib NMJ and 1 Hz at m4-Is NMJ; (Newman et al., 2017)); thus, if elimination of Is MNs does not affect the rate of Ib spontaneous release, overall mEPSP frequencies should decrease about one third. However, we did not observe any reduction of mEPSP frequencies on m6, m12, and m4 when comparing *A8>GFP* and *A8>GFP,hid,rpr* animals, and m12 even showed an increased rate of spontaneous release (Figure 3.5A-C, H).

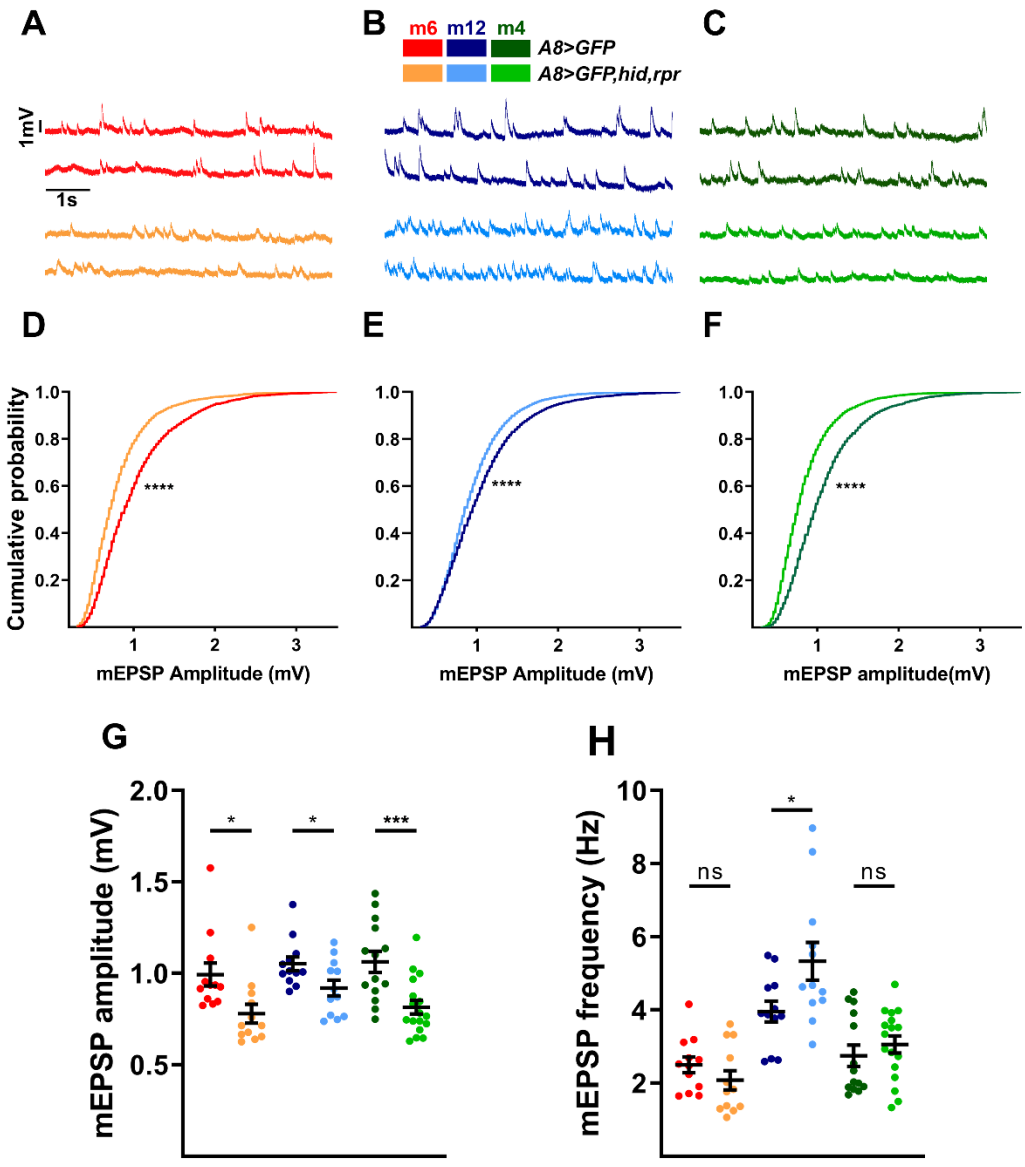

Figure 3.5 **Loss of Is MNs decreases overall mEPSP amplitudes and increases Ib mEPSP frequencies.**

(A-C) Representative mEPSP recordings of (A) m6, (B) m12, and (C) m4 in control (*A8>GFP*) and Is ablated (*A8>GFP,hid,rpr*) animals. Traces and graphs are color-coded as indicated in the color key. (D-F) Pooled cumulative probability distributions of (D) m6 ($p<0.0001$, K-S test), (E) m12 ($p<0.0001$, K-S test), and (F) m4 ($p<0.0001$, K-S test). (G) Quantification of mEPSP amplitude of m6 ($t_{(22)}=2.630$, $p=0.0153$, unpaired t test), m12 ($t_{(22)}=2.294$, $p=0.0317$, unpaired t test), and m4 ($t_{(29)}=3.700$, $p=0.0009$, unpaired t test) in control and Is ablated animals. Each data point represents the average mEPSP amplitude from one sample. (H) Quantification of mEPSP frequencies of m6 ($t_{(22)}=1.224$, $p=0.2339$, unpaired t test), m12 ($t_{(22)}=2.331$, $p=0.0293$, unpaired t test), and m4 ($t_{(29)}=0.8369$, $p=0.4095$, unpaired t test) in control and Is ablated animals. Each data point represents the average mEPSP frequency from one sample. Error bars indicate ±SEM. *$p<0.05$, **$p<0.01$, ***$p<0.001$, ****$p<0.0001$. n (NMJs/larva) are 12/9, 12/11, 12/9, 12/12, 14/11, and 17/14 respectively.

Importantly, these spontaneous events correspond to Ib-derived mEPSPs since a) the mean amplitudes decrease (Figure 3.5G), and b) there are no remaining Is NMJs (Figure 3.2I-J). These results strongly suggest that Ib MN synaptic plasticity mechanisms respond to the loss of Is inputs and elevate their rate of spontaneous neurotransmitter release. Spontaneous neurotransmitter release has been implicated in synaptic maturation (Andreae and Burrone, 2018; Cho et al., 2015; Kavalali, 2015), and thus, the increased mEPSP frequencies we observe could underlie the increased Ib bouton numbers.

3.2.5 Ib MNs elevate evoked neurotransmission upon loss of Is MNs in a target-specific manner

Having demonstrated Ib synaptic plasticity of spontaneous activity, we next examined whether Ib evoked neurotransmission could also be modified by the loss of Is MNs. Unlike spontaneous neurotransmitter release, EPSPs require stimulation to depolarize the presynaptic neuron above threshold. This suprathreshold stimulation triggers an action potential to induce neurotransmitter release and elicit a postsynaptic response. In order to examine if Ib MNs can compensate for the loss of Is synaptic drive, we recorded EPSPs in both *A8>GFP* and *A8>GFP,hid,rpr* (Figure 3.6A-F). To determine if Ib-derived EPSP amplitudes are affected by loss of Is inputs, we normalized the EPSPs (*A8>GFP,hid,rpr* EPSP/*A8>GFP* EPSP) and compared these values to the calculated Ib/Ib+Is ratio in Figure 3.1I. This analysis allows for the comparison of Ib-derived EPSPs with and without Is MNs.

We observed target-specific changes in Ib-derived EPSPs (Figure 3.6G-I). At m4, we observed a significant increase in Ib-derived EPSPs compared to the control Ib/Ib+Is ratio (Figure 3.6I). By repeating the analysis at other muscles, we found a mild increase in Ib-derived

EPSPs at m6 (Figure 3.6G), and surprisingly, no change at m12 (Figure 3.6H). When comparing the degree of EPSP compensations (Figure 3.6G-I) to the wild type Ib contribution to total EPSP at each muscle (Figure 3.1I), a pattern arises whereby the m4-Ib has both the most compensation and the largest Ib contribution. Meanwhile, m12-Ib did not compensate and displayed the smallest Ib contribution.

Next, we examined quantal content (QC), a calculation of the approximate amount of neurotransmitter released per stimulation. We found that the normalized QC of MN4-Ib in *A8>GFP,hid,rpr* was significantly increased compared to the MN4-Ib baseline QC, whereas there was no change at MN6-Ib, and even a decrease at MN12-Ib (Figure 3.6J-L).

To test if loss of Is MNs perturbed short-term Ib NMJ plasticity, we examined paired-pulse facilitation (PPF) as it is a measure of evoked release probability (P_r). We measured m6 PPF in *A8>GFP,hid,rpr* and found an enhancement compared to *A8>GFP* controls (Figure 3.7). Although this data suggests an increase in Ib P_r, this can also be explained by the loss of Is-specific synaptic depression (Newman et al., 2017) as both MNs are stimulated in controls. Furthermore, we were unable to definitively isolate Ib-specific PPF in controls as the second EPSC could be either Ib-derived or Ib+Is-derived (Peled et al., 2014). Overall, when ablating Is MNs, Ib MNs that innervate the same muscle upregulated their rate of spontaneous release, and importantly, the MN4-Ib significantly compensated the total EPSP by increasing neurotransmitter release.

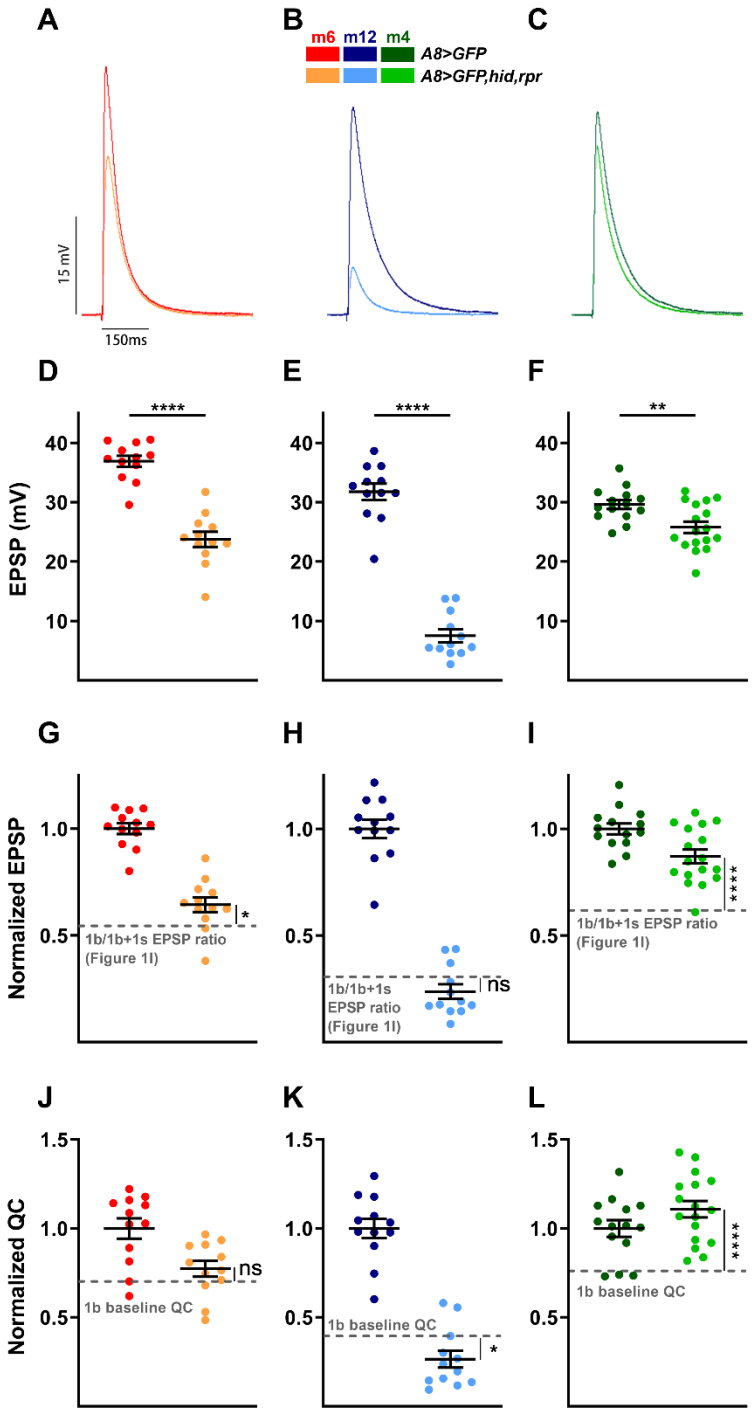

Figure 3.6 **Ib NMJs elevate evoked neurotransmission in a target-specific manner in the absence Is inputs.**

(A-C) Representative EPSP traces of Ib+Is and Ib alone of (A) m6, (B) m12, and (C) m4. Traces and graphs are color-coded as indicated in the color key. (D-F) Quantification of EPSP amplitudes in (D) m6 ($t_{(22)}$=8.306, p<0.0001, unpaired t test), (E) m12 ($t_{(22)}$=13.82, p<0.0001, unpaired t test), and (F) m4 ($t_{(29)}$=3.057, p=0.0048, unpaired t test) in control (*A8>GFP*) and Is

Figure 3.6 (continued) ablated (*A8>GFP,hid,rpr*) animals. (G-I) Normalized EPSPs of (G) m6 ($t_{(25)}$=2.301, p=0.0300, unpaired t test), (H) m12 ($t_{(25)}$=1.552, p=0.1332, unpaired t test), and (I) m4 ($t_{(31)}$=4.605, p<0.0001, unpaired t test) in control and Is ablated third instar larvae. Normalized EPSPs in *A8>GFP,hid,rpr* are compared to the EPSP ratio of Ib/Ib+Is calculated from corresponding muscles in Figure 3.1I, indicated by grey dashed line. Note MN6-Ib slightly compensates, MN12-Ib does not compensate and MN4-Ib largely compensates the loss of Is MNs. (J-L) Normalized quantal content (QC) of (J) m6 ($t_{(25)}$=1.239, p=0.2268, unpaired t test), (K) m12 ($t_{(25)}$=2.119, p=0.0442, unpaired t test), and (L) m4 ($t_{(31)}$=4.639, p<0.0001, unpaired t test) in control and Is ablated larvae. Normalized QCs were compared to Ib baseline QC. Note MN4-Ib shows increased QC, while MN12-Ib shows a decrease. Error bars indicate ±SEM. *p<0.05, **p<0.01, ****p<0.0001. n (NMJs/larva) are 12/9, 12/11, 12/9, 12/12, 14/11, and 17/14 respectively.

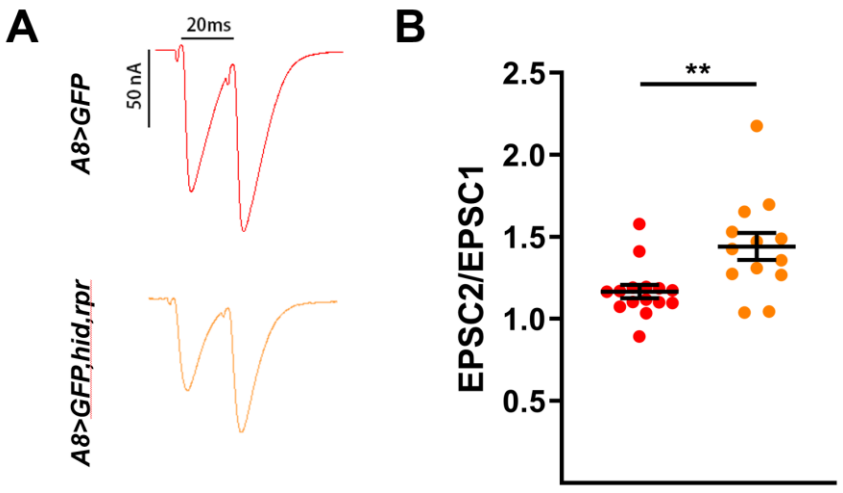

Figure 3.7 **Overall paired-pulse ratio is increased upon the ablation of Is MNs.** (A) Representative paired-pulse recordings of m6 in control (*A8>GFP*) and Is ablated (*A8>GFP,hid,rpr*) animals. (B) Quantification of paired-pulse ratio (EPSC2/EPSC1) in control (red) and Is ablated animals (orange) ($t_{(26)}$=3.120, p=0.0044, unpaired t test). n (NMJs/larva) are 15/10, 13/10. Error bars indicate ±SEM. **p<0.01.

3.2.6 Ib synaptic plasticity is induced by Is MN ablation, but not by the loss of Is synapses

Next, we sought to examine the mechanisms by which Is ablation induces Ib plasticity. Ablating Is MNs is a gross manipulation as it removes axons, cell bodies, and dendrites in

addition to the Is synapses. Therefore, we are unable to determine if the trigger of Ib plasticity is the loss of convergent Is synapses or instead, ablation of the entire Is MN. Specifically, loss of co-innervated Is synapses may be sensed by muscles which then induce Ib plasticity through a retrograde signal. Conversely, ablating the entire Is MN may induce a glial response which then signals to nearby healthy neurons. To distinguish these possibilities, we examined mutants that specifically perturb local innervation while keeping the MN intact and muscles that receive Ib innervation from the same nerve but no Is input.

3.2.6.1 Ib synaptic plasticity is not induced in DIP-α mutants

We focused on m4 since MN4-Ib shows the strongest plasticity (Figure 3.6). In a previous study, we found that *DIP-α* mutants lack Is innervation on m4 (Figure 3.8A-B). We confirmed that no Is boutons are observed on m4 in *DIP-α*^{null} even in early first instar larvae (Figure 3.8C). Quantification of m4-Ib boutons and satellite boutons in *DIP-α*^{null} mutants showed no difference from controls (Figure 3.8D-E). Also, in *DIP-α*^{null} mutants, m4 mEPSP frequency was significantly reduced (Figure 3.8F-G), in contrast to the Is ablation (Figure 3.5H). These results suggest that the MN4-Ib failed to compensate when the corresponding Is NMJ never formed. Next, we examined EPSPs (Figure 3.8F and H). Surprisingly, lack of Is innervation in *DIP-α*^{null} mutant larvae revealed only a slight increase in the Ib-derived EPSP amplitude on m4 (Figure 3.8I) and no change in QC (Figure 3.8J). Thus, MN4-Ib synaptic plasticity is not as robust in *DIP-α*^{null} larvae compared to *A8>GFP,hid,rpr*.

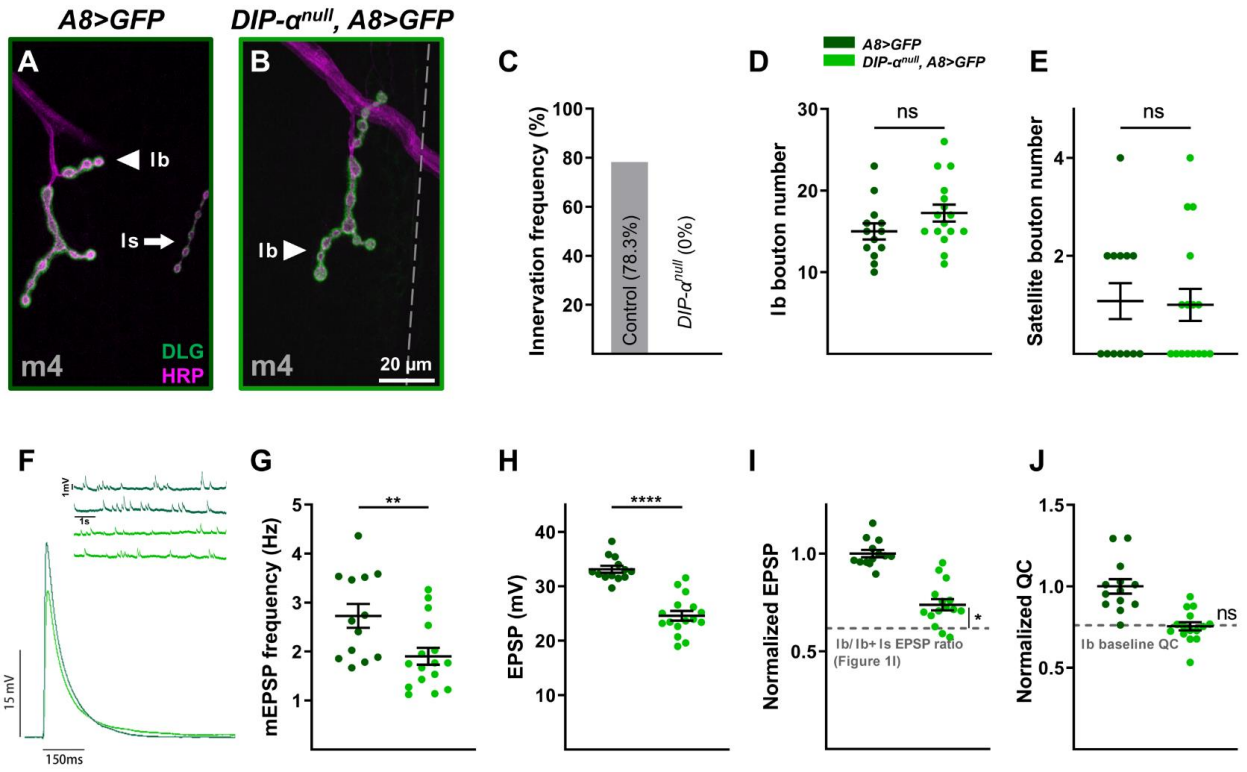

Figure 3.8 **Lack of Is innervation on m4 is not sufficient to induce robust Ib plasticity.** (A-B) Representative m4 NMJs labeled with DLG (green) and HRP (magenta) in (A) control (*A8>GFP*: dark green) and (B) mutant (*DIP-α^null^, A8>GFP*: light green) animals. (C) Quantification of Is innervation frequency in control and mutant first instar larvae. No m4-Is NMJs observed in mutants. (D) Quantification of Ib boutons from m4 in control and mutant animals ($t_{(27)}$=1.552, p=0.1323, unpaired t test). Images, representative traces, and graphs are color-coded as indicated in the color key. (E) Quantification of satellite boutons from m4 in control and mutant animals ($t_{(27)}$=0.1563, p=0.8770, unpaired t test). (F) Representative mEPSP and EPSP recordings from control and mutant animals. (G) Quantification of mEPSP frequencies from m4 in control and mutant animals ($t_{(27)}$=2.824, p=0.0088, unpaired t test). (H) Quantification of EPSP amplitudes in control and mutant animals ($t_{(27)}$=7.505, p<0.0001, unpaired t test). (I) Normalized EPSPs from m4 in control and mutant animals ($t_{(29)}$=2.215, p=0.0348, unpaired t test). Normalized mutant EPSP is compared to the EPSP ratio of Ib/Ib+Is calculated from m4 in Figure 3.1I, indicated by grey dashed line. Note MN4-Ib-derived EPSP increases 23% in *DIP-α* mutants but increases 45% in *A8>GFP,hid,rpr* (Figure 3.6I). (J) Normalized QC from m4 in control and mutant animals ($t_{(20.14)}$=0.086, p=0.9326, unpaired t test with Welch's correction). Normalized QC was compared to Ib baseline QC. Error bars indicate ±SEM. *p<0.05, **p<0.01, ****p<0.0001. n (NMJs/larva) are 46/8, 20/4 for (C), 13/8,16/8 for (D,E) and 13/10, 16/10 for (F-J).

3.2.6.2 Ib synaptic plasticity is not induced on m4s that naturally lack Is innervation

Utilizing *DIP-α* mutants is not ideal because *DIP-α* is also expressed in interneurons that may connect to MNs, and interneuron-MN communication may affect synaptic plasticity. Therefore, we examined Ib structural and functional plasticity in another context where m4 is naturally missing Is innervation. In wild type larvae, approximately 20% of m4s lack Is NMJs (Figure 3.9C). However, comparing wild type m4s that naturally lack Is innervation with those that have Is innervation, we observed no change in Ib bouton numbers (Figure 3.9A-B). Similarly, Ib-derived EPSP and QC were unaffected (Figure 3.9C-F). This confirms that lack of synaptic plasticity in *DIP-α*^{null} larvae is not due to the genetic manipulation. Further, these data show that MN4-Ib NMJs that naturally lack adjacent Is NMJs are unable to compensate, suggesting that robust MN4-Ib synaptic plasticity is not due to the loss of Is co-innervation.

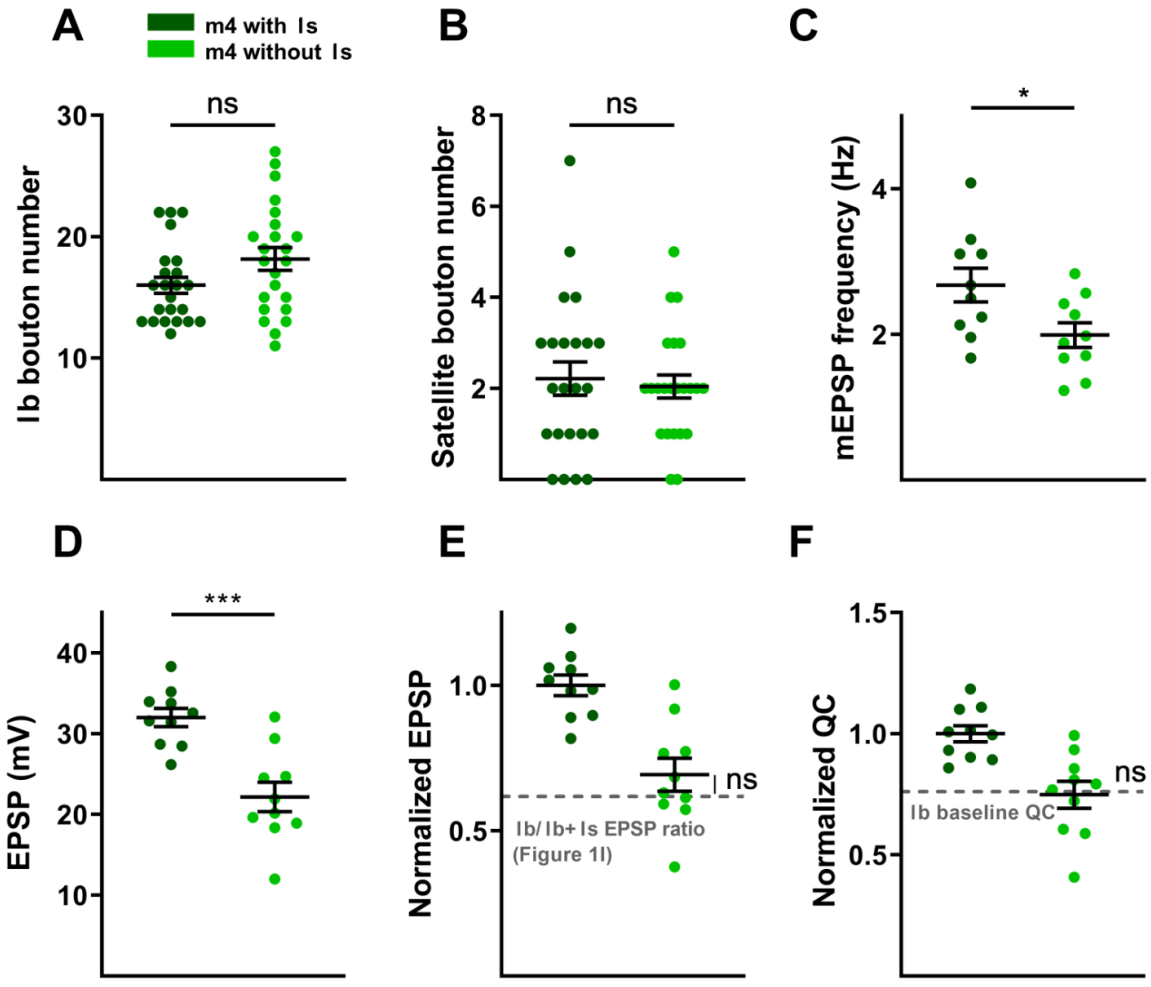

Figure 3.9 **m4s that naturally lack Is innervation do not show Ib plasticity.**
(A) Quantification of Ib boutons from m4s with and without Is innervation ($t_{(44)}$=1.885, p=0.0661, unpaired t test). (B) Quantification of satellite boutons from m4s with and without Is innervation ($t_{(44)}$=0.3895, p=0.6988, unpaired t test). (C) Quantification of mEPSP frequencies from m4s with and without Is innervation ($t_{(18)}$=2.414, p=0.0267, unpaired t test). (D) Quantification of EPSP amplitudes from m4s with and without Is innervation ($t_{(18)}$=4.576, p=0.0002, unpaired t test). (E) Normalized EPSPs from m4s without Is innervation is compared to the EPSP ratio of Ib/Ib+Is calculated from m4 in Figure 3.1I, indicated by grey dashed line ($t_{(24)}$=1.263, p=0.2186, unpaired t test). (F) Normalized QC from m4s without Is innervation is compared to the Ib baseline QC ($t_{(24)}$=0.1449, p=0.8860, unpaired t test). Error bars indicate ±SEM. *p<0.05, ***p<0.001. n (NMJs/larva) are 23/17 and 23/17 for (A-B), 10/7 and 10/9 for (C-F).

3.2.6.3 Synaptic plasticity can be induced at Ib MNs that do not have Is co-innervation

Given that loss of Is co-innervation does not trigger Ib plasticity, we hypothesized that the Is MN ablation (i.e., removal of the entire neuron) is likely the trigger of Ib plasticity. Further, because MN axons are surrounded by glia, we hypothesized that Is ablation may trigger a glial response that transmits a signal to all nearby Ib axons within the nerve. Thus, structural and functional plasticity in Ib MNs would be induced even if the muscle target is not co-innervated by a Is MN. To test this model, we examined MN11-Ib that innervates m11, which never receives Is input. Surprisingly, we observed an increase of MN11-Ib bouton number, EPSP amplitude, and QC when Is MNs are ablated (Figure 3.10A-D). These results suggest that even without Is co-innervation of m11, MN11-Ib responds to Is MN ablation in the shared nerve.

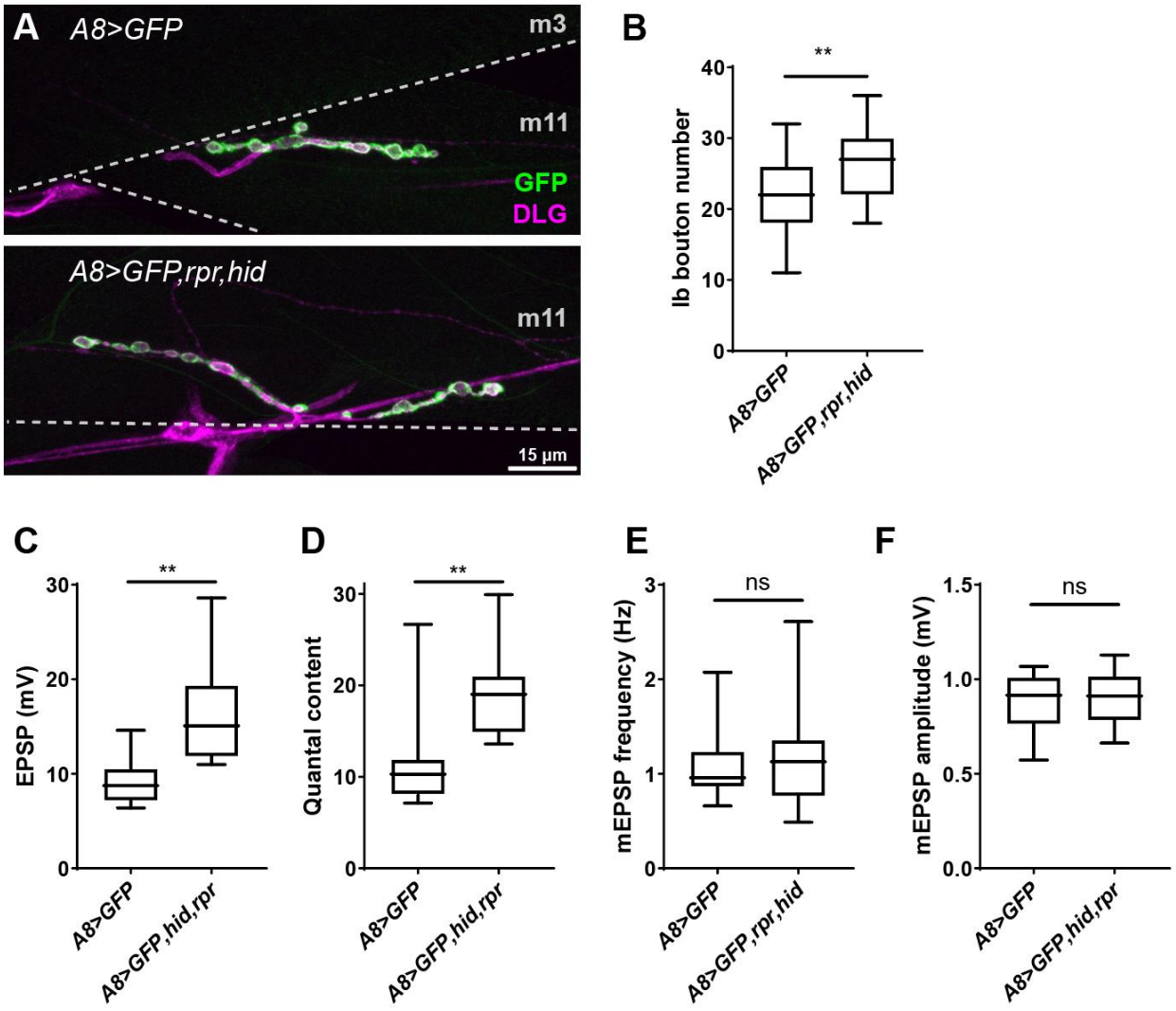

Figure 3.10 **Is MN ablation induces synaptic plasticity in MN11-Ib.**
(A) Representative m11 NMJs labeled with DLG (green) and HRP (magenta) in control (*A8>GFP*) and Is ablated (*A8>GFP,rpr,hid*) animals. (B) Quantification of Ib boutons from m11 in control and Is ablated animals ($t_{(61)}$=3.408, p=0.0012, unpaired t test). (C) Quantification of EPSP amplitudes in control and Is ablated animals ($t_{(17)}$=3.823, p=0.0021, unpaired t test with Welch's correction). (D) Quantification of QC in control and Is ablated animals ($t_{(17)}$=3.068, p=0.0070, unpaired t test). (E) Quantification of mEPSP frequency in control and Is ablated animals ($t_{(17)}$=0.4256, p=0.6758, unpaired t test). (F) Quantification of mEPSP amplitudes in control and Is ablated animals ($t_{(17)}$=0.2435, p=0.8106, unpaired t test). Error bars indicate ±SEM. **p<0.01. n (NMJs/larva) are 31/10 and 32/10 for (A-B), 9/9 and 10/8 for (C-F).

Interestingly, we did not observe an increase of mEPSP frequency or mEPSP amplitude at MN11-Ib NMJ after Is ablation (Figure 3.10E-F), whereas other Ib MNs innervating m6, m12 and m4 show compensation of mEPSP frequency (Figure 3.5). We reason that this is due to different regulatory mechanisms of individual MNs, as each MNs displays plasticity at different levels (Figure 3.11). Specifically, MN6-Ib and MN4-Ib show structural (i.e., bouton numbers), spontaneous, and evoked plasticity. MN12-Ib and MN11-Ib show structural plasticity, whereas MN12-Ib lacks evoked plasticity and MN11-Ib lacks the spontaneous release plasticity. In addition, another study revealed that MN1-Ib compensates the evoked activity but no change in structure (Aponte-Santiago et al., 2020). Taken together, these results suggest that (1) Ib synaptic plasticity is induced by neuron ablation, rather than loss of local synaptic inputs, (2) different MNs show different levels of synaptic plasticity, and (3) each form of synaptic plasticity is likely uncoupled.

Compensation capability of	Structure	mEPSP frequency	EPSP (QC)
MN6-Ib	Yes	Yes	Yes
MN12-Ib	Yes	Yes	No
MN4-Ib	Yes	Yes	Yes
MN11-Ib	Yes	No	Yes
MN1-Ib	No	N.A.	Yes

Figure 3.11 **Summary of Ib synaptic plasticity after Is ablation.**
Different MNs show plasticity on different levels after Is ablation, including the bouton number increase (structure plasticity), increase of mEPSP frequency (plasticity of spontaneous release), and the increase of EPSP amplitude (or QC, plasticity of evoked release). N.A. = not applicable.

3.3 Discussion

The major gap this study addresses is to what extent one synaptic input can influence a nearby input's structural and functional plasticity. Here, we examine the *Drosophila* neuromuscular circuit and demonstrate Ib synaptic plasticity upon the ablation of Is MNs. First, we established an activity baseline in wild type and uncovered that Ib MNs contribute a unique percentage of the total EPSP in a muscle-specific manner. Genetic ablation of Is MNs (vCE and dCE) led to expansion of Ib NMJs and elevation of their spontaneous release rates. Furthermore, some Ib MNs elevated evoked neurotransmission while others remained unchanged. Here, we term this non-cell autonomous synaptic plasticity phenomenon as cross-neuron plasticity. A recent study examining m1 found similar Ib functional plasticity when m1-Is was ablated (Aponte-Santiago et al., 2020), but no structural compensation. This target specificity indicates heterogeneity in the mechanisms of cross-neuron plasticity.

3.3.1 Potential mechanisms underlying cross-neuron plasticity

As motor neurons, Ib and Is MNs do not form direct synapses with each other. How do the Ib MNs detect the ablation of Is MNs? What is the signal that instructs Ib MNs to compensate? One important player may be the muscle since muscles normally should receive both Ib and Is inputs. After Is MN ablation, the muscle could transmit a signal to the Ib NMJs to trigger compensation. Another hypothesis is that glial cells that wrap the MN axons transmit the signal. In support of this model, glial cells can detect axonal injuries and affect axon transportation in nearby healthy neurons (Hsu et al., 2020). To distinguish these two possibilities, we examined muscles that do not receive Is innervation (Figures 3.8-3.10). Surprisingly, we observed cross-neuron plasticity in corresponding Ib MNs, suggesting that the signal that triggers

cross-neuron plasticity in Ib MNs is likely not transmitted through muscles, but instead, through glial cells in the segmental nerve or in the VNC. In addition, these results indicate that cross-neuron plasticity relies on the ablation of Is MNs, rather than loss of the co-innervated Is MNs. In Chapter 4, I will examine the mechanisms underlying cross-neuron plasticity.

3.3.2 Correlation between synaptic weight and target-specific plasticity

In complex neural circuits, dissecting contributions of individual inputs to the total postsynaptic activity, also referred to as synaptic weight (Bhalla, 2008; Magee and Cook, 2000), remains difficult due to thousands of converging inputs on a single cell. The larval NMJ facilitates the partitioning of synaptic inputs as each muscle is innervated by few MNs. In this study, we combined electrophysiology with calcium imaging and found that Ib synaptic weights differ on m6, m12, and m4. Taken together with the degree of EPSP compensation after ablation of Is MNs, there was a direct correlation with the level of target-specific synaptic weight. Thus, robust Ib MNs that carry more synaptic drive may be endowed with certain synaptic plasticity mechanisms that respond to loss of adjacent inputs. However, we cannot rule out regulatory roles for type II and type III MNs (Chang and Keshishian, 1996; Gorczyca et al., 1993; Koon et al., 2010) that are present on some muscles.

Interestingly, a similar correlation exists in Hebbian plasticity, where stronger synapses are more likely strengthened than weaker ones (Babadi and Abbott, 2010; Song et al., 2000). This correlation is also reflected in PHP. Two studies examined input-specific PHP on different muscles: on m4, PHP can be only induced at Ib NMJs (Newman et al., 2017); however, on m6, PHP can be induced on both Ib and Is NMJs (Genç and Davis, 2019). This correlates with our observation that the MN4-Ib has more synaptic weight than m4-Is, whereas MN6-Ib and m6-Is

have similar synaptic weights. Taken together, homeostatic plasticity varies in target-specific and input-specific manners, suggesting heterogeneous mechanisms.

3.3.3 Cross-neuron plasticity in other neural circuits

Mechanisms uncovered at the NMJ can act in more complex circuits in vertebrates. Similar to cross-neuron plasticity, cross modal plasticity happens on a larger scale and is triggered by sensory deprivation. For example, in blind people the visual cortex is not silent but instead, recruited for other sensory processing to augment perceptual, auditory, and attentional sensation. In deaf individuals, although the auditory cortex no longer receives input from the ears, they can still use specific regions of the cortex to process visual stimuli. In addition, in age- and disease-related conditions (A. and William, 2002; Griffith et al., 2014; Mattson and Magnus, 2006; Salvadores et al., 2017), such as patients and animal models of Alzheimer's disease, while some neurons are depressed in amyloid-β plaque enriched regions, other neurons show a compensatory hyperactivation (Busche et al., 2012; Merlo et al., 2019). However, the mechanisms underlying these compensatory changes is not clear. Thus, future studies at the NMJ and other circuits will elucidate the mechanisms governing how neurons respond to dysfunctional neighbors and provide new prospective to therapies for neurodegenerative disease.

3.4 Methods and materials

Methods and materials for Chapter 3 are described together in Chapter 4.

CHAPTER 4

DRAPER IS REQUIRED FOR CROSS-NEURON PLASTICITY

4.1 Introduction

In Chapter 3, we described cross-neuron plasticity, a novel form of synaptic plasticity that enables nearby MNs to structural and functional compensate when other MNs are ablated. The mechanism underlying cross-neuron plasticity is unknown, and here, we examine potential signaling pathways.

The Is MN axons are housed in nerve bundles that include other MN and SN axons and surrounded by three glial cell types (Crews, 2019). Glial processes are interdigitated between and around axons and may provide direct signaling between axons (Ackerman et al., 2021; Ahtiainen et al., 2021; Hsu et al., 2020; Kottmeier et al., 2020; Lee et al., 2020; Ribot et al., 2021). We hypothesize that ablation of Is MNs is detected by glia which then signal to healthy adjacent MNs to activate cross-neuron plasticity. Glial cells actively remove axonal debris during development and during axon injury through Draper, an engulfment receptor, that recognizes "eat me" signals exposed from the axon (Awasaki et al., 2006; Hoopfer et al., 2006; MacDonald et al., 2006). Thus, the Draper pathway is an excellent candidate for the detection/delivery of the compensatory signal to healthy Ib MNs. Previous studies utilized physical injury to demonstrate Draper-dependent axon debris removal (McPhee et al., 2010; Purice et al., 2016; Wu et al., 2009; Ziegenfuss et al., 2008), whereas we use genetic ablation to kill specific MNs. Although the perturbations are different, they may utilize similar clearance and downstream pathways. Therefore, we first examined Draper's role in debris clearance after MN ablation. Indeed, we found that Draper is required to clear Is MN debris in both the VNC and segmental nerve. Next,

we examined cross-neuron plasticity and found that loss of *draper* impairs structural and functional changes in MN4-Ib. This result, combined with the requirement of Draper for axon debris removal, suggests that the Draper mediated signaling underlies cross-neuron plasticity. A recent study using wing sensory neurons demonstrated that Draper signaling in glia is required to modulate axonal transport in bystander neurons (Hsu et al., 2020); a similar mechanism may detect the ablated MNs and instruct compensatory changes in nearby healthy MNs. Thus, glial mechanisms utilized during normal development, such as Draper signaling, may also instruct responses to perturbations such as neuron injury and death.

4.2 Results

4.2.1 Draper is required to efficiently clear debris from degenerating neurons

Draper-JNK signaling is implicated in axonal debris clearance in several *Drosophila* nerve injury models including axotomy of olfactory and wing sensory neurons (Awasaki et al., 2006; Logan et al., 2012). However, whether Draper is also involved in clearance of axonal debris generated by *rpr,hid*-induced cell death is not clear. Here, we ablated Is MNs in a *draper* mutant background and examined the morphology and function of MN4-Ib. In the nerve bundle, *A8>GFP* labels the Is axons (Figure 4.1A and A'), which are absent in *A8>GFP,rpr,hid* larvae (Figure 4.1B and B'). However, ablation of Is MNs in *draper* mutant animals lead to significant accumulation of GFP in the segmental nerve (Figure 4.1C-C' and D-D'), suggesting a failure of axonal debris clearance. In addition, the retained GFP signal co-localized with the glial cell marker, Repo (Figure 4.1D'). GFP positive glial cells were only observed when Is MNs were ablated in *draper* mutants (Figure 4.1F). There are three types of glial cells in the segmental nerve – perineurial glial cells (PG), sub-perineurial glial cells (SPG), and wrapping glial cells

(WG). In *draper* mutant NMJs, GFP was occasionally observed in filopodia-like structures (Figure 4.1E and E'). SPG processes can extend into the NMJ, suggesting that these GFP positive filopodia may be from SPGs (Fuentes-Medel et al., 2009).

Next, we examined the VNC where Is cell bodies and dendrites are located. We found complete clearance of VNC debris in wild type animals, but a significant retention of GFP when repeating the experiment in *draper* mutants (Figure 4.1G-K). Interestingly, unlike the GFP accumulation in segmental nerve, the GFP signal in the VNC is more diffuse and sometimes accumulated in specific cells (Figure 4.1J, arrows). To determine which cell type clears VNC debris independent of Draper, we immunolabeled with Repo, a glial cell marker, and Elav, a neuronal marker. Interestingly, these GFP positive cells were not labeled with Repo (Figure 4.2A-D) or Elav (Figure 4.2E-H), suggesting other cells may be capable of clearing neuronal debris in the VNC. In summary, we showed that Draper is required to efficiently remove neuronal debris in both the segmental nerve and the VNC.

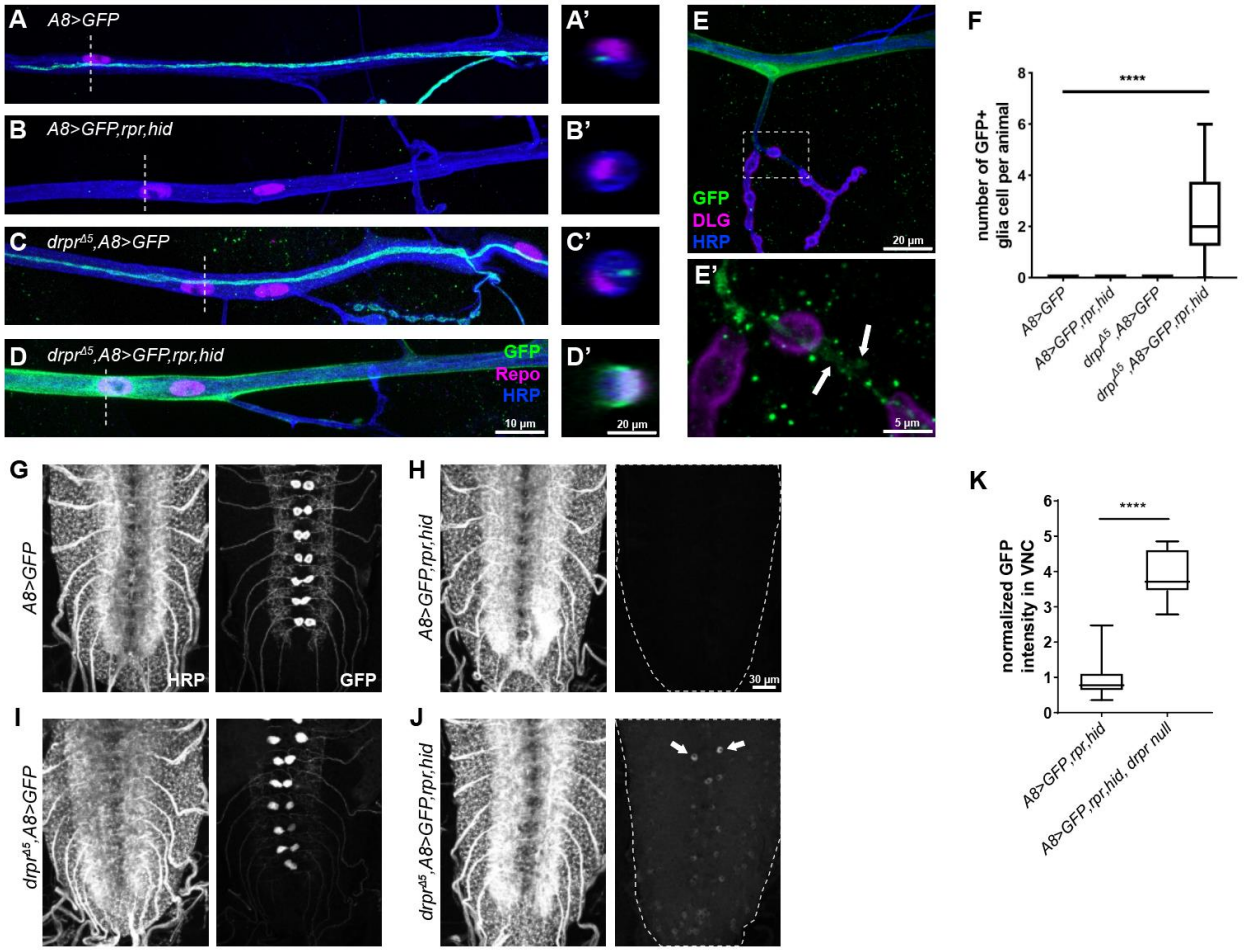

Figure 4.1 **Draper is required to remove neuronal debris in segmental nerves and the VNC.**

(A-D) Representative images showing the nerve (anti HRP, blue), Is axon (GFP, green) and glial cell nuclei (Repo, magenta), in wild type (*A8>GFP*), Is ablated animals (*A8>GFP,rpr,hid*), *draper* mutant (*draper*$^{\Delta 5}$) and Is ablation in *draper* mutant (*draper*$^{\Delta 5}$, *A8>GFP,rpr,hid*). Dashed line indicates place of cross section displayed in A'-D'. Note that GFP signal is retained in the outer layer of segmental nerve in D. (E and E') Representative images of NMJ showing GFP positive extension at the NMJ. (F) Quantification of the number of GFP+ glial cells per animal ($F_{(3,57)}$=14.09, p<0.0001, one-way ANOVA). (G-J) Representative images of VNC stained with HRP and GFP, showing GFP is retained within the VNC when ablating Is MNs in *draper* mutants. Arrows in J denote GFP accumulation in some cells. (K) Quantification of normalized GFP intensity in VNC, ($t_{(12)}$=7.703, p<0.0001, unpaired t test). ****p<0.0001. n (larva) are 15, 14, 16 and 16 for (F), 7 and 7 for (K).

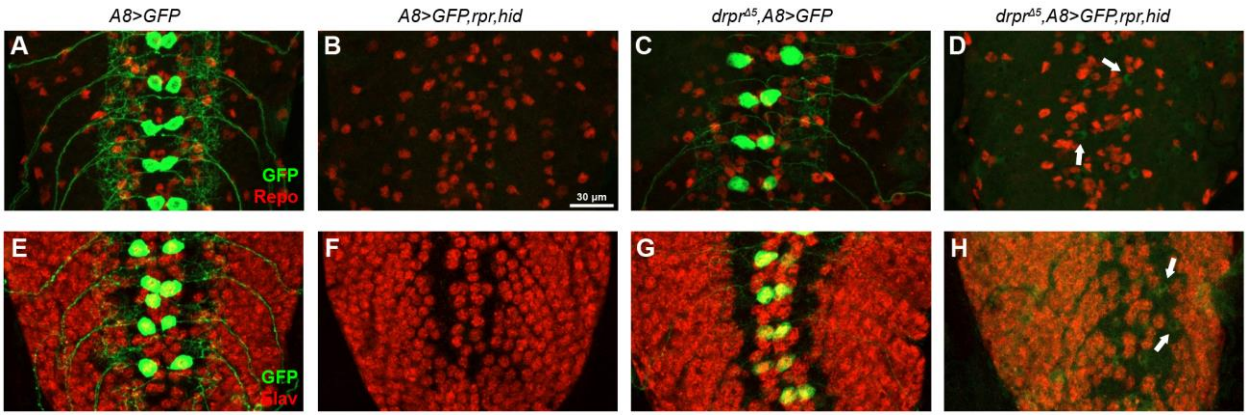

Figure 4.2 **GFP+ debris accumulate in unknown cell type in the VNC.**
(A-D) Representative images showing the Is MNs (GFP, green) and glial cell nuclei (Repo, red), in wild type (*A8>GFP*), Is ablated animals (*A8>GFP,rpr,hid*), *draper* mutant (*draper*$^{\Delta 5}$) and Is ablation in *draper* mutant (*draper*$^{\Delta 5}$, *A8>GFP,rpr,hid*). Arrows in (D)mark GFP+ cells. Note that these GFP+ cells are Repo negative. (E-H) Representative images showing the Is MNs (GFP, green) and neuronal cell nuclei (Elav, red). Arrows in (H) mark GFP+ cells. Note that these GFP+ cells are also Elav negative.

4.2.2 Draper is required for cross-neuron plasticity

After establishing that Draper is required for neuronal debris clearance after Is ablation, we asked whether Draper is required for cross-neuron plasticity. We focused on MN4-Ib as it shows robust structural and functional plasticity when the adjacent Is MN is ablated. First we examined the NMJ size. A previous study reported that *draper* mutants have enlarged boutons with satellite boutons (Fuentes-Medel et al., 2009); therefore, to faithfully analyze Ib NMJ size, we labeled Brp to quantify the AZ number of MN4-Ib. We found that Is ablation induced an increase in the number of AZs per NMJ, similar to our previously study (Figure 4.3A,B and E). In *draper* mutants, the number of AZs on m4 is similar to wild type, suggesting Draper itself does not affect NMJ size (Figure 4.3C and E). Interestingly, when ablating Is MNs in *draper* mutants, we did not observe the increase in AZ number (Figure 4.3D-E). These results suggest that Draper is required for the structural changes in cross-neuron plasticity.

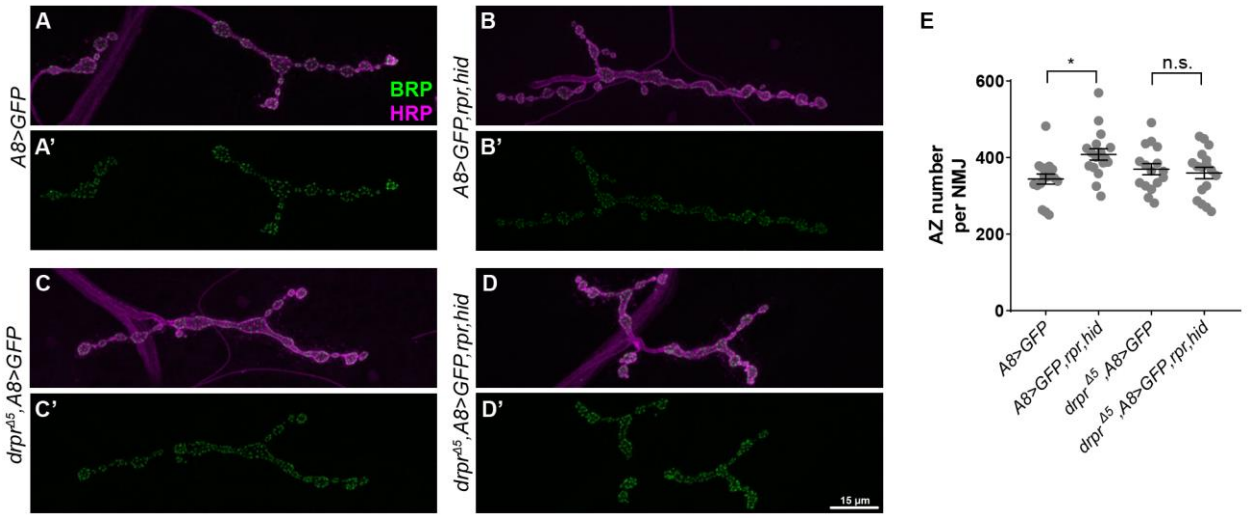

Figure 4.3 **Structural plasticity is absent when Is neurons are ablated in *draper* mutants.** (A-D) Representative images showing the AZs (Brp, green) and HRP (magenta), in wild type (*A8>GFP*), Is ablated animals (*A8>GFP,rpr,hid*), *draper* mutant (*draper*$^{\Delta 5}$) and Is ablation in *draper* mutant (*draper*$^{\Delta 5}$, *A8>GFP,rpr,hid*). (E) Quantification of AZ number per NMJ ($F_{(3,63)}$=0.3050, overall p=0.8217, one-way ANOVA). *p<0.05. n (NMJs/larva) are 17/12, 17/12, 16/12, 17/12, respectively.

Next, we examined whether Draper is required for Ib MN functional plasticity. Ablation of Is MNs in a wild type background lead to a decrease in mEPSP amplitude compared to control larvae (Figure 4.4A), indicating the loss of the Is-derived mEPSP. Interestingly, we did not observe a decrease of mEPSP amplitude when ablating Is MNs in the *draper* mutant (Figure 4.4A). This may suggest an increase in postsynaptic glutamate receptor density at Ib NMJs, as the removal of Is normally leads to a decrease of overall mEPSP amplitude. Another parameter of spontaneous activity is the frequency of release. In a previous study, we found that Is ablation elevates mEPSP frequency of Ib MNs. Here, we confirmed the elevated spontaneous release, and interestingly, we found that ablation of Is MNs in *draper* mutants showed the same level of mEPSP frequency (Figure 4.4B), suggesting that Draper is not required for spontaneous release plasticity.

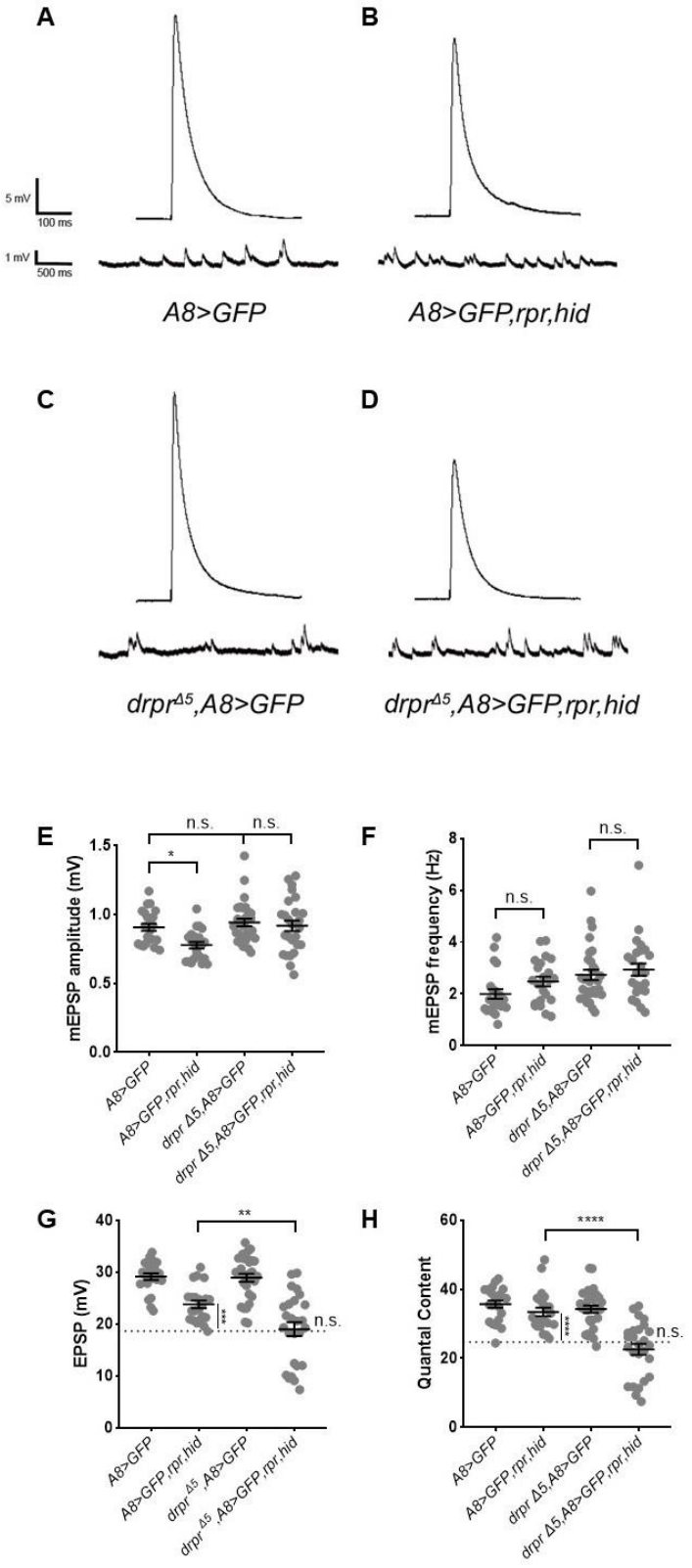

Figure 4.4 **Functional plasticity is impaired in *draper* mutants.**

Figure 4.4 (continued) (A-D) Representative traces of electrophysiological recordings of wild type (*A8>GFP*), Is ablated animals (*A8>GFP,rpr,hid*), *draper* mutants (*draper*$^{\Delta 5}$) and Is ablation in *draper* mutants (*draper*$^{\Delta 5}$*, A8>GFP,rpr,hid*). (E-H) Quantification of electrophysiological properties of wild type (*A8>GFP*), Is ablated animals (*A8>GFP,rpr,hid*), *draper* mutants (*draper*$^{\Delta 5}$) and Is ablation in *draper* mutants (*draper*$^{\Delta 5}$*, A8>GFP,rpr,hid*). (E) Quantification of mEPSP amplitude ($F_{(3,96)}$=3.056, overall p=0.0320, one-way ANOVA). (F) Quantification of mEPSP frequency ($F_{(3,96)}$=0.8153, overall p=0.4885, one-way ANOVA). (G) Quantification of EPSP ($F_{(3,96)}$=6.390, overall p=0.005, one-way ANOVA). Grey dashed line represents the baseline Ib EPSP. Comparison between Is ablated animals to baseline Ib EPSP: $t_{(32)}$=4.221, p=0.0002, unpaired t test. Comparison between Is ablation in *draper* mutant to baseline Ib EPSP: $t_{(36)}$=0.1714, p=0.8649, unpaired t test. (H) Quantification of QC ($F_{(3,96)}$=1.773, overall p=0.1575, one-way ANOVA). Grey dashed line represents the baseline Ib QC. Comparison between Is ablated animals with baseline Ib QC: $t_{(32)}$=3.981, p=0.0004, unpaired t test. Comparison between Is ablation in *draper* mutants with baseline Ib QC: $t_{(32)}$=0.8048, p=0.4262, unpaired t test. *p<0.05, **p<0.01, ***p<0.001, ****p<0.001. n (NMJs/larva) are 22/14, 22/11, 30/22, 26/15, respectively.

MNs also release neurotransmitter in response to action potentials. We examined changes in evoked neurotransmission after Is MN ablation in *draper* mutants. Surprisingly, we found no change in EPSP or QC when compared to the control Ib baseline EPSP and QC (Figure 4.4C-D), indicating Draper is required for Ib MN evoked neurotransmission plasticity. Taken together, these results suggest that (1) functional plasticity is significantly impaired in *draper* mutants, (2) compensation of spontaneous release and evoked release are likely regulated independently, and (3) Draper may also function in postsynaptic muscles to regulate glutamate receptor density.

4.3 Discussion

Cross-neuron plasticity is a new type of synaptic plasticity, and the underlying mechanisms are not known. In this study, we examined *Drosophila* Draper and validated its role in cross-neuron plasticity. My preliminary results suggest that Draper is required for clearance of neuronal debris generated by programmed cell death, and further, is essential for structural and

functional cross-neuron plasticity. This work provides an entry point to further characterize the downstream signaling cascade of cross-neuron plasticity.

4.3.1 Specific cell types are responsible for neuronal debris clearance through Draper

In this study, we found that Draper is required to remove neuronal debris in both the VNC and segmental nerves. In *draper* mutants, significant amounts of GFP positive debris remain. We reasoned that this is due to defective engulfment in the primary debris clearing cells of the nervous system. Glial cells are important for axonal debris engulfment in many injury models (Hsu et al., 2020; MacDonald et al., 2006; Wu et al., 2009), and we hypothesize that glial cells are responsible for clearance of Is debris after ablation. Future experiments to validate this model will utilize a glial specific driver, *Repo-GAL4*, to knock down *draper* with and without ablation of Is MNs. In addition, GAL4s that target glial cell subtypes will identify the specific glial cell type that requires Draper.

Interestingly, we noticed that in *draper* mutants, GFP positive debris are sometimes retained in specific cells, such as SPG in the segmental nerve and unknown cells in the VNC. These results suggest that additional cells may provide secondary debris clearance if the glia cannot efficiently remove the debris. It will be interesting to examine the molecular differences between the primary engulfment cells and the secondary cells with regards to debris clearance, and whether different pathways are utilized in the secondary cells. This Draper independent debris engulfment could enhance our knowledge of glial cell specialization and their unique function in nervous system development.

4.3.2 Draper mediates the glial cell response during axonal injury

In a previous study, Draper-JNK signaling is required in glial cells to efficiently remove axonal debris (McPhee et al., 2010; Purice et al., 2016). Activation of JNK signaling leads to the activation of the transcription factors dAP-1 and STAT92E which can trigger expression of genes involved in cell death/survival, proliferation, metabolism, and migration (Doherty et al., 2014; Hilu-Dadia et al., 2018; Lu et al., 2017; Purice et al., 2016). However, it is not understood how these glial responses will affect the glial cells themselves and the status of nearby healthy neurons. My preliminary results showed an essential role for Draper in cross-neuron plasticity. Loss of *draper* impairs neuronal debris clearance and structural and functional cross-neuron plasticity, thus providing a link between the Draper signaling pathway and the compensatory neuronal responses. However, a major gap of remains since the current study did not determine where Draper is required. In the neuromuscular system, Draper is expressed in muscles and glial cells so it is essential to distinguish the role of glial- and muscle-derived Draper (Draper et al., 2019; Fuentes-Medel et al., 2009; Fullard and Baker, 2014). Given that ablation of Is MNs in *draper* mutants leads to an increase in Ib mEPSP amplitude (no change in overall mEPSP amplitude when comparing *draper* mutants to the Is ablated *draper* mutants), we hypothesize that Draper may function in the muscle to modulate the excessive glutamate receptor expression or localization. Tissue specific *draper* knock down will allow us to tease apart the glial and muscle Draper function.

4.3.3 What is the ligand that Draper recognizes?

Phagocytotic removal of cells and cellular debris is essential for animal development and tissue homeostasis. In the *Drosophila* nervous system, Draper mediated phagocytosis is activated

by “eat-me” signals expressed in the degenerating neuron. Several molecules have been reported to function as “eat-me” signals, including Six-microns-under (SIMU) (Kurant et al., 2008), Pretaporter (Kuraishi et al., 2009), and phosphatidylserine (PS) (Ji et al., 2022; Mazaheri et al., 2014; Shacham-Silverberg et al., 2018; Tung et al., 2013). SIMU is required for efficient apoptotic cell clearance by glial cells. Genetic analysis showed that SIMU acts upstream of Draper and likely enables glial cells to recognize apoptotic neurons (Kurant et al., 2008). In addition, PS was found on injured axons of mouse neurons and on the severed dendrites of *Drosophila* SNs. Clearance of injured axons and dendrites requires Draper binding to PS (Ji et al., 2022; Mazaheri et al., 2014; Shacham-Silverberg et al., 2018; Tung et al., 2013). Additionally, another Draper ligand, Pretaporter, was found expressed in apoptotic cells but loss of *pretaporter* did not impair the clearance of the γ neurons during metamorphosis (Kuraishi et al., 2009). Therefore, SIMU and PS are potential ligands for Draper to recognize during cross-neuron plasticity. To test this hypothesis, we can ectopically express SIMU or induce PS exposure in Is MNs and examine whether the plasticity in Ib MNs is activated. Alternatively, we can generate *simu* mutations to test if cross-neuron plasticity is blocked as we observed in *draper* mutants.

In summary, this study generates an intriguing model that the Draper pathway mediates cross-neuron plasticity. However, additional research is needed to examine the Draper ligand, downstream mechanisms, and the corresponding synaptic changes in Ib MNs (see Chapter 5).

4.4 Methods and materials for Chapter 3 and Chapter 4

4.4.1 *Drosophila* and antibody resources

Drosophila strains used in Chapter 3 and 4 are listed in table 4.1. Antibodies used in Chapter 3 and 4 are listed in table 4.2.

4.4.2 Dissection and Immunocytochemistry

Embryonic dissections were performed as previously described (Ashley et al., 2019). Egg laying chambers were setup with adult flies (15-20 females and 10-15 males) and capped with grape juice plates (3% agar, 1.3% sucrose, 25% grape juice in water). After six-hour laying periods, grape plates covered in embryos were collected. Embryos were staged on double sided tape using the autofluorescence and shape of the gut under a Zeiss V20 stereoscope, and then dechorionated with a sharpened metal probe and placed on grape juice agar. Embryos were transferred to double-sided tape on a Superfrost Plus slide (ThermoFisher #22-037-246) with the dissecting area outlined by a PAP pen (Research Products International, #195506), and then covered with 0.22µm filtered phosphate buffered saline (PBS) (0.01M Sodium Phosphate, 150mM Sodium Chloride). Embryos were opened with an electrolytically sharpened tungsten wire, removed from the vitellin membrane and then adhered to the charged slide. Dissected embryos were washed once with PBS, and then fixed for 30 minutes at room temperature using 4% paraformaldehyde (Electron Microscopy Sciences). Samples were then washed three times in 0.05% PBST (PBS with 0.05% TritonX100), and then blocked for 1 hour in 5% normal goat serum (5% Goat serum diluted in 0.05% PBST). Samples were incubated in primary antibody solutions overnight at 4°C and washed three times in PBST. Samples were then incubated with secondary antibody solutions at room temperature for 2 hours and washed three times with

PBST. Samples were finally mounted in vectashield (Vector Laboratories) and the coverslip sealed with nail polish.

First and third instar larval dissections were performed as previously described (Ashley et al., 2019). Wandering third instar larvae were dissected in PBS on Sylgard-184 (Dow) dishes and pinned down using sharpened 0.1 mm Insect Pins (FST #26002-10). For first instar larvae, electrolytically sharpened tungsten pins were used to accommodate the size of smaller larvae. Samples were then fixed for 30 minutes using 4% paraformaldehyde (or 5 minutes in Bouin's solution for GluRIIA) and then transferred to 0.5 ml Eppendorf tubes. Samples were blocked and treated with primary and secondary antibodies as embryo samples above. All larval washes and antibody incubations were performed with mild agitation on a nutator.

4.4.3 Image Acquisition

All imaging was acquired on a Zeiss LSM800 confocal microscope with either a 20X plan-apo 0.8NA objective, a 40X plan-neofluar 1.3NA objective, or a 63X plan-apo 1.4NA objective. Laser intensity, pinhole and gain were adjusted to increase the signal but avoid overexposure. All samples from the same experiment were imaged under identical conditions. Representative images are the maximum projection of the corresponding confocal Z stack (ImageJ).

4.4.4 Image Analysis

dCE and vCE identification: Existence of vCE and dCE MNs (two Is type MNs) was confirmed in embryos and first instars. dCE was identified by the expression of GFP (*A8>GFP*), Eve and their positions in the ventral nerve cord (VNC). vCE motor neurons were identified by the

expression of GFP and their positions in the VNC. Final confirmation was done by identifying the muscle innervation patterns in larval abdominal hemisegments.

Ib bouton counting: Ib bouton counting was performed in third instar samples. Boutons were examined using HRP and scored as Is or Ib based on DLG signal, as Is boutons have a smaller and dimmer DLG signal than Ib boutons. Satellite boutons were identified as small bud-like structures emerging from "parent" boutons.

BRP and GluRIIA quantification: BRP and GluRIIA signals at Ib NMJs were quantified similar to (Han et al., 2020). Briefly, BRP and GluRIIA in Is NMJs were excluded in controls by using the GFP signal *(A8>GFP*) to create a surface boundary (Imaris, Oxford Instruments) and setting the BRP and GluRIIA signal intensities inside Is NMJs to zero. Next, a Ib NMJ surface was created based on the masked BRP, or GluRIIA, channel and the total intensities of HRP, DLG, and BRP or GluRIIA were collected. For normalization, *A8>hid,rpr* and control samples were normalized to corresponding mean control values. For BRP/HRP and GluRIIA/DLG ratios each sample was normalized to the sum intensity of either HRP or DLG, respectively.

4.4.5 Electrophysiology and Analysis

Current clamp recordings were performed as previously described (Meng et al., 2020). Third instar larvae were dissected in modified HL3 saline (70 mM NaCl, 5 mM KCl, 10 mM MgCl2, 10 mM NaHCO3, 5 mM Trehelose, 115 mM Sucrose, 5 mM HEPES) with 0.3 mM calcium. Segmental nerves were cut near the ventral nerve cord to remove VNC input and then the larval fillet was perfused with modified HL3 saline containing 0.5 mM calcium. Body-wall muscle 6, 12 or 4 in abdominal segment 3 were impaled with 15-30 MΩ sharp electrode filled with 3 M KCl and recorded for miniature excitatory postsynaptic potentials (mEPSPs) for 2

minutes. All mEPSP amplitudes from the same genotype were pooled together and binned with at 0.01mV increments to calculate the cumulative probability.

Nerves were drawn into a suction electrode and stimulated to elicit excitatory postsynaptic potentials (EPSPs). Specifically, for muscle 6 and 12 EPSP recording, the whole segmental nerve bundle was stimulated whereas for muscle 4 and muscle 11 EPSP recording, the intersegmental nerve (ISN) above muscle 5 was stimulated. For each muscle, 24 EPSPs were elicited at 0.2 Hz and the largest 12 EPSPs were averaged to indicate the mean EPSP (while measuring EPSPs in *A8>hid,rpr*, we sometimes observed smaller EPSPs, similar to (Lnenicka and Keshishian, 2000).

Due to non-linear summation of quantal units of large EPSPs, we calculated corrected EPSPs using the equation defined by (Martin, 1955) and elaborated by (Feeney et al., 1998). Quantal content (QC) was then calculated by dividing the corrected mean EPSP amplitude by the mean mEPSP amplitude for each muscle. Specifically, in genotypes where Ib and Is NMJs were both present, the mean of the smaller two thirds of mEPSP amplitudes was used to represent the Ib-derived mEPSP. This assumption was based on the published spontaneous frequencies of Ib and Is MNs (Newman et al., 2017). Then the Ib-derived EPSP was divided by the Ib-derived mEPSP amplitude to estimate the Ib-derived QC. Similarly, the Ib+Is EPSP was divided by the overall mEPSP amplitude to represent Ib+Is QC. Finally, the Ib-derived QC was normalized to the Ib+Is QC to indicate the estimated Ib baseline QC (Ib QC/Ib+Is QC).

Paired pulse recordings were performed under two-electrode voltage clamp configuration in modified HL3 saline with 0.5 mM calcium. A second sharp electrode with 10-15 MΩ resistance was used to inject current. Muscle 6 was clamped at -70 mV and the nerve was stimulated by two pulses 20 ms apart at 0.1 Hz. Only muscles with a leak current less than 10 nA

were subjected to analysis. Paired pulse ratios (EPSC2/EPSC1) were calculated by dividing the second EPSC by the first EPSC.

Signals were amplified using a MultiClamp 700B (Molecular Devices, MD) (for EPSP and mEPSP recordings) or a Geneclamp 500B (MD) (for paired pulse recordings) and digitized with a Digidata 1550B (MD). Stimulus was triggered via a Master-9 stimulator (A.M.P.I.). Data was acquired in pCLAMP 10 software (MD) and analyzed using Mini Analysis software (Synaptosoft).

4.4.6 GCaMP Imaging coupled with Electrophysiology

Third instar larvae of *MHC-CD8::GCaMP6f-Sh* were dissected in modified HL3 saline with 0.5 mM calcium and followed the same procedure of electrophysiology. Larval fillets were visualized using a Nikon FS microscope with a 40× long-working distance objective and GCaMP positive Ib and Is NMJs of muscle 6, 12 and 4 were illuminated by an Aura II solid state illuminator. Together with electrophysiology stimulation, each stimulus triggered a GCaMP firing event with the corresponding EPSP. GCaMP signals were scanned and recorded by a PCO Edge 4.2 camera and NIS element software. Electrophysiology data was collected as described above. Given that Ib MNs have a lower evoked threshold than Is MNs, stimulating voltage was tuned to isolate Ib alone firing events and Ib+Is firing events. If a stimulation only triggered CaMP firing event at Ib NMJs but not Is NMJs, the corresponding EPSP was counted as Ib alone EPSP. If a stimulation triggered GCaMP firing events at both Ib and Is NMJs, the corresponding EPSP was counted as Ib+Is EPSP. For each sample, Ib alone EPSPs and Ib+Is EPSPs were averaged respectively. Ib alone/Ib+Is was calculated by dividing the mean Ib alone EPSP by the mean Ib+Is EPSP of each sample.

4.4.7 Experimental design and statistical analysis

In all experiments, we included *A8>GFP* to ensure that Is NMJs were present in control animals. For experiments with *DIP-α*^{null}*;A8>GFP* larvae, males were selected as *DIP-α* is on the X chromosome. For *A8>GFP*/+ controls, males were also selected. All statistical analyses were performed using Prism 8 software (Graphpad). Average and standard error of the mean (SEM) are reported. Outliers are determined by Q-test and excluded from the sample pools. For each data point at least eight animals per genotype were dissected and at least two biological replicates were examined. All data was assumed to follow a Gaussian distribution. As we were making comparisons within specific target cells, and not between targets, most comparisons were performed by student t-test (Welch's correction was used in cases of unequal variance) or Kolmogorov-Smirnov test (K-S test). Comparisons between target cells was performed with one-way ANOVA followed by Tukey test.

Table 4.1 ***Drosophila* lines used in this study.**

Genotype	Source
w^{1118}	(Carrillo et al., 2015)
A8-GAL4	(Venkatasubramanian et al., 2019)
10XUAS-mCD8::GFP	BL#32184
10XUAS-mCD8::GFP,A8-GAL4	This study
DIP-α^{null}	(Xu et al., 2018)
UAS-hid,rpr	(Zhou et al., 1997)
UAS-TNT	BL#28838
MHC-CD8::GCaMP6f-Sh	(Newman et al., 2017)
$drpr^{\Delta 5}$	(Fuentes-Medel et al., 2009)

Table 4.2 **Antibodies used in this study.**

Antibody	Source
Rabbit anti-GFP	1:500, ThermoFisher #A11122
Chicken anti-GFP	1:500, ThermoFisher #A10262
Rabbit anti-Fas2	1:3,500, Budnik Lab (Koh et al., 1999)
Rabbit anti-DLG	1:40,000, Budnik Lab (Koh et al., 1999)
Mouse anti-DLG	1:100, 4F3, Developmental Studies Hybridoma Bank (DSHB)
Mouse anti-Eve	1:50, 3C10, Developmental Studies Hybridoma Bank (DSHB)
Mouse anti-Bruchpilot (BRP)	1:50, nc82, Developmental Studies Hybridoma Bank (DSHB)
Mouse anti-GluRIIA	1:50, 8B4D2, Developmental Studies Hybridoma Bank (DSHB)
Goat anti-HRP 405	1:50, Jackson Immunological Research #123-475-021
Goat anti-HRP-Alexa647	1:50, Jackson Immunological Research #123-605-021
Goat anti-Mouse-Alexa568	1:500, ThermoFisher #A11031
Goat anti-Chicken-Alexa488	1:500, ThermoFisher #A11039
Goat anti-Rabbit-Alexa405	1:500, ThermoFisher #A31556
Goat anti-Rabbit-Alexa568	1:500, ThermoFisher #A11036
Goat anti-Rabbit-Alexa647	1:500, ThermoFisher #A32733

CHAPTER 5

DISCUSSION AND FUTURE DIRECTIONS

5.1 Summary

Brain development is a complex process. Understanding how neurons recognize specific synaptic partners to form stereotyped neural circuits requires systematic knowledge about the function of wiring molecules expressed in these neurons. Furthermore, after establishing synaptic connections, neurons need to maintain robust synaptic function and counteract perturbations. My thesis work focused on two distinct but related areas: synaptic connectivity and synaptic plasticity. Specifically, in the first study, I asked how two *Drosophila* CSP subfamilies, the Dprs and DIPs, control synaptic recognition by profiling the expression patterns of *dprs* and *DIPs* using a collection of GAL4 driver lines. I described the expression map of *dprs* and *DIPs* in all *Drosophila* larval MNs, muscles, glial cells, and SNs with detailed precision. The diverse but unique expression patterns of *dprs* and *DIPs* allowed me to identify new MNs and revealed a wiring mechanism mediated by Dpr15. This work is recently accepted by the journal *Development* (Wang et al., 2021b).

Correct synaptic wiring builds the foundation for synaptic function. However, proper brain function also relies on synaptic plasticity that allows for alterations in activity, as required for learning and memory, or maintenance of brain homeostasis. A knowledge gap in the field of synaptic plasticity is whether and how neurons respond to injured neighbors. Using genetic ablation of specific MNs, we found that healthy neurons morphologically and functionally compensate for the loss of their neighbors, a process we termed as cross-neuron plasticity. This work was published in the *Journal of Neuroscience* in 2021 (Wang et al., 2021a). To delve into

the mechanisms underlying cross-neuron plasticity, I examined the Draper signaling pathway which has been implicated in clearance of axon debris during normal synaptic pruning and in response to axon injury. Indeed, I found that Draper is required to transmit a signal to nearby neurons to drive cross-neuron plasticity. I plan to submit a manuscript for this project later this year. Taken together, my Ph.D. work sets the stage for the field to examine Dpr-DIP mediated synaptic recognition and described a new form of synaptic plasticity that may be utilized in healthy neurons to detect and respond to circuit damage.

In the following sections, I discuss some outstanding questions in Dpr-DIP mediated synaptic recognition and Draper mediated cross-neuron plasticity and provide my thoughts about the approaches to address these questions.

5.2 Elucidating the role of Dprs and DIPs in synaptic development

Neurons recognize each other through the interactions between CSPs. The *Drosophila* Dprs and DIPs, two subfamilies of the IgSF, have recently been implicated in many aspects of neural development, including synaptic recognition, cell survival, synaptic growth, and synaptic maintenance (Ashley et al., 2019; Bornstein et al., 2021; Carrillo et al., 2015; Courgeon and Desplan, 2019; Menon et al., 2019; Sanes and Zipursky, 2020; Venkatasubramanian et al., 2019; Xu et al., 2019, 2022, 2018). Here, I discuss several open questions waiting for the field to answer.

5.2.1 Where do Dpr-DIP interactions occur?

As potential synaptic partner recognition molecules, Dprs and DIPs should localize to pre- and postsynaptic structures before synaptogenesis to guide recognition. Indeed, several

studies observed localization of Dprs and DIPs to dendritic and axon endings before circuit assembly (Ashley et al., 2019; Courgeon and Desplan, 2019). However, Dprs and DIPs are also observed at the cell body or along the axon (unpublished data), and we found that glial cells also express *dpr1*. These results suggest that Dpr-DIP pairs may interact at other locations in addition to synapses. Studies in the olfactory lobe found that knocking down *DIP-η* in Or47b ORNs lead to Or47b axon mistargeting into Or88a glomerulus without disrupting Or88a integrity (i.e., no ectopic synapses between Or47b ORNs and Or88a PNs) (Barish et al., 2018). Therefore, the mistargeting of Or47b axons caused by *DIP-η* knock down is likely due to defects of Or47b ORN axon sorting, implying a role of DIP-η in axon-axon or axon-glia interactions.

5.2.2 Could Dpr-DIP interactions negatively regulate synaptic recognition and synaptic growth?

During synaptic development, the default program may allow a neuron to make superfluous synapses. Some published evidence supports this model as CSPs not only instruct attractive interaction but also mediate repulsive signals or repress synaptic growth (Daiber et al., 2021; Hughes et al., 2007; Soba et al., 2007; Zarin et al., 2014; Zipursky and Grueber, 2013). The Dpr-DIP interactions are also multifaceted because some are absolutely required for specific synaptic partner recognition, whereas others may function as repressors of synaptic growth. At the larval NMJ, the recognition between the Is MN and m4 completely relies on the interaction between Dpr10 and DIP-α (Ashley et al., 2019). Disrupting the Dpr10-DIP-α interaction in any form impairs the m4-Is connection, suggesting the Dpr10-DIP-α interaction positively regulates m4-Is recognition. In addition, loss of this interaction leads to a partial decrease in innervation frequency of the Is MN on other muscles. However, preliminary data indicates that removing

other DIPs, such as *DIP-ζ*, *DIP-η*, or *DIP-θ,* in combination with *DIP-α*, restores the innervation frequency on all muscles except m4 (see Appendix B). This suggests that although the Dpr10-DIP-α interaction promotes the recognition between muscles and Is MN, other DIPs may act as negative regulators but are dominated by DIP-α in the wild type condition.

In addition, the Dpr11-DIP-γ interaction appears to repress synaptic growth as the lack of this interaction leads to the addition of immature satellite boutons on m4 (Carrillo et al., 2015). A similar phenotype is observed in the adult visual system where knocking down or overexpressing *DIP-β* or *DIP-γ* lead to ectopic synapse formation by the L cells (Xu et al., 2019). Taken together, these results suggest that Dpr-DIP interactions are more complicated than initially proposed. Dpr-DIP hetero- and homophilic interactions encompass 52 potential pairs but only a small subset has been examined. Future experiments will determine if other Dpr-DIP pairs are attractive, repulsive, or both depending on the context.

5.2.3 What are the underlying mechanisms of Dpr and DIP interactions?

Although many studies have examined the role of Dpr-DIP interactions, the underlying mechanism(s) remains unknown. Some insight in Dpr-DIP mediated signaling was revealed from experiments in the *Drosophila* NMJ. Genetic interaction tests showed that the Dpr11-DIP-γ interaction may regulate synaptic development through the BMP signaling pathway (Carrillo et al., 2015); however, we lack details about whether they interact directly or indirectly. Here, we discuss potential mechanisms underlying Dpr-DIP interactions.

Most Dprs and DIPs do not contain obvious transmembrane domains. Preliminary results from my colleagues, Meike Lobb-Rabe and Viola Nawrocka, showed that many Dprs and DIPs have a GPI anchor which can be cleaved by phospholipase C. These data suggest that Dprs and

DIPs may act as co-receptors or may even be released to the extracellular space. Previous interactome screens only focused on a subset of cell surface proteins so additional interactors may exist. For example, in (Özkan et al., 2013), the Zinn and Garcia labs examined 202 CSPs out of approximately 1000 CSPs encoded in the *Drosophila* genome. Therefore, Dprs and DIPs may interact directly with other CSPs and/or the interactions between Dprs and DIPs may recruit other CSPs to transmit a downstream signal. To identify new interactors, potential approaches include in vivo proximity labeling (Li et al., 2020), high-throughput interaction assays, immunoprecipitation/mass spectrometry, and yeast two-hybrid.

Extracellular vesicles (EVs) are a novel communication strategy to transmit signals or cellular contents between cells, including MNs and muscles (Ashley et al., 2018) and interneuronally (Vilcaes et al., 2021). Thus, EVs are another potential mechanism to convey Dpr-DIP interaction to the downstream intercellular signal. EVs are generated by invagination of a multivesicular body and contain cytosolic proteins, membrane associated proteins, and even RNAs, which were found to affect synaptic growth, synaptic function, and plasticity (Abels and Breakefield, 2016). One open question is whether EVs are non-selective or instead, targeted to specific cells (Mulcahy et al., 2014). CSPs are presented on the outer leaflet of EVs suggesting that CSP interactions may contribute to EV-target cell recognition. One interesting hypothesis is that Dpr-DIP interactions may guide, or promote, EV fusion to transfer intercellular signals without the need of a transmembrane domain. Profiling the membrane proteins in purified EVs derived from cultured neurons will provide insight into whether Dprs and DIPs are involved. If so, dampening the EV generation process may recapitulate some of the *dpr* and *DIP* mutant phenotypes.

5.3 How do Ib MNs respond to Draper mediated signals and Is ablation?

In Chapter 4, I demonstrated cross-neuron plasticity upon Is ablation and showed that Draper is involved in the signal transduction pathway. However, MNs do not form direct contacts with each other, suggesting that Draper mediated signals must be mediated through intermediate cells. In the Discussion section of Chapter 4, I proposed potential sites of Draper function, including muscles and glial cells. Notably, no matter where Draper is required, significant changes in Ib MNs accommodate the structural and functional plasticity that occurs after Is ablation. Here, I propose experiments to elucidate the detailed changes of Ib MNs.

5.3.1 Examining the transcriptome of Ib MNs upon Is ablation

Is ablation induced structural compensation in Ib MNs requires additional synaptic materials to be produced, or at least, to be transported into terminal boutons. It would be of great interest to examine the Ib MN transcriptome as it will reveal genes required for cross-neuron plasticity. To isolate Ib MNs in wild type and Is ablated animals, we can label Ib and Is MNs with different fluorescent proteins, followed by VNC dissociation and Fluorescence-activated cell sorting (FACS). Sorted Ib MN cell bodies can be subjected to bulk RNAseq or single cell RNAseq. We would expect to uncover up- or down- regulation of specific genes upon Is ablation. These genes can be further examined by loss-of-function and gain-of-function analyses in the Ib MNs together with Is ablation. Ideally, we could uncover a signal cascade in the Ib MNs as they respond to Is ablation. Similar approaches can also be used to examine the transcriptional changes in glial cells upon Is ablation.

5.3.2 Exploring the synaptic machinery of Ib NMJs

In addition to structural plasticity, Ib MNs also display significant changes of synaptic release, which can be regulated independent of transcription and translation. In addition to the systematic transcriptome profiling of Ib MNs, we can also take a bottom-up approach by examining known synaptic machinery components. For example, the increase of evoked neurotransmitter release could be due to an increase of Ca^{2+} channel abundance, and the increase of spontaneous release may be caused by a reduction of the spontaneous release inhibitor, Complexin (Cho et al., 2014; Choi et al., 2014). These proteins can be examined by endogenous tagging or antibody staining. If any changes in protein abundance or localization are observed, we can proceed to examine the upstream regulators of these proteins.

In addition to these synaptic machinery proteins, subcellular dynamics of synaptic vesicles are also under precise control and are highly tunable during synaptic plasticity. For example, the size of the readily releasable pool (RRP) was found to increase during PHP, thus leading to an increase in QC (Guan et al., 2020; Li et al., 2018a; Ruiz et al., 2011; Wang et al., 2016). In addition, the number of functional release sites and release probability (*Pr*) were found to decrease after application of an anesthetic drugs (Karunanithi et al., 2020a). Several methods can be used to examine the dynamics of synaptic vesicles. For example, focal macropatch recordings can specifically predict the number of functional release sites and *Pr* at individual synapses (Karunanithi et al., 2020b, 2020a, 2018). These parameters can also be measured by Ca^{2+} imaging which allows direct visualization of synaptic vesicle fusion (Akbergenova and Littleton, 2017; Newman et al., 2022, 2017; Peled et al., 2014). In addition, traditional dye fill experiments or electron microscopy can provide information about the size of RRP (Gaffield and

Betz, 2006; Hoopmann et al., 2012). Overall, if any of these factors change upon Is ablation, we can begin to examine upstream mechanisms.

5.4 Conclusions

My research in the *Drosophila* neuromuscular system uncovered fundamental mechanisms of neural development and plasticity. In the first part of my thesis work, the expression map of Dprs and DIPs greatly expands our knowledge of the spatial and temporal dynamics of these CSPs and provides insights to further examine their function. Specifically, the expression map can guide candidate selection, such as those commonly or differentially expressed Dprs and DIPs and can instruct examination of Dprs and DIPs that may act redundantly. In the second part of my work, I examined synaptic activity from individual inputs and demonstrated a new form of synaptic plasticity, which we named cross-neuron plasticity. We showed the potential for healthy neurons to compensate, both structurally and functionally, for the loss of damaged circuit components. Additionally, we characterized a key protein, Draper, as a component of the cross-neuron plasticity signaling pathway. The mechanisms underlying synaptic connectivity and plasticity revealed in the *Drosophila* neuromuscular circuit will benefit our understanding of vertebrate neural development, ageing, and the progression of neurodegenerative diseases.

APPENDIX A

Deficiency screen uncovers transcriptional regulators of *DIP-α*

Dpr-DIP interactions are implicated in multiple processes such as synaptic recognition, cell survival, and synaptic growth (Ashley et al., 2019; Bornstein et al., 2021; Carrillo et al., 2015; Courgeon and Desplan, 2019; Menon et al., 2019; Sanes and Zipursky, 2020; Venkatasubramanian et al., 2019; Xu et al., 2019, 2022, 2018). However, outstanding questions about Dprs and DIPs remain (see 1.2.4), including signaling pathways and mechanisms that regulate their expression. One approach to uncover upstream and downstream mechanisms is to identify genetic interactors.

Here, we conducted an F1 dominant modifier screen using the Bloomington Deficiency (Df) Kit to identify interactors in the Dpr10-DIP-α pathway. We previously showed that the Dpr10-DIP-α interaction is required for innervation of larval m4: loss of *DIP-α* or *dpr10* results in complete loss of m4-Is innervation (Ashley et al., 2019). Based on this phenotype, we created a transheterozygous sensitized background (*DIP-α-GAL4/+; UAS-2×EGFP/+; dpr10*^{null}*/+*) which expresses GFP in Is MNS; this sensitized line revealed a decrease to 50% m4-Is innervation (Figure A1). This sensitized background was combined with third chromosome Df lines, and the Is innervation frequency was scored on m13, m12, m4 and m3 (Figure A2.A-D). If a Df lines exacerbates or rescues the innervation defect on m4, we hypothesize that a gene within the Df may be part of the Dpr10/DIP-α pathway. Here, we found one Df line (BL#9226) that significantly decreased m4-Is innervation when combined in the sensitized background (Figure A2.D). Interestingly, we also observed many Df lines that rescue the defect of m4-Is innervation frequency (Figure A2.D). BL#9226 has a 900kb deletion that covers 25 genes. To map the loci of our gene(s) of interest, we conducted a sub-screen using additional Df lines that overlap with

the deletion in BL#9226 (Figure A3.A-B). We observed a similar decrease of m4-Is innervation frequency with one partially overlapping Df and proceeded to examine all genes with known neuronal function within this region, including Auxilin, Abstrakt, Complexin, Vps24, Huckebein, Contactin, Tube, Lost, 5-HT2A, Spartin, Opa and Ctrip. We found that partial loss of *huckebein* (*hkb*) in the sensitized background significantly decreased m4-Is innervation (Figure A3.C), suggesting *hkb* genetically interacts with *dpr10* or *DIP-α*.

Next, we asked how *hkb* may interact with *dpr10* or *DIP-α*. Hkb is a hox gene expressed in a subset of neurons, including the dorsal Is MN that innervates m4 and expresses *DIP-α* (Bossing et al., 1996; Brönner and Jäckle, 1996; Chu-LaGraff et al., 1995; Lundell et al., 1996). Hkb is known to control the expression of a transcriptional repressor, Eve, specifically in the dorsal Is MN (also known as RP2) and is required for RP2 fate determination and pathfinding (Bossing et al., 1996). We hypothesized that Hkb is part of the regulatory mechanism that instructs *DIP-α* expression. To test this model, I combined an endogenously tagged *DIP-α* (*DIP-α-EGFP*) with different *hkb* mutants to examine *DIP-α* expression. *hkb* mutants are lethal by embryonic stage 16 so we examined embryonic stage 15. In control animals, we observed expression of DIP-α-EGFP in the Eve positive RP2 MN and the Eve negative RP5 MN (Figure A4.A). Surprisingly, two different *hkb* mutants showed a complete loss of *DIP-α* expression in RP2, but not in RP5, suggesting that Hkb controls *DIP-α* expression specifically in RP2 (Figure A4.B-C). This result correlates with the m4 innervation defects we observed in *hkb*, *DIP-α*, *dpr10* triple heterozygotes.

Taken together, we found that the transcription factor Hkb is required for *DIP-α* expression specifically in RP2. Further studies are required to examine how Hkb controls RP2 pathfinding, and to explore how Hkb regulates *DIP-α* expression.

Materials and Methods

Drosophila and antibody resources

Drosophila lines used for screen is listed in Table A1. Other lines used in this study are: *DIP-α>GAL4; UAS-2×EGFP/CyO* (sensitized line)*; DIP-α-EGFP*(Ashley et al., 2019)*; dpr10^{null}/TM6,Tb*; *hkb$^{[A321A1]}$/TM6* (BL#2059)*; hkb^{2}/TM6* (BL#5457)*;* Antibodies used in this study is listed in Table A2.

Deficiency screen

Males from each Df line were crossed to females from the sensitized line and 6-30 larvae were dissected and analyzed for Is innervation of m13, m12, m4 and m3. If any boutons were observed on respective muscles, then it is scored as "1", otherwise "0". Analyses were performed on A2-A6. Significant threshold was determined by Chi-square test.

Dissection and immunostaining

Dissection and immunostaining were performed as previous described in Chapter 2-4 unless otherwise noted.

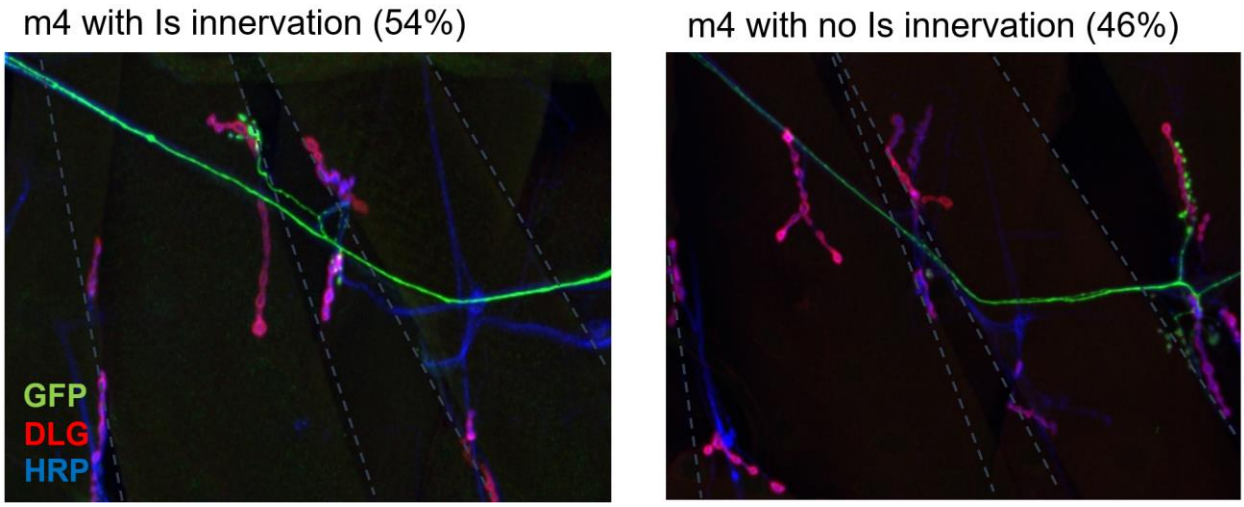

Figure A1 **m4-Is innervation frequency is approximately 50% in the sensitized background.**
Representative images stained with GFP (green), DLG (red), and HRP (blue) in sensitized background (*DIP-α>GAL4/+; UAS-2×EGFP/+; dpr10^{null}/+*), showing m4 with Is MN innervation (left) and m4 without Is innervation (right).

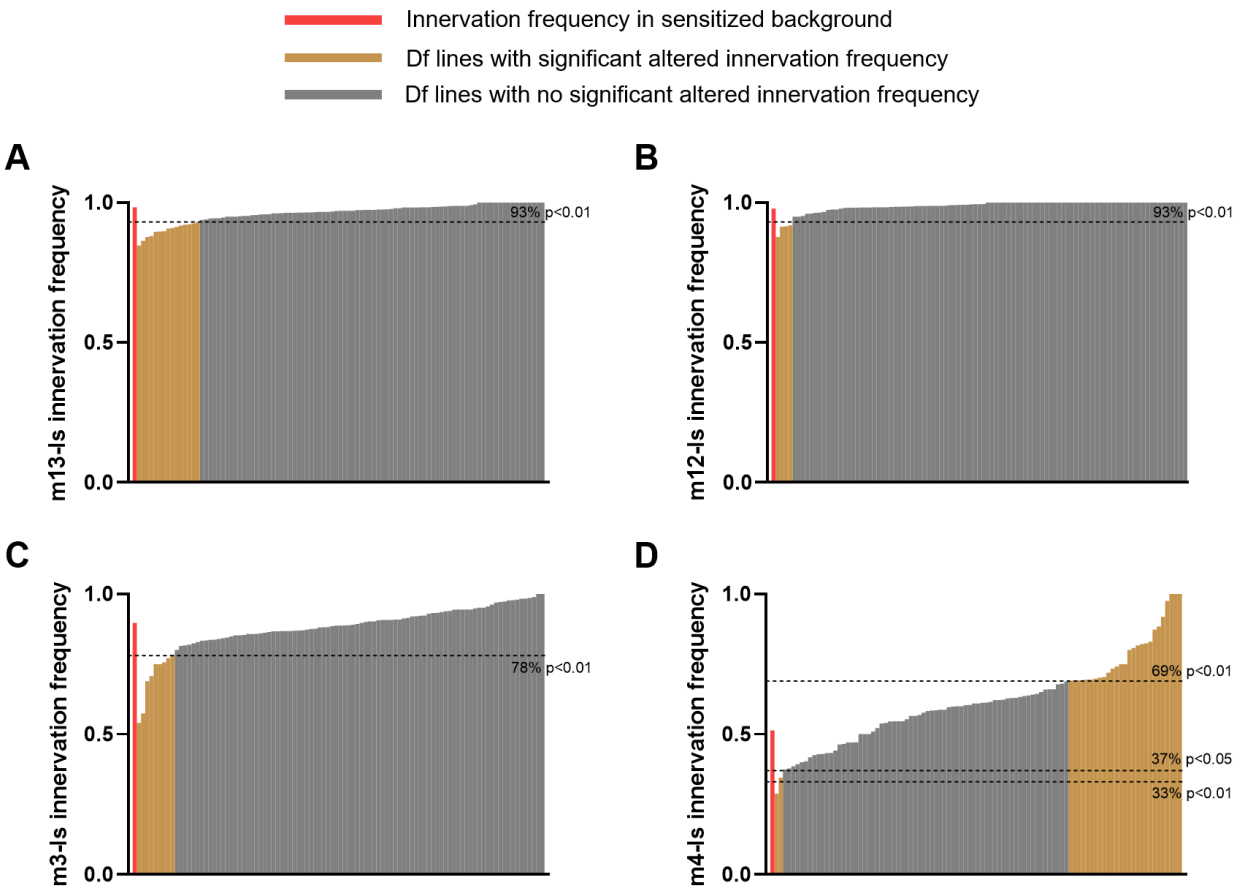

Figure A2 **Innervation frequency of screened Df lines.**
(A-D) Innervation frequency of m13-Is (A), m12-Is (B), m3-Is (C) and m4-Is (D) when combining the Df line with the sensitized background. Each column represents one Df line. Grey dashed lines represent significance threshold. Chi-square test, threshold is set at p=0.05, p=0.01.

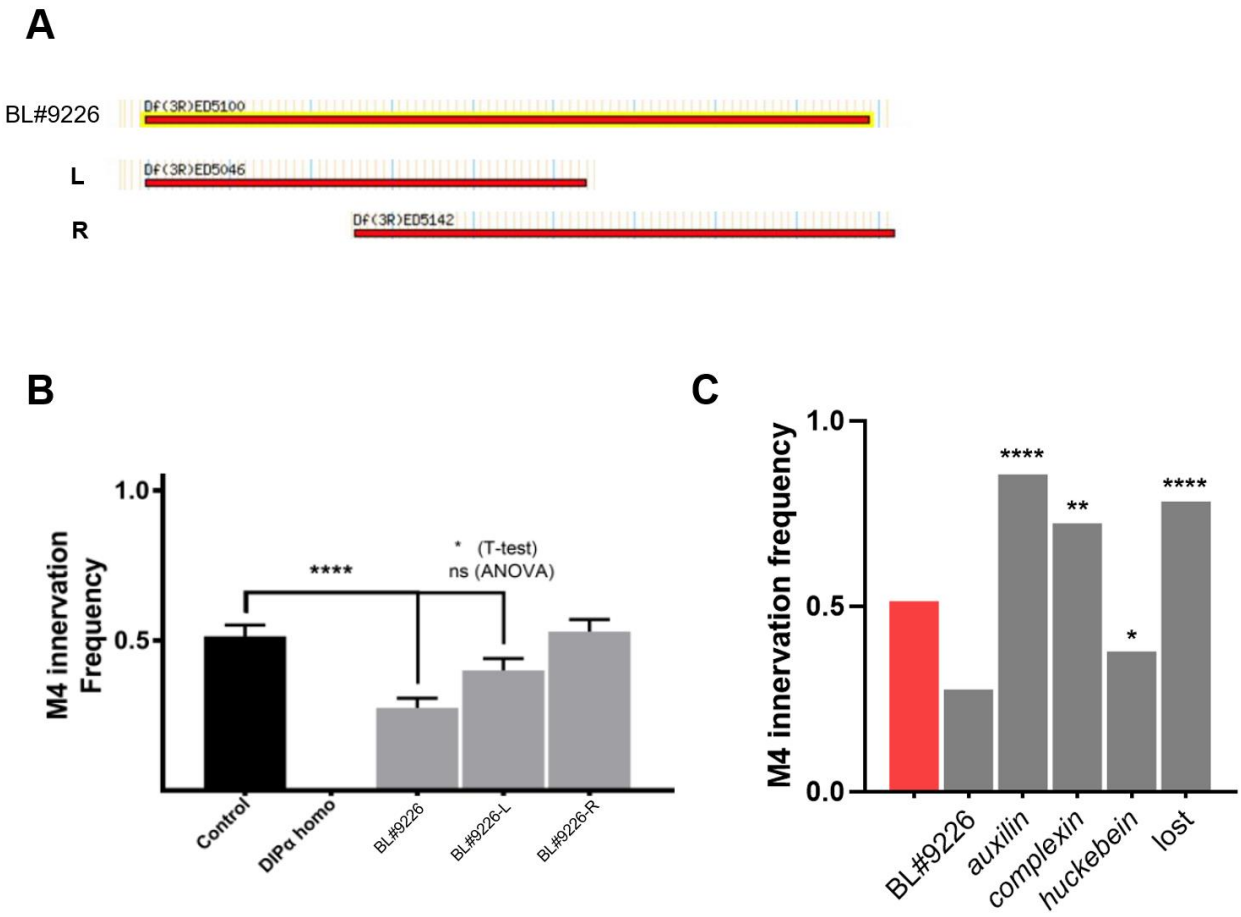

Figure A3 **Sub-screen of BL#9226 identifies the *DIP-α* genetic interactor, *hkb*.**
(A) Schematic showing the region of the Df deletion and the overlapping Df lines (L and R). (B) Sub-screen of overlapping Df lines found that the left Df also shows a decrease of m4-Is innervation frequency. (C) Sub-screen of individual genes found that *hkb* is a genetic interactor of *dpr10* or *DIP-α*. Interestingly, other mutations, including *auxilin*, *complexin* and *lost*, could rescue the decrease of m4-Is innervation. Chi-square test, *p<0.05, **p<0.01, ****p<0.0001.

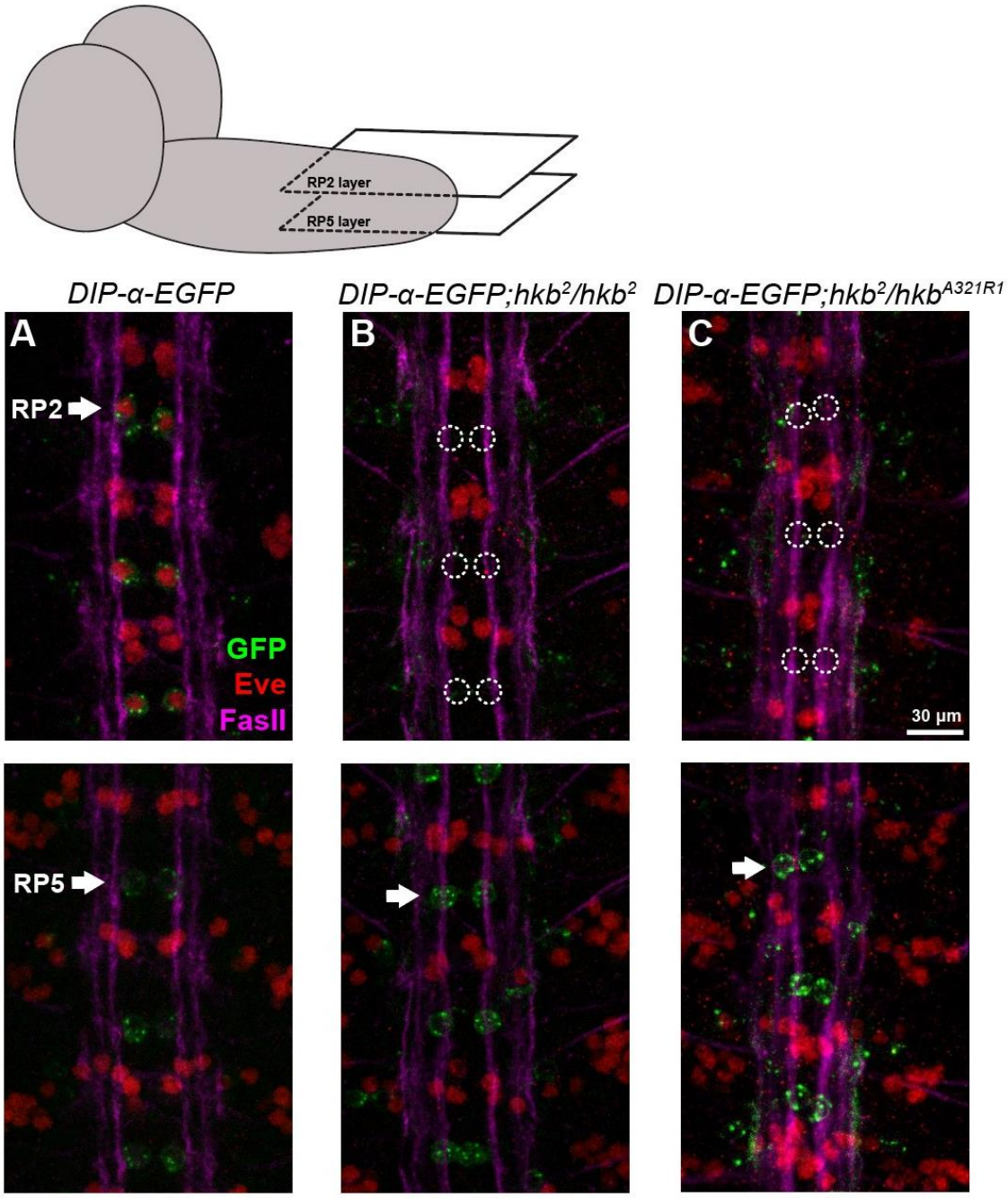

Figure A4 **Expression of DIP-α-EGFP in *hkb* mutants.**
(A-C) Representative images showing DIP-α-EGFP (green), Eve (red), and FasII (magenta) in control (*DIP-α-EGFP*), hkb^{2} mutant (*DIP-α-EGFP;* hkb^{2}/hkb^{2}), and hkb^{2}/hkb^{A321R1} (*DIP-α-EGFP;* hkb^{2}/hkb^{A321R1}). In control animals, DIP-α-EGFP is expressed in both RP2 and RP5 by stage 15, highlighted by arrows (A). In *hkb* mutants, DIP-α-EGFP is no longer expressed in RP2. Also, Eve staining is lost in RP2 (marked by dashed circles), and DIP-α-EGFP expression in RP5 is not affected (highlighted by arrows in B and C).

Table A1 **Df lines used in this study.**

BL Number or targeted gene	Genotype
1842	*Df(3R)Antp17/TM3, Sb[1] Ser[1]*
1990	*Df(3R)Tpl10, Dp(3;3)Dfd[rv1], kni[ri-1] Dfd[rv1] p[p] Doa[10]/TM3, Sb[1]*
2352	*Df(3R)X3F, P{ry[+t7.2]=RP49}mtg[P2] e[1]/MKRS*
2596	*Df(3L)6B-29+Df(3R)6B-29, kni[ri-1] p[p]/TM3, Ser[1]*
2597	*Df(3R)10-65, kni[ri-1] p[p]/TM3, Ser[1]*
3486	*Df(3R)Ubx109/Dp(3;3)P5*
6962	*w[1118]; Df(3R)ED2, P{w[+mW.Scer\FRT.hs3]=3'.RS5+3.3'}koko[ED2]/TM6C, cu[1] Sb[1]*
7443	*Df(3R)BSC47, st[1] ca[1]/TM3, P{w[+m*]=Ubx-lacZ.w[+]}TM3, Sb[1]*
8029	*w[1118]; Df(3R)ED5577, P{w[+mW.Scer\FRT.hs3]=3'.RS5+3.3'}ED5577/TM6C, cu[1] Sb[1]*
8103	*w[1118]; Df(3R)ED5177, P{w[+mW.Scer\FRT.hs3]=3'.RS5+3.3'}ED5177/TM6C, cu[1] Sb[1]*
8105	*w[1118]; Df(3R)ED6232, P{w[+mW.Scer\FRT.hs3]=3'.RS5+3.3'}ED6232/TM6C, cu[1] Sb[1]*
8684	*w[1118]; Df(3R)ED6096, P{w[+mW.Scer\FRT.hs3]=3'.RS5+3.3'}ED6096/TM6C, cu[1] Sb[1]*
8685	*w[1118]; Df(3R)ED7665, P{w[+mW.Scer\FRT.hs3]=3'.RS5+3.3'}ED7665/TM6C, cu[1] Sb[1]*
8957	*w[1118]; Df(3R)ED5514, P{w[+mW.Scer\FRT.hs3]=3'.RS5+3.3'}ED5514/TM6C, cu[1] Sb[1]*
8964	*w[1118]; Df(3R)ED6025, P{w[+mW.Scer\FRT.hs3]=3'.RS5+3.3'}ED6025/TM6C, cu[1] Sb[1]*
8965	*w[1118]; Df(3R)ED5156, P{w[+mW.Scer\FRT.hs3]=3'.RS5+3.3'}ED5156/TM6C, cu[1] Sb[1]*
9077	*w[1118]; Df(3R)ED5330, P{w[+mW.Scer\FRT.hs3]=3'.RS5+3.3'}ED5330/TM6C, cu[1] Sb[1]*
9082	*w[1118]; Df(3R)ED5474, P{w[+mW.Scer\FRT.hs3]=3'.RS5+3.3'}ED5474/TM6C, cu[1] Sb[1]*
9084	*w[1118]; Df(3R)ED5518, P{w[+mW.Scer\FRT.hs3]=3'.RS5+3.3'}ED5518/TM6C, cu[1] Sb[1]*
9090	*w[1118]; Df(3R)ED5644, P{w[+mW.Scer\FRT.hs3]=3'.RS5+3.3'}ED5644/TM6C, cu[1] Sb[1]*
9152	*w[1118]; Df(3R)ED5705, P{w[+mW.Scer\FRT.hs3]=3'.RS5+3.3'}ED5705/TM3, Ser[1]*
9204	*w[1118]; Df(3R)ED5339, P{w[+mW.Scer\FRT.hs3]=3'.RS5+3.3'}ED5339/TM6C, cu[1] Sb[1]*
9210	*w[1118]; Df(3R)ED6255, P{w[+mW.Scer\FRT.hs3]=3'.RS5+3.3'}ED6255/TM6C, cu[1] Sb[1]*
9211	*w[1118]; Df(3R)ED6220, P{w[+mW.Scer\FRT.hs3]=3'.RS5+3.3'}ED6220/TM6C, cu[1] Sb[1]*
9226	*w[1118]; Df(3R)ED5100, P{w[+mW.Scer\FRT.hs3]=3'.RS5+3.3'}ED5100/TM6C, cu[1] Sb[1]*

Table A1 continued

9227	*w[1118]; Df(3R)ED5428, P{w[+mW.Scer\FRT.hs3]=3'.RS5+3.3'}ED5428/TM6C, cu[1] Sb[1]*
9481	*w[1118]; Df(3R)ED10639, P{w[+mW.Scer\FRT.hs3]=3'.RS5+3.3'}ED10639/TM6C, cu[1] Sb[1]*
9482	*w[1118]; Df(3R)ED10642, P{w[+mW.Scer\FRT.hs3]=3'.RS5+3.3'}ED10642/TM6C, cu[1] Sb[1]*
9487	*w[1118]; Df(3R)ED10845, P{w[+mW.Scer\FRT.hs3]=3'.RS5+3.3'}ED10845/TM6C, cu[1] Sb[1]*
24137	*w[1118]; Df(3R)ED5664, P{w[+mW.Scer\FRT.hs3]=3'.RS5+3.3'}ED5664/TM6C, cu[1] Sb[1]*
24139	*w[1118]; Df(3R)ED5938, P{w[+mW.Scer\FRT.hs3]=3'.RS5+3.3'}ED5938/TM6C, cu[1] Sb[1]*
24142	*w[1118]; Df(3R)ED6346, P{w[+mW.Scer\FRT.hs3]=3'.RS5+3.3'}ED6346/TM6C, cu[1] Sb[1]*
24143	*w[1118]; Df(3R)ED6361, P{w[+mW.Scer\FRT.hs3]=3'.RS5+3.3'}ED6361/TM6C, cu[1] Sb[1]*
24516	*w[1118]; Df(3R)ED50003, P{w[+mW.Scer\FRT.hs3]=3'.RS5+3.3'}ED50003/TM6C, cu[1] Sb[1]*
24909	*w[1118]; Df(3R)BSC321/TM6C, Sb[1] cu[1]*
24965	*w[1118]; Df(3R)BSC461/TM6C, Sb[1] cu[1]*
24968	*w[1118]; Df(3R)BSC464/TM6C, Sb[1] cu[1]*
24970	*w[1118]; Df(3R)BSC466/TM6C, Sb[1] cu[1]*
24971	*w[1118]; Df(3R)BSC467/TM6C, Sb[1] cu[1]*
24973	*w[1118]; Df(3R)BSC469/TM6C, Sb[1] cu[1]*
24980	*w[1118]; Df(3R)BSC476/TM6C, Sb[1] cu[1]*
24983	*w[1118]; Df(3R)BSC479/TM6C, Sb[1] cu[1]*
24990	*w[1118]; Df(3R)BSC486/TM6C, Sb[1] cu[1]*
24993	*w[1118]; Df(3R)BSC489/TM6C, Sb[1] cu[1]*
25001	*w[1118]; Df(3R)BSC497/TM6C, Sb[1] cu[1]*
25005	*w[1118]; Df(3R)BSC501/TM6C, Sb[1] cu[1]*
25006	*w[1118]; Df(3R)BSC502/TM6C, Sb[1] cu[1]*
25007	*w[1118]; Df(3R)BSC503/TM6C, Sb[1] cu[1]*
25008	*w[1118]; Df(3R)BSC504/TM6C, Sb[1] cu[1]*
25011	*w[1118]; Df(3R)BSC507/TM6C, Sb[1] cu[1]*
25019	*w[1118]; Df(3R)BSC515/TM6C, Sb[1] cu[1]*
25075	*w[1118]; Df(3R)BSC547/TM6C, Sb[1]*
25077	*w[1118]; Df(3R)BSC549/TM6C, Sb[1]*
25390	*w[1118]; Df(3R)BSC567/TM6C, Sb[1]*
25694	*w[1118]; Df(3R)BSC619/TM6C, cu[1] Sb[1]*
25695	*w[1118]; Df(3R)BSC620/TM6C, cu[1] Sb[1]*
25696	*w[1118]; Df(3R)BSC621/TM6C, cu[1] Sb[1]*
25724	*w[1118]; Df(3R)BSC633/TM6C, cu[1] Sb[1]*
25740	*w[1118]; Df(3R)BSC650/TM6C, Sb[1] cu[1]*

Table A1 continued

26529	*w[1118]; Df(3R)BSC677, P+PBac{w[+mC]=XP3.WH3}BSC677/TM6C, Sb[1] cu[1]*
26533	*w[1118]; Df(3R)BSC681, P+PBac{w[+mC]=XP3.RB5}BSC681/TM6C, Sb[1] cu[1]*
26580	*w[1118]; Df(3R)BSC728, P+PBac{w[+mC]=XP3.RB5}BSC728/TM6C, Sb[1] cu[1]*
26836	*w[1118]; Df(3R)BSC738/TM6C, Sb[1] cu[1]*
26839	*w[1118]; Df(3R)BSC741/TM6C, Sb[1] cu[1]*
26846	*w[1118]; Df(3R)BSC748, P+PBac{w[+mC]=XP3.WH3}BSC748/TM6C, Sb[1] cu[1]*
26847	*w[1118]; Df(3R)BSC749, P+PBac{w[+mC]=XP3.WH3}BSC749/TM6C, Sb[1] cu[1]*
26848	*w[1118]; Df(3R)BSC750/TM6C, Sb[1] cu[1]*
27362	*w[1118]; Df(3R)BSC790, P+PBac{w[+mC]=XP3.WH3}BSC790/TM6C, Sb[1] cu[1]*
27365	*w[1118]; Df(3R)BSC793/TM6C, Sb[1] cu[1]*
27404	*w[1118]; Df(3R)FDD-0317950/TM6C, Sb[1] cu[1]*
27580	*w[1118]; Df(3R)BSC819, P+PBac{w[+mC]=XP3.RB5}BSC819/TM6C, Sb[1] cu[1]*
29667	*w[1118]; Df(3R)ED6280, P{w[+mW.Scer\FRT.hs3]=3'.RS5+3.3'}ED6280/TM6C, cu[1] Sb[1]*
29997	*w[1118]; Df(3R)BSC874, P+PBac{w[+mC]=XP3.WH3}BSC874/TM6C, Sb[1] cu[1]*
64425	*w[*]; Df(3R)ED10555, P{w[+mW.Scer\FRT.hs3]=3'.RS5+3.3'}ED10555/P{ry[+t7.2]=neoFRT}82B P{w[+mC]=ovoD1-18}3R/TM3, Sb[1]*
7633	*w[1118]; Df(3R)Exel6154, P{w[+mC]=XP-U}Exel6154/TM6B, Tb[1]*
7634	*w[1118]; Df(3R)Exel6155, P{w[+mC]=XP-U}Exel6155/TM6B, Tb[1]*
7638	*w[1118]; Df(3R)Exel6159, P{w[+mC]=XP-U}Exel6159/TM6B, Tb[1]*
7675	*w[1118]; Df(3R)Exel6196, P{w[+mC]=XP-U}Exel6196/TM6B, Tb[1]*
7676	*w[1118]; Df(3R)Exel6197, P{w[+mC]=XP-U}Exel6197/TM6B, Tb[1]*
7680	*w[1118]; Df(3R)Exel6201, P{w[+mC]=XP-U}Exel6201/TM6B, Tb[1]*
7681	*w[1118]; Df(3R)Exel6202, P{w[+mC]=XP-U}Exel6202/TM6B, Tb[1]*
7682	*w[1118]; Df(3R)Exel6203, P{w[+mC]=XP-U}Exel6203/TM6B, Tb[+]*
7692	*w[1118]; Df(3R)Exel6214, P{w[+mC]=XP-U}Exel6214/TM6B, Tb[1]*
7731	*w[1118]; Df(3R)Exel6264, P{w[+mC]=XP-U}Exel6264/TM6B, Tb[+]*
7737	*w[1118]; Df(3R)Exel6270, P{w[+mC]=XP-U}Exel6270/TM6B, Tb[1]*
7739	*w[1118]; Df(3R)Exel6272, P{w[+mC]=XP-U}Exel6272/TM6B, Tb[1]*
7983	*w[1118]; Df(3R)Exel7328/TM6B, Tb[+]*
7997	*w[1118]; Df(3R)Exel7378/TM6B, Tb[1]*
9497	*w[1118]; Df(3R)BSC137/TM6B, Tb[+]*
9500	*w[1118]; Df(3R)BSC140/TM6B, Tb[+]*
9501	*w[1118]; Df(3R)BSC141/TM6B, Tb[+]*
30592	*w[1118]; Df(3R)BSC887/TM6B, Tb[+]*

Table A1 continued

9347	*w[1118]; Df(3R)ED6187, P{w[+mW.Scer\FRT.hs3]=3'.RS5+3.3'}ED6187/TM2*
8923	*w[1118]; Df(3R)ED6085, P{w[+mW.Scer\FRT.hs3]=3'.RS5+3.3'}ED6085/TM2*
7413	*Df(3R)BSC43, st[1] ca[1]/TM2, p[p]*
8104	*w[1118]; Df(3R)ED5780, P{w[+mW.Scer\FRT.hs3]=3'.RS5+3.3'}ED5780/TM2*
9208	*w[1118]; Df(3R)ED5815, P{w[+mW.Scer\FRT.hs3]=3'.RS5+3.3'}ED5815/TM2*
25021	*w[1118]; Df(3R)BSC517/TM2*
37537	*w[1118]; Df(3R)ED5623, P{w[+mW.Scer\FRT.hs3]=3'.RS5+3.3'}ED5623/TM2*
8967	*y[*] w[1118]/Dp(1;Y)y[+]; Df(3R)ED5147, P{w[+mW.Scer\FRT.hs3]=3'.RS5+3.3'}ED5147/TM6C, cu[1] Sb[1]*
1467	*Dp(3;1)P115/+; Df(3R)P115, e[11]/TM1, Sb*
2155	*Df(3R)A113/In(3R)C, Sb[1] cd[1] Tb[1] ca[1]; Dp(3;1)34*
2234	*Df(3R)R133, B[S]/TM3, Sb[1]; Dp(3;1)124P*
3547	*Df(3R)L127/TM6; Dp(3;1)B152*
6367	*Df(3R)slo3/MKRS; Dp(3;2)slo3/+*
auxilin	*w[*]; aux[D128]/TM6B, P{w[+mW.hs]=Ubi-GFP.S65T}PAD2, Tb[1]*
abstrakt	*P{ry[+t7.2]=PZ}abs[00620] ry[506]/TM3, ry[RK] Sb[1] Ser[1]*
complexin	*y[1] w[*]; Mi{y[+mDint2]=MIC}cpx[MI00784]/TM3, Sb[1] Ser[1]*
vps24	*y[1] w[67c23]; P{w[+mC] y[+mDint2]=EPgy2}Vps24[EY04708]/TM3, Sb[1] Ser[1]*
huckebein	*hkb[A321R1]/TM3, Sb[1] Ser[1]*
contactin	*w[1118]; P{w[+mC]=EP}Cont[G5080]/TM6C, Sb[1]*
tube	*y[1] w[67c23]; P{w[+mC] y[+mDint2]=EPgy2}tub[EY12337]*
tube	*st[1] tub[2] e[1]/TM8, l(3)DTS4[1]*
tube	*y[1] sc[*] v[1] sev[21]; P{y[+t7.7] v[+t1.8]=TRiP.HMS05426}attP40*
lost	*y[1] w[67c23]; P{w[+mC] y[+mDint2]=EPgy2}lost[EY11645]*
5-HT2A	*y[1] w[*]; Mi{y[+mDint2]=MIC}5-HT2A[MI03299]*
spartin	*y[1] sc[*] v[1] sev[21]; P{y[+t7.7] v[+t1.8]=TRiP.HMS01641}attP40*
opa	*opa[tsl25]/TM3, Sb[1]*
ctrip	*y[1] w[*]; Mi{y[+mDint2]=MIC}ctrip[MI14762]/TM3, Sb[1] Ser[1]*

Table A2 **Antibodies used in this study.**

Antibody	Concentration and Source
Rabbit anti-GFP	1:40k, gift from Michael Glozter, University of Chicago
Rabbit anti-Eve	1:1000, gift from Ellie Heckscher, University of Chicago
Mouse anti-DLG	1:100, Developmental Studies Hybridoma Bank 4F3
Mouse anti-FasII	1:100, Developmental Studies Hybridoma Bank 1D4
Goat anti-Rabbit Alexa 488	1:500, Invitrogen A11008
Goat anti-Rabbit Alexa 568	1:500, Invitrogen A11036
Goat anti-Mouse Alexa 568	1:500, Invitrogen A11031
Goat anti-Mouse Alexa 647	1:500, Invitrogen A32728
Goat anti-HRP Alexa 647	1:100, Jackson Immunological Research 123-605-021
Goat anti-HRP Alexa 405	1:100, Jackson Immunological Research 123-475-021

APPENDIX B

Examining the redundancy of DIPs in Is MN innervation

A previous study from our lab found that Dpr10-DIP-α interactions are required for m4-Is innervation. Loss of *DIP-α* in Is MNs lead to a complete loss of Is innervation on m4, but only partial loss of Is innervation on other muscles, including m12, m13 and m3, suggesting redundant mechanisms are required for Is innervation on these muscles (Ashley et al., 2019). From the expression map of *dprs* and *DIPs* (Chapter 3), we found that Is MNs express several *DIPs*, including *DIP-γ, -ε, -ζ, -η, -θ* and *-κ*. We hypothesized that some of these DIPs act redundantly with DIP-α to instruct Is MN-muscle recognition. Here, we focused on DIP-ζ, -η and -θ as they are expressed at high levels in Is MNs. We generated a series of mutations including single, double, triple or quadruple knock outs of different *DIP-α, -ζ, -η* and *-θ* combinations, and examined the Is innervation frequency on m13, m12, m4 and m3.

We found that simultaneous loss of *DIP-η* and *DIP-θ*, or *DIP-η*, *DIP-θ*, and *DIP-ζ* do not affect the innervation frequency of all four muscles compared to controls (Figure B1.A-D, dark grey bars), in contrast to the *DIP-α* single mutant. Interestingly, when we combined the *DIP-α* mutant with other *DIP* mutants, we observed two phenotypes. For m3 and m4, which are innervated by dCE, the other *DIPs* are not involved in MN-muscle recognition (Figure B1.A-B), as in the double mutant of *DIP-α* and *DIP-θ*, the triple mutant of *DIP-α*, *DIP-η* and *DIP-θ*, or the quadruple mutant of *DIP-α*, *DIP-η*, *DIP-θ* and *DIP-ζ*, m3-Is and m4-Is innervation frequencies are the same as in the *DIP-α* single mutant. Conversely, for m12 and m13, which are innervated by vCE, other *DIPs* are involved (Figure B1.C-D), as in the double mutant of *DIP-α* and *DIP-θ*, the triple mutant of *DIP-α*, *DIP-η* and *DIP-θ*, or the quadruple mutant of *DIP-α*, *DIP-η*, *DIP-θ*

and *DIP-ζ*, m12-Is and m13-Is innervation frequency are significantly rescued compared to *DIP-α* single mutant.

These results suggest that (1) different DIPs may act in the same pathway to control MN-muscle recognition; (2) different MNs may utilize different mechanisms. Further experiments including MN specific knock down or MN specific rescue are required to tease apart the unique functions of each DIP.

Material and method

Drosophila and antibody resources

Drosophila lines used in this study are: *DIP-α*$^{7\text{-}1}$; *DIP-η/θ-Df*; *DIP-ζ*^{CR} (generated by Dr. James Ashley); *DIP-η/θ-Df*, *DIP-ζ*^{CR} (generated by Dr. James Ashley); *A8-GAL4,10XUAS-GFP*. Antibodies used in this study are: Mouse anti-DLG (1:100, Developmental Studies Hybridoma Bank 4F3); Rabbit anti-GFP (1:40k, gift from Michael Glozter, University of Chicago); Goat anti-Mouse Alexa 568 (1:500, Invitrogen A11031); Goat anti-Rabbit Alexa 488 (1:500, Invitrogen A11008); Goat anti-HRP Alexa 647 (1:100, Jackson Immunological Research 123-605-021).

Dissection and immunostaining

Dissection and immunostaining were performed as previous described in Chapter 2-4 unless otherwise noted.

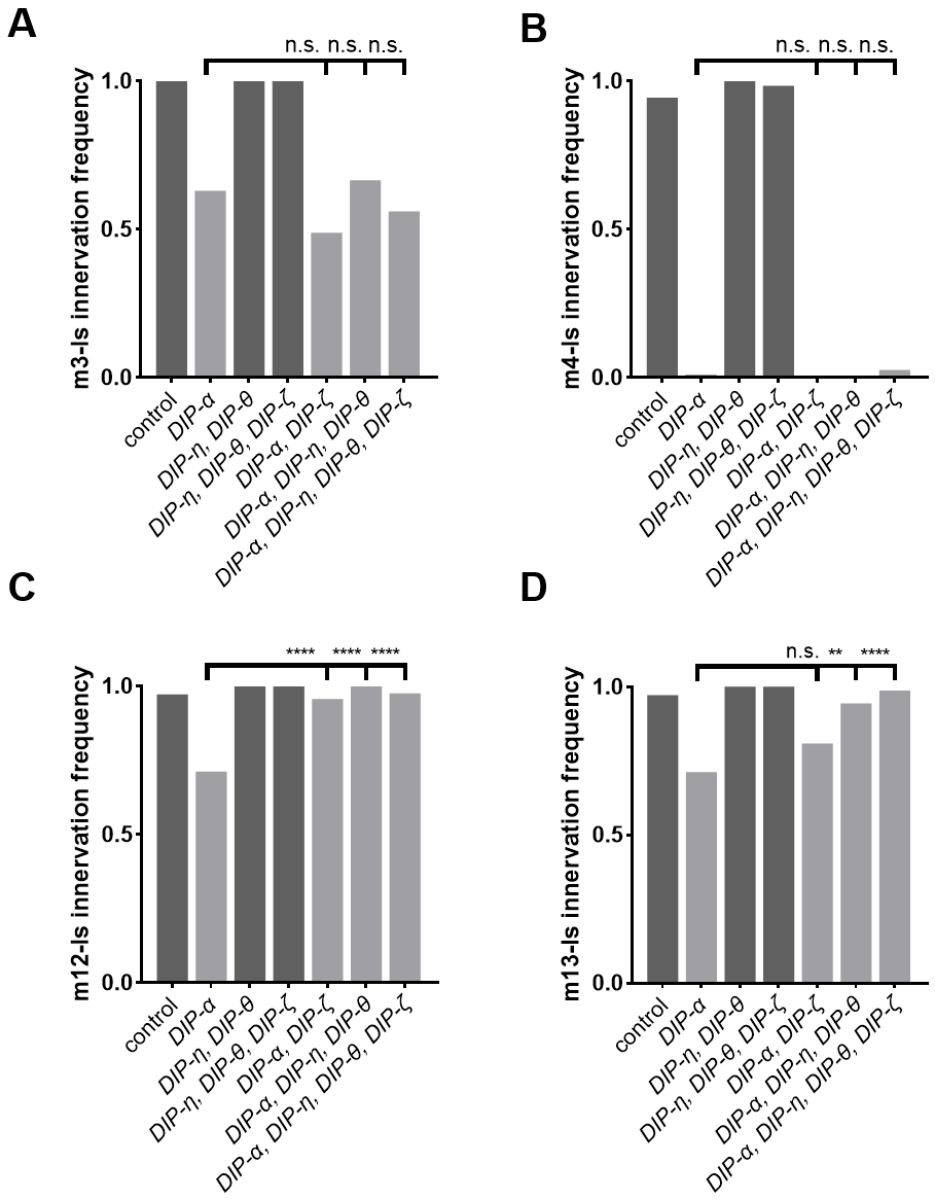

Figure B1 **Is innervation frequency of m3, m4, m12 and m13 in different *DIP* mutant backgrounds.**

(A-B) Innervation frequency of m3-Is (A) and m4-Is (B). In control animals, m3 and m4 have a near 100% Is innervation frequency, which is impaired by loss of *DIP-α* but not affected in other *DIP* mutants, including the *DIP-η* and *DIP-θ* double mutant and the *DIP-η*, *DIP-θ*, and *DIP-ζ* triple mutant. Mutating *DIP-α* together with other *DIPs* lead to a decrease of m3-Is and m4-Is innervation frequency, similar to the *DIP-α* single mutant. (C-D) Innervation frequency of m12-Is (C) and m13-Is (D). In control animals, m12 and m13 have a near 100% Is innervation frequency, which is impaired by loss of *DIP-α* but not affected in other *DIP* mutants, including the *DIP-η* and *DIP-θ* double mutant and the *DIP-η*, *DIP-θ*, and *DIP-ζ* triple mutant. When simultaneously mutating *DIP-α* with other *DIPs*, the Is innervation frequency is gradually rescued to a wild type level. One-way ANOVA, p=0.2500, 0.9996, 0.8481 in A, p=0.9990, 0.9999, 0.9737 in B, p<0.0001, <0.0001, <0.0001 in C, p=0.2887, 0.0054, <0.0001 in D.

APPENDIX C

Examining Ib synaptic machinery during cross-neuron plasticity

Synaptic transmission requires a presynaptic action potential and Ca^{2+} influx through Ca^{2+} channels to trigger synaptic vesicle fusion and neurotransmitter release (Chou et al., 2020). At the *Drosophila* larval NMJ, the abundance of the Ca^{2+} channel, Cacophony (Cac), correlates to the vesicle release probability (*Pr*) (Akbergenova et al., 2018). Thus, an interesting hypothesis is that cross-neuron plasticity induces an increase of Cac abundance at individual active zones (AZs) to allow for elevated evoked activity. Utilizing an endogenously tagged *cac* allele, *cac-GFP* (Gratz et al., 2019), I examined the number of Cac clusters (i.e., AZ numbers) and the protein abundance at individual clusters. I found that upon Is ablation, there is a significant increase of Cac clusters (Figure C1.A-C), indicating an increase of AZ number as previously observed with Brp staining (Figure 4.3A-B). However, at each AZ level, I did not observe a change in Cac abundance (Figure C1.D). These results suggest that the increase of spontaneous and evoke release during cross-neuron plasticity are not due to an increase in Cac.

Alternatively, although the *Pr* of individual AZ is not changed, the increased total AZ number could lead to an increase of total *Pr* per NMJ (Akbergenova et al., 2018; Ghelani and Sigrist, 2018; Harris and Littleton, 2015; Peled et al., 2014; Peled and Isacoff, 2011). In a previous study, we observed that the total mEPSP frequency did not decrease after Is ablation. Because Is MNs contribute approximately one third of the total mEPSP frequency (Newman et al., 2017), we concluded that the mEPSP frequency of Ib MNs were elevated to maintain total mEPSP frequency. However, we lack direct evidence to prove the increase of mEPSP frequency in Ib MNs. Here, in collaboration with Sihao Huang, we developed a Python program to recognize synaptic vesicle release events from GCaMP imaging. Specifically, the program

locates the position and timing of each release event from a recorded GCaMP movie and generates a release map of an entire NMJ (Figure C2.A-B). Together with post-hoc Brp staining, we can overlay the release map with the AZ map (Figure C2.C-D). This allows us to calculate the *Pr* of the entire NMJ. Currently we are attempting to capture a GCaMP movie with higher resolution using spinning disc microscopy, and we will adapt the code to the new data format.

Material and method

Drosophila and antibody resources

Drosophila lines used in this study are: *cac-GFP* (Gratz et al., 2019), *MHC-CD8::GCaMP6f-Sh* (Newman et al., 2017), *A8-GAL4, UAS-hid,rpr.* Antibodies used in this study are: Mouse anti-Bruchpilot (BRP) (1:50, nc82, Developmental Studies Hybridoma Bank), Goat anti-Mouse-Alexa568 (1:500, ThermoFisher #A11031) and Goat anti-HRP-Alexa647 (1:100, Jackson Immunological Research #123-605-021).

Dissection, immunostaining and image analysis

Dissection, immunostaining and GCaMP movie recording were performed as previous described in Chapter 2-4 unless otherwise noted.

Cac cluster analysis

To examine Cac clusters in Ib NMJs, we first utilized Imaris (Oxford Instruments) to create a HRP surface and set the Cac-GFP signal outside HRP surface to zero. Next, we generated a new surface for Cac-GFP with the following settings: surface detail = 0.100 μm, background subtraction = 0.800 μm, split touching objects = enable (diameter = 0.400 μm), filter = “Quality above 3.00”. To specifically analyze Cac clusters in the Ib NMJs, Cac clusters in Is NMJs were manually deleted.

GCaMP movie analysis

Movies are recorded using Nikon FS microscope with a 40× long-working distance objective. Ib NMJs from m4 are recorded. Movies are processed by customized python codes to generate an AZ map. Post-hoc Brp staining follows the standard immunostaining protocol. Python codes used in this study are available at https://github.com/YupuWang/GCaMP-imaging.

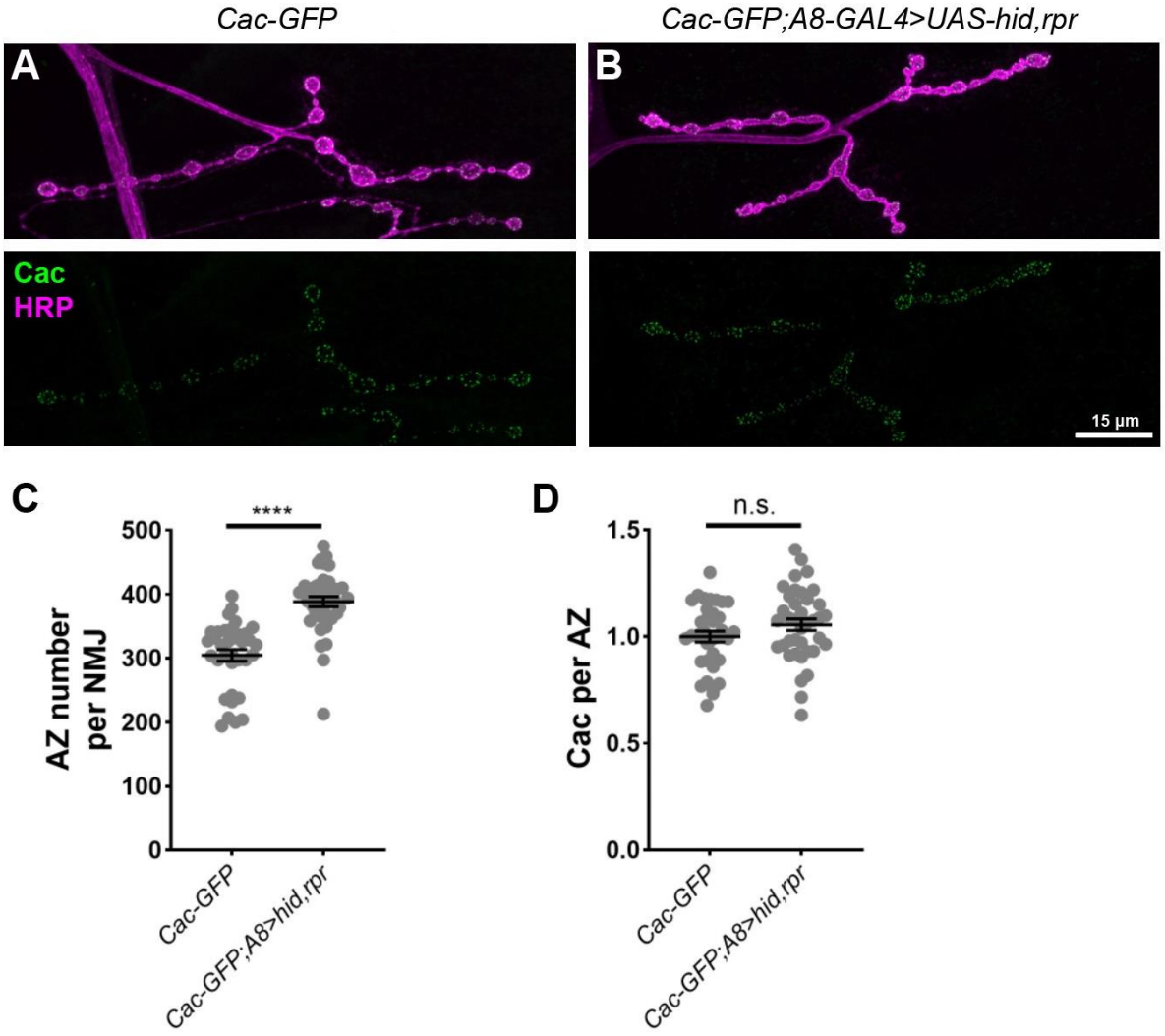

Figure C1 **Cac abundance is not changed at individual AZs.**
(A-B) Representative images showing Cac (green) and HRP (magenta) in controls (*Cac-GFP*) (A) and Is ablated animals (*Cac-GFP;A8-GAL4>UAS-hid,rpr*) (B). (C) Quantification of AZ number per NMJ in control and Is ablated animals revealed significant increase of AZ number upon Is ablation ($t_{(71)}$=7.004, p<0.0001, unpaired t test). (D) Quantification of Cac abundance per AZ in control and Is ablated animals revealed no change ($t_{(71)}$=1.446, p=0.1527, unpaired t test).

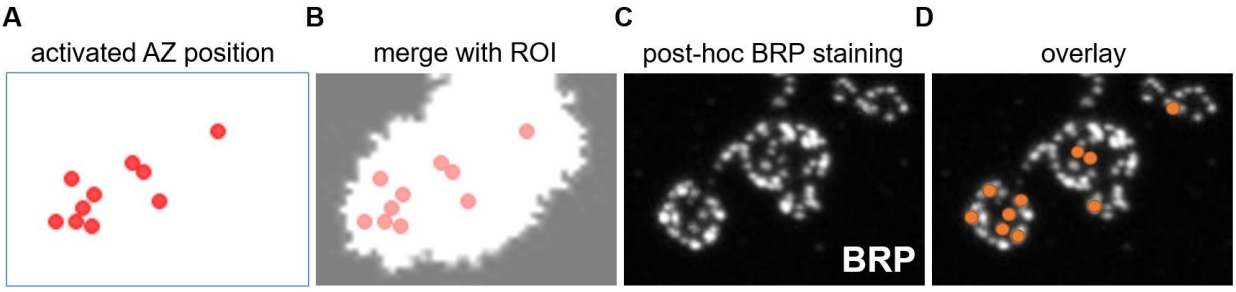

Figure C2 **A custom Python program recognizes release sites.**
(A) Release sites from a pre-selected region of interest (ROI) retrieved from a GCaMP movie. Each red dot represents one synaptic vesicle release event. (B) Release map is merged with the ROI. (C) Post-hoc BRP immunostaining shows the all AZ positions in boutons. (D) Overlay of the release map and BRP immunostaining reveals the position of active AZs.

REFERENCES

A. B Jorge, William A. 2002. Aging and Synaptic Plasticity: A Review. *Neural Plast* 9:217–232. doi:10.1155/np.2002.217

Abels ER, Breakefield XO. 2016. Introduction to Extracellular Vesicles: Biogenesis, RNA Cargo Selection, Content, Release, and Uptake. *Cell Mol Neurobiol* 36:301–312. doi:10.1007/s10571-016-0366-z

Ackerman SD, Perez-Catalan NA, Freeman MR, Doe CQ. 2021. Astrocytes close a motor circuit critical period. *Nature* 1–7. doi:10.1038/s41586-021-03441-2

Agudelo A, Amand VSt, Grissom L, Lafond D, Achilli T, Sahin A, Reenan R, Stilwell G. 2020. Age-dependent degeneration of an identified adult leg motor neuron in a Drosophila SOD1 model of ALS. *Biol Open* bio.049692. doi:10.1242/bio.049692

Aguilar JI, Dunn M, Mingote S, Karam CS, Farino ZJ, Sonders MS, Choi SJ, Grygoruk A, Zhang Y, Cela C, Choi BJ, Flores J, Freyberg RJ, McCabe BD, Mosharov EV, Krantz DE, Javitch JA, Sulzer D, Sames D, Rayport S, Freyberg Z. 2017. Neuronal Depolarization Drives Increased Dopamine Synaptic Vesicle Loading via VGLUT. *Neuron* 95:1074-1088.e7. doi:10.1016/j.neuron.2017.07.038

Ahtiainen A, Genocchi B, Tanskanen JMA, Barros MT, Hyttinen JAK, Lenk K. 2021. Astrocytes Exhibit a Protective Role in Neuronal Firing Patterns under Chemically Induced Seizures in Neuron–Astrocyte Co-Cultures. *Int J Mol Sci* 22:12770. doi:10.3390/ijms222312770

Akbergenova Y, Cunningham KL, Zhang YV, Weiss S, Littleton JT. 2018. Characterization of developmental and molecular factors underlying release heterogeneity at Drosophila synapses. *Elife* 7:e38268. doi:10.7554/elife.38268

Akbergenova Y, Littleton JT. 2017. Pathogenic Huntington Alters BMP Signaling and Synaptic Growth through Local Disruptions of Endosomal Compartments. *J Neurosci* 37:3425–3439. doi:10.1523/jneurosci.2752-16.2017

Altenhein B, Cattenoz PB, Giangrande A. 2016. The early life of a fly glial cell. *Wiley Interdiscip Rev Dev Biology* 5:67–84. doi:10.1002/wdev.200

Andreae LC, Burrone J. 2018. The role of spontaneous neurotransmission in synapse and circuit development. *J Neurosci Res* 96:354–359. doi:10.1002/jnr.24154

Aponte-Santiago NA, Littleton JT. 2020. Synaptic Properties and Plasticity Mechanisms of Invertebrate Tonic and Phasic Neurons. *Frontiers in Physiology* 11:611982. doi:10.3389/fphys.2020.611982

Aponte-Santiago NA, Ormerod KG, Akbergenova Y, Littleton JT. 2020. Synaptic plasticity induced by differential manipulation of tonic and phasic motoneurons in Drosophila. *J Neurosci Official J Soc Neurosci* JN-RM-0925-20. doi:10.1523/jneurosci.0925-20.2020

Ashley J, Cordy B, Lucia D, Fradkin LG, Budnik V, Thomson T. 2018. Retrovirus-like Gag Protein Arc1 Binds RNA and Traffics across Synaptic Boutons. *Cell* 172:262-274.e11. doi:10.1016/j.cell.2017.12.022

Ashley J, Sorrentino V, Lobb-Rabe M, Nagarkar-Jaiswal S, Tan L, Xu S, Xiao Q, Zinn K, Carrillo RA. 2019. Transsynaptic interactions between IgSF proteins DIP-α and Dpr10 are required for motor neuron targeting specificity. *eLife* 8:e42690. doi:10.7554/eLife.42690

Avalos CB, Maier GL, Bruggmann R, Sprecher SG. 2019. Single cell transcriptome atlas of the Drosophila larval brain. *Elife* 8:e50354. doi:10.7554/elife.50354

Awasaki T, Tatsumi R, Takahashi K, Arai K, Nakanishi Y, Ueda R, Ito K. 2006. Essential Role of the Apoptotic Cell Engulfment Genes draper and ced-6 in Programmed Axon Pruning during Drosophila Metamorphosis. *Neuron* 50:855–867. doi:10.1016/j.neuron.2006.04.027

Babadi B, Abbott LF. 2010. Intrinsic Stability of Temporally Shifted Spike-Timing Dependent Plasticity. *Plos Comput Biol* 6:e1000961. doi:10.1371/journal.pcbi.1000961

Banerjee S, Bainton RJ, Mayer N, Beckstead R, Bhat MA. 2008. Septate junctions are required for ommatidial integrity and blood–eye barrier function in Drosophila. *Dev Biol* 317:585–599. doi:10.1016/j.ydbio.2008.03.007

Barish S, Nuss S, Strunilin I, Bao S, Mukherjee S, Jones CD, Volkan PC. 2018. Combinations of DIPs and Dprs control organization of olfactory receptor neuron terminals in Drosophila. *Plos Genet* 14:e1007560. doi:10.1371/journal.pgen.1007560

Bate M. 1990. The embryonic development of larval muscles in Drosophila. *Dev Camb Engl* 110:791–804.

Bauke A-C, Sasse S, Matzat T, Klämbt C. 2015. A transcriptional network controlling glial development in the Drosophila visual system. *Development* 142:2184–2193. doi:10.1242/dev.119750

Baumann N, Pham-Dinh D. 2001. Biology of Oligodendrocyte and Myelin in the Mammalian Central Nervous System. *Physiol Rev* 81:871–927. doi:10.1152/physrev.2001.81.2.871

Beckervordersandforth RM, Rickert C, Altenhein B, Technau GM. 2008. Subtypes of glial cells in the Drosophila embryonic ventral nerve cord as related to lineage and gene expression. *Mech Develop* 125:542–557. doi:10.1016/j.mod.2007.12.004

Berry KP, Nedivi E. 2017. Spine Dynamics: Are They All the Same? *Neuron* 96:43–55. doi:10.1016/j.neuron.2017.08.008

Bhalla US. 2008. How To Record a Million Synaptic Weights in a Hippocampal Slice. *Plos Comput Biol* 4:e1000098. doi:10.1371/journal.pcbi.1000098

Bhatheja K, Field J. 2006. Schwann cells: Origins and role in axonal maintenance and regeneration. *Int J Biochem Cell Biology* 38:1995–1999. doi:10.1016/j.biocel.2006.05.007

Bittern J, Pogodalla N, Ohm H, Brüser L, Kottmeier R, Schirmeier S, Klämbt C. 2020. Neuron-Glia Interaction in the Drosophila nervous system. *Dev Neurobiol*. doi:10.1002/dneu.22737

Bloom T. 1996. Patterning the Drosophila embryo. *Curr Biol* 6:6–8. doi:10.1016/s0960-9822(02)00406-2

Böhme MA, McCarthy AW, Grasskamp AT, Beuschel CB, Goel P, Jusyte M, Laber D, Huang S, Rey U, Petzoldt AG, Lehmann M, Göttfert F, Haghighi P, Hell SW, Owald D, Dickman D, Sigrist SJ, Walter AM. 2019. Rapid active zone remodeling consolidates presynaptic potentiation. *Nat Commun* 10:1085. doi:10.1038/s41467-019-08977-6

Bornstein B, Meltzer H, Adler R, Alyagor I, Berkun V, Cummings G, Reh F, Keren-Shaul H, David E, Riemensperger T, Schuldiner O. 2021. Transneuronal Dpr12/DIP-δ interactions facilitate compartmentalized dopaminergic innervation of Drosophila mushroom body axons. *Embo J* e105763. doi:10.15252/embj.2020105763

Bossing T, Technau GM, Doe CQ. 1996. huckebein is required for glial development and axon pathfinding in the neuroblast 1-1 and neuroblast 2-2 lineages in the Drosophila central nervous system. *Mech Develop* 55:53–64. doi:10.1016/0925-4773(95)00490-4

Broadie K, Bate M. 1993. Development of the embryonic neuromuscular synapse of Drosophila melanogaster. *J Neurosci* 13:144–166. doi:10.1523/jneurosci.13-01-00144.1993

Broadus J, Skeath JB, Spana EP, Bossing T, Technau G, Doe CQ. 1995. New neuroblast markers and the origin of the aCC/pCC neurons in the Drosophila central nervous system. *Mech Develop* 53:393–402. doi:10.1016/0925-4773(95)00454-8

Brönner G, Jäckle H. 1996. Regulation and function of the terminal gap gene huckebein in the Drosophila blastoderm. *Int J Dev Biology* 40:157–65.

Brovero SG, Fortier JC, Hu H, Lovejoy PC, Newell NR, Palmateer CM, Tzeng R-Y, Lee P-T, Zinn K, Arbeitman MN. 2021. Investigation of Drosophila fruitless neurons that express Dpr/DIP cell adhesion molecules. *Elife* 10:e63101. doi:10.7554/elife.63101

Brussel LV, Gerits A, Arckens L. 2011. Evidence for Cross-Modal Plasticity in Adult Mouse Visual Cortex Following Monocular Enucleation. *Cereb Cortex* 21:2133–2146. doi:10.1093/cercor/bhq286

Budnik V, Zhong Y, Wu C. 1990. Morphological plasticity of motor axons in Drosophila mutants with altered excitability. *J Neurosci* 10:3754–3768. doi:10.1523/jneurosci.10-11-03754.1990

Buhl LK, Jorquera RA, Akbergenova Y, Huntwork-Rodriguez S, Volfson D, Littleton JT. 2013. Differential regulation of evoked and spontaneous neurotransmitter release by C-terminal modifications of complexin. *Mol Cell Neurosci* 52:161–172. doi:10.1016/j.mcn.2012.11.009

Busche MA, Chen X, Henning HA, Reichwald J, Staufenbiel M, Sakmann B, Konnerth A. 2012. Critical role of soluble amyloid-β for early hippocampal hyperactivity in a mouse model of Alzheimer's disease. *Proc National Acad Sci* 109:8740–8745. doi:10.1073/pnas.1206171109

Carlson SD, Juang J-L, Hilgers SL, Garment MB. 2000. Blood Barriers of the Insect. *Annu Rev Entomol* 45:151–174. doi:10.1146/annurev.ento.45.1.151

Carrillo RA, Özkan E, Menon KP, Nagarkar-Jaiswal S, Lee P-T, Jeon M, Birnbaum ME, Bellen HJ, Garcia KC, Zinn K. 2015. Control of Synaptic Connectivity by a Network of Drosophila IgSF Cell Surface Proteins. *Cell* 163:1770–1782. doi:10.1016/j.cell.2015.11.022

Carvalho AL, Caldeira MV, Santos SD, Duarte CB. 2008. Role of the brain-derived neurotrophic factor at glutamatergic synapses. *Brit J Pharmacol* 153:S310–S324. doi:10.1038/sj.bjp.0707509

Chang TN, Keshishian H. 1996. Laser Ablation of Drosophila Embryonic Motoneurons Causes Ectopic Innervation of Target Muscle Fibers. *J Neurosci* 16:5715–5726. doi:10.1523/jneurosci.16-18-05715.1996

Chen C, Agrawal S, Mark B, Mamiya A, Sustar A, Phelps JS, Lee W-CA, Dickson BJ, Card GM, Tuthill JC. 2021. Functional architecture of neural circuits for leg proprioception in Drosophila. *Curr Biol*. doi:10.1016/j.cub.2021.09.035

Chen T-W, Wardill TJ, Sun Y, Pulver SR, Renninger SL, Baohan A, Schreiter ER, Kerr RA, Orger MB, Jayaraman V, Looger LL, Svoboda K, Kim DS. 2013. Ultrasensitive fluorescent proteins for imaging neuronal activity. *Nature* 499:295–300. doi:10.1038/nature12354

Cheng S, Ashley J, Kurleto JD, Lobb-Rabe M, Park YJ, Carrillo RA, Özkan E. 2019a. Molecular basis of synaptic specificity by immunoglobulin superfamily receptors in Drosophila. *Elife* 8:e41028. doi:10.7554/elife.41028

Cheng S, Park Y, Kurleto JD, Jeon M, Zinn K, Thornton JW, Özkan E. 2019b. Family of neural wiring receptors in bilaterians defined by phylogenetic, biochemical, and structural evidence. *Proc National Acad Sci* 116:201818631. doi:10.1073/pnas.1818631116

Chiba A, Snow P, Keshishian H, Hotta Y. 1995. Fasciclin III as a synaptic target recognition molecule in Drosophila. *Nature* 374:166–168. doi:10.1038/374166a0

Chistiakova M, Ilin V, Roshchin M, Bannon N, Malyshev A, Kisvárday Z, Volgushev M. 2019. Distinct Heterosynaptic Plasticity in Fast Spiking and Non-Fast-Spiking Inhibitory Neurons in Rat Visual Cortex. *J Neurosci* 39:6865–6878. doi:10.1523/jneurosci.3039-18.2019

Cho K-O, Hunt CA, Kennedy MB. 1992. The rat brain postsynaptic density fraction contains a homolog of the drosophila discs-large tumor suppressor protein. *Neuron* 9:929–942. doi:10.1016/0896-6273(92)90245-9

Cho RW, Buhl LK, Volfson D, Tran A, Li F, Akbergenova Y, Littleton JT. 2015. Phosphorylation of Complexin by PKA Regulates Activity-Dependent Spontaneous Neurotransmitter Release and Structural Synaptic Plasticity. *Neuron* 88:749–761. doi:10.1016/j.neuron.2015.10.011

Cho RW, Kümmel D, Li F, Baguley SW, Coleman J, Rothman JE, Littleton JT. 2014. Genetic analysis of the Complexin trans-clamping model for cross-linking SNARE complexes in vivo. *Proc National Acad Sci* 111:10317–10322. doi:10.1073/pnas.1409311111

Cho RW, Song Y, Littleton JT. 2010. Comparative analysis of Drosophila and mammalian complexins as fusion clamps and facilitators of neurotransmitter release. *Mol Cell Neurosci* 45:389–397. doi:10.1016/j.mcn.2010.07.012

Choi BJ, Imlach WL, Jiao W, Wolfram V, Wu Y, Grbic M, Cela C, Baines RA, Nitabach MN, McCabe BD. 2014. Miniature Neurotransmission Regulates Drosophila Synaptic Structural Maturation. *Neuron* 82:618–634. doi:10.1016/j.neuron.2014.03.012

Choi JC, Park D, Griffith LC. 2004. Electrophysiological and Morphological Characterization of Identified Motor Neurons in the Drosophila Third Instar Larva Central Nervous System. *J Neurophysiol* 91:2353–2365. doi:10.1152/jn.01115.2003

Chou VT, Johnson SA, Vactor DV. 2020. Synapse development and maturation at the drosophila neuromuscular junction. *Neural Dev* 15:11. doi:10.1186/s13064-020-00147-5

Chu-LaGraff Q, Schmid A, Leidel J, Bro¨nner G, Ja¨ckle H, Doe CQ. 1995. huckebein specifies aspects of CNS precursor identity required for motoneuron axon pathfinding. *Neuron* 15:1041–1051. doi:10.1016/0896-6273(95)90093-4

Citri A, Malenka RC. 2008. Synaptic Plasticity: Multiple Forms, Functions, and Mechanisms. *Neuropsychopharmacol* 33:18–41. doi:10.1038/sj.npp.1301559

Cosmanescu F, Katsamba PS, Sergeeva AP, Ahlsen G, Patel SD, Brewer JJ, Tan L, Xu S, Xiao Q, Nagarkar-Jaiswal S, Nern A, Bellen HJ, Zipursky SL, Honig B, Shapiro L. 2018. Neuron-Subtype-Specific Expression, Interaction Affinities, and Specificity Determinants of DIP/Dpr Cell Recognition Proteins. *Neuron* 100:1385-1400.e6. doi:10.1016/j.neuron.2018.10.046

Courgeon M, Desplan C. 2019. Coordination between stochastic and deterministic specification in the Drosophila visual system. *Science* 366:eaay6727. doi:10.1126/science.aay6727

Courtine G, Gerasimenko Y, Brand R van den, Yew A, Musienko P, Zhong H, Song B, Ao Y, Ichiyama RM, Lavrov I, Roy RR, Sofroniew MV, Edgerton VR. 2009. Transformation of nonfunctional spinal circuits into functional states after the loss of brain input. *Nat Neurosci* 12:1333–1342. doi:10.1038/nn.2401

Crews ST. 2019. Drosophila Embryonic CNS Development: Neurogenesis, Gliogenesis, Cell Fate, and Differentiation. *Genetics* 213:1111–1144. doi:10.1534/genetics.119.300974

Crews ST. 2010. Axon–glial interactions at the Drosophila CNS midline. *Cell Adhes Migr* 4:67–71. doi:10.4161/cam.4.1.10208

Curry MJ, Gordon G. 1972. The spinal input to the posterior group in the cat. An electrophysiological investigation. *Brain Res* 44:417–437. doi:10.1016/0006-8993(72)90312-5

Daiber T, VanderZwan-Butler CJ, Bashaw GJ, Evans TA. 2021. Conserved and divergent aspects of Robo receptor signaling and regulation between Drosophila Robo1 and C. elegans SAX-3. *Genetics* 217:iyab018. doi:10.1093/genetics/iyab018

Dana H, Sun Y, Mohar B, Hulse BK, Kerlin AM, Hasseman JP, Tsegaye G, Tsang A, Wong A, Patel R, Macklin JJ, Chen Y, Konnerth A, Jayaraman V, Looger LL, Schreiter ER, Svoboda K, Kim DS. 2019. High-performance calcium sensors for imaging activity in neuronal populations and microcompartments. *Nat Methods* 16:649–657. doi:10.1038/s41592-019-0435-6

Daniels RW, Collins CA, Chen K, Gelfand MV, Featherstone DE, DiAntonio A. 2006. A Single Vesicular Glutamate Transporter Is Sufficient to Fill a Synaptic Vesicle. *Neuron* 49:11–16. doi:10.1016/j.neuron.2005.11.032

Davis GW, Müller M. 2015. Homeostatic Control of Presynaptic Neurotransmitter Release. *Annual Review of Physiology* 77:251–270. doi:10.1146/annurev-physiol-021014-071740

Davis GW, Schuster CM, Goodman CS. 1997. Genetic Analysis of the Mechanisms Controlling Target Selection: Target-Derived Fasciclin II Regulates the Pattern of Synapse Formation. *Neuron* 19:561–573. doi:10.1016/s0896-6273(00)80372-4

DiAntonio A. 2006. Glutamate Receptors At The Drosophila Neuromuscular Junction. *Int Rev Neurobiol* 75:165–179. doi:10.1016/s0074-7742(06)75008-5

Diao Fengqiu, Ironfield H, Luan H, Diao Feici, Shropshire WC, Ewer J, Marr E, Potter CJ, Landgraf M, White BH. 2015. Plug-and-Play Genetic Access to Drosophila Cell Types using Exchangeable Exon Cassettes. *Cell Reports* 10:1410–1421. doi:10.1016/j.celrep.2015.01.059

Dickman DK, Lu Z, Meinertzhagen IA, Schwarz TL. 2006. Altered Synaptic Development and Active Zone Spacing in Endocytosis Mutants. *Curr Biol* 16:591–598. doi:10.1016/j.cub.2006.02.058

Doe CQ, Smouse D, Goodman CS. 1988. Control of neuronal fate by the Drosophila segmentation gene even-skipped. *Nature* 333:376–378. doi:10.1038/333376a0

Doherty J, Sheehan AE, Bradshaw R, Fox AN, Lu T-Y, Freeman MR. 2014. PI3K Signaling and Stat92E Converge to Modulate Glial Responsiveness to Axonal Injury. *Plos Biol* 12:e1001985. doi:10.1371/journal.pbio.1001985

Dong A, He K, Dudok B, Farrell JS, Guan W, Liput DJ, Puhl HL, Cai R, Wang H, Duan J, Albarran E, Ding J, Lovinger DM, Li B, Soltesz I, Li Y. 2021. A fluorescent sensor for spatiotemporally resolved imaging of endocannabinoid dynamics in vivo. *Nat Biotechnol* 1–12. doi:10.1038/s41587-021-01074-4

Draper I, Saha M, Stonebreaker H, Salomon RN, Matin B, Kang PB. 2019. The impact of Megf10/Drpr gain-of-function on muscle development in Drosophila. *Febs Lett* 593:680–696. doi:10.1002/1873-3468.13348

Duan X, Krishnaswamy A, De la Huerta I, Sanes JR. 2014. Type II Cadherins Guide Assembly of a Direction-Selective Retinal Circuit. *Cell* 158:793–807. doi:10.1016/j.cell.2014.06.047

Duan X, Krishnaswamy A, Laboulaye MA, Liu J, Peng Y-R, Yamagata M, Toma K, Sanes JR. 2018. Cadherin Combinations Recruit Dendrites of Distinct Retinal Neurons to a Shared Interneuronal Scaffold. *Neuron* 99:1145-1154.e6. doi:10.1016/j.neuron.2018.08.019

Erkkinen MG, Kim M-O, Geschwind MD. 2018. Clinical Neurology and Epidemiology of the Major Neurodegenerative Diseases. *Csh Perspect Biol* 10:a033118. doi:10.1101/cshperspect.a033118

Estacio-Gómez A, Díaz-Benjumea FJ. 2013. Roles of Hox genes in the patterning of the central nervous system of Drosophila. *Fly* 8:26–32. doi:10.4161/fly.27424

Evans CJ, Olson JM, Ngo KT, Kim E, Lee NE, Kuoy E, Patananan AN, Sitz D, Tran P, Do M-T, Yackle K, Cespedes A, Hartenstein V, Call GB, Banerjee U. 2009. G-TRACE: rapid Gal4-based cell lineage analysis in Drosophila. *Nat Methods* 6:603–605. doi:10.1038/nmeth.1356

Featherstone DE. 2005. An Essential Drosophila Glutamate Receptor Subunit That Functions in Both Central Neuropil and Neuromuscular Junction. *J Neurosci* 25:3199–3208. doi:10.1523/jneurosci.4201-04.2005

Feeney CJ, Karunanithi S, Pearce J, Govind CK, Atwood HL. 1998. Motor nerve terminals on abdominal muscles in larval flesh flies, Sarcophaga bullata: Comparisons with Drosophila. *J Comp Neurol* 402:197–209. doi:10.1002/(sici)1096-9861(19981214)402:2<197::aid-cne5>3.0.co;2-q

France G, Volianskis R, Ingram R, Bannister N, Rothärmel R, Irvine MW, Fang G, Burnell ES, Sapkota K, Costa BM, Chopra DA, Dravid SM, Michael-Titus AT, Monaghan DT, Georgiou J, Bortolotto ZA, Jane DE, Collingridge GL, Volianskis A. 2022. Differential regulation of

STP, LTP and LTD by structurally diverse NMDA receptor subunit-specific positive allosteric modulators. *Neuropharmacology* 202:108840. doi:10.1016/j.neuropharm.2021.108840

Frank CA, James TD, Müller M. 2020. Homeostatic control of Drosophila neuromuscular junction function. *Synapse* 74:e22133. doi:10.1002/syn.22133

Freeman MR. 2015. Drosophila Central Nervous System Glia. *Csh Perspect Biol* 7:a020552. doi:10.1101/cshperspect.a020552

Freeman MR, Delrow J, Kim J, Johnson E, Doe CQ. 2003. Unwrapping Glial Biology Gcm Target Genes Regulating Glial Development, Diversification, and Function. *Neuron* 38:567–580. doi:10.1016/s0896-6273(03)00289-7

Fricker M, Tolkovsky AM, Borutaite V, Coleman M, Brown GC. 2018. Neuronal Cell Death. *Physiol Rev* 98:813–880. doi:10.1152/physrev.00011.2017

Fuentes-Medel Y, Logan MA, Ashley J, Ataman B, Budnik V, Freeman MR. 2009. Glia and Muscle Sculpt Neuromuscular Arbors by Engulfing Destabilized Synaptic Boutons and Shed Presynaptic Debris. *Plos Biol* 7:e1000184. doi:10.1371/journal.pbio.1000184

Fullard JF, Baker NE. 2014. Signaling by the Engulfment Receptor Draper: A Screen in Drosophila melanogaster Implicates Cytoskeletal Regulators, Jun N-Terminal Kinase, and Yorkie. *Genetics* 199:117–134. doi:10.1534/genetics.114.172544

Gaffield MA, Betz WJ. 2006. Imaging synaptic vesicle exocytosis and endocytosis with FM dyes. *Nat Protoc* 1:2916–2921. doi:10.1038/nprot.2006.476

Garrett AM, Khalil A, Walton DO, Burgess RW. 2018. DSCAM promotes self-avoidance in the developing mouse retina by masking the functions of cadherin superfamily members. *Proc National Acad Sci* 115:201809430. doi:10.1073/pnas.1809430115

Genç Ö, Davis GW. 2019. Target-wide Induction and Synapse Type-Specific Robustness of Presynaptic Homeostasis. *Curr Biology Cb* 29:3863-3873.e2. doi:10.1016/j.cub.2019.09.036

Gerhard S, Andrade I, Fetter RD, Cardona A, Schneider-Mizell CM. 2017. Conserved neural circuit structure across Drosophila larval development revealed by comparative connectomics. *Elife* 6:e29089. doi:10.7554/elife.29089

Ghelani T, Sigrist SJ. 2018. Coupling the Structural and Functional Assembly of Synaptic Release Sites. *Front Neuroanat* 12:81. doi:10.3389/fnana.2018.00081

Goel P, Dickman D. 2021. Synaptic homeostats: latent plasticity revealed at the Drosophila neuromuscular junction. *Cell Mol Life Sci* 1–21. doi:10.1007/s00018-020-03732-3

Goel P, Khan M, Howard S, Kim G, Kiragasi B, Kikuma K, Dickman D. 2019. A Screen for Synaptic Growth Mutants Reveals Mechanisms That Stabilize Synaptic Strength. *J Neurosci* 39:4051–4065. doi:10.1523/jneurosci.2601-18.2019

Goel P, Li X, Dickman D. 2017. Disparate Postsynaptic Induction Mechanisms Ultimately Converge to Drive the Retrograde Enhancement of Presynaptic Efficacy. *Cell Reports* 21:2339–2347. doi:10.1016/j.celrep.2017.10.116

Gorczyca M, Augart C, Budnik V. 1993. Insulin-like receptor and insulin-like peptide are localized at neuromuscular junctions in Drosophila. *J Neurosci* 13:3692–3704. doi:10.1523/jneurosci.13-09-03692.1993

Gowda SBM, Salim S, Mohammad F. 2021. Anatomy and Neural Pathways Modulating Distinct Locomotor Behaviors in Drosophila Larva. *Biology* 10:90. doi:10.3390/biology10020090

Gratz SJ, Goel P, Bruckner JJ, Hernandez RX, Khateeb K, Macleod GT, Dickman D, O'Connor-Giles KM. 2019. Endogenous tagging reveals differential regulation of Ca2+ channels at single AZs during presynaptic homeostatic potentiation and depression. *J Neurosci* 39:3068–18. doi:10.1523/jneurosci.3068-18.2019

Griffith WH, DuBois DW, Fincher A, Peebles KA, Bizon JL, Murchison D. 2014. Characterization of age-related changes in synaptic transmission onto F344 rat basal forebrain cholinergic neurons using a reduced synaptic preparation. *J Neurophysiol* 111:273–286. doi:10.1152/jn.00129.2013

Grueber WB, Jan LY, Jan YN. 2002. Tiling of the Drosophila epidermis by multidendritic sensory neurons. *Dev Camb Engl* 129:2867–78.

Grueber WB, Ye B, Yang C-H, Younger S, Borden K, Jan LY, Jan Y-N. 2007. Projections of Drosophila multidendritic neurons in the central nervous system: links with peripheral dendrite morphology. *Development* 134:55–64. doi:10.1242/dev.02666

Guan B, Hartmann B, Kho Y-H, Gorczyca M, Budnik V. 1996. The Drosophila tumor suppressor gene, dlg, is involved in structural plasticity at a glutamatergic synapse. *Curr Biol* 6:695–706. doi:10.1016/s0960-9822(09)00451-5

Guan Z, Quiñones-Frías MC, Akbergenova Y, Littleton JT. 2020. Drosophila Synaptotagmin 7 negatively regulates synaptic vesicle release and replenishment in a dosage-dependent manner. *Elife* 9:e55443. doi:10.7554/elife.55443

Halpern M, Chiba A, Johansen J, Keshishian H. 1991. Growth cone behavior underlying the development of stereotypic synaptic connections in Drosophila embryos. *J Neurosci* 11:3227–3238. doi:10.1523/jneurosci.11-10-03227.1991

Han C, Song Y, Xiao H, Wang D, Franc NC, Jan LY, Jan Y-N. 2014. Epidermal Cells Are the Primary Phagocytes in the Fragmentation and Clearance of Degenerating Dendrites in Drosophila. *Neuron* 81:544–560. doi:10.1016/j.neuron.2013.11.021

Han TH, Vicidomini R, Ramos CI, Wang Q, Nguyen P, Jarnik M, Lee C-H, Stawarski M, Hernandez RX, Macleod GT, Serpe M. 2020. Neto-α Controls Synapse Organization and Homeostasis at the Drosophila Neuromuscular Junction. *Cell Reports* 32:107866. doi:10.1016/j.celrep.2020.107866

Harris KP, Littleton JT. 2015. Transmission, Development, and Plasticity of Synapses. *Genetics* 201:345–75. doi:10.1534/genetics.115.176529

Hattori D, Chen Y, Matthews BJ, Salwinski L, Sabatti C, Grueber WB, Zipursky SL. 2009. Robust discrimination between self and non-self neurites requires thousands of Dscam1 isoforms. *Nature* 461:644–648. doi:10.1038/nature08431

Heckscher ES, Long F, Layden MJ, Chuang C-H, Manning L, Richart J, Pearson JC, Crews ST, Peng H, Myers E, Doe CQ. 2014. Atlas-builder software and the eNeuro atlas: resources for developmental biology and neuroscience. *Development* 141:2524–2532. doi:10.1242/dev.108720

Heckscher ES, Zarin AA, Faumont S, Clark MQ, Manning L, Fushiki A, Schneider-Mizell CM, Fetter RD, Truman JW, Zwart MF, Landgraf M, Cardona A, Lockery SR, Doe CQ. 2015. Even-Skipped+ Interneurons Are Core Components of a Sensorimotor Circuit that Maintains Left-Right Symmetric Muscle Contraction Amplitude. *Neuron* 88:314–329. doi:10.1016/j.neuron.2015.09.009

Hedrick NG, Harward SC, Hall CE, Murakoshi H, McNamara JO, Yasuda R. 2016. Rho GTPase complementation underlies BDNF-dependent homo- and heterosynaptic plasticity. *Nature* 538:104–108. doi:10.1038/nature19784

Herculano-Houzel S. 2012. The remarkable, yet not extraordinary, human brain as a scaled-up primate brain and its associated cost. *Proc National Acad Sci* 109:10661–10668. doi:10.1073/pnas.1201895109

Hilchen CM von, Beckervordersandforth RM, Rickert C, Technau GM, Altenhein B. 2008. Identity, origin, and migration of peripheral glial cells in the Drosophila embryo. *Mech Develop* 125:337–352. doi:10.1016/j.mod.2007.10.010

Hilchen CM von, Bustos ÁE, Giangrande A, Technau GM, Altenhein B. 2013. Predetermined embryonic glial cells form the distinct glial sheaths of the Drosophila peripheral nervous system. *Development* 140:3657–3668. doi:10.1242/dev.093245

Hilu-Dadia R, Hakim-Mishnaevski K, Levy-Adam F, Kurant E. 2018. Draper-mediated JNK signaling is required for glial phagocytosis of apoptotic neurons during Drosophila metamorphosis. *Glia* 66:1520–1532. doi:10.1002/glia.23322

Hoang B, Chiba A. 2001. Single-Cell Analysis of Drosophila Larval Neuromuscular Synapses. *Dev Biol* 229:55–70. doi:10.1006/dbio.2000.9983

Holland ND. 2016. Nervous systems and scenarios for the invertebrate-to-vertebrate transition. *Philosophical Transactions Royal Soc B Biological Sci* 371:20150047. doi:10.1098/rstb.2015.0047

Hong W, Mosca TJ, Luo L. 2012. Teneurins instruct synaptic partner matching in an olfactory map. *Nature* 484:201–207. doi:10.1038/nature10926

Honig B, Shapiro L. 2020. Adhesion Protein Structure, Molecular Affinities, and Principles of Cell-Cell Recognition. *Cell* 181:520–535. doi:10.1016/j.cell.2020.04.010

Hooper JE. 1986. Homeotic gene function in the muscles of Drosophila larvae. *Embo J* 5:2321–2329. doi:10.1002/j.1460-2075.1986.tb04500.x

Hoopfer ED, McLaughlin T, Watts RJ, Schuldiner O, O'Leary DDM, Luo L. 2006. Wlds Protection Distinguishes Axon Degeneration following Injury from Naturally Occurring Developmental Pruning. *Neuron* 50:883–895. doi:10.1016/j.neuron.2006.05.013

Hoopmann P, Rizzoli SO, Betz WJ. 2012. Imaging Synaptic Vesicle Recycling by Staining and Destaining Vesicles with FM Dyes. *Cold Spring Harb Protoc* 2012:pdb.prot067603. doi:10.1101/pdb.prot067603

Hsu J-M, Kang Y, Corty MM, Mathieson D, Peters OM, Freeman MR. 2020. Injury-Induced Inhibition of Bystander Neurons Requires dSarm and Signaling from Glia. *Neuron*. doi:10.1016/j.neuron.2020.11.012

Hu K, Carroll J, Rickman C, Davletov B. 2002. Action of Complexin on SNARE Complex*. *J Biol Chem* 277:41652–41656. doi:10.1074/jbc.m205044200

Hughes ME, Bortnick R, Tsubouchi A, Bäumer P, Kondo M, Uemura T, Schmucker D. 2007. Homophilic Dscam Interactions Control Complex Dendrite Morphogenesis. *Neuron* 54:417–427. doi:10.1016/j.neuron.2007.04.013

Huntwork S, Littleton JT. 2007. A complexin fusion clamp regulates spontaneous neurotransmitter release and synaptic growth. *Nat Neurosci* 10:1235–1237. doi:10.1038/nn1980

Hutson TH, Kathe C, Palmisano I, Bartholdi K, Hervera A, Virgiliis FD, McLachlan E, Zhou L, Kong G, Barraud Q, Danzi MC, Medrano-Fernandez A, Lopez-Atalaya JP, Boutillier AL, Sinha SH, Singh AK, Chaturbedy P, Moon LDF, Kundu TK, Bixby JL, Lemmon VP, Barco A, Courtine G, Giovanni SD. 2019. Cbp-dependent histone acetylation mediates axon regeneration induced by environmental enrichment in rodent spinal cord injury models. *Sci Transl Med* 11. doi:10.1126/scitranslmed.aaw2064

Imlach W, McCabe BD. 2009. Electrophysiological Methods for Recording Synaptic Potentials from the NMJ of Drosophila Larvae. *J Vis Exp Jove* 1109. doi:10.3791/1109

Inaki M, Shinza-Kameda M, Ismat A, Frasch M, Nose A. 2010. Drosophila Tey represses transcription of the repulsive cue Toll and generates neuromuscular target specificity. *Dev Camb Engl* 137:2139–46. doi:10.1242/dev.046672

Ito K, Urban J, Technau GM. 1995. Distribution, classification, and development ofDrosophila glial cells in the late embryonic and early larval ventral nerve cord. *Roux's Archives Dev Biology* 204:284–307. doi:10.1007/bf02179499

Jan LY, Jan YN. 1982. Antibodies to horseradish peroxidase as specific neuronal markers in Drosophila and in grasshopper embryos. *Proc National Acad Sci* 79:2700–2704. doi:10.1073/pnas.79.8.2700

Jan LY, Jan YN. 1976. Properties of the larval neuromuscular junction in Drosophila melanogaster. *J Physiology* 262:189–214. doi:10.1113/jphysiol.1976.sp011592

Jarecki J, Keshishian H. 1995. Role of neural activity during synaptogenesis in Drosophila. *J Neurosci Official J Soc Neurosci* 15:8177–90. doi:10.1523/jneurosci.15-12-08177.1995

Ji H, Sapar ML, Sarkar A, Wang B, Han C. 2022. Phagocytosis and self-destruction break down dendrites of Drosophila sensory neurons at distinct steps of Wallerian degeneration. *Proc National Acad Sci* 119:e2111818119. doi:10.1073/pnas.2111818119

Jontes JD. 2017. The Cadherin Superfamily in Neural Circuit Assembly. *Csh Perspect Biol* 10:a029306. doi:10.1101/cshperspect.a029306

Jorquera RA, Huntwork-Rodriguez S, Akbergenova Y, Cho RW, Littleton JT. 2012. Complexin Controls Spontaneous and Evoked Neurotransmitter Release by Regulating the Timing and Properties of Synaptotagmin Activity. *J Neurosci* 32:18234–18245. doi:10.1523/jneurosci.3212-12.2012

Jungenitz T, Beining M, Radic T, Deller T, Cuntz H, Jedlicka P, Schwarzacher SW. 2018. Structural homo- and heterosynaptic plasticity in mature and adult newborn rat hippocampal granule cells. *Proc National Acad Sci* 115:201801889. doi:10.1073/pnas.1801889115

Kanca O, Zirin J, Garcia-Marques J, Knight SM, Yang-Zhou D, Amador G, Chung H, Zuo Z, Ma L, He Y, Lin W-W, Fang Y, Ge M, Yamamoto S, Schulze KL, Hu Y, Spradling AC, Mohr SE, Perrimon N, Bellen HJ. 2019. An efficient CRISPR-based strategy to insert small and large fragments of DNA using short homology arms. *Elife* 8:e51539. doi:10.7554/elife.51539

Karunanithi S, Cylinder D, Ertekin D, Zalucki OH, Marin L, Lavidis NA, Atwood HL, Swinderen B van. 2020a. Proportional downscaling of glutamatergic release sites by the

general anesthetic propofol at Drosophila motor nerve terminals. *Eneuro* ENEURO.0422-19.2020. doi:10.1523/eneuro.0422-19.2020

Karunanithi S, Lin YQ, Odierna GL, Menon H, Gonzalez JM, Neely GG, Noakes PG, Lavidis NA, Moorhouse AJ, Swinderen B van. 2020b. Activity-Dependent Global Downscaling of Evoked Neurotransmitter Release across Glutamatergic Inputs in Drosophila. *J Neurosci* 40:8025–8041. doi:10.1523/jneurosci.0349-20.2020

Karunanithi S, Troup M, Swinderen B van. 2018. Using Drosophila to Understand General Anesthesia: From Synapses to Behavior. *Methods Enzymol* 602:153–176. doi:10.1016/bs.mie.2018.02.003

Kavalali ET. 2015. The mechanisms and functions of spontaneous neurotransmitter release. *Nat Rev Neurosci* 16:5–16. doi:10.1038/nrn3875

Kawasaki F, Felling R, Ordway RW. 2000. A Temperature-Sensitive Paralytic Mutant Defines a Primary Synaptic Calcium Channel in Drosophila. *J Neurosci* 20:4885–4889. doi:10.1523/jneurosci.20-13-04885.2000

Kim AJ. 2017. Descending Neurons in Drosophila: Bridging the Gap between Vision and Action. *J Neurosci* 37:3738–3740. doi:10.1523/jneurosci.0128-17.2017

Kim MD, Wen Y, Jan Y-N. 2009. Patterning and organization of motor neuron dendrites in the Drosophila larva. *Dev Biol* 336:213–221. doi:10.1016/j.ydbio.2009.09.041

Kinoshita T. 2020. Biosynthesis and biology of mammalian GPI-anchored proteins. *Open Biol* 10:190290. doi:10.1098/rsob.190290

Kittel RJ, Wichmann C, Rasse TM, Fouquet W, Schmidt M, Schmid A, Wagh DA, Pawlu C, Kellner RR, Willig KI, Hell SW, Buchner E, Heckmann M, Sigrist SJ. 2006. Bruchpilot Promotes Active Zone Assembly, Ca^{2+} Channel Clustering, and Vesicle Release. *Science* 312:1051–1054. doi:10.1126/science.1126308

Knodel MM, Geiger R, Ge L, Bucher D, Grillo A, Wittum G, Schuster CM, Queisser G. 2014. Synaptic bouton properties are tuned to best fit the prevailing firing pattern. *Front Comput Neurosc* 8:101. doi:10.3389/fncom.2014.00101

Koon AC, Ashley J, Barria R, DasGupta S, Brain R, Waddell S, Alkema MJ, Budnik V. 2010. Autoregulatory and paracrine control of synaptic and behavioral plasticity by octopaminergic signaling. *Nature neuroscience* 14:190–9. doi:10.1038/nn.2716

Kose H, Rose D, Zhu X, Chiba A. 1997. Homophilic synaptic target recognition mediated by immunoglobulin-like cell adhesion molecule Fasciclin III. *Dev Camb Engl* 124:4143–52.

Kottmeier R, Bittern J, Schoofs A, Scheiwe F, Matzat T, Pankratz M, Klämbt C. 2020. Wrapping glia regulates neuronal signaling speed and precision in the peripheral nervous system of Drosophila. *Nat Commun* 11:4491. doi:10.1038/s41467-020-18291-1

Kremer MC, Jung C, Batelli S, Rubin GM, Gaul U. 2017. The glia of the adult Drosophila nervous system. *Glia* 65:606–638. doi:10.1002/glia.23115

Krishnaswamy A, Yamagata M, Duan X, Hong YK, Sanes JR. 2015. Sidekick 2 directs formation of a retinal circuit that detects differential motion. *Nature* 524:466–470. doi:10.1038/nature14682

Kruijssen DLH, Wierenga CJ. 2019. Single Synapse LTP: A Matter of Context? *Front Cell Neurosci* 13:496. doi:10.3389/fncel.2019.00496

Kuraishi T, Nakagawa Y, Nagaosa K, Hashimoto Y, Ishimoto T, Moki T, Fujita Y, Nakayama H, Dohmae N, Shiratsuchi A, Yamamoto N, Ueda K, Yamaguchi M, Awasaki T, Nakanishi Y. 2009. Pretaporter, a Drosophila protein serving as a ligand for Draper in the phagocytosis of apoptotic cells. *Embo J* 28:3868–3878. doi:10.1038/emboj.2009.343

Kurant E, Axelrod S, Leaman D, Gaul U. 2008. Six-Microns-Under Acts Upstream of Draper in the Glial Phagocytosis of Apoptotic Neurons. *Cell* 133:498–509. doi:10.1016/j.cell.2008.02.052

Kurdyak P, Atwood HL, Stewart BA, Wu C-F. 1994. Differential physiology and morphology of motor axons to ventral longitudinal muscles in larvalDrosophila. *J Comp Neurology* 350:463–472. doi:10.1002/cne.903500310

Kurmangaliyev YZ, Yoo J, Valdes-Aleman J, Sanfilippo P, Zipursky SL. 2020. Transcriptional Programs of Circuit Assembly in the Drosophila Visual System. *Neuron* 108. doi:10.1016/j.neuron.2020.10.006

Kurusu M, Cording A, Taniguchi M, Menon K, Suzuki E, Zinn K. 2008. A screen of cell-surface molecules identifies leucine-rich repeat proteins as key mediators of synaptic target selection. *Neuron* 59:972–85. doi:10.1016/j.neuron.2008.07.037

Kwon JY, Dahanukar A, Weiss LA, Carlson JR. 2014. A map of taste neuron projections in the Drosophila CNS. *J Biosciences* 39:565–574. doi:10.1007/s12038-014-9448-6

Lahey T, Gorczyca M, Jia X-X, Budnik V. 1994. The drosophila tumor suppressor gene dlg is required for normal synaptic bouton structure. *Neuron* 13:823–835. doi:10.1016/0896-6273(94)90249-6

Landgraf M, Bossing T, Technau GM, Bate M. 1997. The Origin, Location, and Projections of the Embryonic Abdominal Motorneurons of Drosophila. *J Neurosci* 17:9642–9655. doi:10.1523/jneurosci.17-24-09642.1997

Landgraf M, Jeffrey V, Fujioka M, Jaynes JB, Bate M. 2003a. Embryonic Origins of a Motor System: Motor Dendrites Form a Myotopic Map in Drosophila. *Plos Biol* 1:e41. doi:10.1371/journal.pbio.0000041

Landgraf M, Sánchez-Soriano N, Technau GM, Urban J, Prokop A. 2003b. Charting the Drosophila neuropile: a strategy for the standardised characterisation of genetically amenable neurites. *Dev Biol* 260:207–225. doi:10.1016/s0012-1606(03)00215-x

Landgraf M, Thor S. 2006. Development of Drosophila motoneurons: Specification and morphology. *Semin Cell Dev Biol* 17:3–11. doi:10.1016/j.semcdb.2005.11.007

Lee H-K, Whitt JL. 2015. Cross-modal synaptic plasticity in adult primary sensory cortices. *Curr Opin Neurobiol* 35:119–126. doi:10.1016/j.conb.2015.08.002

Lee J, Wu C-F. 2010. Orchestration of Stepwise Synaptic Growth by K+ and Ca2+ Channels in Drosophila. *J Neurosci* 30:15821–15833. doi:10.1523/jneurosci.3448-10.2010

Lee J-H, Kim J, Noh S, Lee H, Lee SY, Mun JY, Park H, Chung W-S. 2020. Astrocytes phagocytose adult hippocampal synapses for circuit homeostasis. *Nature* 1–6. doi:10.1038/s41586-020-03060-3

Lee P-T, Zirin J, Kanca O, Lin W-W, Schulze KL, Li-Kroeger D, Tao R, Devereaux C, Hu Y, Chung V, Fang Y, He Y, Pan H, Ge M, Zuo Z, Housden BE, Mohr SE, Yamamoto S, Levis RW, Spradling AC, Perrimon N, Bellen HJ. 2018. A gene-specific T2A-GAL4 library for Drosophila. *Elife* 7:e35574. doi:10.7554/elife.35574

Lee T, Luo L. 2001. Mosaic analysis with a repressible cell marker (MARCM) for Drosophila neural development. *Trends Neurosci* 24:251–254. doi:10.1016/s0166-2236(00)01791-4

Lee T, Luo L. 1999. Mosaic Analysis with a Repressible Cell Marker for Studies of Gene Function in Neuronal Morphogenesis. *Neuron* 22:451–461. doi:10.1016/s0896-6273(00)80701-1

Li H. 2020. Single-cell RNA sequencing in Drosophila: Technologies and applications. *Wiley Interdiscip Rev Dev Biology* e396. doi:10.1002/wdev.396

Li H, Peng X, Cooper RL. 2002. Development of Drosophila larval neuromuscular junctions: maintaining synaptic strength. *Neuroscience* 115:505–513. doi:10.1016/s0306-4522(02)00380-9

Li H-H, Kroll JR, Lennox SM, Ogundeyi O, Jeter J, Depasquale G, Truman JW. 2014. A GAL4 Driver Resource for Developmental and Behavioral Studies on the Larval CNS of Drosophila. *Cell Reports* 8:897–908. doi:10.1016/j.celrep.2014.06.065

Li J, Han S, Li H, Udeshi ND, Svinkina T, Mani DR, Xu C, Guajardo R, Xie Q, Li T, Luginbuhl DJ, Wu B, McLaughlin CN, Xie A, Kaewsapsak P, Quake SR, Carr SA, Ting AY, Luo L.

2020. Cell-Surface Proteomic Profiling in the Fly Brain Uncovers Wiring Regulators. *Cell* 180:373-386.e15. doi:10.1016/j.cell.2019.12.029

Li X, Goel P, Chen C, Angajala V, Chen X, Dickman DK. 2018a. Synapse-specific and compartmentalized expression of presynaptic homeostatic potentiation. *Elife* 7:e34338. doi:10.7554/elife.34338

Li X, Goel P, Wondolowski J, Paluch J, Dickman D. 2018b. A Glutamate Homeostat Controls the Presynaptic Inhibition of Neurotransmitter Release. *Cell Reports* 23:1716–1727. doi:10.1016/j.celrep.2018.03.130

Lin A. 2003. Activation of the JNK signaling pathway: Breaking the brake on apoptosis. *Bioessays* 25:17–24. doi:10.1002/bies.10204

Lnenicka GA, Keshishian H. 2000. Identified motor terminals in Drosophila larvae show distinct differences in morphology and physiology. *J Neurobiol* 43:186–197. doi:10.1002/(sici)1097-4695(200005)43:2<186::aid-neu8>3.0.co;2-n

Logan J, Falck-Pedersen E, Darnell JE, Shenk T. 1987. A poly(A) addition site and a downstream termination region are required for efficient cessation of transcription by RNA polymerase II in the mouse beta maj-globin gene. *Proc National Acad Sci* 84:8306–8310. doi:10.1073/pnas.84.23.8306

Logan MA, Hackett R, Doherty J, Sheehan A, Speese SD, Freeman MR. 2012. Negative regulation of glial engulfment activity by Draper terminates glial responses to axon injury. *Nat Neurosci* 15:722–730. doi:10.1038/nn.3066

Lu T-Y, Doherty J, Freeman MR. 2014. DRK/DOS/SOS converge with Crk/Mbc/dCed-12 to activate Rac1 during glial engulfment of axonal debris. *Proc National Acad Sci* 111:12544–12549. doi:10.1073/pnas.1403450111

Lu T-Y, MacDonald JM, Neukomm LJ, Sheehan AE, Bradshaw R, Logan MA, Freeman MR. 2017. Axon degeneration induces glial responses through Draper-TRAF4-JNK signalling. *Nat Commun* 8:14355. doi:10.1038/ncomms14355

Lundell MJ, Chu-LaGraff Q, Doe CQ, Hirsh J. 1996. TheengrailedandhuckebeinGenes Are Essential for Development of Serotonin Neurons in theDrosophilaCNS. *Mol Cell Neurosci* 7:46–61. doi:10.1006/mcne.1996.0004

Ma D, Przybylski D, Abruzzi KC, Schlichting M, Li Q, Long X, Rosbash M. 2021. A transcriptomic taxonomy of Drosophila circadian neurons around the clock. *Elife* 10:e63056. doi:10.7554/elife.63056

MacDonald JM, Beach MG, Porpiglia E, Sheehan AE, Watts RJ, Freeman MR. 2006. The Drosophila Cell Corpse Engulfment Receptor Draper Mediates Glial Clearance of Severed Axons. *Neuron* 50:869–881. doi:10.1016/j.neuron.2006.04.028

MacNamee SE, Liu KE, Gerhard S, Tran CT, Fetter RD, Cardona A, Tolbert LP, Oland LA. 2016. Astrocytic glutamate transport regulates a Drosophila CNS synapse that lacks astrocyte ensheathment. *J Comp Neurol* 524:1979–1998. doi:10.1002/cne.24016

Magee JC, Cook EP. 2000. Somatic EPSP amplitude is independent of synapse location in hippocampal pyramidal neurons. *Nat Neurosci* 3:895–903. doi:10.1038/78800

Marrus SB. 2004. Differential Localization of Glutamate Receptor Subunits at the Drosophila Neuromuscular Junction. *J Neurosci* 24:1406–1415. doi:10.1523/jneurosci.1575-03.2004

Martin AR. 1955. A further study of the statistical composition of the end-plate potential. *J Physiology* 130:114–122. doi:10.1113/jphysiol.1955.sp005397

Mattson MP, Magnus T. 2006. Ageing and neuronal vulnerability. *Nat Rev Neurosci* 7:278–294. doi:10.1038/nrn1886

Matzat T, Sieglitz F, Kottmeier R, Babatz F, Engelen D, Klämbt C. 2015. Axonal wrapping in the Drosophila PNS is controlled by glia-derived neuregulin homolog Vein. *Development* 142:1336–1345. doi:10.1242/dev.116616

Mauss A, Tripodi M, Evers JF, Landgraf M. 2009. Midline Signalling Systems Direct the Formation of a Neural Map by Dendritic Targeting in the Drosophila Motor System. *Plos Biol* 7:e1000200. doi:10.1371/journal.pbio.1000200

Mazaheri F, Breus O, Durdu S, Haas P, Wittbrodt J, Gilmour D, Peri F. 2014. Distinct roles for BAI1 and TIM-4 in the engulfment of dying neurons by microglia. *Nat Commun* 5:4046. doi:10.1038/ncomms5046

McLaughlin CN, Perry-Richardson JJ, Coutinho-Budd JC, Broihier HT. 2019. Dying Neurons Utilize Innate Immune Signaling to Prime Glia for Phagocytosis during Development. *Dev Cell* 48:506-522.e6. doi:10.1016/j.devcel.2018.12.019

McPhee CK, Logan MA, Freeman MR, Baehrecke EH. 2010. Activation of autophagy during cell death requires the engulfment receptor Draper. *Nature* 465:1093–1096. doi:10.1038/nature09127

Megías M, Emri Z, Freund TF, Gulyás AI. 2001. Total number and distribution of inhibitory and excitatory synapses on hippocampal CA1 pyramidal cells. *Neuroscience* 102:527–540. doi:10.1016/s0306-4522(00)00496-6

Meng JL, Heckscher ES. 2020. Development of motor circuits: From neuronal stem cells and neuronal diversity to motor circuit assembly. *Curr Top Dev Biol*. doi:10.1016/bs.ctdb.2020.11.010

Meng JL, Wang Y, Carrillo RA, Heckscher E. 2020. Temporal transcription factors determine circuit membership by permanently altering motor neuron-to-muscle synaptic partnerships. *Elife* 9:e56898. doi:10.7554/elife.56898

Menon KP, Carrillo RA, Zinn K. 2013. Development and plasticity of the Drosophila larval neuromuscular junction. *Wiley Interdiscip Rev Dev Biology* 2:647–70. doi:10.1002/wdev.108

Menon KP, Kulkarni V, Takemura S, Anaya M, Zinn K. 2019. Interactions between Dpr11 and DIP-γ control selection of amacrine neurons in Drosophila color vision circuits. *Elife* 8:e48935. doi:10.7554/elife.48935

Merlo S, Spampinato SF, Sortino MA. 2019. Early compensatory responses against neuronal injury: A new therapeutic window of opportunity for Alzheimer's Disease? *Cns Neurosci Ther* 25:5–13. doi:10.1111/cns.13050

Merritt D, Whitington P. 1995. Central projections of sensory neurons in the Drosophila embryo correlate with sensory modality, soma position, and proneural gene function. *J Neurosci* 15:1755–1767. doi:10.1523/jneurosci.15-03-01755.1995

Merritt DJ, Murphey RK. 1992. Projections of leg proprioceptors within the CNS of the fly Phormia in relation to the generalized insect ganglion. *J Comp Neurol* 322:16–34. doi:10.1002/cne.903220103

Meyer D, Bonhoeffer T, Scheuss V. 2014. Balance and Stability of Synaptic Structures during Synaptic Plasticity. *Neuron* 82:430–443. doi:10.1016/j.neuron.2014.02.031

Miura SK, Martins A, Zhang KX, Graveley BR, Zipursky SL. 2013. Probabilistic Splicing of Dscam1 Establishes Identity at the Level of Single Neurons. *Cell* 155:1166–1177. doi:10.1016/j.cell.2013.10.018

Moraud EM, Capogrosso M, Formento E, Wenger N, DiGiovanna J, Courtine G, Micera S. 2016. Mechanisms Underlying the Neuromodulation of Spinal Circuits for Correcting Gait and Balance Deficits after Spinal Cord Injury. *Neuron* 89:814–828. doi:10.1016/j.neuron.2016.01.009

Morin F, Schwartz HG, O'Leary JL. 1951. EXPERIMENTAL STUDY OF THE SPINOTHALAMIC AND RELATED TRACTS. *Acta Psychiat Scand* 26:371–396. doi:10.1111/j.1600-0447.1951.tb09681.x

Mrestani A, Pauli M, Kollmannsberger P, Repp F, Kittel RJ, Eilers J, Doose S, Sauer M, Sirén A-L, Heckmann M, Paul MM. 2021. Active zone compaction correlates with presynaptic homeostatic potentiation. *Cell Reports* 37:109770. doi:10.1016/j.celrep.2021.109770

Mulcahy LA, Pink RC, Carter DRF. 2014. Routes and mechanisms of extracellular vesicle uptake. *J Extracell Vesicles* 3:24641. doi:10.3402/jev.v3.24641

Müller M, Genç Ö, Davis GW. 2015. RIM-binding protein links synaptic homeostasis to the stabilization and replenishment of high release probability vesicles. *Neuron* 85:1056–69. doi:10.1016/j.neuron.2015.01.024

Murphey RK, Possidente D, Pollack G, Merritt DJ. 1989. Modality-specific axonal projections in the CNS of the flies Phormia and Drosophila. *J Comp Neurol* 290:185–200. doi:10.1002/cne.902900203

Nagarkar-Jaiswal S, DeLuca SZ, Lee P-T, Lin W-W, Pan H, Zuo Z, Lv J, Spradling AC, Bellen HJ. 2015a. A genetic toolkit for tagging intronic MiMIC containing genes. *Elife* 4:e08469. doi:10.7554/elife.08469

Nagarkar-Jaiswal S, Lee P-T, Campbell ME, Chen K, Anguiano-Zarate S, Gutierrez MC, Busby T, Lin W-W, He Y, Schulze KL, Booth BW, Evans-Holm M, Venken KJ, Levis RW, Spradling AC, Hoskins RA, Bellen HJ. 2015b. A library of MiMICs allows tagging of genes and reversible, spatial and temporal knockdown of proteins in Drosophila. *Elife* 4:e05338. doi:10.7554/elife.05338

Nakai J, Ohkura M, Imoto K. 2001. A high signal-to-noise Ca2+ probe composed of a single green fluorescent protein. *Nat Biotechnol* 19:137–141. doi:10.1038/84397

Nakamura M, Baldwin D, Hannaford S, Palka J, Montell C. 2002. Defective Proboscis Extension Response (DPR), a Member of the Ig Superfamily Required for the Gustatory Response to Salt. *J Neurosci* 22:3463–3472. doi:10.1523/jneurosci.22-09-03463.2002

Namiki S, Ros IG, Morrow C, Rowell WJ, Card GM, Korff W, Dickinson MH. 2022. A population of descending neurons that regulates the flight motor of Drosophila. *Curr Biol* 32:1189-1196.e6. doi:10.1016/j.cub.2022.01.008

Nern A, Pfeiffer BD, Rubin GM. 2015. Optimized tools for multicolor stochastic labeling reveal diverse stereotyped cell arrangements in the fly visual system. *Proc National Acad Sci* 112:E2967–E2976. doi:10.1073/pnas.1506763112

Neuhuber WL, Wörl J. 2016. Enteric co-innervation of striated muscle in the esophagus: still enigmatic? *Histochem Cell Biol* 146:721–735. doi:10.1007/s00418-016-1500-1

Newman ZL, Bakshinskaya D, Schultz R, Kenny SJ, Moon S, Aghi K, Stanley C, Marnani N, Li R, Bleier J, Xu K, Isacoff EY. 2022. Determinants of synapse diversity revealed by super-resolution quantal transmission and active zone imaging. *Nat Commun* 13:229. doi:10.1038/s41467-021-27815-2

Newman ZL, Hoagland A, Aghi K, Worden K, Levy SL, Son JH, Lee LP, Isacoff EY. 2017. Input-Specific Plasticity and Homeostasis at the Drosophila Larval Neuromuscular Junction. *Neuron* 93:1388-1404.e10. doi:10.1016/j.neuron.2017.02.028

Nguyen CT, Stewart BA. 2016. The influence of postsynaptic structure on missing quanta at the Drosophila neuromuscular junction. *Bmc Neurosci* 17:53. doi:10.1186/s12868-016-0290-7

Nguyen TH, Vicidomini R, Choudhury SD, Coon SL, Iben J, Brody T, Serpe M. 2021. Single-Cell RNA Sequencing Analysis of the Drosophila Larval Ventral Cord. *Curr Protoc* 1:e38. doi:10.1002/cpz1.38

Niven JE, Graham CM, Burrows M. 2008. Diversity and Evolution of the Insect Ventral Nerve Cord. *Entomology* 53:253–271. doi:10.1146/annurev.ento.52.110405.091322

Nose A. 2012. Generation of neuromuscular specificity in Drosophila: novel mechanisms revealed by new technologies. *Front Mol Neurosci* 5:62. doi:10.3389/fnmol.2012.00062

Nose A, Mahajan VB, Goodman CS. 1992. Connectin: A homophilic cell adhesion molecule expressed on a subset of muscles and the motoneurons that innervate them in Drosophila. *Cell* 70:553–567. doi:10.1016/0092-8674(92)90426-d

Nose A, Umeda T, Takeichi M. 1997. Neuromuscular target recognition by a homophilic interaction of connectin cell adhesion molecules in Drosophila. *Dev Camb Engl* 124:1433–41.

Omoto JJ, Lovick JK, Hartenstein V. 2016. Origins of glial cell populations in the insect nervous system. *Curr Opin Insect Sci* 18:96–104. doi:10.1016/j.cois.2016.09.003

Omoto JJ, Yogi P, Hartenstein V. 2015. Origin and development of neuropil glia of the Drosophila larval and adult brain: Two distinct glial populations derived from separate progenitors. *Dev Biol* 404:2–20. doi:10.1016/j.ydbio.2015.03.004

Orgogozo V, Grueber WB. 2005. FlyPNS, a database of the Drosophila embryonic and larval peripheral nervous system. *Bmc Dev Biol* 5:4. doi:10.1186/1471-213x-5-4

Orr BO, Fetter RD, Davis GW. 2017. Retrograde semaphorin–plexin signalling drives homeostatic synaptic plasticity. *Nature* 550:109–113. doi:10.1038/nature24017

Osterloh JM, Yang J, Rooney TM, Fox AN, Adalbert R, Powell EH, Sheehan AE, Avery MA, Hackett R, Logan MA, MacDonald JM, Ziegenfuss JS, Milde S, Hou Y-J, Nathan C, Ding A, Brown RH, Conforti L, Coleman M, Tessier-Lavigne M, Züchner S, Freeman MR. 2012. dSarm/Sarm1 Is Required for Activation of an Injury-Induced Axon Death Pathway. *Science* 337:481–484. doi:10.1126/science.1223899

Özkan E, Carrillo RA, Eastman CL, Weiszmann R, Waghray D, Johnson KG, Zinn K, Celniker SE, Garcia KC. 2013. An Extracellular Interactome of Immunoglobulin and LRR Proteins Reveals Receptor-Ligand Networks. *Cell* 154:228–239. doi:10.1016/j.cell.2013.06.006

Park JH, Chung CG, Seo J, Lee B-H, Lee Y-S, Kweon JH, Lee SB. 2020. C9orf72-Associated Arginine-Rich Dipeptide Repeat Proteins Reduce the Number of Golgi Outposts and

Dendritic Branches in Drosophila Neurons. *Mol Cells* 43:821–830. doi:10.14348/molcells.2020.0130

Park Y-J, Kim S, Shim H-P, Park JH, Lee G, Kim T-Y, Jo M-C, Kwon A-Y, Lee M, Lee S, Yeo J, Chung H-L, Bellen HJ, Kwon S-H, Jeon S-H. 2021. Phosphatidylserine synthase plays an essential role in glia and affects development, as well as the maintenance of neuronal function. *Iscience* 24:102899. doi:10.1016/j.isci.2021.102899

Pauls D, Essen A von, Lyutova R, Giesen L van, Rosner R, Wegener C, Sprecher SG. 2014. Potency of Transgenic Effectors for Neurogenetic Manipulation in Drosophila Larvae. *Genetics* 199:25–37. doi:10.1534/genetics.114.172023

Peco E, Davla S, Camp D, Stacey SM, Landgraf M, Meyel DJ van. 2016. Drosophila astrocytes cover specific territories of the CNS neuropil and are instructed to differentiate by Prospero, a key effector of Notch. *Development* 143:1170–1181. doi:10.1242/dev.133165

Pederick DT, Lui JH, Gingrich EC, Xu C, Wagner MJ, Liu Y, He Z, Quake SR, Luo L. 2021. Reciprocal repulsions instruct the precise assembly of parallel hippocampal networks. *Science* 372:1068–1073. doi:10.1126/science.abg1774

Peled ES, Isacoff EY. 2011. Optical quantal analysis of synaptic transmission in wild-type and rab3-mutant Drosophila motor axons. *Nat Neurosci* 14:519–26. doi:10.1038/nn.2767

Peled ES, Newman ZL, Isacoff EY. 2014. Evoked and Spontaneous Transmission Favored by Distinct Sets of Synapses. *Curr Biol* 24:484–493. doi:10.1016/j.cub.2014.01.022

Peng J, Santiago IJ, Ahn C, Gur B, Tsui CK, Su Z, Xu C, Karakhanyan A, Silies M, Pecot MY. 2018. Drosophila Fezf coordinates laminar-specific connectivity through cell-intrinsic and cell-extrinsic mechanisms. *Elife* 7:e33962. doi:10.7554/elife.33962

Pereanu W, Shy D, Hartenstein V. 2005. Morphogenesis and proliferation of the larval brain glia in Drosophila. *Dev Biol* 283:191–203. doi:10.1016/j.ydbio.2005.04.024

Pereanu W, Spindler S, Cruz L, Hartenstein V. 2007. Tracheal development in the Drosophila brain is constrained by glial cells. *Dev Biol* 302:169–180. doi:10.1016/j.ydbio.2006.09.022

Pérez-Moreno JJ, O'Kane CJ. 2018. GAL4 Drivers Specific for Type Ib and Type Is Motor Neurons in Drosophila. *G3 Genes Genomes Genetics* g3.200809.2018. doi:10.1534/g3.118.200809

Perry S, Goel P, Tran NL, Pinales C, Buser C, Miller DL, Ganetzky B, Dickman D. 2020. Developmental arrest of Drosophila larvae elicits presynaptic depression and enables prolonged studies of neurodegeneration. *Development* 147:dev186312. doi:10.1242/dev.186312

Peters R. 2006. Ageing and the brain. *Postgrad Med J* 82:84. doi:10.1136/pgmj.2005.036665

Pfeiffer BD, Jenett A, Hammonds AS, Ngo T-TB, Misra S, Murphy C, Scully A, Carlson JW, Wan KH, Laverty TR, Mungall C, Svirskas R, Kadonaga JT, Doe CQ, Eisen MB, Celniker SE, Rubin GM. 2008. Tools for neuroanatomy and neurogenetics in Drosophila. *P Natl Acad Sci Usa* 105:9715–20. doi:10.1073/pnas.0803697105

Pfeiffer BD, Ngo T-TB, Hibbard KL, Murphy C, Jenett A, Truman JW, Rubin GM. 2010. Refinement of Tools for Targeted Gene Expression in Drosophila. *Genetics* 186:735–755. doi:10.1534/genetics.110.119917

Ponton F, Chapuis M-P, Pernice M, Sword GA, Simpson SJ. 2011. Evaluation of potential reference genes for reverse transcription-qPCR studies of physiological responses in Drosophila melanogaster. *J Insect Physiol* 57:840–850. doi:10.1016/j.jinsphys.2011.03.014

Purice MD, Speese SD, Logan MA. 2016. Delayed glial clearance of degenerating axons in aged Drosophila is due to reduced PI3K/Draper activity. *Nat Commun* 7:12871. doi:10.1038/ncomms12871

Ribot J, Breton R, Calvo C-F, Moulard J, Ezan P, Zapata J, Samama K, Moreau M, Bemelmans A-P, Sabatet V, Dingli F, Loew D, Milleret C, Billuart P, Dallérac G, Rouach N. 2021. Astrocytes close the mouse critical period for visual plasticity. *Science* 373:77–81. doi:10.1126/science.abf5273

Rose D, Zhu X, Kose H, Hoang B, Cho J, Chiba A. 1997. Toll, a muscle cell surface molecule, locally inhibits synaptic initiation of the RP3 motoneuron growth cone in Drosophila. *Dev Camb Engl* 124:1561–71.

Ruiz R, Cano R, Casañas JJ, Gaffield MA, Betz WJ, Tabares L. 2011. Active Zones and the Readily Releasable Pool of Synaptic Vesicles at the Neuromuscular Junction of the Mouse. *J Neurosci* 31:2000–2008. doi:10.1523/jneurosci.4663-10.2011

Salman MM, Al-Obaidi Z, Kitchen P, Loreto A, Bill RM, Wade-Martins R. 2021. Advances in Applying Computer-Aided Drug Design for Neurodegenerative Diseases. *Int J Mol Sci* 22:4688. doi:10.3390/ijms22094688

Salvadores N, Sanhueza M, Manque P, Court FA. 2017. Axonal Degeneration during Aging and Its Functional Role in Neurodegenerative Disorders. *Front Neurosci-switz* 11:451. doi:10.3389/fnins.2017.00451

Sanes JR, Zipursky SL. 2020. Synaptic Specificity, Recognition Molecules, and Assembly of Neural Circuits. *Cell* 181:536–556. doi:10.1016/j.cell.2020.04.008

Sanes JR, Zipursky SL. 2010. Design Principles of Insect and Vertebrate Visual Systems. *Neuron* 66:15–36. doi:10.1016/j.neuron.2010.01.018

Sauvola CW, Littleton JT. 2021. SNARE Regulatory Proteins in Synaptic Vesicle Fusion and Recycling. *Front Mol Neurosci* 14:733138. doi:10.3389/fnmol.2021.733138

Scanziani M, Häusser M. 2009. Electrophysiology in the age of light. *Nature* 461:930–939. doi:10.1038/nature08540

Schmid A, Chiba A, Doe CQ. 1999. Clonal analysis of Drosophila embryonic neuroblasts: neural cell types, axon projections and muscle targets. *Development* 126:4653–4689. doi:10.1242/dev.126.21.4653

Schneider-Mizell CM, Gerhard S, Longair M, Kazimiers T, Li F, Zwart MF, Champion A, Midgley FM, Fetter RD, Saalfeld S, Cardona A. 2016. Quantitative neuroanatomy for connectomics in Drosophila. *Elife* 5:e12059. doi:10.7554/elife.12059

Schnell B, Ros IG, Dickinson MH. 2017. A Descending Neuron Correlated with the Rapid Steering Maneuvers of Flying Drosophila. *Curr Biol* 27:1200–1205. doi:10.1016/j.cub.2017.03.004

Schrader S, Merritt DJ. 2000. Central projections of Drosophila sensory neurons in the transition from embryo to larva. *J Comp Neurol* 425:34–44. doi:10.1002/1096-9861(20000911)425:1<34::aid-cne4>3.0.co;2-g

Schwabe T, Bainton RJ, Fetter RD, Heberlein U, Gaul U. 2005. GPCR Signaling Is Required for Blood-Brain Barrier Formation in Drosophila. *Cell* 123:133–144. doi:10.1016/j.cell.2005.08.037

Sergeeva AP, Katsamba PS, Cosmanescu F, Brewer JJ, Ahlsen G, Mannepalli S, Shapiro L, Honig B. 2020. DIP/Dpr interactions and the evolutionary design of specificity in protein families. *Nat Commun* 11:2125. doi:10.1038/s41467-020-15981-8

Shacham-Silverberg V, Shalom HS, Goldner R, Golan-Vaishenker Y, Gurwicz N, Gokhman I, Yaron A. 2018. Phosphatidylserine is a marker for axonal debris engulfment but its exposure can be decoupled from degeneration. *Cell Death Dis* 9:1116. doi:10.1038/s41419-018-1155-z

Shao L, Zhang Y, Hao Y, Ping Y. 2022. Upregulation of IP3 receptor mediates APP-induced defects in synaptic downscaling and sleep homeostasis. *Cell Reports* 38:110594. doi:10.1016/j.celrep.2022.110594

Shen K, Bargmann CI. 2003. The Immunoglobulin Superfamily Protein SYG-1 Determines the Location of Specific Synapses in C. elegans. *Cell* 112:619–630. doi:10.1016/s0092-8674(03)00113-2

Shen K, Fetter RD, Bargmann CI. 2004. Synaptic Specificity Is Generated by the Synaptic Guidepost Protein SYG-2 and Its Receptor, SYG-1. *Cell* 116:869–881. doi:10.1016/s0092-8674(04)00251-x

Shishido E, Takeichi M, Nose A. 1998. Drosophila Synapse Formation: Regulation by Transmembrane Protein with Leu-Rich Repeats, CAPRICIOUS. *Science* 280:2118–2121. doi:10.1126/science.280.5372.2118

Shoykhet M, Clark RSB. 2011. Pediatric Critical Care (Fourth Edition). *Sect Iv Central Nerv Syst* 783–804. doi:10.1016/b978-0-323-07307-3.10057-6

Sigrist SJ, Reiff DF, Thiel PR, Steinert JR, Schuster CM. 2003. Experience-Dependent Strengthening of Drosophila Neuromuscular Junctions. *J Neurosci* 23:6546–6556. doi:10.1523/jneurosci.23-16-06546.2003

Silies M, Yuva Y, Engelen D, Aho A, Stork T, Klambt C. 2007. Glial Cell Migration in the Eye Disc. *J Neurosci* 27:13130–13139. doi:10.1523/jneurosci.3583-07.2007

Simon F, Konstantinides N. 2021. Single-cell transcriptomics in the Drosophila visual system: Advances and perspectives on cell identity regulation, connectivity, and neuronal diversity evolution. *Dev Biol* 479:107–122. doi:10.1016/j.ydbio.2021.08.001

Sink H, Whitington P. 1991a. Pathfinding in the central nervous system and periphery by identified embryonic Drosophila motor axons. *Development (Cambridge, England)* 112:307—316.

Sink H, Whitington PM. 1991b. Location and connectivity of abdominal motoneurons in the embryo and larva of Drosophila melanogaster. *J Neurobiol* 22:298–311. doi:10.1002/neu.480220309

Soba P, Zhu S, Emoto K, Younger S, Yang S-J, Yu H-H, Lee T, Jan LY, Jan Y-N. 2007. Drosophila Sensory Neurons Require Dscam for Dendritic Self-Avoidance and Proper Dendritic Field Organization. *Neuron* 54:403–416. doi:10.1016/j.neuron.2007.03.029

Song S, Miller KD, Abbott LF. 2000. Competitive Hebbian learning through spike-timing-dependent synaptic plasticity. *Nat Neurosci* 3:919–926. doi:10.1038/78829

Spéder P, Brand AH. 2018. Systemic and local cues drive neural stem cell niche remodelling during neurogenesis in Drosophila. *Elife* 7:e30413. doi:10.7554/elife.30413

Sperry RW. 1963. CHEMOAFFINITY IN THE ORDERLY GROWTH OF NERVE FIBER PATTERNS AND CONNECTIONS. *Proc National Acad Sci* 50:703–710. doi:10.1073/pnas.50.4.703

Srinivasan B, Samaddar S, Mylavarapu SVS, Clement JP, Banerjee S. 2021. Homeostatic scaling is driven by a translation-dependent degradation axis that recruits miRISC remodeling. *Plos Biol* 19:e3001432. doi:10.1371/journal.pbio.3001432

Stathakis DG, Hoover KB, You Z, Bryant PJ. 1997. Human Postsynaptic Density-95 (PSD95): Location of the Gene (DLG4) and Possible Function in Nonneural as Well as in Neural Tissues. *Genomics* 44:71–82. doi:10.1006/geno.1997.4848

Stewart BA, Atwood HL, Renger JJ, Wang J, Wu C-F. 1994. Improved stability of Drosophila larval neuromuscular preparations in haemolymph-like physiological solutions. *J Comp Physiology* 175:179–191. doi:10.1007/bf00215114

Stork T, Engelen D, Krudewig A, Silies M, Bainton RJ, Klambt C. 2008. Organization and Function of the Blood Brain Barrier in Drosophila. *J Neurosci* 28:587–597. doi:10.1523/jneurosci.4367-07.2008

Stork T, Sheehan A, Tasdemir-Yilmaz OE, Freeman MR. 2014. Neuron-Glia Interactions through the Heartless FGF Receptor Signaling Pathway Mediate Morphogenesis of Drosophila Astrocytes. *Neuron* 83:388–403. doi:10.1016/j.neuron.2014.06.026

Suárez I, Bodega G, Rubio M, Fernández B. 1995. Neuron-Glia Interrelations During Phylogeny, I. Phylogeny and Ontogeny of Glial Cells 41–57. doi:10.1007/978-1-59259-467-2_2

Szymczak-Workman AL, Vignali KM, Vignali DAA. 2012. Design and Construction of 2A Peptide-Linked Multicistronic Vectors. *Cold Spring Harb Protoc* 2012:pdb.ip067876. doi:10.1101/pdb.ip067876

Takai Y, Miyoshi J, Ikeda W, Ogita H. 2008. Nectins and nectin-like molecules: roles in contact inhibition of cell movement and proliferation. *Nat Rev Mol Cell Bio* 9:603–615. doi:10.1038/nrm2457

Takizawa E, Komatsu A, Tsujimura H. 2007. Identification of Common Excitatory Motoneurons in Drosophila melanogaster Larvae. *Zool Sci* 24:504–513. doi:10.2108/zsj.24.504

Tan L, Zhang KX, Pecot MY, Nagarkar-Jaiswal S, Lee P-T, Takemura S, McEwen JM, Nern A, Xu S, Tadros W, Chen Z, Zinn K, Bellen HJ, Morey M, Zipursky SL. 2015. Ig Superfamily Ligand and Receptor Pairs Expressed in Synaptic Partners in Drosophila. *Cell* 163:1756–69. doi:10.1016/j.cell.2015.11.021

Tang F, Barbacioru C, Wang Y, Nordman E, Lee C, Xu N, Wang X, Bodeau J, Tuch BB, Siddiqui A, Lao K, Surani MA. 2009. mRNA-Seq whole-transcriptome analysis of a single cell. *Nat Methods* 6:377–382. doi:10.1038/nmeth.1315

Tao C, Zhang X. 2014. Development of astrocytes in the vertebrate eye. *Dev Dynam* 243:1501–1510. doi:10.1002/dvdy.24190

Taoufik E, Kouroupi G, Zygogianni O, Matsas R. 2018. Synaptic dysfunction in neurodegenerative and neurodevelopmental diseases: an overview of induced pluripotent stem-cell-based disease models. *Open Biol* 8:180138. doi:10.1098/rsob.180138

Tung TT, Nagaosa K, Fujita Y, Kita A, Mori H, Okada R, Nonaka S, Nakanishi Y. 2013. Phosphatidylserine recognition and induction of apoptotic cell clearance by Drosophila engulfment receptor Draper. *J Biochem* 153:483–491. doi:10.1093/jb/mvt014

Unhavaithaya Y, Orr-Weaver TL. 2012. Polyploidization of glia in neural development links tissue growth to blood–brain barrier integrity. *Gene Dev* 26:31–36. doi:10.1101/gad.177436.111

Urbach R, Jussen D, Technau GM. 2016. Gene expression profiles uncover individual identities of gnathal neuroblasts and serial homologies in the embryonic CNS of Drosophila. *Dev Camb Engl* 143:1290–1301. doi:10.1242/dev.133546

Urbach R, Technau GM. 2003. Molecular markers for identified neuroblasts in the developing brain of Drosophila. *Development* 130:3621–3637. doi:10.1242/dev.00533

Valdes-Aleman J, Fetter RD, Sales EC, Heckman EL, Venkatasubramanian L, Doe CQ, Landgraf M, Cardona A, Zlatic M. 2021. Comparative Connectomics Reveals How Partner Identity, Location, and Activity Specify Synaptic Connectivity in Drosophila. *Neuron* 109. doi:10.1016/j.neuron.2020.10.004

Veling MW, Li Y, Veling MT, Litts C, Michki N, Liu H, Ye B, Cai D. 2019. Identification of Neuronal Lineages in the Drosophila Peripheral Nervous System with a “Digital” Multi-spectral Lineage Tracing System. *Cell Reports* 29:3303-3312.e3. doi:10.1016/j.celrep.2019.10.124

Venkatasubramanian L, Guo Z, Xu S, Tan L, Xiao Q, Nagarkar-Jaiswal S, Mann RS. 2019. Stereotyped terminal axon branching of leg motor neurons mediated by IgSF proteins DIP-α and Dpr10. *Elife* 8:e42692. doi:10.7554/elife.42692

Venken KJT, Schulze KL, Haelterman NA, Pan H, He Y, Evans-Holm M, Carlson JW, Levis RW, Spradling AC, Hoskins RA, Bellen HJ. 2011. MiMIC: a highly versatile transposon insertion resource for engineering Drosophila melanogaster genes. *Nat Methods* 8:737–743. doi:10.1038/nmeth.1662

Verhaart DrWJC, Kramer DrW. 1952. THE UNCROSSED PYRAMIDAL TRACT. *Acta Psychiat Scand* 27:181–200. doi:10.1111/j.1600-0447.1952.tb04651.x

Vicidomini R, Nguyen TH, Choudhury SD, Brody T, Serpe M. 2021. Assembly and Exploration of a Single Cell Atlas of the Drosophila Larval Ventral Cord. Identification of Rare Cell Types. *Curr Protoc* 1:e37. doi:10.1002/cpz1.37

Vilcaes AA, Chanaday NL, Kavalali ET. 2021. Interneuronal exchange and functional integration of synaptobrevin via extracellular vesicles. *Neuron* 109:971-983.e5. doi:10.1016/j.neuron.2021.01.007

Volianskis A, Collingridge GL, Jensen MS. 2013. The roles of STP and LTP in synaptic encoding. *Peerj* 1:e3. doi:10.7717/peerj.3

Volkenhoff A, Weiler A, Letzel M, Stehling M, Klämbt C, Schirmeier S. 2015. Glial Glycolysis Is Essential for Neuronal Survival in Drosophila. *Cell Metab* 22:437–447. doi:10.1016/j.cmet.2015.07.006

Walsh KT, Doe CQ. 2017. Drosophila embryonic type II neuroblasts: origin, temporal patterning, and contribution to the adult central complex. *Development* 144:4552–4562. doi:10.1242/dev.157826

Walter AM, Haucke V, Sigrist SJ. 2014. Neurotransmission: Spontaneous and Evoked Release Filing for Divorce. *Curr Biol* 24:R192–R194. doi:10.1016/j.cub.2014.01.037

Wan J, Peng W, Li X, Qian T, Song K, Zeng J, Deng F, Hao S, Feng J, Zhang P, Zhang Y, Zou J, Pan S, Shin M, Venton BJ, Zhu JJ, Jing M, Xu M, Li Y. 2021. A genetically encoded sensor for measuring serotonin dynamics. *Nat Neurosci* 1–7. doi:10.1038/s41593-021-00823-7

Wang J, Ma X, Yang JS, Zheng X, Zugates CT, Lee C-HJ, Lee T. 2004. Transmembrane/Juxtamembrane Domain-Dependent Dscam Distribution and Function during Mushroom Body Neuronal Morphogenesis. *Neuron* 43:663–672. doi:10.1016/j.neuron.2004.06.033

Wang J, Zhai Q, Chen Y, Lin E, Gu W, McBurney MW, He Z. 2005. A local mechanism mediates NAD-dependent protection of axon degeneration. *J Cell Biology* 170:349–355. doi:10.1083/jcb.200504028

Wang M, Li A, Sekiya M, Beckmann ND, Quan X, Schrode N, Fernando MB, Yu A, Zhu L, Cao J, Lyu L, Horgusluoglu E, Wang Q, Guo L, Wang Y, Neff R, Song W, Wang E, Shen Q, Zhou X, Ming C, Ho S-M, Vatansever S, Kaniskan HÜ, Jin J, Zhou M-M, Ando K, Ho L, Slesinger PA, Yue Z, Zhu J, Katsel P, Gandy S, Ehrlich ME, Fossati V, Noggle S, Cai D, Haroutunian V, Iijima KM, Schadt E, Brennand KJ, Zhang B. 2020. Transformative Network Modeling of Multi-omics Data Reveals Detailed Circuits, Key Regulators, and Potential Therapeutics for Alzheimer's Disease. *Neuron*. doi:10.1016/j.neuron.2020.11.002

Wang T, Jones RT, Whippen JM, Davis GW. 2016. α2δ-3 Is Required for Rapid Transsynaptic Homeostatic Signaling. *Cell Reports* 16:2875–2888. doi:10.1016/j.celrep.2016.08.030

Wang Y, Lobb-Rabe M, Ashley J, Anand V, Carrillo RA. 2021a. Structural and functional synaptic plasticity induced by convergent synapse loss in the Drosophila neuromuscular circuit. *J Neurosci* JN-RM-1492-20. doi:10.1523/jneurosci.1492-20.2020

Wang Y, Lobb-Rabe M, Ashley J, Chatterjee P, Anand V, Bellen HJ, Kanca O, Carrillo RA. 2021b. Systematic expression profiling of dprs and DIPs reveals cell surface codes in Drosophila larval peripheral neurons. *Biorxiv* 2021.10.20.465173. doi:10.1101/2021.10.20.465173

Wen W, Turrigiano GG. 2021. Developmental Regulation of Homeostatic Plasticity in Mouse Primary Visual Cortex. *J Neurosci* 41:9891–9905. doi:10.1523/jneurosci.1200-21.2021

Winberg ML, Mitchell KJ, Goodman CS. 1998. Genetic Analysis of the Mechanisms Controlling Target Selection: Complementary and Combinatorial Functions of Netrins, Semaphorins, and IgCAMs. *Cell* 93:581–591. doi:10.1016/s0092-8674(00)81187-3

Wit J de, Ghosh A. 2016. Specification of synaptic connectivity by cell surface interactions. *Nat Rev Neurosci* 17:4–4. doi:10.1038/nrn.2015.3

Wu H-H, Bellmunt E, Scheib JL, Venegas V, Burkert C, Reichardt LF, Zhou Z, Fariñas I, Carter BD. 2009. Glial precursors clear sensory neuron corpses during development via Jedi-1, an engulfment receptor. *Nat Neurosci* 12:1534–1541. doi:10.1038/nn.2446

Wu Z, He K, Chen Y, Li H, Pan S, Li B, Liu T, Xi F, Deng F, Wang H, Du J, Jing M, Li Y. 2022. A sensitive GRAB sensor for detecting extracellular ATP in vitro and in vivo. *Neuron* 110:770-782.e5. doi:10.1016/j.neuron.2021.11.027

Xie Q, Brbic M, Horns F, Kolluru SS, Jones RC, Li J, Reddy AR, Xie A, Kohani S, Li Z, McLaughlin CN, Li T, Xu C, Vacek D, Luginbuhl DJ, Leskovec J, Quake SR, Luo L, Li H. 2021. Temporal evolution of single-cell transcriptomes of Drosophila olfactory projection neurons. *Elife* 10:e63450. doi:10.7554/elife.63450

Xu C, Theisen E, Maloney R, Peng J, Santiago I, Yapp C, Werkhoven Z, Rumbaut E, Shum B, Tarnogorska D, Borycz J, Tan L, Courgeon M, Griffin T, Levin R, Meinertzhagen IA, Bivort B de, Drugowitsch J, Pecot MY. 2019. Control of Synaptic Specificity by Establishing a Relative Preference for Synaptic Partners. *Neuron* 103:865-877.e7. doi:10.1016/j.neuron.2019.06.006

Xu S, Sergeeva AP, Katsamba PS, Mannepalli S, Bahna F, Bimela J, Zipursky SL, Shapiro L, Honig B, Zinn K. 2022. Affinity requirements for control of synaptic targeting and neuronal cell survival by heterophilic IgSF cell adhesion molecules. *Cell Reports* 39:110618. doi:10.1016/j.celrep.2022.110618

Xu S, Sergeeva AP, Katsamba PS, Mannepalli S, Bahna F, Bimela J, Zipursky SL, Shapiro L, Honig B, Zinn K. 2021. Affinity requirements for control of synaptic targeting and neuronal cell survival by heterophilic IgSF cell adhesion molecules. *BioRxiv*. doi:10.1101/2021.02.16.431482

Xu S, Xiao Q, Cosmanescu F, Sergeeva AP, Yoo J, Lin Y, Katsamba PS, Ahlsen G, Kaufman J, Linaval NT, Lee P-T, Bellen HJ, Shapiro L, Honig B, Tan L, Zipursky SL. 2018. Interactions between the Ig-Superfamily Proteins DIP-α and Dpr6/10 Regulate Assembly of Neural Circuits. *Neuron* 100:1369-1384.e6. doi:10.1016/j.neuron.2018.11.001

Yamagata M. 2020. Structure and Functions of Sidekicks. *Front Mol Neurosci* 13:139. doi:10.3389/fnmol.2020.00139

Yamagata M, Sanes JR. 2019. Expression and Roles of the Immunoglobulin Superfamily Recognition Molecule Sidekick1 in Mouse Retina. *Front Mol Neurosci* 11:485. doi:10.3389/fnmol.2018.00485

Yeates CJ, Frank CA. 2021. Homeostatic Depression Shows Heightened Sensitivity to Synaptic Calcium. *Front Cell Neurosci* 15:618393. doi:10.3389/fncel.2021.618393

Yildirim K, Petri J, Kottmeier R, Klämbt C. 2019. Drosophila glia: Few cell types and many conserved functions. *Glia* 67:5–26. doi:10.1002/glia.23459

Yoshihara M, Rheuben MB, Kidokoro Y. 1997. Transition from Growth Cone to Functional Motor Nerve Terminal inDrosophila Embryos. *J Neurosci* 17:8408–8426. doi:10.1523/jneurosci.17-21-08408.1997

Zarin AA, Asadzadeh J, Hokamp K, McCartney D, Yang L, Bashaw GJ, Labrador J-P. 2014. A Transcription Factor Network Coordinates Attraction, Repulsion, and Adhesion Combinatorially to Control Motor Axon Pathway Selection. *Neuron* 81:1297–1311. doi:10.1016/j.neuron.2014.01.038

Zarin AA, Labrador J-P. 2019. Motor axon guidance in Drosophila. *Semin Cell Dev Biol* 85:36–47. doi:10.1016/j.semcdb.2017.11.013

Zarin AA, Mark B, Cardona A, Litwin-Kumar A, Doe CQ. 2019. A multilayer circuit architecture for the generation of distinct locomotor behaviors in Drosophila. *Elife* 8:e51781. doi:10.7554/elife.51781

Zhan X-L, Clemens JC, Neves G, Hattori D, Flanagan JJ, Hummel T, Vasconcelos ML, Chess A, Zipursky SL. 2004. Analysis of Dscam Diversity in Regulating Axon Guidance in Drosophila Mushroom Bodies. *Neuron* 43:673–686. doi:10.1016/j.neuron.2004.07.020

Zhang B, Stewart B. 2010. Electrophysiological Recording from Drosophila Larval Body-Wall Muscles. *Cold Spring Harb Protoc* 2010:pdb.prot5487. doi:10.1101/pdb.prot5487

Zhang H, Rigo F, Martinson HG. 2015. Poly(A) Signal-Dependent Transcription Termination Occurs through a Conformational Change Mechanism that Does Not Require Cleavage at the Poly(A) Site. *Mol Cell* 59:437–448. doi:10.1016/j.molcel.2015.06.008

Zhang X, Noyes NC, Zeng J, Li Y, Davis RL. 2019. Aversive Training Induces Both Presynaptic and Postsynaptic Suppression in Drosophila. *J Neurosci* 39:9164–9172. doi:10.1523/jneurosci.1420-19.2019

Zhou L, Schnitzler A, Agapite J, Schwartz LM, Steller H, Nambu JR. 1997. Cooperative functions of the reaper and head involution defective genes in the programmed cell death of Drosophila central nervous system midline cells. *Proc National Acad Sci* 94:5131–5136. doi:10.1073/pnas.94.10.5131

Ziegenfuss JS, Biswas R, Avery MA, Hong K, Sheehan AE, Yeung Y-G, Stanley ER, Freeman MR. 2008. Draper-dependent glial phagocytic activity is mediated by Src and Syk family kinase signalling. *Nature* 453:935–939. doi:10.1038/nature06901

Ziegenfuss JS, Doherty J, Freeman MR. 2012. Distinct molecular pathways mediate glial activation and engulfment of axonal debris after axotomy. *Nat Neurosci* 15:979–987. doi:10.1038/nn.3135

Zinn K, Özkan E. 2017. Neural immunoglobulin superfamily interaction networks. *Curr Opin Neurobiol* 45:99–105. doi:10.1016/j.conb.2017.05.010

Zipursky SL, Grueber WB. 2013. The Molecular Basis of Self-Avoidance. *Annu Rev Neurosci* 36:547–568. doi:10.1146/annurev-neuro-062111-150414

Zuko A, Bouyain S, Zwaag B van der, Burbach JPH. 2011. Contactins Structural aspects in relation to developmental functions in brain disease. *Adv Protein Chem Str* 84:143–180. doi:10.1016/b978-0-12-386483-3.00001-x